Engineering Hierarchical Functionalized-Nanowire and Nanotube Networks as Self-supported Electrodes for Electrochemical Applications: Sensors, Water Splitting, and Supercapacitors

Vom Fachbereich Material- und Geowissenschaften

der Technischen Universität Darmstadt

Zur Erlangung des akademischen Titels

Dr. rer. nat.

Genehmigte **Dissertation**

Von

Khaled Amin, M. Sc.

aus Beheira, Ägypten

Darmstadt 2023

D 17

Engineering Hierarchical Functionalized-Nanowire and Nanotube Networks as Self-supported Electrodes for Electrochemical Applications: Sensors, Water Splitting, and Supercapacitors

Vom Fachbereich Material- und Geowissenschaften

der Technischen Universität Darmstadt

Zur Erlangung des akademischen Titels **Dr. rer. nat.**

Genehmigte Dissertation von **Khaled Amin, M. Sc.,**

aus Beheira, Ägypten

1. Gutachten: Prof. Dr. Wolfgang Ensinger

2. Gutachten: Prof. Dr. Leopoldo Molina-Luna

Darmstadt 2023 – D 17

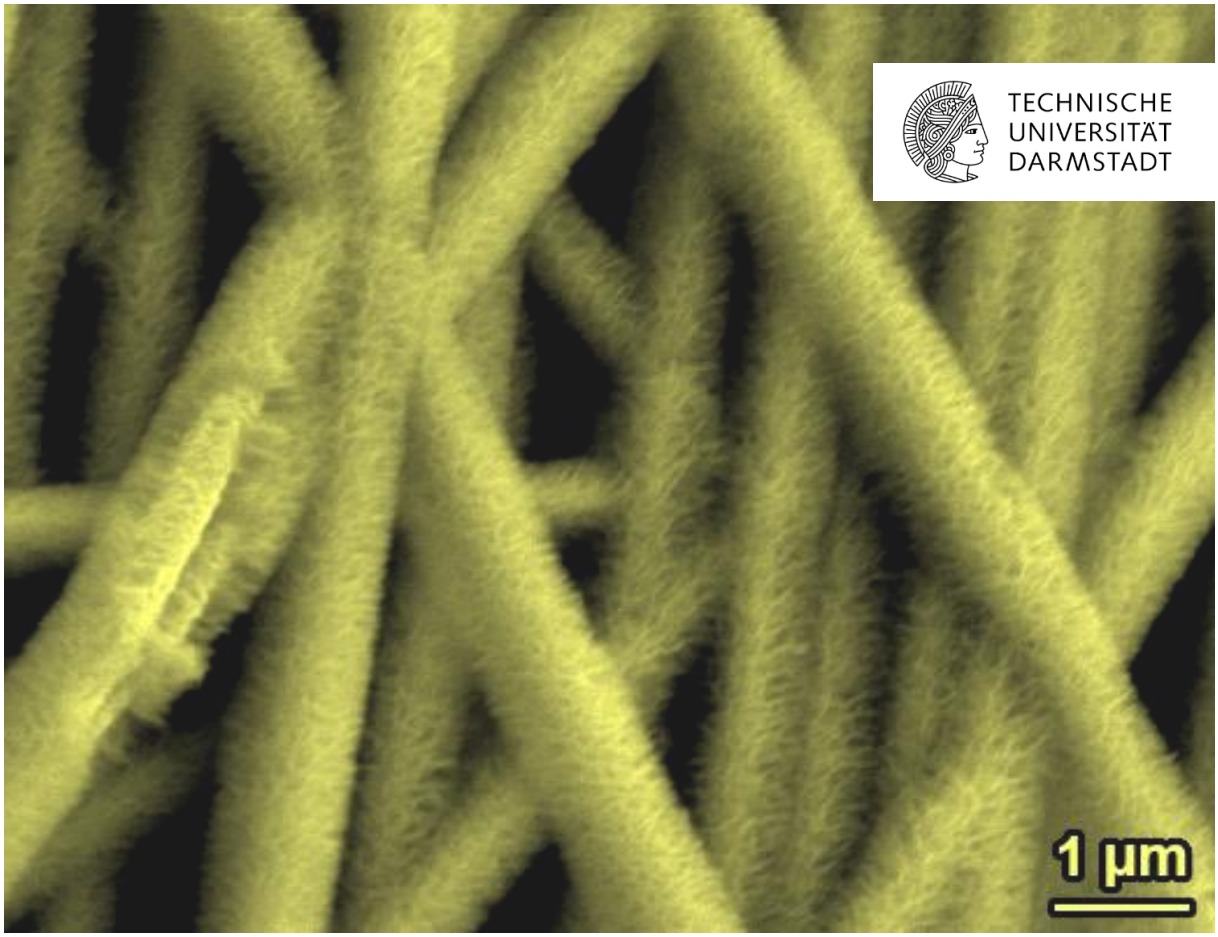

Engineering Hierarchical LDH-decorated Nanowire and Nanotube Networks as Self-supported Electrodes for Electrochemical Applications: Energy Storage, Catalysis, and Sensing

Genehmigte Dissertation von **Khaled Amin,** aus Beheira (Ägypten)

Darmstadt, Technische Universität Darmstadt

1. Gutachten: Prof. Dr. Wolfgang Ensinger

2. Gutachten: Prof. Dr. Leopoldo Molina-Luna

Tag der Einreichung: 04.10.2023

Tag der Prüfung: 22.11.2023

Jahr der Veröffentlichung der Dissertation auf TUprints: 2023

Darmstadt 2023 – D 17

Please cite this document as:

URN: urn:nbn:de:tuda-tuprints-263689

URL: https://tuprints.ulb.tu-darmstadt.de/26368

This document is published by tuprints,
TU Darmstadt publication service
http://tuprints.ulb.tu-darmstadt.de
tuprints@ulb.tu-darmstadt.de

Erklärungen laut Promotionsordnung

1.1. §8 Abs. 1 lit. c PromO

Ich versichere hiermit, dass die elektronische Version meiner Dissertation mit der schriftlichen Version übereinstimmt.

1.2. §8 Abs. 1 lit. d PromO

Ich versichere hiermit, dass zu einem vorherigen Zeitpunkt noch keine Promotion versucht wurde. In diesem Fall sind nähere Angaben über Zeitpunkt, Hochschule, Dissertationsthema und Ergebnis dieses Versuchs mitzuteilen.

1.3. §9 Abs. 1 PromO

Ich versichere hiermit, dass die vorliegende Dissertation selbstständig und nur unter Verwendung der angegebenen Quellen verfasst wurde.

1.4. §9 Abs. 2 PromO

Die Arbeit hat bisher noch nicht zu Prüfungszwecken gedient.

Darmstadt, 02.10.2023

_____

Khaled Amin

To my parents

Acknowledgments

All praises and thanks to Almighty ALLAH to whom I attribute all success in my life and for guiding me on the path to completing this work in its present form.

I would like to express my deepest gratitude to my supervisor ***Prof. Dr. Wolfgang Ensinger****, for his continuous and kind support, both on a personal and academic level, throughout my Ph.D. journey. His mentorship has enriched my experience and his unwavering belief in my abilities has been a constant source motivation to excel in my work.*

Thanks to all the members of the Ph.D. committee: ***Prof. Dr. Leopoldo Molina-Luna****,* ***Prof. Dr. Jan Philipp Hofmann****, and* ***Prof. Dr. Christina Roth*** *for their interest and availability to evaluate my thesis.*

I am thankful to ***Dr. Falk Münch****, for his insightful discussions and worthy suggestions. Collaboration with him was fruitful and resulted in two scientific publications. I am also indebted to all the people who have collaborated with me within the scope of this thesis:* ***Prof. Etzold,*** *and* ***Dr. Konrad Krois*** *(assembly of the hybrid supercapacitor),* ***Prof. Molina-Luna, Dr. Duerrschnabel,*** *and* ***Ulrike Kunz*** *(TEM and SAED measurements),* ***Jean-Christophe Jaud*** *(XRD measurements),* ***Christopher Gort*** *(measurement and scientific discussions about XPS analysis, and My master student,* ***Kuan-Hsun Lin*** *(synthesis of nanowire networks for OER).*

My sincere appreciation goes to the ***Ministry of Higher Education of Egypt*** *and the German Academic Exchange Service* ***(DAAD)*** *for providing funding for my Ph.D. studies, making it possible for me to pursue my research and academic aspirations.*

I extend my heartfelt appreciation to my colleagues and lab mates from the Materials Analysis group for creating a stimulating research environment. Special thanks go to ***Patrick****,* ***Martin****,* ***Tim****,* ***Hamza, Tobi, Ivana, Marco,*** *and* ***Kristina*** *for the great for the great time and the enjoyable lunch breaks we shared together,* ***Torsten*** *for his friendly and professional support, and* ***Maria*** *for her kind help in administration.*

To my family, especially my beloved mother ***Nashwa Amin*** *and father* ***Magdy Amin****, I owe my deepest gratitude for their unconditional love, prayers, support, and encouragement during stressful times. Their belief in me never faltered. I am also grateful to my brother* ***Hatem Amin*** *for providing constant support throughout my academic journey and my brother* ***Ahmed Amin*** *for being my pillar of strength.*

I would like to thank my wonderful friends, especially ***Yusuf Elbadry, Mazen Gabal****,* ***Hany Mohamed****,* ***Mohamed Ghonim****,* ***Azza Halim,*** *and* ***Aya Tarek*** *for the joyous times we shared during weekends and various activities. Extended thanks go to* ***Haroon, Amr, Yassin*** *and* ***Adham*** *for the unforgettable football matches we played together. Your presence has been a comforting backup, providing me with the strength to heal during difficult moments. Lastly, I want to thank all those who have contributed to my growth as a researcher. Your support and encouragement have been invaluable, and I am truly grateful for each one of you.*

Abstract

To meet the pressing need for green and sustainable energy sources, many researchers are engaged in the field of electrochemical energy conversion and storage. Likewise, the development of efficient portable electrochemical sensors and biosensors has emerged as a key player in disease diagnosis. In this context, the performance of such electrochemical devices critically depends on the intrinsic properties and structure of the applied electrode materials. Conventional electrode designs typically rely on bulk materials of microscale dimensions that are loaded on supporting electrodes such as foams, meshes, and 3D-printed substrates, and thus often require the use of binders. However, this fabrication approach limits the performance and reduces the mechanical stability of such electrodes, necessitating the exploration of advanced nanostructured architectures and alternative design approaches to achieve enhanced efficiency and meet diverse application requirements. In this thesis, the development and characterization of advanced electrode materials for electrochemical applications including nonenzymatic glucose sensing, supercapacitors, and the oxygen evolution reaction (OER) are presented.

The fabrication of hierarchical 3D structures in core-shell form as self-supported electrodes offers numerous benefits for electrochemical applications. In particular, this work introduces a new strategy for the synthesis of 3D nanowire and nanotube networks decorated with various LDH nanosheets. This design approach utilizes feasible and simple synthetic routes, including template-assisted synthesis, electroless plating, and electrodeposition. The prepared 3D architecture, with its unique "*2D on 1D*" structure, exhibits synergistic effects through combining the advantages of the individual components at multiple levels of architecture: i) the 1D core networks provide continuous pathways for electron transfer, while the 2D nanosheets as the shell enlarge the surface area and boost the electrocatalytic activity, ii) these interconnected 3D networks provide both mechanical robustness and high porosity for efficient mass transport, and iii) the direct growth of catalytical active LDH over the interconnected nanotubes or nanowires accelerates the charge transfer due to the high electric conductivity of the core and the intimate junction between the active material and the substrate.

In this thesis, a detailed introduction on the topic, theoretical background, and a wider literature survey are presented in ***Chapter I***. Three peer-reviewed articles reporting the main results of this work were published and are presented in this cumulative thesis. Briefly, two electrode designs were developed and systematically characterized. The first design is based on a Ni nanowires network (Ni-NWN) (***Chapter II)*** whilst the second is built on a Ni nanotube network (Ni-NTNW) (***Chapter III***). Both systems were decorated with different LDH nanosheets. The as-synthesized active electrodes were investigated for the following three applications.

For the water splitting process, the focus was on engineering active sites enriched NiCo LDH/Ni-NWN and NiFe LDH/Ni-NWN electrocatalysts for the OER, which is the bottleneck

step in water oxidation. Herein, LDH-decorated nanowire networks were investigated as efficient OER electrocatalysts. Transmission electron microscopy (TEM) images confirmed the conformal growth of LDH sheets over the entire wires, while X-ray photoelectron spectroscopy revealed the presence of a metal hydroxide shell. The NiFe LDH/Ni-NWN electrocatalyst demonstrated remarkable performance with a low overpotential of 222 mV to achieve a current density of 10 mA cm^{-2} and a small Tafel slope of 42 mV dec^{-1}, suggesting favorable OER kinetics. The 3D architecture, featuring a "nanosheet on nanowire" configuration, not only secured mechanical stability but also promoted ion diffusion through the porous network and facilitated the charge transfer through the metallic Ni-NWN. These factors ensured the regeneration of active species during the OER, resulting in excellent stability over 50 hours.

For the hybrid supercapacitor (HSC) application, the NiCo-LDH@Ni-NTNW electrode was investigated. The proposed ultrathin electrode (20 µm) overcomes the shortcomings of classical electrode designs that rely on macroscopic support materials. Increasing the mass loading of the active material is a typical tactic to enhance the volumetric energy density. However, this approach results in reduced porosity, morphology distortions, and demolition of portions of the active material and dead mass, thus reducing the electrical contact. In contrast, the micro- and nano-structuring of a hierarchical electrode combines the highly porous Ni-NTNW with the large interface of the LDH nanosheets. In addition to the achieved high rate-capability and cycling stability, the electrode demonstrated a remarkable volumetric capacity of 126.4 C cm^{-3}. Furthermore, when assembled with activated carbon (AC) into an HSC, it delivered a high energy density of 14.7 mWh cm^{-3}, outperforming state-of-the-art high volumetric energy density supercapacitors.

For glucose electrooxidation, $Ni(OH)_2$@Ni-NTNW and NiCo-LDH@Ni-NTNW were explored as binder-free electrodes that represent a hierarchical paradigm to overcome the inherent limitations of LDH materials. Electroless plating was employed as a simple and scalable method to fabricate the Ni-NTNW substrate, followed by an optimized electrodeposition step to grow LDH nanosheets over the Ni-NTNW. Scanning electron microscopy (SEM) micrographs, energy dispersive X-ray analysis (EDX), and X-ray diffraction (XRD) measurements confirmed the deposition of conformal NiCo-LDH nanosheets on the inner and outer surfaces of the Ni-NTNW. The NiCo-LDH reinforced network exhibited superior activity compared to the $Ni(OH)_2$ modification. The optimized catalyst layer demonstrated excellent sensitivity of 4.6 mA mM^{-1} cm^{-2}, low detection limit of 0.2 mM, wide linear range of 0.03 to 2.5 mM glucose, high selectivity, and stability.

To summarize, this PhD thesis emphasizes the significance of tailored electrode architectures and nano-structuring strategies in improving the performance of electrochemical devices. The research outcomes contribute to the development of an emerging design paradigm that can be extended to other customized electrocatalysts for widespread applications.

Zusammenfassung

Um den dringendsten Anforderungen an umweltfreundliche und nachhaltige Energieressourcen gerecht zu werden, beschäftigen sich viele Forscher mit der elektrochemischen Energieumwandlung und -speicherung. Außerdem hat sich die Entwicklung effizienter mobiler elektrochemischer Sensorik und Biosensorik als wichtiger Schlüssel zur Diagnose von Krankheiten erwiesen. In diesem Zusammenhang hängt die Leistung solcher elektrochemischer Systeme wesentlich von den intrinsischen Eigenschaften und Strukturen der verwendeten Elektrodenmaterialien ab. Herkömmliche Elektrodendesigns bestehen in der Regel aus Nanomaterialien, die auf Trägerelektroden wie z.B. Gewebe oder 3D-gedruckten Substraten aufgebracht werden, und erfordern daher häufig die Verwendung von Bindemitteln. Dieser Herstellungsansatz schränkt jedoch die Leistung ein und verringert die mechanische Stabilität solcher Elektroden. Weshalb ist die Erforschung neuartiger nanostrukturierter Architekturen und alternativer Designansätze erforderlich, um eine höhere Effizienz zu erzielen und verschiedene Anwendungsanforderungen zu erfüllen. In dieser Arbeit wurden neuartige Elektrodenmaterialien für elektrochemische Anwendungen wie nicht-enzymatische Glukosesensorik, Superkondensatoren und Sauerstoffentwicklungsreaktionen (OER) entwickelt und charakterisiert.

Die Herstellung von hierarchischen 3D-Strukturen in Kern-Schale-Form als selbsttragende Elektroden bietet zahlreiche Vorteile für elektrochemische Anwendungen. In dieser Arbeit wurde eine neue Synthesestrategie für 3D-Nanodraht- und Nanoröhrennetzwerke entwickelt, die mit verschiedenen LDH-Nanoschichten beschichtet wurden. Dieser Designansatz setzt praktikable und einfache Syntheserouten ein, einschließlich Templategestützten Synthese, stromlose Beschichtung und Elektroabscheidung. Die vorbereitete 3D-Architektur mit ihrer einzigartigen "2D auf 1D"-Struktur zeigt synergistische Effekte durch die Kombination der Vorteile der einzelnen Komponenten auf mehreren Architekturebenen: i) die 1D-Kernnetzwerke bieten kontinuierliche Übertragungswege für Elektronen, während die 2D-Nanoschichten als Hülle die Oberfläche vergrößern und die elektrokatalytische Aktivität steigern, ii) diese miteinander verbundenen 3D-Netzwerke bieten sowohl mechanische Stabilität als auch hohe Porosität für einen effizienten Stofftransport, und iii) das direkte Wachstum von katalytisch aktivem LDH über den verbundenen Nanoröhren oder Nanodrähten beschleunigt die Ladungsübertragung aufgrund der hohen elektrischen Leitfähigkeit des Kerns und der direkten Verbindung zwischen dem aktiven Material und dem Substrat.

In dieser Dissertation wird zunächst in ***Kapitel I*** eine ausführliche Einführung in das Thema, der theoretische Hintergrund und ein umfassenderer Literaturüberblick gegeben. Es folgen drei peer-reviewed Artikel, in denen die wichtigsten Ergebnisse dieser Arbeit veröffentlicht wurden und die in dieser kumulativen Dissertation aufgeführt sind. Im Wesentlichen wurden zwei Elektrodendesigns entwickelt und systematisch charakterisiert. Das erste Design basiert auf einem Ni-Nanodraht-Netzwerk (Ni-NWN) (***Kapitel II***), während das Zweite auf einem Ni-Nanoröhren-Netzwerk (Ni-NTNW) besteht (***Kapitel III***). Beide Systeme wurden mit verschiedenen LDH-Nanoschichten modifiziert. Die hergestellten aktiven Elektroden wurden für die nachfolgend erläuterten Anwendungsbereiche untersucht.

Bei der Wasserspaltung lag der Arbeitsschwerpunkt auf der Entwicklung hochaktiver NiCo LDH/Ni-NWN- und NiFe LDH/Ni-NWN-Elektroden für die OER, den Engpassschritt bei der Wasseroxidation. Die Transmissionselektronenmikroskopie (TEM) bestätigte das konforme Wachstum von LDH-Schichten über die gesamten Drähte, während die Röntgen-Photoelektronenspektroskopie (XPS) das Auftreten einer Metallhydroxidhülle nachwies. Der NiFe LDH/Ni-NWN-Elektrokatalysator erbrachte eine bemerkenswerte Leistung mit einer niedrigen Überspannung von nur 222 mV bei einer Stromdichte von 10 mA cm^{-2}, und einer geringen Tafelsteigung von 42 mV dec^{-1}, was auf eine günstige OER-Kinetik hindeutet. Die 3D-Architektur mit einer " *Nanoschicht auf Nanodraht*"-Konfiguration sicherte nicht nur die mechanische Stabilität, sondern verbesserte auch die Ionendiffusion durch das poröse Netzwerk und erleichterte den Ladungstransfer durch das metallische Ni-NWN. Diese Faktoren sorgten für die Regeneration der aktiven Spezies während der OER, was zu einer hervorragenden Stabilität über 50 Stunden führte.

Für die Hybrid-Superkondensator (HSC) wurde eine NiCo-LDH@Ni-NTNW-Elektrode untersucht. Die vorgeschlagene ultradünne Elektrode (20 µm) überwindet die Nachteile klassischer Elektrodendesigns, die auf makroskopischen Trägermaterialien basieren. Die Erhöhung der Masse des aktiven Materials ist eine typische Strategie, um die volumetrische Energiedichte zu erhöhen. Dieser Ansatz führt jedoch zu einer verringerten Porosität, zu morphologischen Verzerrungen und zum Abbruch von Teilen des aktiven Materials, was den elektrischen Kontakt verringert. Im Gegensatz dazu kombiniert die Mikro- und Nanostrukturierung einer hierarchischen Elektrode die hochporösen Ni-NTNW mit der großen Grenzfläche der LDH-Nanoschichten. Neben der erreichten hohen Kapazität und Zyklenstabilität zeigte die Elektrode eine bemerkenswerte volumetrische Kapazität von 126.4 C cm^{-3}. Wenn die Elektrode mit Aktivkohle (AC) zu einem HSC zusammengebaut wurde, lieferte sie außerdem eine höhere Energiedichte von 14.7 mWh cm^{-3} und übertraf damit den Stand der Technik bei Superkondensatoren mit hoher volumetrischer Energiedichte.

Zur Glucose-Elektrooxidation wurden $Ni(OH)_2$@Ni-NTNW und NiCo-LDH@Ni-NTNW als bindemittelfreie Elektroden untersucht, die ein hierarchisches Paradigma zur Überwindung der inhärenten Einschränkungen von LDH-Materialien bieten. Rasterelektronenmikroskopische (REM) Aufnahmen, energiedispersive Röntgenanalyse (EDX) und Röntgenbeugungsmessungen (XRD) bestätigten die Abscheidung von konformen NiCo-LDH-Nanoschichten auf den inneren und äußeren Oberflächen des Ni-NTNW. Das mit NiCo-LDH verstärkte Netzwerk zeigte im Vergleich zur $Ni(OH)_2$-Modifikation eine höhere Aktivität. Die optimierte Katalysatorschicht wies eine ausgezeichnete Sensitivität von 4.6 mA mM^{-1} cm^{-2}, eine niedrige Detektionsgrenze von 0.2 mM, einen breiten linearen Bereich von 0.03 bis 2.5 mM Glukose, sowie eine hohe Selektivität und Stabilität auf.

Zusammenfassend weist diese Doktorarbeit die besondere Signifikanz von maßgeschneiderten Elektrodenarchitekturen und Nanostrukturierungsstrategien zur Steigerung der Performance von elektrochemischen Systemen nach. Die Forschungsergebnisse tragen zur Entwicklung eines neuartigen Strukturdesign bei, das auf andere maßgeschneiderte Elektrokatalysatoren für zahlreiche Anwendungen angewendet werden könnte.

Scientific contributions

1. Publications included in this thesis

[1] **K.M. Amin,** K. Krois, F. Muench, B.J.M. Etzold, W. Ensinger, Hierarchical pipe cactus-like Ni/NiCo-LDH core-shell nanotube networks as a self-supported battery-type electrode for supercapacitors with high volumetric energy density, *J. Mater. Chem. A.* 10 (2022) 12473–12488.

[2] **K.M. Amin**, F. Muench, U. Kunz, W. Ensinger, 3D NiCo-Layered double Hydroxide@Ni nanotube networks as integrated free-standing electrodes for nonenzymatic glucose sensing, *J. Colloid Interface Sci.* 591 (2021) 384–395.

[3] **K.M. Amin**, K-H Lin, M. Duerrschnabel, L. Molina-Luna, W. Ensinger, Engineering Active Sites Enriched 2D-on-1D NiFe and NiCo LDH-decorated Ni Nanowire Networks for Oxygen Evolution Reaction, *ACS Sus. Chem. Eng*, 11 (2023) 15410–15422.

2. Other Publications

[1] M.A. Abbasi, **K.M. Amin**, M. Ali, Z. Ali, M. Atif, W. Ensinger, W. Khalid, Synergetic effect of adsorption-photocatalysis by GO−CeO_2 nanocomposites for photodegradation of doxorubicin, *J. Environ. Chem. Eng.* 10 (2022) 107078.

[2] **K.M. Amin**, H.M.A. Amin, Carbon Nanoallotropes-Based Anticorrosive Coatings, in: H.M.A. Amin, A. Galal (Eds.), Corrosion Protection of Metals and Alloys Using Graphene and Biopolymer Based Nanocomposites, 1st Ed, *CRC Press*, 2021: pp. 81–98.

[3] **K.M. Amin**, A.M. Partila, H.A. Abd El-Rehim, N.M. Deghiedy, Antimicrobial ZnO Nanoparticle–Doped Polyvinyl Alcohol/Pluronic Blends as Active Food Packaging Films, *Part. Part. Syst. Charact.* 37 (2020).

[4] M.A. Aldeeb, N. Morgan, A. Abouelsayed, **K.M. Amin**, S. Hassaballa, Electrical and Optical Characterization of Acetylene RF CCP for Synthesis of Different Forms of Hydrogenated Amorphous Carbon Films, *Plasma Chem. Plasma Process.* 40 (2020) 387–406.

[5] M.A. Aldeeb, N. Morgan, A. Abouelsayed, **K.M. Amin**, S. Hassablla, Correlation of acetylene plasma discharge environment and the optical and electronic properties of the hydrogenated amorphous carbon films, *Diam. Relat. Mater.* 96 (2019) 74–84.

[6] A. Galal, **K.M. Amin**, N.F. Atta, H.A. Abd El-Rehim, Protective ability of graphene prepared by γ-irradiation and impregnated with organic inhibitor applied on AISI 316 stainless steel, *J. Alloys Compd.* 695 (2017) 638–647.

[7] N.F. Atta, **K.M. Amin**, H.A. Abd El-Rehim, A. Galal, Graphene prepared by gamma irradiation for corrosion protection of stainless steel 316 in chloride containing electrolytes, *RSC Adv.* 5 (2015) 71627–71636

[8] H.A. Hamad, N. Eldeeb, Z. Gargar, I. Mohamed, M. Elsenity, **K.M. Amin**, M. Emara, M. Abd Elkodous, M. Abouelela, P. Ibrahim, A. Ayed, Recent progress in the design strategy of spinel ferrite nanomaterials for photocatalytic degradation of emerging pollutants and CO_2 reduction, *J. Hazard. Mater.*, submitted.

[9] H.A. Hamad, M. Emara, **K.M. Amin**, M. Elsenity, I. Mohamed, Z. Gargar, M. Abouelela, N. Eldeeb, I. Ibrahim, A. Hassan, A. Bedir, A. Hassan, M. El Abboubi, Recent progress of ferrite-carbon-semiconductor photocatalysts for energy and environmental applications, *J. Mater. Chem. A.*, submitted.

3. Conferences

[1] **K.M. Amin**, T. Boettcher, M.C. Scheuerlein, W. Ensinger, Exotemplate-based Fabrication of 1-dimensional Hybrid Nanostructures for Catalysis and Sensing, in: *Proceedings of the 7th World Congress on Recent Advances in Nanotechnology (RAN'22), ICNNFC 173*, Int. ASET Inc., Ottawa 2022, pp. 173-1–5, DOI: 10.11159/icnnfc22.173.

[2] **K.M. Amin**, W. Ensinger, Self-supported LDH-decorated Nanotube Networks as 3D Platforms for Electrochemical Applications, in: *Proceedings of the 7th World Congress on Recent Advances in Nanotechnology (RAN'22), ICNNFC 173*, Int. ASET Inc., Ottawa 2022, pp. 140-1–2, DOI: 10.11159/icnnfc22.140.

Authors' contributions to presented papers

This thesis comprises a compilation of scientific research findings that have previously been published in peer-reviewed journals. The articles have been included in the thesis following the guidelines provided by TU Darmstadt, with adjustments made to figures and table numbers for improved coherence within the thesis. Any minor errors or typographical mistakes identified in the original articles have been rectified. Apart from these revisions, the original publications remain unchanged. The following list outlines the publications included in this cumulative dissertation, accompanied by the author's individual contributions.

[1] **K.M. Amin**, F. Muench, U. Kunz, W. Ensinger, 3D NiCo-Layered double Hydroxide@Ni nanotube networks as integrated free-standing electrodes for nonenzymatic glucose sensing, *J. Colloid Interface Sci.* 591 (2021) 384-395.

The sample preparation, cyclic voltammetry, amperometry, impedance spectroscopy, and SEM measurements were planned, performed, and analyzed by me. XRD measurements were conducted by Martin C. Scheuerlein, Tim Boettcher, and myself. TEM measurements were carried out by Ulrike Kunz. The manuscript draft was written and composed by me, and it was reviewed and proofread by Dr. Falk Muench and Prof. Wolfgang Ensinger. All authors actively participated in the discussions and provided feedback that contributed to the final version of the published article.

[2] **K.M. Amin**, K. Krois, F. Muench, B.J.M. Etzold, W. Ensinger, Hierarchical pipe cactus-like Ni/NiCo-LDH core-shell nanotube networks as a self-supported battery-type electrode for supercapacitors with high volumetric energy density, *J. Mater. Chem. A.* 10 (2022) 12473–12488.

The sample preparation, SEM, EDX, XRD, and Raman spectroscopies were conducted and analyzed by me. TEM measurements were carried out by Ulrike Kunz, analyzed, and represented by me. All electrochemical measurements for the three electrodes in the three-electrode setup, including cyclic voltammetry, galvanostatic charge and discharge, and impedance spectroscopy, were planned, performed, and analyzed by me. The assembly and electrochemical evaluation of the hybrid supercapacitor device in the two-electrode system was conducted by both Dr. K. Krois and me. The manuscript draft was written and composed by me and proofread by Dr. K. Krois, Dr. Falk Muench, Prof. B.J.M. Etzold, and Prof. Wolfgang Ensinger.

[3] **K.M. Amin**, K-H Lin, Michael Duerrschnabel, Leopoldo Molina-Luna, W. Ensinger, Engineering Active Sites Enriched 2D-on-1D NiFe and NiCo LDH-decorated Ni Nanowire Networks for Oxygen Evolution Reaction, *ACS Sus. Chem. Eng, 11 (2023) 15410–15422*.

The sample preparation, SEM, cyclic voltammetry, and linear sweep voltammetry were conducted by both me and K-H Lin as part of his advanced research lab project. Chronopotentiometry and electrochemical impedance spectroscopy were carried out by me. The TEM measurements were coordinated and executed by Michael Duerrschnabel and Leopoldo Molina-Luna, with support in sample preparation from Ulrike Kunz. XRD measurements were conducted with the assistance of Jean-Christophe Jaud from the Strukturforschung Group at TU Darmstadt, and the data was analyzed and represented by me. XPS measurement was carried out by Christopher Gort (Surface Science Group at TU Darmstadt), analyzed, and represented by me. The manuscript draft was written and composed by me and reviewed by all the authors.

List of Abbreviations

CC	Carbon Cloth
OER	Oxygen Evolution Reaction
CVD	Chemical Vapor Deposition
AAO	Anodic Aluminum Oxide
Ni-NWN	Ni Nanowire Networks
Ni-NTNW	Ni Nanotube Networks
LDHs	Layered Double Hydroxides
HER	Hydrogen Evolution Reaction
ΔG^{o}	Standard Gibbs Free Energy
η	Overpotential
η_{10}	Overpotential At 10 mA Cm^{-2}
η_{100}	Overpotential At 100 mA Cm^{-2}
GOx	Glucose Oxidase
GDHs	Glucose Dehydrogenases
EES	Electrochemical Energy Storage
EDLC	Electrochemical Double-Layer Capacitance
TMHs	Transition Metal Hydroxides
rGO	Reduced Graphene Oxide
R_{ct}	Charge Transfer Resistance
SEM	Scanning Electron Microscopy
XRD	X-Ray Diffraction
TEM	Transmission Electron Microscopy
SAED	Selected Area Electron Diffraction
EDX	Energy-Dispersive X-Ray
XPS	X-Ray Photoelectron Spectroscopy
WE	Working Electrode
RE	Reference Electrode
CE	Counter Electrode
RHE	Reversible Hydrogen Electrode
LSV	Linear Sweep Voltammetry

CV	Cyclic Voltammetry
EIS	Electrochemical Impedance Spectroscopy
CP	Chronopotentiometry
ESCA	Electrochemically Active Surface Area
$\mathbf{C_{dl}}$	Double-Layer Capacitance
DFT	Density Functional Theory
$\boldsymbol{R_s}$	Solution Resistance
1D	One-Dimensional
2D	Two-Dimensional
3D	Three-Dimentional
EP	Electroless Plating
$\boldsymbol{I_{pc}}$	Cathodic Peak Current
$\boldsymbol{I_{pa}}$	Anodic Peak Current
$\boldsymbol{E_{pa}}$	Anodic Peak Potential
$\boldsymbol{E_{pc}}$	Cathodic Peak Potential
LOD	Limit Of Detection
UA	Uric Acid
AA	Ascorbic Acid
Glu	Glutamine
HSC	Hybrid Supercapacitors
AC	Activated Carbon
GCD	Galvanostatic Charge-Discharge
$\boldsymbol{q_m}$	Gravimetric Capacity
$\boldsymbol{q_a}$	Areal Capacity
$\boldsymbol{q_d}$	Volumetric Capacity
$\boldsymbol{C_m}$	Gravimetric Capacitance
$\boldsymbol{C_a}$	Areal Capacitance
$\boldsymbol{C_d}$	Volumetric Capacitance
$\boldsymbol{E_m}$	Gravimetric Energy Density
$\boldsymbol{E_a}$	Areal Energy Density
$\boldsymbol{E_d}$	Volumetric Energy Density

Table of Contents

CHAPTER I

1. Introduction

1.1. Nanostructured catalyst electrodes for electrochemical applications

With the emergence of the technological revolution and the increased demand for electronic devices such as smartphones, electric vehicles, and other portable devices, the development of electrochemical technology has become a long-term strategic target worldwide.[1] Electrochemical technology has positioned itself at the forefront of basic research and applied trends, not only because of its wide application in various industries but also due to its environmentally friendly nature, as it mainly relies on electrons as "clean" reagents to initiate processes. Consequently, it has found extensive use in various areas including energy storage,[2,3] catalysis,[4] electrochemical sensing,[5–7] wastewater treatment,[8,9] and environmental monitoring.[10]

For instance, the expansion of green and sustainable energy technologies represents a challenge in the current century, considering the increasing consumer needs and emerging environmental concerns.[11] The urgent need for low-cost and efficient energy sources to replace fossil fuel in various applications has compelled researchers to develop advanced electrochemical energy conversion and storage devices such as fuel cells, batteries, and supercapacitors, that are environmentally friendly. Another example is the construction of efficient electrodes with high sensitivity, selectivity, and stability for electrochemical sensors and biosensors, which hold significant societal impact, as they can address environmental challenges and aid in disease diagnosis and management.[12]

As the performance of the electrochemical devices intimately relies on the electrode materials and their structure, extensive research has focused on the development of advanced functional materials and rationale design approaches to achieve higher efficiencies and meet the optimum performance requirements of each application.

Traditional bulk electrode materials in the microscale, with their inherent performance limitations, are insufficient to meet the growing demands for electrochemical devices or satisfy consumer expectations. The expanding use of microelectronics for new applications requires miniaturized energy sources with high efficiency. Generally, the electrode performance can be enhanced by increasing the mass and area of the active material, however, sluggish reactions

and long paths for ion and electron transport in thick or bulk electrodes retards the performance.[13] Therefore, the development and engineering of new advanced materials are crucial to push the limits of electrode materials. The significant advances in nanotechnology enable various approaches to engineer highly efficient catalyst materials. Unlike bulk materials, which suffer from limitations such as small active surface area, low electronic conductivity, limited control of morphology, and long diffusion paths for electrons and ions, nanostructured materials provide alternative solutions that overcome these challenges.[14] Nanostructured electrode materials possess remarkable physical properties, including large surface areas that maximize the number of exposed active sites and promote fast electron transport, thereby enhancing the electrochemical process.

Ideally, the rational design of the electrode should adopt a thin and light fashion that accommodates as much active material as possible. Additionally, the electrode architecture should be constructed to provide the largest interface area and improve ion diffusion and electron transportation. Therefore, a support material with a large surface area and porous structure is a prerequisite for developing efficient electrodes for electrochemical applications and addressing the challenges that limit the performance of conventional electrodes.

1.2. Self-supported nanowire and nanotube networks as 3D porous substrates

1.2.1. Advantages of the self-supported electrodes

Despite significant advancements achieved with conventional electrode designs in various fields, their performance remains limited due to their bulky nature and electrode morphology. Traditional powdery electrodes comprise conductive materials and binders beside the active material, resulting in a film with microscale dimensions. This structure, with its disordered distribution of active material and applied binder materials, hampers mass and charge transfer rates, leading to incomplete electrochemical processes. Additionally, the inclusion of additives like binders and conductive materials obstructs the exposure of active sites and increases the weight of the electrode, resulting in a dense structure and potential cracks.[15]

Nanostructured electrodes, with their distinct morphological and geometric advantages, have emerged as promising alternatives to bulk materials in electrochemical applications. These electrodes are typically grown over a substrate of nanoarrays and nanonetworks, which not only support the structure but also act as current collectors. Self-supported arrays and networks

possess intrinsic characteristics that ensure enhanced performance compared to classical bulky electrodes. The main advantages can be summarized as follows:

(i) Uniform distribution of the active material: Nanoarrays and nanonetworks offer a more uniform distribution of the active material compared to powder-based electrodes, enabling better mass transfer and improved catalytic efficiency.

(ii) Large surface area: The large surface area of nanoarrays and networks serves as a platform for high loadings of active material, providing a multitude of active sites.[16]

(iii) Porous structure: The porous structure of arrays and networks allows self-supported electrodes to operate effectively in various applications, including high current-density electrolysis.[17]

Self-supported nanoarrays and networks can be classified according to their dimensionality into 1D structures (such as nanowires and nanotubes), 2D structures (such as nanosheets and nanoplates), and 3D structures (such as networks and nanopores) as illustrated in Figure 1.1. Besides the large surface area and enriched active sites, 1D nanoarrays and networks facilitate excellent charge transfer through their axial tracks. The interspaces between the wires or the tubes enable easy diffusion of electrolytes and release of gas bubbles.[18,19] 2D arrays and networks provide the additional advantage of exposing different crystal faces. 3D architectures allow the fabrication of heterostructures, exposing more edge sites for adsorption. Furthermore, the electron distribution can be controlled by incorporating different components into the heterostructure, which is crucial for applications like water splitting.[20] The 3D heterostructure, such as the core-shell structure, provides enhanced protection for active sites, improving the stability of the catalyst. The morphology of the substrate influences the mechanical and dynamic properties of the electrode, as well as the modulation of mass and charge transfer, as shown in Figure 1.2.[21]

In contrast to physical adhesion, the in-situ growth of the active material on the substrate results in an interface with lower resistance. This method enhances the mechanical strength of the electrode by providing direct contact, unlike physical adhesion in bulky powder electrodes, which can prevent the loss or detachment of active material during bending. Therefore, it is crucial for the electrode architecture used in electrochemical applications to have high mechanical stability to retain its structure, even under the high current density generated by gas bubble formation. Finding a suitable strategy for growing nanoactive materials over a suitable substrate is essential to improve the durability of catalyst electrodes. It's worth noting that the

presence of air bubbles on the electrode surface can hinder the interaction between the active species in the solution and the catalytic sites on the electrode. The microstructure of the catalyst electrode plays a vital role in controlling wettability, and increasing the hydrophilicity of the electrode can promote the desorption and release of gas bubbles, ultimately enhancing catalytic performance in terms of kinetics and thermodynamics.[19]

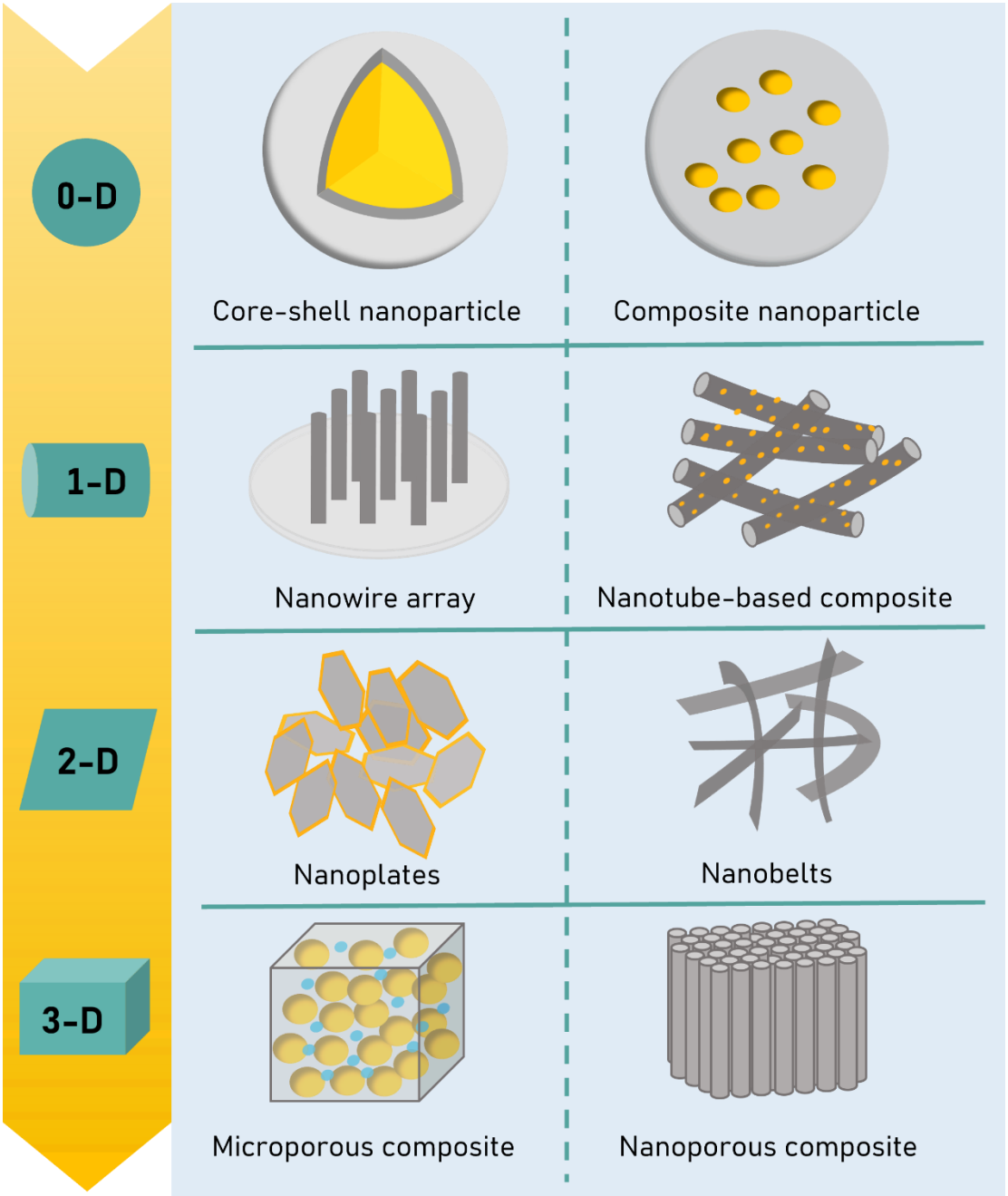

Figure 1.1. *Schematic of different nanostructured materials based on their dimensions.*

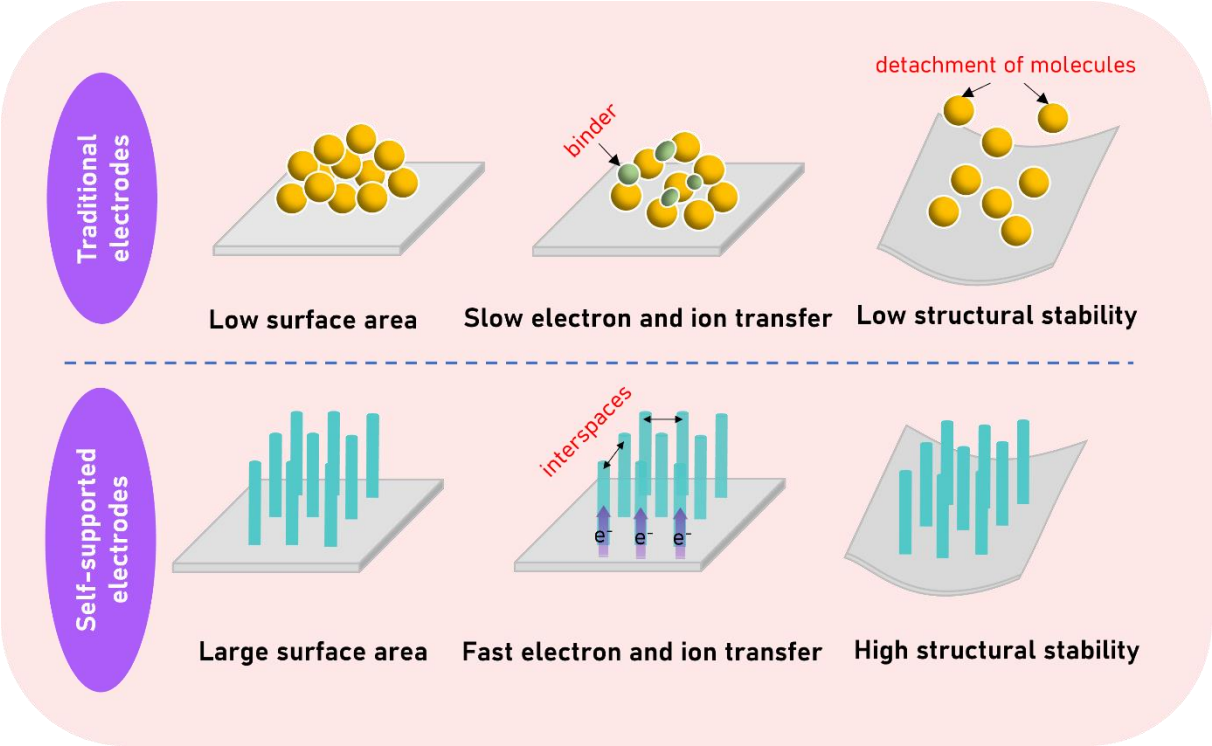

Figure 1.2. *Schematic of differences between the traditional electrode architectures with powder loading and the self-supported electrode architectures with catalysts grown over the substrate.*

The selection of a suitable substrate is a key factor in optimizing the structure and controlling the performance of self-supported nanoarrays. The substrate serves as a bifunctional element in the catalyst architecture, providing structural support and acting as a current collector. Various categories of materials have been used as substrates, including carbonaceous substrates such as graphene and Carbon Cloth (CC), as well as metal substrates like foams and meshes.[22] Carbonaceous materials offer structural strength and stability, making them widely employed in energy storage applications. Graphene, in particular, is an ideal substrate for flexible power sources due to its excellent electrochemical activity, conductivity, and mechanical flexibility.[23] CC, on the other hand, is a conventional substrate with a large area and high strength, making it suitable for diverse applications.[24]

For metal-based supports, the electrochemical activity of the substrate must be considered as it can contribute to the electrocatalytic processes. Ni foam, for example, is commonly used as a substrate in oxygen evolution reaction (OER) processes, leading to the formation of NiOOH, a favorable catalytic species for OER. Additionally, the coupling interface between the supporting substrate, especially metal substrates, and the array/network structure can decrease Gibbs energy, enhancing electrocatalytic activity.[25] Careful selection of the substrate material

and its morphology offers versatility in catalyst applications, considering factors such as mechanical properties, corrosion resistance, and other factors.

Efforts to improve the performance of support materials are combined with strategies aimed at eliminating the support layer in electrode architectures. These approaches involve precise structuring at the nano- and micro-scale to overcome current limitations and drawbacks.[26,27]

Metallic 1D nanostructures, including nanowires and nanotubes, have garnered significant interest due to their unique properties.[28,29] They exhibit resistance against common degradation mechanisms, ensuring long-term catalyst durability. These structures offer extended electrical conduction pathways attributed to their anisotropy and are less prone to agglomeration and detachment due to their coherent structure and corrosion resistance. As a result, they surpass nanoparticle-decorated substrates, nanopowders, and metal blacks in terms of both surface and normalized mass activities.[30]

Utilizing metal nanotube and nanowire networks as core building blocks enables the fabrication of interconnected superstructures, offering opportunities for further tuning and functionalization with various active materials. This designed nanoarchitecture combines the benefits of individual nanostructures with the advantages of an ordered superstructure. For instance, *Ni et al*. achieved a macroscale 2D interconnected nanowire network with enhanced electrical conductivity of the individual nanowires.[31] Fabricating 3D networks of interconnected nanotubes and nanowires presents a promising strategy for constructing monolithic electrocatalysts with a large surface area, high porosity, and mechanical strength.[30,32,33]

To sum up, the rationale for designing an efficient self-supported nanowire or nanotube network electrode should consider the following principles: (i) A well-structured architecture with a large surface area is essential for high current density applications like electrocatalysis. (ii) The nanowire or nanotube network should possess high electrical conductivity to minimize overpotential caused by charge transfer resistance. (iii) The nanonetwork should exhibit sufficient mechanical strength to withstand solution flow conditions. (iv) Suitable approaches must be established to grow a network architecture with abundant active sites exposed to the active species in the solution and strongly bonded to the substrate.

1.2.2. Ni-based self-supported nanonetworks

Transition metal-based structures have gained significant attention in various applications due to their natural abundance, low cost, feasible preparation approaches, variety of compositions,

and high redox activity. Numerous studies have explored the utilization of different transition metals in the construction of nanowire and nanotube networks, particularly for energy storage applications.[34,35] *Zhao et al*. provided a comprehensive summary of the progress in designing self-supported nanoelectrodes for supercapacitors, emphasizing the impact of nanoscale merits on performance.[36] *Liu et al.* conducted an extensive overview of the compositions, properties, and advantages of transition metal-based self-supported structures, including Ni, Co, Mn, Mo, Cu, and V.[22] Among these transition metals, nickel has received significant attention as a material for self-supported electrodes due to its abundance. It has a big family of compounds, including oxides (e.g. NiO and $NiCo_2O_4$), hydroxides (e.g. $Ni(OH)_2$), sulfides (e.g. NiS_x), LDH (e.g. NiCo-LDH and NiFe-LDH), phosphides (e.g. NiP_x), and other related compounds.

1.2.3. Synthetic techniques of self-supported nanonetworks

Self-supported nanonetworks offer a solution to the complex synthetic approaches involved in constructing traditional electrode composites on flat substrates. Transition metal-based substrates, which provide large exposed interfaces and stable spatial structures, have emerged as attractive alternatives. Various techniques have been employed to develop transition-metal-based substrates, including electrodeposition, hydro/solvothermal methods, chemical vapor deposition, and template-directed synthesis.

1- **Electrodeposition** is a promising method for developing self-supported nanonetworks, offering advantages such as feasible mass production, high deposition rates, and compatibility with different substrate shapes.[37] Additionally, electrodeposition enables the tuning of different chemical compounds by optimizing the deposition parameters.

2- **Hydro/solvothermal techniques** are commonly used for preparing self-supported transition metal-based nanoarrays and networks through "one-pot" reactions at high temperatures. A conductive substrate is employed to promote the uniform growth of nanoarrays via heterogeneous nucleation. The substrate also prevents rapid nucleation and crystal growth, which could lead to particle aggregation. Hydro/solvothermal techniques have been successfully employed to fabricate various networks based on transition-metal oxides, hydroxides, and sulfides.[38]

3- **Chemical vapor deposition (CVD)** has been utilized to create self-supported nanostructures on different substrates. This technique involves the use of a template and a gas transformation process, allowing for the production of diverse heterostructures by controlling phase transformation.[22] However, large-scale production is limited due to the specialized equipment required for this method.

4- **Template-assisted synthesis** is another effective strategy for constructing nanonetworks composed of 1D nanowires, nanotubes, or nanorods with adjustable lengths, diameters, and interspaces. This approach typically involves the use of Si arrays, hard templates, anodic aluminum oxide (AAO), or ZnO. The process usually includes depositing materials onto the substrates and subsequently removing or dissolving the template. However, recent reports have utilized self-sacrificing templates of metal oxides and hydroxides, which can transform in-situ into the desired nanonetwork while preserving the original structure. Numerous self-supported metal-based nanonetworks have been successfully synthesized using this template-assisted approach.[39,40]

While significant progress has been made in the synthetic techniques of self-supported nanonetworks, further research is required to transform these laboratory-scale methods into large-scale production and industrial applications at low cost using a variety of materials. The main challenge lies in fabricating nanonetworks while controlling phase purity, morphology, and chemical composition.[22] Improved understanding of the chemistry during the synthetic processes can aid in controlling the products and their performance. Furthermore, a better comprehension of mass and heat transfer mechanisms can facilitate mass production.[36]

1.3. Template–assisted synthesis of 1D nanowire and nanotube networks

Various approaches have been employed to assemble individual 1D nanostructures into 3D superstructures, but template-assisted synthesis offers distinct advantages over other techniques. It enables the deposition of metals in pre-connected networks, allowing for better control over the network by tuning the pore architecture. This method also facilitates the direct deposition of highly isotropic metals into complex patterns. A template with a predetermined shape is required to obtain a 3D interconnected metal network, which can be a network of pores to be filled or a network of fibers to be overcoated during the deposition process. Template-assisted synthesis eliminates the need for intermediate steps such as purification and aggregation, as metal networks can be directly deposited. However, the synthesis and subsequent removal of the template add extra steps to the fabrication process. Commonly used porous templates for the deposition of parallel arrays of 1D nanowires and nanotubes include nanoporous AAO and ion-track etched polymer membranes, which can be adapted to produce interconnected 3D nanowire and nanotube networks.[30,41,42]

Track-etched membranes are typically obtained through the selective etching of the created tracks in the polymer membranes that have been exposed to swift heavy ions. Unlike self-growing nanoporous AAO foils, ion-track etching allows for better control over pore density and orientation In this process, each pore is precisely generated by the trajectory of a single ion. By employing successive irradiation and etching, templates with hierarchical porosity can be created. Moreover, precise control over the diameter and shape of the resulting pores can be achieved by optimizing the etching conditions, enabling better control over the membrane's structure.

During the template preparation process, polymer membranes are bombarded with swift heavy ions, inducing irreversible and localized damage in the template. These ions traverse the template, creating latent tracks (halos) along their trajectories with diameter of few nanometers, as depicted in Figure 1.3a.[43] Track formation in polymers is a complex process that involves primary processes as well as secondary processes, including chemical reactions and the generation of radicals, which occur during the irradiation process. These secondary processes influence the chemical characteristics of the damage along the tracks and the susceptibility of latent tracks to chemical etching. Latent tracks exhibit higher susceptibility to chemical etching compared to the rest of the polymer template. Subsequently, the damaged zone within the latent tracks can be selectively removed using a suitable chemical etchant, transforming them into nanopores (Figure 1.3b). The choice of the chemical etchant depends on the properties of the polymer membrane. The ion-track etched membranes are then subjected to either electrodeposition or electroless plating to deposit metal inside the channels, resulting in the formation of nanowires or nanotubes, respectively.

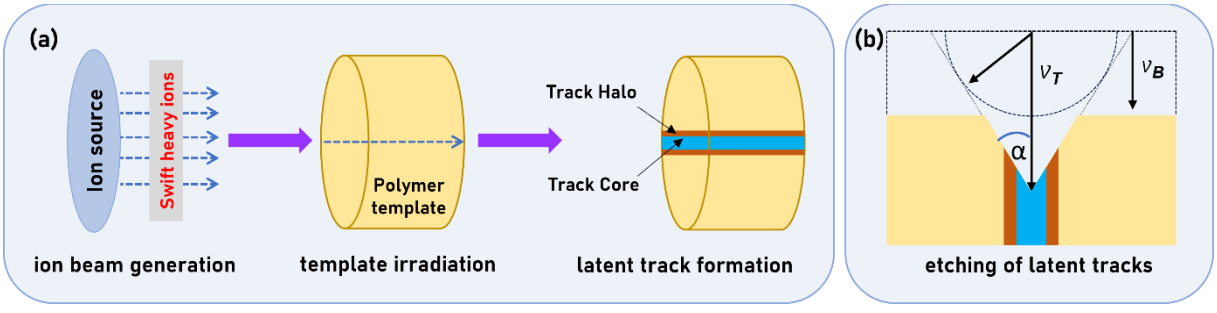

Figure 1.3. *Scheme of irradiation process of polymer templates with swift heavy ions to generate nanopores in the template. (b) Schematic of track and bulk etching rate (v_T and v_B).*

The use of track-etched membranes enables independent manipulation of various factors including pore length, diameter, shape, density, and orientation.[30] Templates with a single pore or templates with a large number of pores up to 10^9 cm^{-2} have been realized using this technique.

Small pore sizes as low as 10 nm have been achieved and can be scaled up to multiple microns. The pore length can be extended up to 100 µm, depending on the kinetic energy of the incident ions. Moreover, the production of 3D networks with specific crosslinking extent and intersection angles can be controlled by adjusting the orientation of the incident ion beam in multiple steps. This process has been successfully employed with various polymers, such as polycarbonate, terephthalate, polyethylene, and polyimide, providing a range of templates that can withstand different thermal and chemical conditions during the deposition process.[44]

Polymer templates are typically irradiated from one direction, perpendicular to the template surface, resulting in a 1D parallel array of nanostructures upon metal deposition, similar to the approach used with AAO templates as shown in Figure 1.4. The as-prepared 1D nanoarray may be disordered or bundled as shown in (Figure 1.4 I and II). On the other hand, multi-directional irradiation with heavy ions leads to intersected pores, yielding a 3D nanowire or nanotube interconnected network through electrodeposition or electroless plating, respectively. Figure 1.5 illustrates the fabrication of a 3D interconnected architecture using this method.

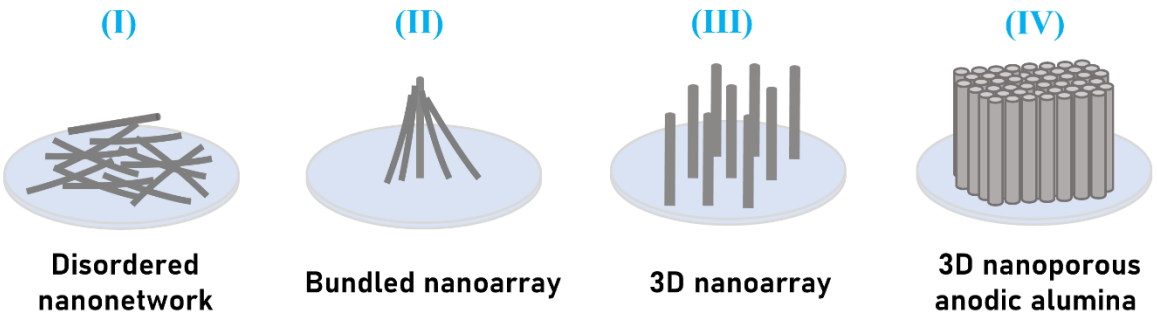

Figure 1.4. *Schematic illustration of different catalyst architectures based on 1D materials.*

Despite the remarkable advantages and the high degree of control over the structure of ion-track etched membranes, it comes with some limitations. Customized ion-track templates require ion irradiation, which can only be achieved at specialized facilities such as linear heavy ion accelerators, cyclotrons, and nuclear reactors.[45] However, commercially available ion-track etched membranes can be used to synthesize nanonetworks as they possess structural merits, such as the random orientation of intersecting pores, resulting in a 3D interconnected nanonetwork.[46,47] Moreover, these commercially available templates come in various variants with different densities and thicknesses. Optimized etching allows for further control over pore diameter, which can be increased to enhance the probability of pore intersection and the mechanical stability of the resulting nanonetworks. This enables the creation of fully self-

supported networks. During the etching process, the etchant penetrates the polymer at specific sites along the track-etched channels, forming wider pores.

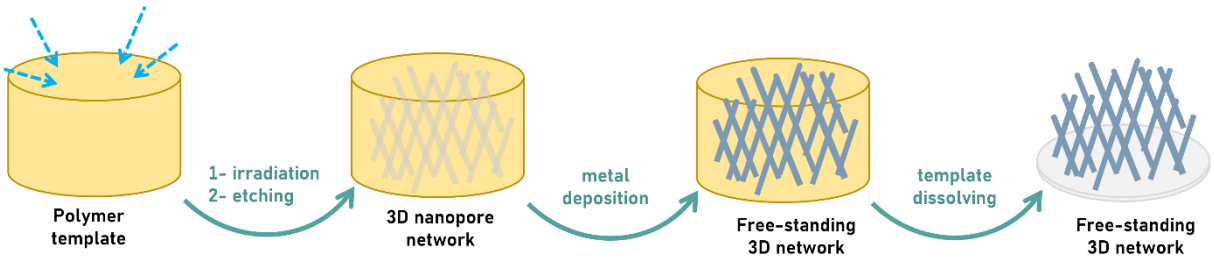

Figure 1.5. *Scheme of the synthetic approach for fabricating 3D nanonetwork architectures.*

1.3.1. Ni nanowire networks (Ni-NWN)

To create 1D nanowire networks, electrodeposition is used to completely fill the interconnected pores of the track-etched membrane with the desired metal, in this case, Ni. An electrically conductive layer is applied as a contact on one side of the template. The electrodeposited Ni starts to fill the pores of the template from the bottom side over the contact layer, creating a 3D nanowire network. Various nanowire networks have been successfully fabricated using single metals like Ni, Co, Pd, and Pt, as well as metal combinations like Ni-Co and Co-Fe.[48–51] It is crucial to strike a balance between the mass activity and mechanical stability of the 3D interconnected network. The diameter of the nanowires should be reduced to increase the mass activity, particularly in catalysis and energy storage applications. However, reducing the nanowire diameter may compromise the mechanical stability of the network, as very thin nanowires can collapse even if they were intersected. *Rauber et al.* studied the synthesis of Pt nanowire networks, exploring parameters such as diameter, orientation, shape, and three-dimensional complexity of the nanowires, and their effect on stability and performance.[52] The interconnectivity between the nanowires reinforces the rigidity of the network. To obtain a free-standing network after electrodeposition, the template matrix needs to be dissolved. This can be achieved by swelling the template in an organic solvent and evaporating the solvent. During the removal of the polymer matrix, it is important to apply minimal force to preserve the delicate integrity of the nanonetworks. Plasma etching can be used as an alternative to dissolving the polymer matrix with organic solvents, which helps avoid capillary effects during supercritical drying.[48,53] As such, the 3D porous template provides a feasible and efficient route to optimize different properties in the resulting nanonetworks. There is a trade-off between achieving a large surface area, which can be realized through a high-density nanowire network, and

outstanding mechanical strength, which can be achieved through a network with larger microwires intersecting within the network, as shown in Figure 1.6.

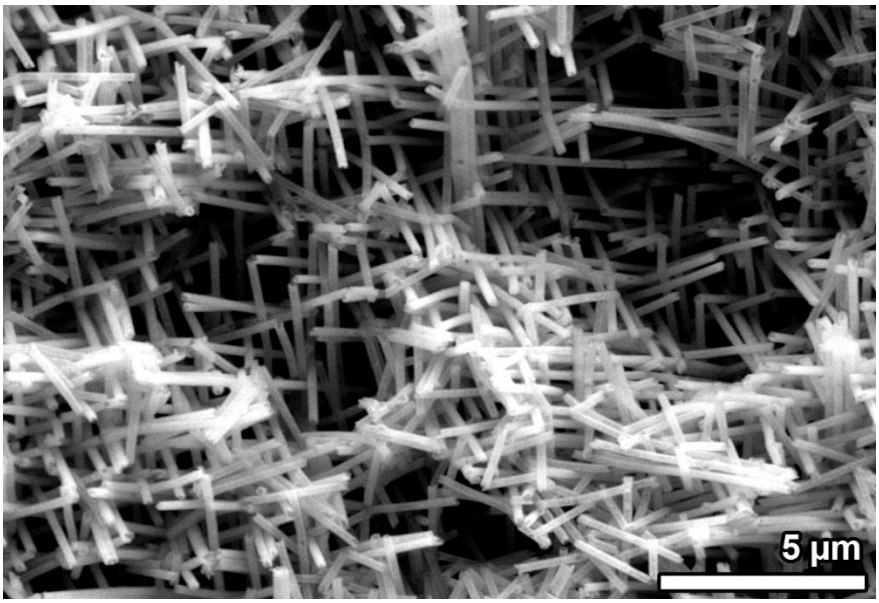

Figure 1.6. *SEM image of a 3D electrodeposited nanowire network.*

1.3.1.1. Synthesis route of Ni-NWN

In this study, a simple and feasible approach has been employed to obtain a free-standing network of Ni nanowires using a template-assisted electrodeposition technique as illustrated in Figure 1.7. Firstly, an appropriate polymer template is exposed to ion-beam irradiation to induce track formation inside the pores. The desired form of nanopores, in terms of number and intersections, can be controlled by adjusting the beam fluency and angle of the incident irradiation beam. The resulting template is then subjected to an etching process to remove the damaged zones, forming nanopores. To form the metal nanowire networks and deposit Ni inside the pores, a thin metallic layer is essential as a conductive layer that provides support to the network. Sputtering is employed to grow a uniform layer of Ni on one side of the template. The thickness of the sputtered layer can be controlled by adjusting the sputtering current and time. Once the surface layer is grown, the template is mounted on an electrochemical cell as the working electrode, with the sputtered side exposed to an electrolyte containing the Ni metal solution, as shown in Figure 1.8. A constant potential is applied to reinforce the support layer and increase its thickness. To ensure a consistent thickness of the supporting Ni layer, the accumulated charge is maintained at a fixed value. Subsequently, the unsputtered side of the template is subjected to the same electrolyte, and electrodeposition is carried out under the same conditions until the nanopores are completely filled with the Ni metal. For the electrodeposition of Ni in the nanopores, another self-developed cell design has been employed to facilitate the

process with horizontally aligned samples (Figure 1.9). To get rid of excess deposition on the surface, the unreinforced Ni layer undergoes meticulous polishing using aqua regia. Ultimately, the polymer matrix is dissolved by immersing it in an organic solvent such as dichloromethane, followed by cleaning with deionized water.

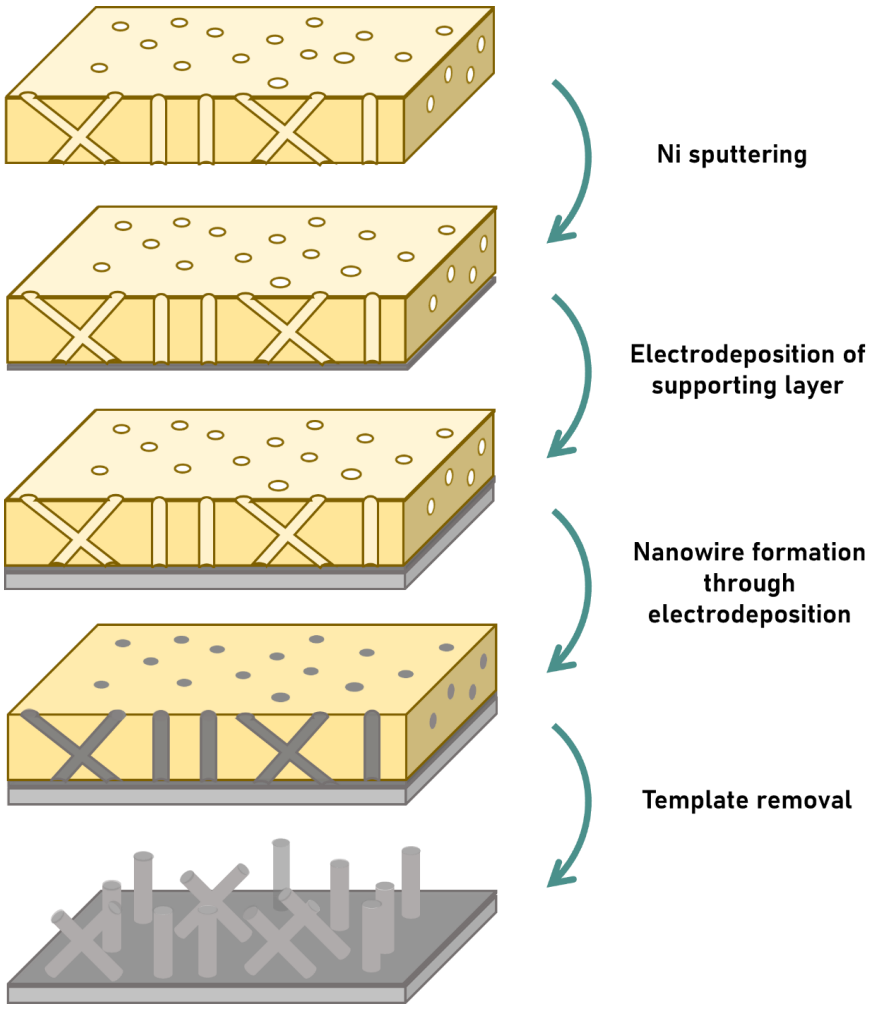

Figure 1.7. *Illustration of the synthetic approach to obtain free-standing Ni-NWN by means of electrodposition. Sputtering is employed to deposit a conductive layer on one side of the template (Step 1), which is further reinforced by a thicker supporting layer by electrodeposition (Step 2). The template is then exposed to electrodeposition to grow Ni from the sputtering layer along the template pores till the full filing of the pores, forming the nanowire network (Step 3). Finally, the polymer matrix is dissolved (Step 4) to obtain the Ni-NWN.*

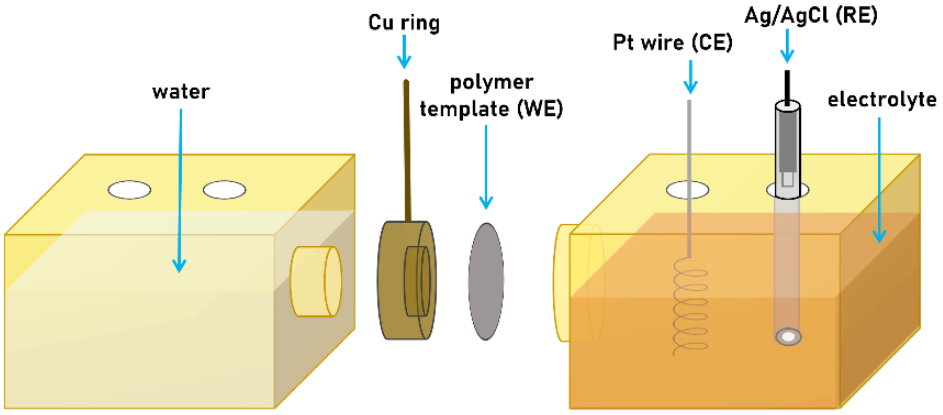

Figure 1.8. *Electrochemical cell (3-electrode setup) employed for electrodeposition with a vertically aligned sample.*

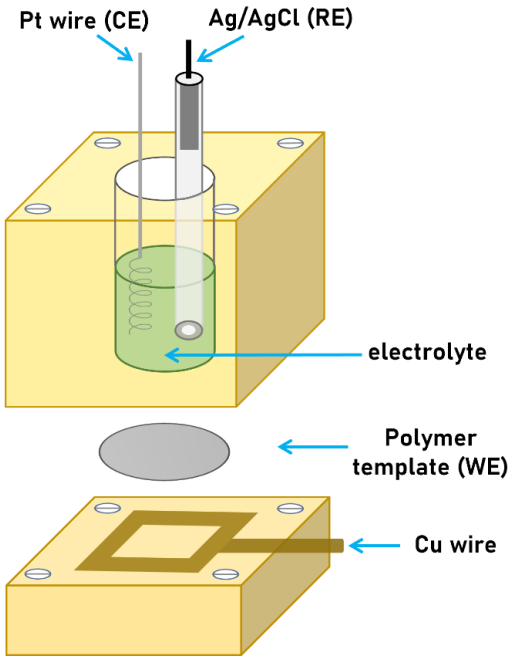

Figure 1.9. *Modified electrochemical cell (3-electrode setup) employed for electrodeposition with a horizontally aligned sample.*

The electrodeposition process within the nanopores involves three distinct stages, as illustrated in Figure 1.10.[54] Firstly, a higher current arises due to cell polarization. In the second stage, a steady current is achieved, indicating progressive filling of the pores. The initiation of the third stage can be distinguished by a notable turning point, which marks the complete filling of the pores and signals the optimal time to terminate the deposition process. Any additional deposition beyond this point leads to overdeposition, creating a thin film over the surface that obstructs access to the underlying nanonetwork. Hence, the subsequent increase in current is attributed to the expanded deposition over the surface. In the end, a free-standing network is

obtained, ready for further functionalization, and different active materials can be grown over the network.

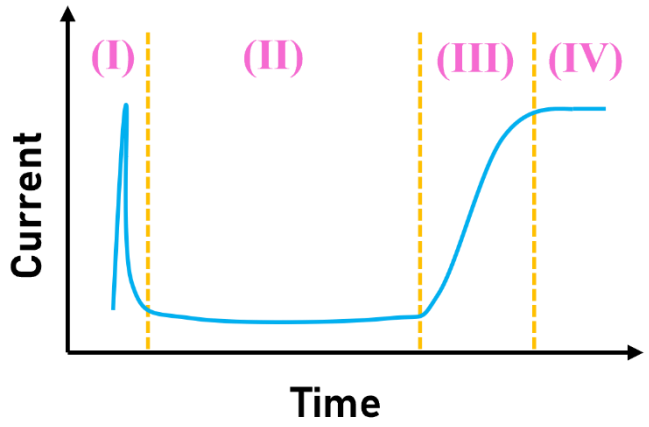

Figure 1.10. *Deposition current as a function of deposition time during preparation of nanowires. Phase (I) represents the polarization step, Phase (II) represents the deposition inside the pores, Phase (III) represents the current increase after the complete filling of pores and deposition of caps on the surface, and Phase (IV) represents the saturation state upon closure of the electrode surface.*

1.3.2. Ni nanotube networks (Ni-NTNW)

On the other hand, a metal nanotube network can be fabricated through electroless plating. The growth mechanism of electroless plating allows for conformal deposition of metal inside the pores of the polymer template. Electroless plating is an autocatalytic process that involves decorating the pore walls with nanoparticles, which act as seeds to initiate the deposition process. These metal nanoparticles then grow until a uniform and coherent layer of metal is formed, resulting in the formation of nanotubes. The seeding nanoparticles can be immobilized on the template surface through various mechanisms, such as the interaction between the reducing agent and the metal ions at the interface between the template and plating solution or through a sensitization-activation process.[55] The thickness of the nanotube walls depends on the deposition time until the pores are completely filled with the metal, resulting in the formation of a nanowire network. Pre-oxidation procedures play a crucial role in increasing the polarity of the templates and enhancing deposition efficiency.[56] Additionally, the nanoparticle seeds can contribute to the catalytic activity of the catalyst, as they remain integrated into the outer surface of the nanotube. This can be exploited to fabricate bimetallic core-shell nanotubes, combining the high catalytic activity of noble metals with the abundant metal serving as the core supporting layer. For example, Pd seeding of ion track-etched templates combined with

Ni electrodeposition has been used to obtain Pd-dotted Ni nanowire networks as electrocatalysts for methanol oxidation.[49]

A wide variety of 3D nanotube networks have been synthesized based on different transition metals, including Pt, Pd, Ag, Ni, Cu, Ir, and Ag, using electroless plating with etched templates.[30,57,58] By adjusting the pore diameters and controlling the degree of pore filling, both nanotube and nanowire networks can be achieved, as shown in Figure 1.11. Moreover, further control over the seeding density during the activation step, combined with terminating the electroless plating at earlier stages, provides the ability to obtain nanotube networks with porous walls.[59] Optimization of the plating bath and plating conditions can lead to the formation of polycrystalline and intrinsically porous films. Furthermore, the formed nanotubes can be restructured to change their composition through galvanic exchange. However, achieving uniform deposition through galvanic exchange, especially in the case of network structures with limited porosity and interspaces, such as caps on some nanowire arrays, can be challenging.[60] Colloidal nanostructure transformation can be a helpful approach to address these limitations, as it allows for precise synthetic control. For example, *Wu et al.* demonstrated the deposition of a second metal on the surface of an Ag nanocrystal, forming bimetallic nanocrystals, by introducing a parallel reduction reaction that competes with galvanic replacement and suppresses it.[61] The intersections between the pores achieved through multiple irradiations with different angles provide mechanical stability to the network, allowing it to retain its architecture without collapsing after dissolving the polymer template, even in the case of templates with low pore densities but high porosity of over 90%. The accessibility of interior active sites is a crucial parameter in determining the activity of the electrocatalyst. The catalyst exposure can be enhanced by decreasing the wall thickness of the nanotubes and increasing the porosity of the template. However, this can potentially compromise the mechanical stability of the network, so careful optimization is necessary to strike a balance. Tuning the porosity of the nanotube network on multiple levels is another important parameter that affects mass transport rates, as it can provide nanoscale confinement through pores in the walls of the nanotubes or inside the nanotubes themselves. These pores in the nanotube walls can improve the performance and activity of electrocatalysts, as they act as nanoreactors that locally concentrate the involved intermediates.[62]

One striking advantage of the 3D nanotube network is its tri-continuous structure, which consists of two separate porous systems linked together and separated by the walls of the tubes. The main system represents the interspaces between the nanotubes, while the other system

represents the pores inside the nanotubes. This provides a nano/micro channel paradigm with adjustable permeation between the two systems based on the porosity of the metallic walls. Such an architecture can be utilized to develop miniaturized flow reactors, taking advantage of the high catalytic activity of the nanotubes and the hollow structure.[30]

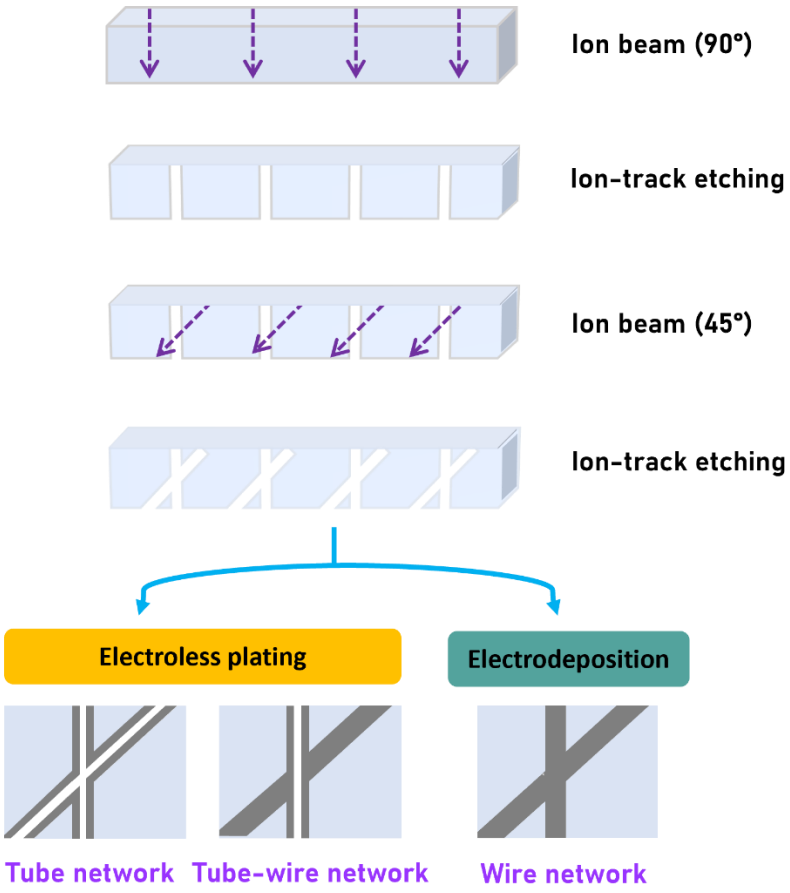

Figure 1.11. *Different categories of nanostructures deposited inside the pores of ion-track etched membranes.*

1.3.2.1. Synthesis route of Ni-NTNW

In order to fabricate Ni-NTNW, a new approach has been adopted that replicates the nanowire network from the parent ion track-etched membranes. The stability of the network relies on a sufficient density of pore intersections, which can be achieved by overlapping tilted pores and increasing the pore size and density.[63] Electroless plating is used to obtain nanotubes instead of nanowires. Since polymer substrates lack intrinsic catalytic activity, metal seeds are required for the electroless plating process. The proposed seeding procedure involves two steps: sensitization and activation. The membrane is immersed successively in Sn^{+2} and Pd^{+2} solutions, leading to the formation of a conformal layer of Pd nanoparticles on the inner walls of the pores, as described by Eq. 1.1 and 1.2: [64,65]

$$Sn_{aq}^{+2} \rightarrow Sn_{ads}^{+2} \qquad \text{(Eq. 1.1)}$$

$$Sn_{ads}^{+2} + Pd_{aq}^{+2} \rightarrow Sn_{ads}^{+4} + Pd_{ads} \qquad \text{(Eq. 1.2)}$$

The reduction of Pd^{2+} from the solution medium arises from the variation in electrochemical reduction potentials between Sn and Pd. Residual Sn may remain on the template surface after the activation process. The density of the seeding nanoparticles can be controlled by adjusting the number of sensitization cycles.[66] The deposited Pd nanoparticles act as catalysts, facilitating the oxidation of the reducing agent in the plating bath and providing electrons for the reduction of Ni^{2+} from its complex to form deposited Ni nanoparticles. Autocatalytic growth of Ni then occurs, with the Ni nanoparticles initially coating the inner walls of the pores, creating islands that eventually merge to generate uniform and continuous nanotubes on the internal surface of the pores, as well as a surface layer on the bottom and top surfaces of the substrate (Figure 1.12, step 1).[67,68] According to previous studies, The seeding Pd nanoparticles have a small size and do not contribute significantly to the catalytic activity of the Ni nanotubes as they are embedded in the Ni film and covered by the deposited Ni nanoparticles.[65,68]

Previous research studied the attachment of independent films of nanotube networks to glassy carbon electrodes via carbon paste.[32,46] However, this approach suffered from some limitations such as the low robustness where the nanotube network could be detached from the surface or completely collapse and the limited conductive connection between the nanotube network and glassy carbon. Moreover, mineral oil can leak from the carbon paste and penetrate the porous network, and the underlying nanotube network could be partially blocked by the metallic surface layer.

To address these challenges, we developed a new approach that allows for the direct integration of the Ni nanotube network into the electrode while retaining its free-standing structure and original orientation. The surface layer on one side of the template, formed during electroless plating, is reinforced by growing additional Ni through electrodeposition (Figure 1.12, step 2). This Ni-reinforced layer is then soldered to a Cu wire, creating a stand-alone electrode that is easy to handle and connect to the potentiostat. The metal surface layer on the other side is etched (Figure 1.12, step 3), and the polymer matrix is removed using an organic solvent, enabling access to the entire network (Figure 1.12, step 4). Successful etching of the Ni layer over the surface is pivotal to ensure the diffusion of the electrolyte used in subsequent steps to further

decorate the nanotube networks with different active materials and achieve uniform coverage of the Ni network via pulsed electrodeposition.

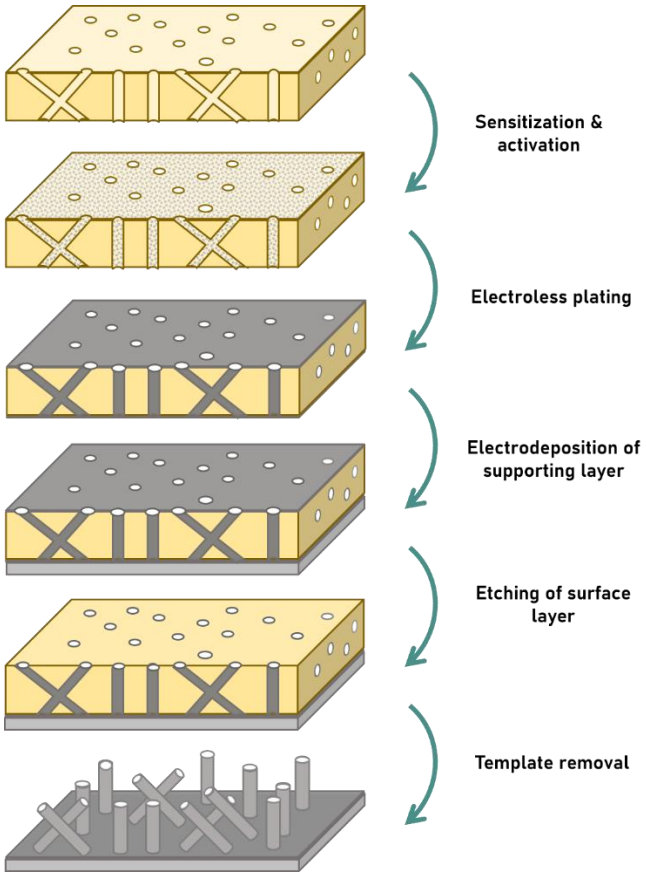

Figure 1.12. *Schematic illustration presenting the fabrication of self-supported Ni-NTNW by means of electroless plating. After sensitization and activation of the template (step 1), electroless plating is conducted (step 2) to deposit Ni inside the pores and over the template surface. Electrodeposition is employed to deposit a thicker supporting layer of Ni on one side of the template (step 3). Subsequently, the other side of the template is exposed to chemical etching to remove the Ni surface layer (step 4). Finally, the polymer template is dissolved to obtain the free-standing Ni-NTNW (step 5).*

1.4. Layered double hydroxides ((LDHs) as active materials

1.4.1. Introduction

As a class of layered materials, LDHs have gained significant attention in the fields of materials science, chemistry, and engineering due to their unique structural, chemical, and physical characteristics, as well as their potential applications in various fields, including drug delivery, wastewater treatment, catalysis, energy applications, adsorption, and electrochemical sensing.[69,70] LDHs belong to the group of anionic clays, comprising positively charged brucite-like layers separated by a variety of interlayer anions to balance the charge, resulting in an overall neutral structure.[71]

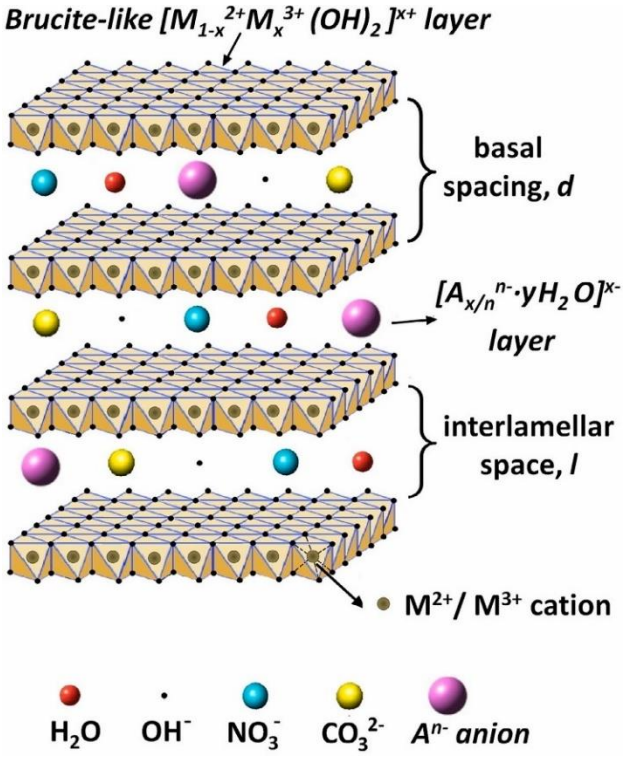

Figure 1.13. *Schematic of the general structural composition of LDHs. Reprinted from Ref. [73] Copyright (2021), with permission from Elsevier.*

The LDH host layers mainly consist of metal hydroxide sheets in the form of $M(OH)_6$ octahedra with edge-sharing. These sheets are stacked in a layered structure with negatively charged interlayer anions as guest layers, forming a 3D structure reinforced by the electrostatic attraction between the cations in the host layers and the anions in the guest layer. The general chemical formula of LDH is typically represented as $[M_{1-x}^{2+}M_x^{3+}(OH)_2]^{x+}[A^{n-}]_{x/n}.mH_2O$, where M^{2+} and M^{3+} correspond to the divalent and trivalent metal ions, respectively. A^{n-} represents the anion in the guest layer, such as CO_3^{2-}, NO^{3-}, and Cl^{1-}, and *X* stands for the molar ratio of $M^{3+}/(M^{2+}$

+M^{3+}) as shown in Figure 1.13.[72] Different metal ions have been employed to synthesize LDH including Ca^{2+}, Mg^{2+}, Ni^{2+}, Co^{2+}, Mn^{2+}, Fe^{2+}, and Zn^{2+} as divalent cations, and Co^{3+}, Al^{3+}, Fe^{3+}, Cr^{3+}, Mn^{3+}, Ga^{3+}, and In^{3+} as trivalent cations. Using metals with similar ion radii improves the stability of the LDH layers. Electrostatic attraction and hydrogen bonding between the host and guest layers play an important role in holding the layers together and maintaining a stable and highly-ordered structure. Additionally, the number, oxidation state, and volume of anions define the interlayer spacing. The ability of interlayer anion exchange is a main characteristic of LDHs, allowing them to exchange interlayer anions with many other organic or inorganic anions, leading to diversity in the chemical and physical properties of the material and enabling the synthesis of a wide range of LDH materials that fit the requirements of each application.

LDHs possess many unique properties, such as a high rate of ion exchange, outstanding thermal stability, enhanced mechanical properties, large surface area, high ion exchange capacity, and tunable porosity.[74] These properties make LDHs desirable materials for a wide range of applications and on different scales. LDHs have been widely investigated as catalyst materials in electrochemical applications including sensing, catalysis, and energy storage applications.[75,76] As electrocatalysts, LDHs have provided enhanced electrochemical activity and stability, which is reflected in long-term cyclability and outstanding performance in different systems. However, LDHs suffer from some limitations that restrict their performance in electrochemical applications. The major limitation of LDHs is their poor electrical conductivity, as they are either insulators or semiconductors, which limits electron transfer rates during electrochemical reactions, resulting in lower efficiency in certain applications, such as OER and supercapacitors.[77] In addition, the interlayer spaces in LDHs are affected by their environment and the structure becomes unstable under certain conditions, leading to degradation or loss of catalytic activity which reduces the stability in certain applications. Furthermore, the complex synthetic process of LDH via the self-assembly of metal and hydroxide ions in aqueous solutions could result in a variety of possible structures and compositions. Moreover, the different conditions employed during the synthesis process, including temperature, pH, and the ratio of precursors, can greatly influence the resulting composition and structure, making it difficult to control the structure and composition of LDHs precisely. Consequently, these limitations make it challenging to tailor the properties of LDHs for specific electrochemical applications precisely. For instance, the activity and selectivity of an LDH-based electrode could be strongly affected by its conductivity, composition, and structure. Moreover, changes in LDH composition and structure can lead to inconsistencies in

performance, making it difficult to fabricate reproducible and reliable LDH-based electrochemical devices.

1.4.2. Enhancing the performance of LDH

To address the challenges mentioned above and enhance the performance of LDH-based electrocatalysts, various strategies have been proposed, including nano-structuring, hybridization, intercalating, and modulation of the electronic structure.[78–81]

Nano-structuring involves tailoring LDH architectures at the nanoscale to create structures with increased surface area. This allows for improved mass and charge transfer, as well as better accessibility to the active sites within the LDH layers, ultimately leading to enhanced activity. Another strategy is hybridization, where LDHs are combined with other active materials or catalysts to form composite structures that fulfill the requirements of each application. For instance, various studies have reported the growth of LDH over metal substrates to enhance their conductivity and secure efficient electron paths to the current collectors.[82,83] This synergistic integration can result in enhanced electrochemical properties and improved performance compared to using individual components alone. Intercalation is another strategy to overcome the limitations through the insertion of ions guest species between the LDHs layers, which can modify the interlayer spacing and influence the overall electrocatalytic behavior. By carefully selecting the intercalating species, it is possible to enhance the catalytic activity and stability of LDH-based electrocatalysts. Furthermore, modulation of the electronic structure of LDHs has been investigated as an efficient strategy to enhance their electrocatalytic performance. This can be achieved through surface functionalization, doping, or controlling the oxidation states of the metal ions in the LDH structure. These modifications optimize the electronic properties of LDHs, leading to improved performance in different aspects including catalytic activity and selectivity. Overall, these strategies offer promising avenues for addressing the challenges associated with LDH-based electrocatalysts and advancing their performance for various applications in catalysis, energy conversion, and storage.

1.5. Functionalization of 3D nanowire and nanotube networks

1.5.1. Advantages of 3D heterogeneous nanostructured electrode materials

Nanomaterials are extensively utilized in electrochemical applications, particularly in catalysis and energy storage, owing to their advantageous properties, including large surface area, short pathways for electron and ion transport, and the ability to exhibit high activity in certain electrochemical reactions that bulk materials cannot achieve, as discussed in detail in Section 1.1. While the synthetic approach to the active nanomaterial is crucial for optimal electrode performance, it is equally important to optimize the design of the electrode itself. In traditional electrode structures, a composite of nanoparticles of the electroactive material, polymer binders, and conductive additives is applied onto the substrate, such as metal foils.

A novel and intensively researched category of electrode architectures, known as 3D self-supported nanostructured electrodes, has emerged to grow the active material over a conductive substrate, such as nanowire or nanotube networks. These structures are characterized by their nano-architectured, non-dense layers consisting of one or more phases grown over nanowire or nanotube networks. For electrochemical applications, these 3D nanostructured nanowires or nanotube networks offer numerous inherent merits over conventional electrode designs, which can be summarized as follows:

1- Large Surface Area: The absence of dense packing results in a large exposed surface area, which plays a pivotal role in electrochemical applications. For instance, in supercapacitors, charges are stored at the electrode surface, and a greater surface area is essential for increasing the capacity and energy density, providing more space for charge storage. Similarly, in Li-ion batteries, the uptake of lithium from the electrolyte is a reversible process, and expanding the surface area enhances the accessibility for lithium ions, thereby improving the electrochemical kinetics.[84]

2- Variety of Nanostructures: Various nanostructures of different shapes, such as nanotubes, nanowires, and vertically aligned platelets, can be obtained based on the preparation method and conditions applied during synthesis. While previous reports have described 3D self-supported nanostructures of various electrode materials, such as metal alloys, phosphides, conducting polymers, and carbon-based materials, the fast-growing field of energy storage and catalysis has primarily focused on self-supported metal oxide and hydroxide nanostructures due to their high functionality.[85–90]

3- Good adherence to substrates: the direct growth of nanostructured active material onto a conductive substrate not only eliminates the need for conductive materials or binders

but also provides better and uniform distribution over the conductive substrate and avoids the aggregation of active material or forming bulky units in contrast to classical electrodes, especially for large-scale energy storage devices, which involves mixing the powder active materials with conductive additives such as carbon additives and polymer binders before coating onto a metal substrate to optimize performance.

4- Tunability of Volume Inside the Nanonetwork: Incomplete packing of the electrode surface is critical to secure enough interior spaces that can accommodate significant volume expansion, especially for oxides that undergo expansion during lithium insertion and form lithium-metal alloys. This allows the electrode material to expand into the unoccupied spaces within nanowires or inside nanotubes. Additionally, it is essential to relieve the aggregation of the active material and volume increase, thereby preventing electrode pulverization and collapse of the nanonetwork. However, optimizing porosity is crucial, as extreme porosity can impact performance in terms of volumetric energy density, for example.

5- Enhanced Electron and Ion Conductivity: Nanowire and nanotube networks provide direct pathways for electrons through the 1D growth of these networks. Such networks possess intrinsic conductivity without using binders, which not only reduces grain boundaries but also decreases interface resistance, allowing electrons to move easily along the networks. This improved electron transfer efficiency within the electrode leads to enhanced performance. Moreover, the direct contact between the nanotubes and nanowires and the substrate or current collector ensures fast and easy electron transportation to the outer circuit, which is crucial in applications with high charge/discharge currents like batteries.[18] Moreover, nanowire and nanotube networks provide free spaces where other ions from the reaction medium can be incorporated as dopants via adsorption on the surface, resulting in surface states, or incorporation into the bulk material, creating additional ionic defects.[91,92] The presence of a significant amount of ions can improve the ionic and electronic conductivity within the networks.[93]

1.5.2. Engineering *2D-on-1D* core-shell structure *via* electrodeposition

Electrodeposition offers a feasible and straightforward technique for depositing various metals and metal composites onto different substrates and structures using electrodes and an electrolyte solution.[94,95] This method is particularly suitable for fabricating 3D nanostructured architectures using template-assisted processes, as it can be achieved for most materials using aqueous solutions at room temperature. The utilization of electrodeposited nanostructured

materials in energy storage and conversion has been extensively investigated due to their favorable characteristics.[96]

Numerous LDH materials have been successfully prepared in different morphologies using electrodeposition by modifying the substrate and deposition parameters.[97,98] In this study, to grow the hydroxide nanosheets ($Ni(OH)_2$, NiCo-LDH, and NiFe-LDH) over the nanotube and nanowire networks, nitrate salts of the desired metals were employed as the electrolyte solution in the electrodeposition process. During electrodeposition, the metal hydroxides grow through the reduction of NO^{3-} ions, leading to the generation of OH^- ions. Subsequently, the metal ions (Ni^{2+}, Co^{2+}, Fe^{2+}) in the electrolyte react with these hydroxide ions, resulting in the formation of Ni/Co hydroxide films. The reduction of NO^{3-} ions and the generation of OH^- ions occur.[99] These hydroxide ions then react with Ni^{2+} or Co^{2+} ions present in the electrolyte, leading to the precipitation of hydroxide layers over the nanotube or nanowire networks. Various electrodeposition times and potentials were tested to control the extent of deposition and determine the optimal preparation conditions, as will be further discussed in the results section. Initially, a continuous potential was applied for the electrodeposition of the hydroxide layer. However, this method did not yield satisfactory deposits. The inadequate deposition could be attributed to the formation of gas bubbles, which impede the efficient penetration of reacting ions into the inner regions of the network. Additionally, reagent depletion occurred within the interior layers of the network. To overcome these challenges, a pulsed deposition approach was employed by reversing the potential for short time intervals.

1.6. Oxygen evolution reaction (OER)

1.6.1. Introduction

Electrochemical water splitting is a highly promising method for producing green energy, where hydrogen generated through this process serves as a renewable and clean source of fuel.[100] Hydrogen is an eco-friendly energy carrier that finds application in various fields, such as transportation, refrigeration, and lighting.[101] Figure 1.14. illustrates a typical water electrolysis system along with different applications. The water splitting process involves two main reactions: (i) OER and (ii) hydrogen evolution reaction (HER). Of these, OER is the critical reaction and acts as a bottleneck for the entire process, facing significant challenges that limit its widespread adoption. The sluggish kinetics of OER due to the four-electron-transfer process and the higher operating potentials required to achieve high current densities restrict the overall efficiency of water splitting processes.[102,103] Therefore, the development of efficient OER electrocatalysts is essential to enhance water splitting efficiency and enable large-scale hydrogen production.

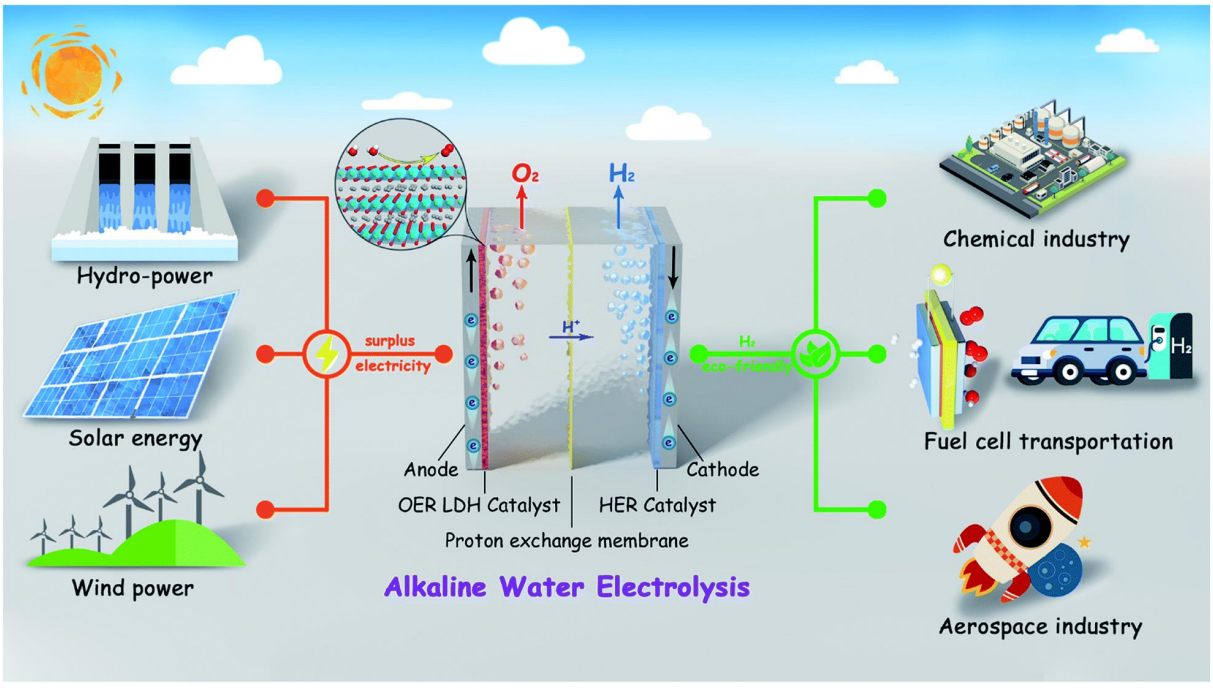

Figure 1.14. *A proposed sustainable energy system that utilizes an integrated water electrolysis setup to produce renewable hydrogen fuel. Reprinted from Ref.* [104] *Copyright (2019), with permission from RSC.*

1.6.2. Determining the efficiency of OER electrocatalysts

The water splitting process can occur in alkaline, neutral, and acidic environments. OER takes place at the anode, while HER occurs at the cathode. The half-reactions for OER and HER differ depending on the reaction medium, as shown below:

In alkaline medium:

1. OER: $4OH^- \rightarrow O_{2(g)} + 2H_2O_{(l)} + 4e^-$ $E_a^0 = -0.40\ V$ (Eq. 1.3)
2. HER: $4H_2O + 4e^- \rightarrow 2H_2 + 4OH^-$ $E_c^0 = 0.83\ V$ (Eq. 1.4)

In acidic medium:

1. OER: $2H_2O_{(l)} \rightarrow O_{2(g)} + 4H^+ + 4e^-$ $E_a^0 = -1.23\ V$ (Eq. 1.5)
2. HER: $4H^+ + 4e^- \rightarrow 2H_2$ $E_c^0 = 0\ V$ (Eq. 1.6)

Equations (1.3) and (1.5) demonstrate that the production of molecular oxygen during OER proceeds through a thermodynamical process that demands four electrons, with a redox potential of 1.23 V and a standard Gibbs free energy (ΔG^o) of +237.2 kJ mol^{-1}.[105] However, an additional energy called overpotential (η) is required to overcome the sluggish electron-transfer kinetics for efficient water oxidation.

To evaluate the activity of an electrocatalyst towards OER, two main parameters are commonly used: Tafel slope and overpotential. Overpotential can be determined from linear sweep voltammetry (LSV) curves by recording the potential required to achieve a specific current density, usually 10 mA cm^{-2} (η_{10}) or 100 mA cm^{-2} (η_{100}). On the other hand, the Tafel slope gives an indication of the reaction kinetics, representing the rate at which the overpotential changes with increasing current density. As the Tafel slope (b) decreases, the reaction kinetics become faster, according to the following equation.

$$\eta = b \log\left(\frac{j}{j_0}\right) \qquad \text{(Eq. 1.7)}$$

where, η represents the overpotential, and j and j_0 are the current density and exchange current density, respectively.

As depicted in the above equations, OER takes place at the anode and involves a four-electron process, resulting in the production of O_2. This reaction is facilitated by the adsorption of H_2O and OH^- on a surface-active metal center denoted as M. Proposed mechanisms for OER share similar intermediates, including MOH and MO.[106] However, the main divergence lies in the

reaction pathway leading to oxygen formation. Notably, two distinct approaches have been identified to generate O_2 from the MO intermediate, as depicted in Figure 1.15. The first approach, represented by the green arrow in Figure 1.15, involves the direct interaction of 2M-O to produce gaseous O_2. The second approach entails the formation of the MOOH intermediate, which decomposes to yield O_2 (black path in Figure 1.15). Despite this disparity, it is widely agreed upon that the electrocatalysis of OER is a heterogeneous reaction, wherein the (M-O) bonding within the MOH, MO, and MOOH intermediates plays a critical role in determining the overall electrocatalytic performance.

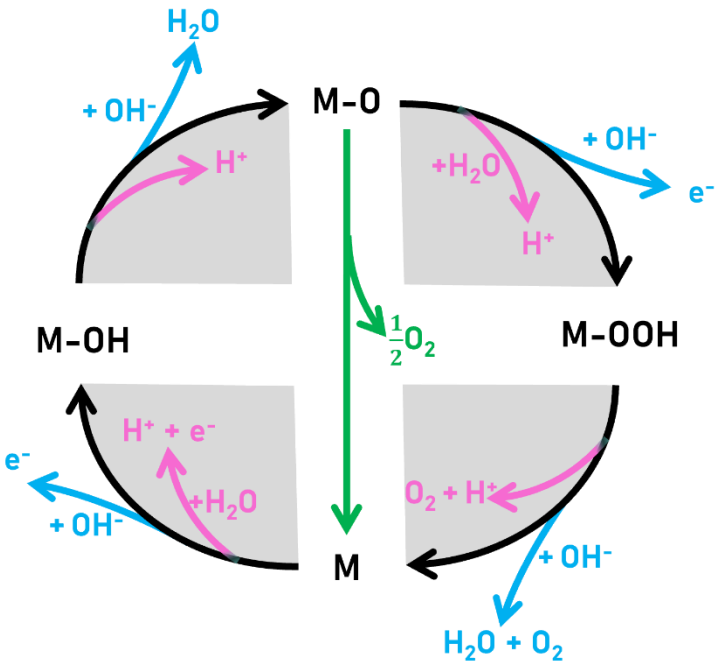

Figure 1.15. *OER mechanism in both alkaline (blue line) and acidic (red line) media. The formation of the intermediates is indicated by the black line, while an alternative route involving the direct reaction of two M-O intermediates* is shown by the green line.

1.6.3. Self-supported LDH-decorated nanonetworks for OER

Currently, noble metal-based electrocatalysts such as RuO_2 and IrO_2 are widely used for OER due to their high activity. However, their high cost, limited availability, and low stability hinder their large-scale application for hydrogen production.[107,108] These catalysts are susceptible to oxidation and dissolution at high anodic potentials during OER, further affecting their stability. To overcome these challenges, researchers have been exploring alternative, low-cost, and noble-metal-free electrocatalysts with enhanced performance and stability. Several materials have been investigated such as mixed metal oxides, non-noble metal-based hydroxides, sulfides phosphides, nitrides, borides, perovskites, and LDHs.[109,110]

Among them, mixed metal hydroxides and their derivatives have gained significant attention as they offer potential synergistic effects, abundance, and high catalytic activity. Particularly, LDHs have shown attractive merits for OER, especially NiCo and NiFe-based ones.[111,112]

Traditionally, electrocatalysts were freestanding particles that could aggregate during electrode assembly, reducing the number of exposed active sites. In contrast, in-situ growth of LDH over 1D nanowires and nanotubes with geometrically ordered structures offers a more stable architecture with numerous exposed active sites on the surface. Nickel has demonstrated remarkable capability for water oxidation in an alkaline environment through its hydroxide species.[113] A recent study has reported the growth of NiFe oxyhydroxide on a NiFe alloy substrate using a magnetic field, forming a hierarchical thin structure that enhances mass transfer. This electrocatalyst exhibited remarkable OER performance (achieving 1000 mA cm^{-2} at 258 mV).[17] To further boost the catalytic activity towards OER, developing a heterogeneous structure of 3D architecture provides an efficient strategy to be adopted. Up to now, various elements and materials have been grown or deposited over 1D or 2D nanoarrays, producing a heterostructure array.[19] These 3D structures grown over the substrates enhance targeted electrocatalytic reactions by promoting ion and charge transfer. Furthermore, the hydrophilicity of the substrates plays a vital role in desorbing gas bubbles evolved during the reaction and retains sustainable mechanical pressure, further improving the electrocatalytic activity. Nevertheless, a comprehensive understanding of the specific mechanisms by which substrates contribute to catalytic activity is still limited, highlighting the need for further research in this area.

In order to improve the OER efficiency of $Ni(OH)_2$, researchers have employed microstructuring and doping methods involving the incorporation of transition metals such as cobalt and/or iron, which show high activity towards OER. A study by *Kim et al.* demonstrated the efficacy of employing a NiFe-coated 3D-ordered nickel electrocatalyst, resulting in remarkable OER capability and long-lasting durability over 300 h.[114] The 3D Ni substrate was prepared using a template-assisted technique followed by electrodeposition. This particular design enhances mechanical stability by efficiently eliminating gas bubbles evolving during electrolysis due to their smaller sizes. Moreover, in contrast to the traditional Ni foam, the incorporation of NiFe onto the 3D Ni substrate demonstrated a notable increase in double-layer capacitance (C_{dl}), reaching a value of 260 μF cm^{-2}. This improvement can be attributed to the larger surface area provided by the 3D structure.

1.7. Electrochemical glucose sensing

1.7.1. Principles of electrochemical glucose sensing

A sensor is a device that detects and converts changes in the system into measurable signals, unveiling the composition of specific substances in an unknown world through chemical, physical, or biological changes. Typically, a sensor consists of three main components: a detector, a transducer, and a signal processor (Figure 1.16). Among different sensor types, electrochemical sensors record changes in substances as electrical signals, offering advantages such as high sensitivity, selectivity, the use of smaller analytical instruments, real-time monitoring capabilities for target analytes, and rapid response times. Consequently, electrochemical sensing finds wide applications in environmental detection, biomedical applications, and the food industry.[115–117]

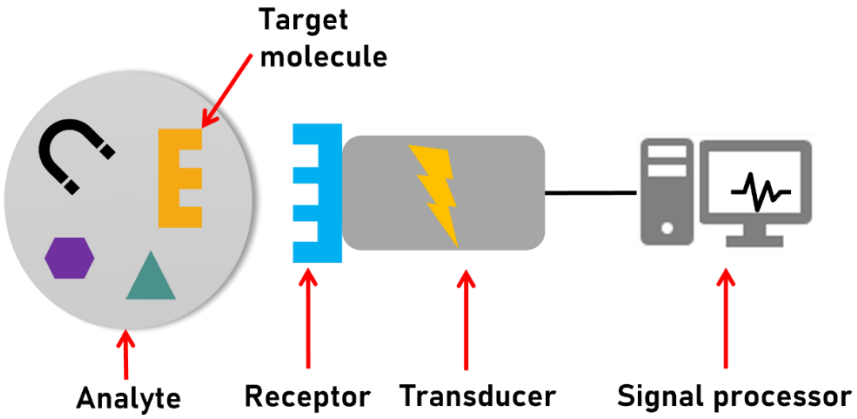

Figure 1.16. *Schematic illustration of the principle of the electrochemical sensor.*

In practical sensing systems, the standard three-electrode setup is commonly employed, with the working electrode typically made of metal or metal oxide. To enhance the electrode's selectivity for the measured analyte, advanced functional nanomaterials are often used to modify the electrode structure, meeting the requirements of reaction detection. Once the target substance is successfully recognized on the electrode surface, various electrochemical techniques, such as CV and chronoamperometry, can be employed to acquire electrochemical signals, providing valuable information about the target analyte's concentration.

As a widely distributed monosaccharide and the main energy source for cells, glucose holds significant importance in various fields, especially clinical diagnosis.[118] Disorders associated with the regulation of blood glucose levels are significant indicators in chronic metabolic diseases, particularly diabetes. Elevated blood glucose levels are closely associated with several renal, nervous, and cardiac diseases.[119] Accordingly, the development of advanced biosensors

for precise and real-time monitoring of blood glucose levels holds immense importance. Traditional enzymatic glucose sensors operate through the interaction between glucose and oxygen, catalyzed by glucose oxidase (GOx), resulting in the production of H_2O_2 and gluconolactone.[120] The pioneering work by *Williams et al.* in 1970 introduced a leading GOx-based biosensor for determining glucose levels.[121] Since that time, extensive research has been conducted on enzymatic glucose sensing, incorporating different nanomaterials that achieve high selectivity, sensitivity, low detection limits, and excellent reproducibility.[122,123]

Combining electrochemical methods with glucose sensing offers new avenues for determining glucose concentration. Glucose sensors are typically classified into enzymatic and nonenzymatic glucose sensors. Enzymatic sensors, the most extensively studied type, have undergone three generations of development (Figure 1.17). Glucose oxidoreductase enzymes, specifically GOx and glucose dehydrogenases (GDHs), have been widely employed as the foundation for numerous glucose biosensors.[124] The first-generation sensors utilized oxygen as the electron acceptor, determining glucose concentration based on oxygen consumption and hydrogen peroxide release.[125] Nevertheless, these sensors had several limitations, including interference with other biomolecules and the sensitivity to oxygen partial pressure, reducing the enzyme's activity. The second-generation enzyme sensors overcame some of these limitations by utilizing a chemically modified layer as the electron acceptor, extending the linear range and lifespan of the sensor. The third-generation enzyme sensors enabled direct electron transfer between the electrode and the enzyme. To enhance the performance of enzymatic glucose sensors, functional nanomaterials, including noble metals (platinum and gold), have been introduced.[118]

While enzymatic glucose sensors offer high selectivity and sensitivity, they also have drawbacks related to enzyme characteristics, such as requiring low temperatures for storage and having poor stability under prolonged operation.[126,127] Additionally, the fixation of enzymes is a complex process that is difficult to control and may be affected by pH, humidity, and temperature variations. Consequently, the realization of enzyme-free glucose sensors (Figure 1.17) with high stability, sensitivity, and feasible preparation methods has gained increasing attention.[122,128] Nonenzymatic sensors offer advantages over enzymatic glucose sensors, as their preparation processes are much easier, and they are less influenced by the surrounding environment, with longer storage periods.

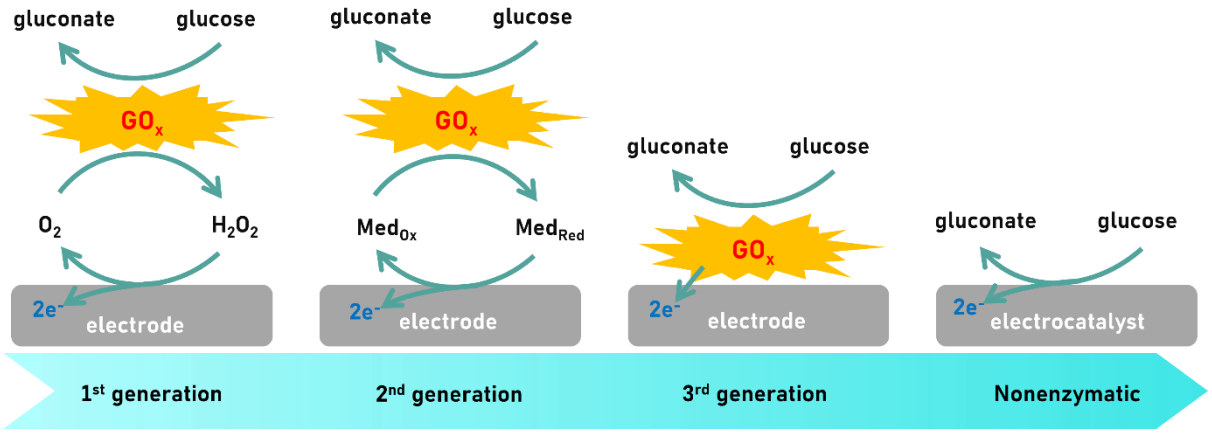

Figure 1.17. *Schematics of the evolution of various generations of enzymatic electrochemical glucose sensors and nonenzymatic glucose sensors that utilize nanomaterials.*

1.7.2. Self-supported LDH-decorated nanonetworks for nonenzymatic glucose sensing

Driven by the substantial advancements in nanotechnology over the past decade, a wide range of nanostructures, including metals, metal oxides, and their combinations with carbon nanomaterials, have found extensive use in nonenzymatic sensing applications.[129,130] The synthesis strategies employed for multifunctional nanomaterials have expanded the scope of nanotechnology and opened up numerous possibilities for electrochemical sensors. Based on current research, three main approaches are utilized for the material synthesis of enzyme-free glucose sensors. Firstly, nanotechnology is employed to synthesize small-sized, porous metal materials with different morphologies, including nanotubes, nanowires, nanoflowers, nanosheets, and nanoclusters. Secondly, combinations of different materials, such as metals, oxides, hydroxides, carbon materials, organic compounds, and metal-organic frameworks, are utilized. Lastly, modifications are made to the surface of the electrode to enhance roughness and introduce additional electrochemically active sites. It has been reported that the faradaic currents during nonenzymatic glucose oxidation are increased upon using nanomaterials with a large surface area and increased roughness factors.[131] In this regard, LDHs have emerged as a promising class of active nanomaterials due to their ability to provide high roughness and an enlarged surface area.[132] Specifically, Ni-based LDHs have shown great potential as they are enriched with Ni^{3+} centers, which can act as oxidizing agents. For instance, *Lu et al.* synthesized ultrathin NiFe-LDH nanosheets on Ni foam using a hydrothermal method to be used as electrodes for glucose sensing.[133] This electrode demonstrated remarkable sensitivity (3680.2 $\mu A\ mM^{-1}\ cm^{-2}$), along with a low detection limit (0.59 µM) and high selectivity. The remarkable electrochemical activity of this system can be attributed to its high rate of charge transfer and

the presence of numerous active sites. Another study reported the fabrication of a flexible bifunctional electrode for glucose oxidation by growing a nanosheet array of CoFe-LDH on a Ni wire.[134] This innovative method employed Ni wire as a micro-substrate, enabling efficient detection of glucose through both colorimetric and electrochemical approaches. The Ni/CoFe-LDH-NSA biosensor demonstrated exceptional performance and long-term stability. *Shen et al.* successfully prepared a nonenzymatic glucose sensor based on Cu foam coated with NiCo-LDH nanoflake arrays-supported Au nanoparticles.[135] The electrode was synthesized via galvanic exchange and electrodeposition, providing a linear detection range between 0.5 and 3000 μM. Furthermore, it delivered outstanding sensitivity of 23100 μA mM^{-1} cm^{-2} and high stability. The enhanced activity of the electrode towards glucose oxidation could be attributed to the synergy between the three-dimensional Cu foam with its high conductivity and the LDH nanoflakes with their high catalytic activity.

1.8. Supercapacitors

1.8.1. Supercapacitors as a sustainable energy storage technology

The need for renewable energy sources has become increasingly evident due to the limited availability of fossil fuels and growing environmental concerns about their negative impact.[136] Transitioning from fossil fuels to renewable sources offers the potential for energy savings and decentralized energy production. However, the intermittent nature of renewable energy sources, such as sunlight and wind, requires efficient energy storage solutions to ensure a continuous and reliable energy supply. To address these challenges and achieve a stable energy supply, the development of electrochemical energy storage (EES) technologies and advanced electrode materials is of paramount importance. Among the various energy storage technologies available (mechanical, electrical, chemical, electrochemical, and thermal energy storage), our focus lies on capacitors, supercapacitors, and batteries. These represent distinct classes of energy storage devices, each with its own unique capabilities and applications.[137] It is important to emphasize that these systems are complementary rather than competitive, providing the opportunity to effectively meet future energy demands by integrating them, particularly supercapacitors and batteries.[138]

Notable progress has been made in the past decade in the development of batteries with high energy densities and supercapacitors with high power densities. However, neither of these technologies alone can fully meet the commercial demands in different applications. As a result, hybrid energy storage systems have been explored to maximize the benefits and move along the Ragone plot's diagonal (Figure 1.18). These hybrid systems combine the high-power characteristics of supercapacitors with the high energy content of rechargeable batteries. By integrating these technologies, it becomes possible to design energy storage systems with both high power and high energy densities, bridging the limitations of individual technologies (batteries and supercapacitors).

In the case of supercapacitors, charge storage occurs through two mechanisms. The first mechanism is the electrical or electrochemical double-layer capacitance (EDLC), where charge separation takes place at the electrode-electrolyte interface. The second mechanism is pseudocapacitance, involving charge transfer through redox reactions.[139] These two mechanisms collectively contribute to the overall charge storage capability of a supercapacitor. On the other hand, batteries operate differently, as they do not directly store electrical energy. Instead, they store energy in the form of chemical energy within the active material of the electrodes, held by chemical bonds. This chemical energy is then converted into electrical

current through redox reactions. In a battery, specific compounds in the anode and cathode, along with the electrolyte, facilitate energy storage.

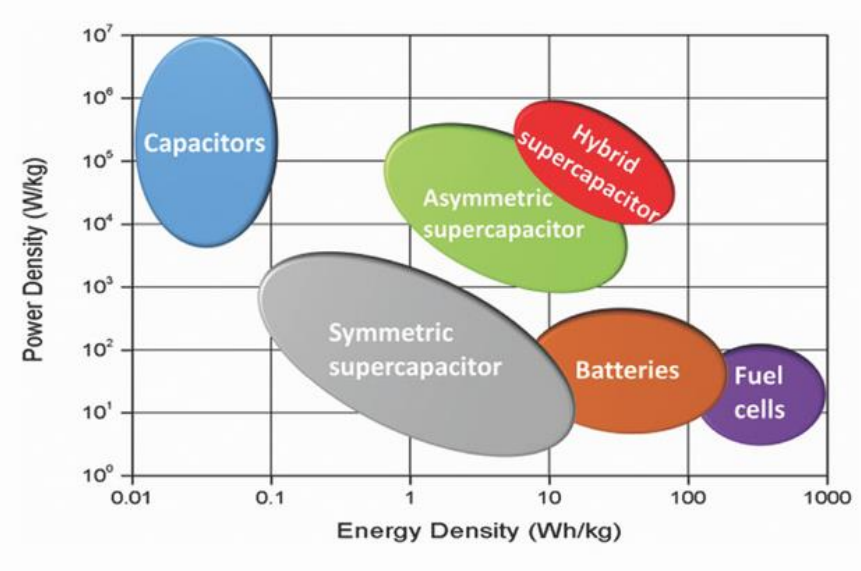

Figure 1.18. *Ragone plot of the specific energy and power densities of energy storage devices. Reprinted from Ref.* [140] *Copyright (2017), with permission from Wiley.*

In addition to extensive research on supercapacitors and batteries, there is growing interest in hybrid energy storage devices known as supercapatteries. These systems combine a battery-type material with a supercapacitor-type electrode material. By utilizing two electrodes with different charge storage behaviors - one exhibiting capacitive behavior (supercapacitor) and the other Faradaic behavior (battery) - supercapatteries provide high power density from the supercapacitor electrode and higher energy density from the battery electrode.[141,142]. This combination offers opportunities to develop energy storage systems with outstanding performance, falling between the capabilities of a traditional battery and a supercapacitor.

In energy storage devices, charges can be stored either on the surface of the material (double layer) or within its bulk (Faradaic behavior). For EDLC, an ideal material should have a large active surface area to facilitate charge accumulation at the electrode-electrolyte interface without involving any electrochemical reactions within the bulk material (Faradaic capacitance) (Figure 1.19a). Rechargeable batteries, on the other hand, store charge through reversible Faradaic reactions in the bulk of the electrode (Figure 1.19b). The design of battery materials should allow for easy diffusion of reacting species within the material. In the case of pseudocapacitors, Faradaic redox reactions occur on or near the electrode surface without significant ion diffusion through the electrode bulk (Figure 1.19c). Finally, hybrid energy storage systems exhibit behavior that is intermediate between Faradaic reactions and EDLC,

combining the characteristics of both batteries and supercapacitors (Figure 1.19d). Realizing energy storage devices that meet these specific needs and provide optimum performance will require groundbreaking advancements, including the utilization of innovative electrode materials with specifically designed nanostructures.

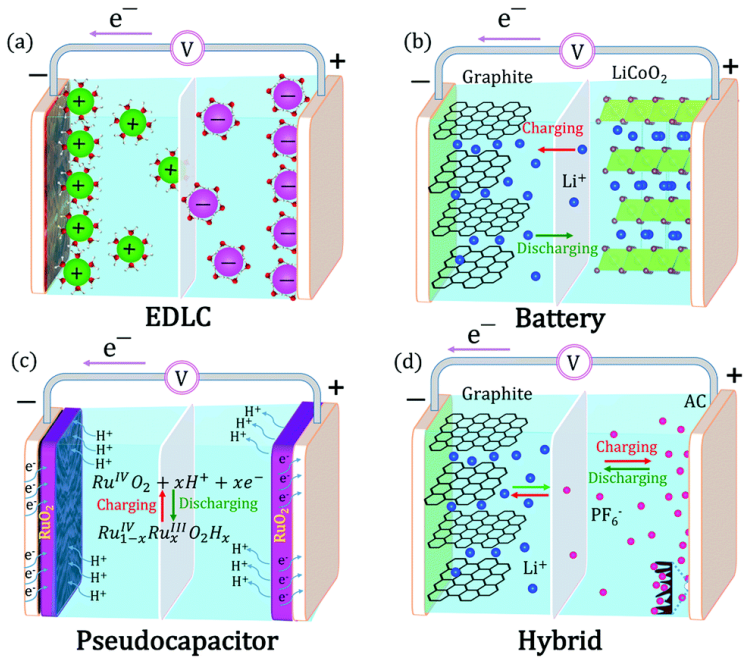

Figure 1.19. *Schematic presents different electrochemical energy storage systems, including (a) an EDLC, (b) a battery, (c) a pseudocapacitor, and (d) a hybrid system combining EDLC and intercalative storage mechanisms. Reprinted from Ref.* [143] *Copyright (2019), with permission from RSC.*

1.8.2. Self-supported LDH-decorated nanonetworks as battery-type electrodes for supercapacitor

Tailoring nanostructured electrode materials can offer significant advantages compared to their bulk counterparts in achieving high performance in energy storage applications. Heterogeneous nanostructured electrodes, composed of multiple nanocomponents tailored to meet specific requirements such as conductivity, high energy density, and mechanical strength, have been successfully synthesized.[84,144] These heterogeneous architectures demonstrate synergy, harnessing the maximum potential of their individual components and delivering enhanced performance in terms of rate capabilities, energy, and power densities.[144,145] Several criteria are used to evaluate the successful utilization of these materials in energy storage:

(i) Suitable synthetic approaches or assembly methods.

(ii) Proper selection of material combinations.

(iii) Morphology optimization of the heterogeneous architectures, such as nanowires, nanotubes, nanosheets, or core-shell nanoparticles.

Transition metal-based electrodes have garnered significant attention as promising candidates for energy storage due to their composition tunability, easy preparation procedures, cost-effectiveness, and high redox activity, enabling high specific capacity. Self-supported transition metal-based nanoarrays and networks, particularly nickel hydroxide ($Ni(OH)_2$), have been extensively researched for supercapacitor applications.[22,34,146] *Wan et al.* summarized the advances in developing self-supported transition metal hydroxides (TMHs) nanosheets for energy storage applications, discussing various synthetic techniques and the composition variation.[72] Another review systematically studied the advantages of self-supported transition metal-based materials, encompassing Ni, Co, Mn, Mo, Cu, and V, along with their diverse electrochemical properties and compositions, followed by an exploration of challenges and outlooks to guide their further development.[22]

$Ni(OH)_2$ exhibits a high theoretical specific capacitance of 2358 F g^{-1} and well-defined faradaic redox reactions.[147] However, its low electrical conductivity (10^{-17} to 10^{-15} S cm^{-1}) limits its capacitance, especially at high current densities, which hampers its practical applications.[148] To tackle this limitation, self-supported $Ni(OH)_2$-based composites have been developed by incorporating materials with high conductivity such as carbon nanotubes and graphene. This composite structure secures efficient electron transfer pathways between $Ni(OH)_2$ and the substrate. For instance, *Min et al.* reported a hydrothermal approach to prepare a reduced graphene oxide (rGO) layer sandwiched between two layers of $Ni(OH)_2$ on a substrate of Ni foam substrate using a hydrothermal approach. This enhanced composite achieved an outstanding specific capacitance of 3328.7 F g^{-1} at 1.5 A g^{-1}. [148]

Additionally, Ni-based LDHs, such as NiFe-LDH and NiCo-LDH, have gained attention as battery-type electrodes for supercapacitors.[149,150] LDHs offer several advantages, including high Faradaic redox activities, the ability to finely tune their chemical compositions, and a uniform distribution of metal ions within the layers. Bimetallic LDHs based on Ni, such as NiFe-LDH and NiCo-LDH, exhibit natural abundance, distinct oxidation states, outstanding cycling durability, environmental friendliness, and promising cycling stability.[151–153] One-step synthesis methods have been employed to fabricate self-supported electrodes of Ni-Co LDH on Ni foam that delivers a specific capacitance of 2682 F g^{-1} at 3 A g^{-1} which is subsequently coupled with rGO in a hybrid supercapacitor.[154] This assembly achieved an energy density of 188 Wh kg^{-1} at 1499 W kg^{-1} while retaining 82% of its capacitance after 5000 cycles. Self-

supported architectures comprising LDHs and other phases of Ni have been established to further enhance performance. *Liang et al.* fabricated a NiCo-LDH@NiOOH electrode with a high capacitance of 2622 F g^{-1} at a current density of 1 A g^{-1}, along with good retention of 88.5% over10000 cycles.[155]

CHAPTER II

2. Nanowire networks-based electrocatalysts

Following a detailed introduction on the topic, theoretical background, and a wider literature survey, this chapter focuses on the results related to the engineering of self-supported Ni nanowire networks decorated with various LDH composites for the OER. The chapter highlights the synthetic approach, physical characterizations, and activity evaluation of these electrocatalysts, providing valuable insights on the active species and the synergistic effects between the nanowire substrates and the incorporated LDH nanosheets and between the different metals in the LDH composites.

This chapter presents the results published in the following peer-reviewed article:

[1] **K.M. Amin**, K-H Lin, M. Duerrschnabel, L. Molina-Luna, W. Ensinger, Engineering Active Sites Enriched 2D-on-1D NiFe and NiCo LDH-decorated Ni Nanowire Networks for Oxygen Evolution Reaction, *ACS Sus. Chem. Eng, 11 (2023) 15410–15422*.

The objective of this work was to demonstrate the potential of the nanowire networks as substrates for enhancing the electrocatalytic activity of the LDH materials. It aimed to estimate the effect of growing LDH with different metal compositions on the electrode performance. These findings contribute to the progress of design approaches and open up possibilities for the creation of electrochemical devices that are both highly efficient and compact in size.

2.1. Engineering Active Sites Enriched *2D-on-1D* NiFe and NiCo Layered Double Hydroxide-Decorated Ni Nanowire Networks for Oxygen Evolution Reaction

Khaled M. Amin,* Kuan-Hsun Lin, Michael Duerrschnabel, Leopoldo Molina-Luna, Wolfgang Ensinger

Author information

Corresponding author

Khaled M. Amin - Department of Materials Science, Technical University of Darmstadt, Darmstadt 64287, Germany; Department of Polymer Chemistry, Atomic Energy Authority, Cairo 11787, Egypt; https://orcid.org/0000-0002-7698-0098; Email: amin@ma.tu-darmstadt.de; khaledamin89@gmail.com

Authors

Kuan-Hsun Lin - Department of Materials Science, Technical University of Darmstadt, Darmstadt 64287, Germany

Michael Duerrschnabel - Institute for Applied Materials - Applied Material Physics, Karlsruhe Institute of Technology, Eggenstein-Leopoldshafen 76344, Germany; https://orcid.org/0000-0002-9047-6541

Leopoldo Molina-Luna - Department of Materials Science, Technical University of Darmstadt, Darmstadt 64287, Germany; https://orcid.org/0000-0002-9412-8093

Wolfgang Ensinger - Department of Materials Science, Technical University of Darmstadt, Darmstadt 64287, Germany

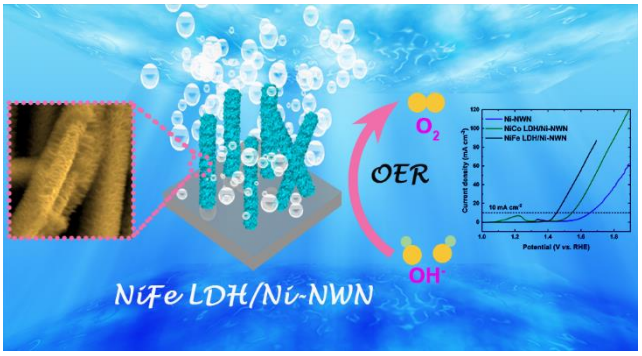

ACS Sus. Chem. Eng., 2023, 11, 15410–15422**, DOI:** 10.1021/acssuschemeng.3c04505**.**

Abstract

Green energy technologies, including water splitting and fuel cells, are being extensively pursued to meet the increased demand for renewable energy and tackle the pollution issues related to fossil fuel consumption. The performance of these technologies primarily relies on noble-metal oxide electrocatalysts, which are typically supported by macroscopic and weighty materials. Therefore, it is urgently needed, although it is still challenging to engineer highly efficient and naturally abundant electrocatalysts in micro- and nanostructures. Herein, we applied a facile strategy to fabricate highly efficient electrocatalysts based on different layered double hydroxides (LDHs), namely NiCo and NiFe, grown over a free-standing 1D Ni nanowire network (Ni-NWN) for oxygen evolution reaction (OER). Benefiting from the synergy of coupling the 2D LDH nanosheets with its high catalytic activity and the Ni-NWN with its interconnected highly conductive structure and high porosity, the as-prepared NiFe LDH/Ni-NWN exhibited excellent OER performance with a low overpotential of only 222 mV to deliver 10 mA cm^{-2}. Furthermore, it revealed favorable kinetics in terms of a 42 mV dec^{-1} Tafel slope and a low charge transfer resistance. The 3D architecture with its “nanosheet on nanowire” structure improves the mechanical stability, besides retaining efficient electron paths through the Ni-NWN and high ionic diffusion rates through the porous network, which in turn promotes the generation of active phases during OER and provides outstanding durability over 50 h. Furthermore, the architectures' proposed strategy and flexible engineering are highly promising and could be adopted to fabricate other electrocatalysts for widespread applications.

Keywords: Track-etched membranes; Layered double hydroxides; Nanowire arrays; Hierarchical structures; Electrodeposition; Self-supported electrodes; OER

2.1.1. Introduction

The relentless pursuit of sustainable energy solutions, aimed at meeting the growing energy demand while mitigating the environmental concerns arising from the utilization of fossil fuel, is a high-priority international target and comes on top of the current research topics.[156–160] Different approaches have been implemented to maximize the market share of renewable energy systems, including energy conversion and storage systems e.g. fuel cells, water splitting, and metal-air batteries.[161–163] As a sustainable and green energy resource, hydrogen represents the major player that can change the future of the energy market.[164] Water splitting is seen as the most promising and scalable strategy for the production of green hydrogen. This process mainly involves two reactions: (i) hydrogen evolution, which occurs at the cathode, and (ii) oxygen evolution, which occurs at the anode. Nevertheless, the OER is commonly regarded as the bottleneck within the water splitting mechanism. This is because the OER encompasses several proton-coupled electron transfer steps that are inherently slow kinetically, subsequently impacting the overall efficiency of the water splitting process.[165,166] Even the commonly used noble metal-based electrocatalysts (RuO_2 and IrO_2) necessitate a high overpotential to overcome the energy barrier essential for the OER.[167] Also, the limited availability and high production costs associated with noble metals impose constraints on the widespread implementation of such catalysts on a large scale. Hence, extensive research is currently being focused on designing abundant and cost-effective transition metal-based electrocatalysts as alternatives with high activity toward OER.[164,168]

Transition metal-based electrocatalysts represent promising competitors that can replace noble metal-based ones, including oxides, hydroxides, sulfides, nitrides, and phosphides.[168–175] Among these materials, LDHs have emerged as a highly promising class capable of meeting the majority of the criteria for effective electrocatalysts in alkaline media due to their distinguished 2D structure with interlayer spaces, large active surface areas, and tunable compositions.[176,177] NiFe LDH is regarded as highly efficient as an electrocatalyst in alkaline media due to its ability to facilitate the OER process with a low overpotential.[178–180] Several studies have been conducted to further enhance the NiFe-LDH activity toward the OER. However, developing an ideal electrocatalyst for OER is not yet accomplished. Most LDHs have low conductivity as they are insulators or semiconductors, which severely affects the OER activity. Additionally, they tend to agglomerate.[181]

Various approaches have been proposed to address these challenges and boost the performance of LDH-based electrocatalysts, such as hybridization, modulating the electronic structure,

intercalating, and nanostructuring.[78–81,182] The engineering of electrocatalysts with nanoscale architectures is gaining increasing attention.[183,184] This approach aims to maximize catalyst efficiency by increasing the surface area and enhancing the mass and charge transfer. Consequently, it provides better accessibility to active sites, leading to improved performance. One-dimensional (1D) nanowire networks such as Ni-NWN can offer a platform with highly conductive pathways for electron transfer, working as a backbone that carries the active material. The overall 3D architecture, which consists of a *2D-on-1D* core-shell structure, merges the advantages of 1D Ni-NWN with its porous structure, namely the high conductivity and the mechanical stability, with those of the 2D LDH nanosheets which act as a shell layer with high redox catalytic activity and great surface area. Additionally, the direct contact between the LDH layer and interconnected Ni nanowires plays a crucial role in accelerating charge transfer. This can be attributed to the robust connection between the LDH layer and Ni-NWN, where each Ni nanowire acts as an individual current collector. The proposed hierarchical structure provides multiple advantages over the common bulk composites due to the synergy between the individual components in such a multilevel hierarchy.

Numerous studies have reported the utilization of NiCo and NiFe LDH-based electrocatalysts for OER, employing different shapes, such as nanosheets, nanotubes, and nanowires, which establish direct contact with the current collector.[185–189] However, the geometry and dimensions of such electrodes are mainly correlated to the dimensions of the parent substrate, which carries the active material and works as a supporting electrode such as foams, felts, and cloths. Most of these substrates have dimensions in the microscale, which limit the active surface area of the electrode and restrict their use in certain applications that require an electrode of smaller thickness or lower mass. Meanwhile, nanowire networks provide an extra striking feature, namely the nanoscale dimensions and the straight orientation, which can dramatically boost the performance of the electrocatalyst besides the common characteristics shared with the other common substrates, including the porous intersected structure. Accordingly, it is essential to establish a rational synthetic approach to create a cost-effective electrocatalyst that meets the criteria for achieving a high OER performance. Designing a nanoscale architecture overgrown by various electrocatalytic active materials of varying dimensionality can effectively address many functionality issues, including better exposure of the active sites, higher conductivity, and faster diffusion rates of ions through these nanoreactors.[182,190]

Inspired by these considerations, herein, we highlighted a new fabrication strategy of self-supported 3D hierarchical NiCo LDH/Ni-NWN and NiFe LDH/Ni-NWN electrocatalysts with

a core-shell structure via facile in situ electrodeposition of LDH nanosheets over Ni-NWN. The free-standing Ni network was obtained through a template-assisted strategy to deposit Ni inside the pores of commercial track etched membranes, forming a self-supported network that acts as a substrate and current collector without needing a binder or conductive material. As such, LDH nanosheets serve as the active material; this coating delivers high electrocatalytic activity through its abundant active sites and excellent stability, while the 3D NWN provides mechanical strength, large surface areas, and high electron conductivity. Furthermore, the 3D self-supported electrodes offer a higher diffusion rate of ions through their tortuous structure. The introduced approach employs scalable and simple techniques that can be customized to prepare a variety of architectures with different compositions and ratios of active materials. Three electrodes (Ni-NWN, NiCo LDH/Ni-NWN, and NiFe LDH/Ni-NWN) have been examined as electrocatalysts for OER. NiFe LDH/Ni-NWN required a very low overpotential of 222 mV to attain 10 mA cm^{-2}, all while retaining outstanding stability over a 50 h duration. Moreover, it possessed a lower charge transfer resistance (R_{ct}) and smaller Tafel slope compared to Ni-NWN and NiCo LDH/Ni-NWN, delivering a better overall electrocatalytic performance. This performance even outperforms most recently reported transition metal-based electrocatalysts. Considering its impressive OER performance, stability, and the abundant availability of LDH metals, as well as the feasible and scalable synthetic approach, it is anticipated that the NiFe LDH/Ni-NWN electrocatalyst presented here holds significant potential to replace noble-metal-based catalysts in real-world applications for OER.

2.1.2. Experimental Section

2.1.2.1. Materials

Polycarbonate template membranes had the following specifications: a thickness of 25 µm, a pore diameter of 400 nm, and a pore density of 1.5×10^8 cm^{-2} (ipPORE from it4ip). The following chemicals were utilized as received: boric acid (H_3BO_3, 99.5%, Sigma), nickel chloride ($NiCl_2$, 98%, Aldrich), nickel nitrate hexahydrate ($Ni(NO_3)_2 \cdot 6H_2O$, GR, Merck), dichloromethane (CH_2Cl_2, puriss. p.a., Sigma-Aldrich), iron sulfate heptahydrate ($FeSO_4 \cdot 7H_2O$, ≥ 99%, Sigma-Aldrich), cobalt nitrate hexahydrate ($Co(NO_3)_2 \cdot 6H_2O$, *99+%, Acros Organics)*, and KOH (Sigma-Aldrich). Deionized water was employed in all procedures.

2.1.2.2. Synthesis of Ni-NWN

To prepare the free-standing Ni-NWN electrodes, a template-assisted electrodeposition method was employed. Briefly, ion track-etched membranes were first sputtered with a thin Ni layer under a current of 100 mA for 180 s to provide conductivity to the template. The sputtered template was then subjected to electrodeposition within a three-electrode setup to reinforce the electrode and retain mechanical stability. The electrodeposition process took place in an electrolyte solution containing 0.5 M $NiCl_2$ and 0.5 M H_3BO_3. A constant potential of -0.9 V *vs.* Ag|AgCl was applied during this process, with the thickness of the Ni supporting layer being regulated by maintaining an accumulated charge of 100 C. In order to obtain the free-standing Ni-NWN, the same electrodeposition parameters and the same electrolyte were employed to deposit Ni until the pores of the template were filled. The upper side of the template was then carefully polished with aqua regia to eliminate any extra deposition over the template surface. Finally, the template was immersed in dichloromethane to dissolve the polymer matrix and then cleaned with deionized water.

2.1.2.3. Synthesis of Core/Shell-like NiCo and NiFe LDH-Decorated Ni-NWN

NiCo and NiFe LDH nanosheets were directly grown over Ni-NWN via pulsed potential electrodeposition. For NiCo LDH, an electrolyte containing a 1:1 molar mixture of 0.05 M $Ni(NO_3)_2{\cdot}6H_2O$ and 0.05 M $Co(NO_3)_2{\cdot}6H_2O$ was used. The pulsed electrodeposition process involved applying -1 V *vs*. Ag|AgCl with intermittent pulses of 1 V vs. Ag|AgCl for 0.5 s every 3 s. This process was carried out for a duration of 90 s. Subsequently, the samples underwent thorough washing with H_2O and were dried. Similarly, for NiFe LDH, an electrolyte containing 0.15 M $Ni(NO_3)_2{\cdot}6H_2O$ and 0.15 M $FeSO_4{\cdot}7H_2O$ was employed, and the pulsed electrodeposition was conducted using the same parameters.

2.1.2.4. Surface and Structural Characterization

Scanning electron microscopy (SEM) measurements were conducted by using a Philips XL30 FEG instrument (Netherlands), operating at acceleration voltages ranging from 10 to 30 kV. X-ray diffraction (XRD) analysis was achieved with a D8 Advance diffractometer (AXS Bruker, Germany) supplied with a Cu anode and utilized Bragg-Brentano geometry along with an SOL X Detector. Additionally, a Seifert XRD 3003 PTS-3 instrument was used with monochromated Cu K_α radiation. The recorded spectra spanned the range of 2θ= 8-90°, with a step size of 0.02° for the complete spectrum and 0.03° for the highlighted areas of interest, employing a slower scan speed. The full spectra were recorded with a scan speed of 2θ = 250 s^{-1}, while the areas of

interest highlighted in the XRD figure were scanned with a slower scan rate of 2θ = 1666 s^{-1}. Transmission electron microscopy (TEM) images and selected area electron diffraction (SAED) patterns were accumulated with a Thermofisher Talos F200X equipped with a Ceta CCD camera, a SuperX energy-dispersive X-ray (EDX) detection system, and a Gatan Enfinium electron energy-loss spectroscope. The microscope operated at an acceleration voltage of 200 kV. Data analysis for TEM was conducted using Thermofisher Velox, Digital Micrograph™, and SingleCrystal[191] softwares. To analyze the composition and elemental oxidation states of the three electrodes, X-ray photoelectron spectroscopy (XPS) was employed, utilizing a SPECS PHOIBOS 150 (Germany). A monochromatized Al K_α line with an excitation energy of 1486.7 eV was employed as the X-ray source. CasaXPS (version 2.3.25) was employed to fit the acquired spectra and subtract the background using the Shirley method.[192] For consistency, the spectra were calibrated by setting the C 1s peak at 284.5 eV.

2.1.2.5. Electrochemical Experiments.

The electrodeposition experiments were conducted in a three-electrode setup using a Keithley 2602 System SourceMeter unit (USA). Sputtered polymer templates served as the working electrodes (WE), while Ag|AgCl functioned as the reference electrode (RE), and a Pt spiral electrode acted as the counter electrode (CE). The deposition of NiCo and NiFe LDH nanosheets was achieved using the previously prepared Ni-NWN as the WE, following the same conditions. Electrochemical measurements were carried out in a custom-designed three-electrode setup utilizing a Gamry Reference 600 potentiostat (USA). The reference electrode employed was Hg|HgO filled with 1 M KOH, the counter electrode was a Pt spiral wire, and the working electrode was a round, free-standing sample with a diameter of 13 mm of the three electrocatalysts (Ni-NWN, NiCo LDH/Ni-NWN, and NiFe LDH/Ni-NWN). All of the experiments were conducted in a 1 M KOH solution as an electrolyte. Potentials were converted to a reversible hydrogen electrode (RHE) scale using the formula:

$$E_{RHE} = E_{Hg/HgO} + 0.059 \cdot pH + 0.98 \qquad \text{(Eq. 2.1)}$$

Before the electrocatalytic performance was assessed, the electrocatalysts were activated by running cyclic voltammetry under a scan rate of 50 mV s^{-1} until reaching a steady state of each electrocatalyst. The activity towards OER was investigated by linear sweep voltammetry (LSV) at a scan rate of 1 mV s^{-1}, and Tafel slopes were calculated from LSV. Overpotential was calculated using the following equation:

$$\eta\ (\mathrm{V}) = E_{RHE} - 1.23 \qquad \text{(Eq. 2.2)}$$

Electrochemical impedance spectroscopy (EIS) was conducted over a frequency range spanning from 0.01 Hz to 100 kHz, using an amplitude of 10 mV (NiFe LDH@Ni-NTNW was represented within the frequency range of 0.5 Hz to 100 kHz for improved fitting). Durability was assessed through chronopotentiometry (CP) performed at a current density of 10 mA cm^{-2} for 50 h.

2.1.3. Results and Discussions

2.1.3.1. Characterization of the Hierarchical Architectures.

In contrast to the traditional methods for synthesizing electrocatalysts, the innovative approach employed in creating hierarchical NiCo LDH/Ni-NWN and NiFe LDH/Ni-NWN architectures (Figure 2.1) represents a feasible and scalable pathway for establishing a flexible model of self-supported electrodes. This model can be adopted to functionalize NWN-based platforms with various active materials, suitable for diverse catalytic applications. The synthesis process began with the electrodeposition of Ni-NWN within the pores of the polymer template on the back sputtered Ni layer. Subsequently, the NiFe LDH and NiCo LDH nanosheets were grown over the core Ni-NWN via controlled pulsed electrodeposition, forming the hierarchical core-shell architectures. Hierarchical architectures, in contrast to bulk materials, exhibit remarkable synergistic effects arising from the combined properties of their individual components within a multilevel structure. It is crucial to emphasize that our 3D porous structure provides a significantly larger interior surface area when compared to conventional substrates like Ni foams or fibers. This synthetic approach offers an integrated and robust design of the catalyst electrode, capitalizing on the extensive surface area and excellent catalytic activity of the 2D LDH nanosheets, as well as the high electrical conductivity, mechanical strength, and efficient electron transfer pathways of the 1D Ni-NWN. The interplay between these components in our hierarchical architecture not only facilitates enhanced activity but also enables easy handling of the electrode without the need for supporting electrodes or binders, retaining the mechanical stability of the stand-alone network without any damage.

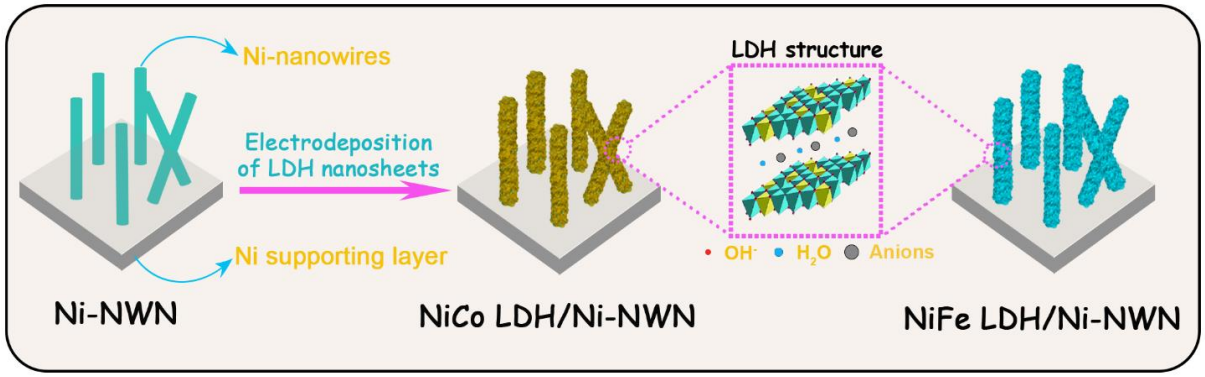

Figure 2.1. *Schematic illustration of the fabrication process of the self-supported NiCo LDH/Ni-NWN and NiFe LDH/Ni-NWN architectures.*

Surface and structural analyses of the electrodes confirmed the successful optimization of the deposition parameters. SEM micrographs of Ni-NWN (Figure 2.2a-c) depicted the conformal deposition of Ni inside the entire pores of the parent templates, creating coherent and uniform Ni nanowires with a diameter of approximately 400 nm, closely mirroring the original nanopore diameter. After the polymer template was dissolved, the as-prepared nanowire network preserved a self-supported architecture growing over the electrodeposited Ni supporting layer, which works as a current collector for this electrode, as represented in Figure S2.1. As for this paradigm, the Ni-NWN acts as a 3D conductive core, which is efficiently connected to a thin layer of Ni that retains the network integer and provides a conductive pathway to the potentiostats. The top view of Ni-NWN (Figure 2.2b) depicts the intersections between the wires, which retain the structure intact and prevent the stacking of the wires. The lateral view of prepared Ni-NWN (Figure 2.2c) reveals the free-standing architectures, which appear free from any polymer residuals while maintaining an intact structure. The resulting 3D interconnected nanowire network serves as a perfect conductive scaffold for the subsequent growth of the NiCo and NiFe LDH nanosheets. These LDH nanosheets were erectly deposited onto the Ni-NWN, creating a well-defined hierarchical “nanosheet on nanowire” architecture. In the case of the NiCo LDH/Ni-NWN architecture, as illustrated in Figure 2.2d-f, the NiCo LDH nanosheets forming the outer layer on the Ni-NWN backbone exhibit a distinct wrinkled structure, which sets them apart. The side view of the network (Figure 2.2f) provides confirmation that the entire length of the nanowires is uniformly coated with a consistent layer of NiCo LDH nanosheets. Similarly, the SEM micrographs of the NiFe LDH/Ni-NWN electrode (Figure 2.2g-i) depict the Ni-NWN skeleton decorated with a layer of NiFe LDH nanosheets. As displayed in Figure 2.2i, the interconnected network appears to be entirely covered with LDH while retaining the porous construction of the network. This ensures that the

micro pathways remain free without clogging arising from overdeposition. This approach is optimal for obtaining a significant amount of active material (NiCo or NiFe LDH), thereby enhancing the catalytic activity of the electrodes while allowing for the unimpeded diffusion of the electrolyte through the catalysts.

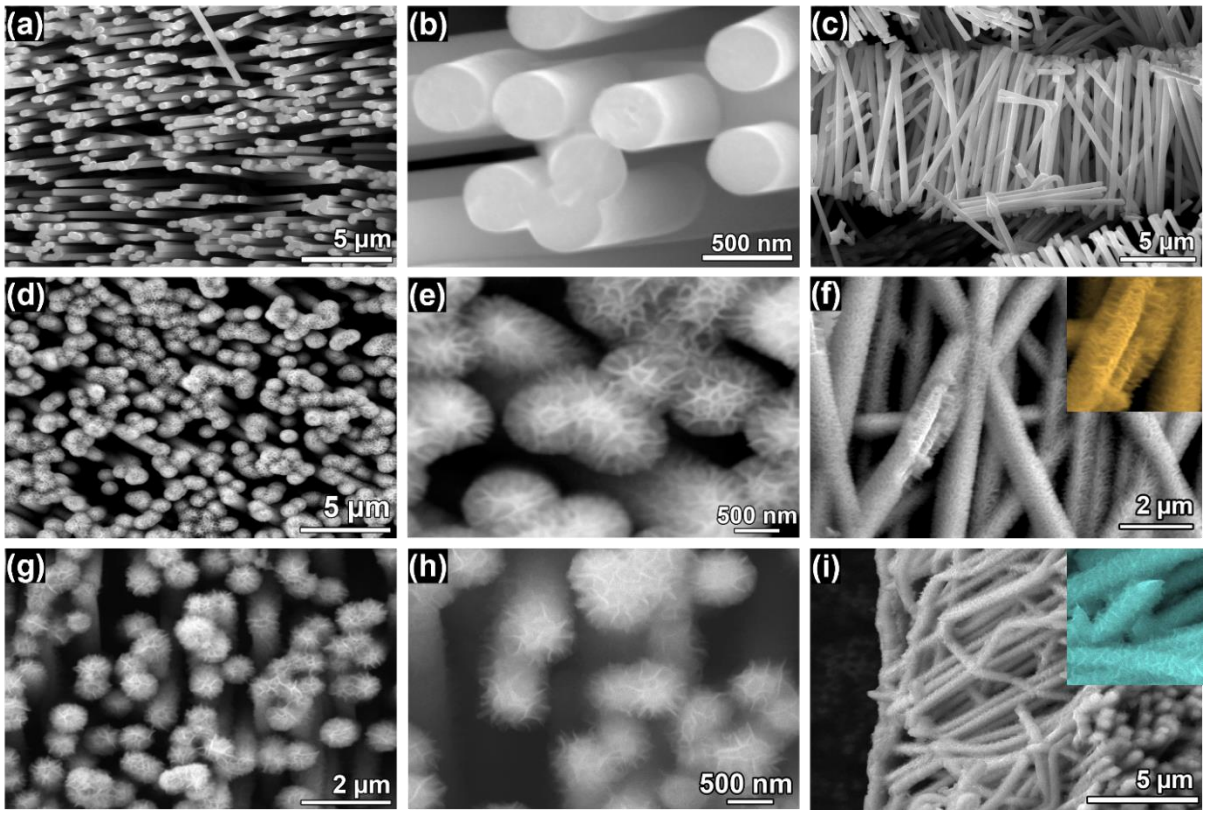

Figure 2.2. *Top-view and side-view SEM of (a-c) Ni-NWN, (d-f) NiCo LDH/Ni-NWN, and (g-i) NiFe LDH/Ni-NWN.*

The hierarchical design of the catalysts was further investigated by using TEM accompanied by SAED on cross-sections of the prepared composites. TEM images of the Ni-NWN catalyst (Figure 2.3a) showed circular-shaped Ni wires with uniform morphology and a diameter of approximately 400 nm along the entire wire length. The SAED pattern displayed diffraction rings (Figure 2.3b, c), indicating the polycrystalline nature of the Ni-NWN with characteristic ring patterns corresponding to the (111), (200), (220), (400), and (420) crystal planes. To validate the synthetically projected core-shell structure of the coated nanowires, TEM analysis was performed on NiCo LDH/Ni-NWN (Figure 2.3d) and NiFe LDH/Ni-NWN (Figure 2.3g). Both catalysts exhibited a uniform coating layer composed of plentiful flaky nanosheets surrounding the Ni-NWN skeleton which appeared darker compared to the surrounding NiCo LDH and NiFe LDH nanosheets as depicted in Figure 2.3d, g, respectively. Further, local SAED measurements were conducted at different spots representing the Ni core and the shell layer of

NiCo LDH and NiFe LDH nanosheets as marked by the dashed circles in Figures 2.3d and g. SAED analysis of NiCo LDH/Ni-NWN and NiFe LDH/Ni-NWN revealed the same characteristic rings of polycrystalline Ni at the centers of the wires (Figure 2.3 e,h), dominated by the Ni core. In contrast, the SAED obtained from the shell layer, where the NiCo LDH and NiFe LDH nanosheets have been deposited (Figure 2.3 f,i, respectively), revealed the characteristic continuous rings of the amorphous LDH structure with ring patterns of (0003), (0006), (1102), (1105), and (11010) planes. EDX mapping images of Ni-NWN (Figure S2.2) confirmed that Ni was the major element present in the wires. Elemental mapping was further conducted on NiCo LDH/Ni-NWN (Figure S2.3) and NiFe LDH/Ni-NWN (Figure 2.3j) to elucidate the spatial distribution of elements throughout the heterostructure of the catalysts. As shown in Figure 2.3j, the EDX mapping images demonstrated a concentrated distribution of Ni in the core, whereas elemental Fe and O were uniformly dispersed within the NiFe LDH shells, aligning with the intended heterostructure design. Such a hierarchical "nanosheet on nanowire" architecture, benefiting from the added LDH layer, not only provides an abundance of redox-active sites due to its expanded surface area but also promotes efficient electrolyte diffusion, through its open porous structure. As a result, these architectures exhibit an enhanced electrocatalytic performance.

XRD analysis of as-synthesized Ni-NWN, NiCo LDH/Ni-NWN, and NiFe LDH/Ni-NWN was conducted to provide more structural information about the crystalline structure. The XRD pattern of Ni-NWN (Figure 2.4 a) revealed the major diffraction peaks at 44.6°, 51.8°, and 76.4°, which match well to the (111), (200), and (220) planes, respectively, of metallic Ni (JCPDS No. 04–0850).[182] Besides the characteristic peaks of the Ni nanowires, the XRD patterns of NiCo LDH/Ni-NWN and NiFe LDH/Ni-NWN exhibited several discernible diffractions with low intensities, which become more apparent at slower scan speeds (highlighted regions in Figure 2.4 a) at 2θ values of 10.5°, 22.6°, 34.4°, and 60.7°. These reflexes could be attributed to the (003), (006), (012), and (110) planes of the hydrotalcite-like LDH phase (JCPDS 33–0429 and JCPDS 40-0215), which agrees with the crystallographic data acquired from SAED measurements.[184,193,194] The low intensity of these peaks may be related to the existence of the NiCo and NiFe LDH sheets in a nanoscale ultrathin structure with poor crystallinity, such weak peaks were buried by the stronger characteristic peaks of Ni-NWN.[193]

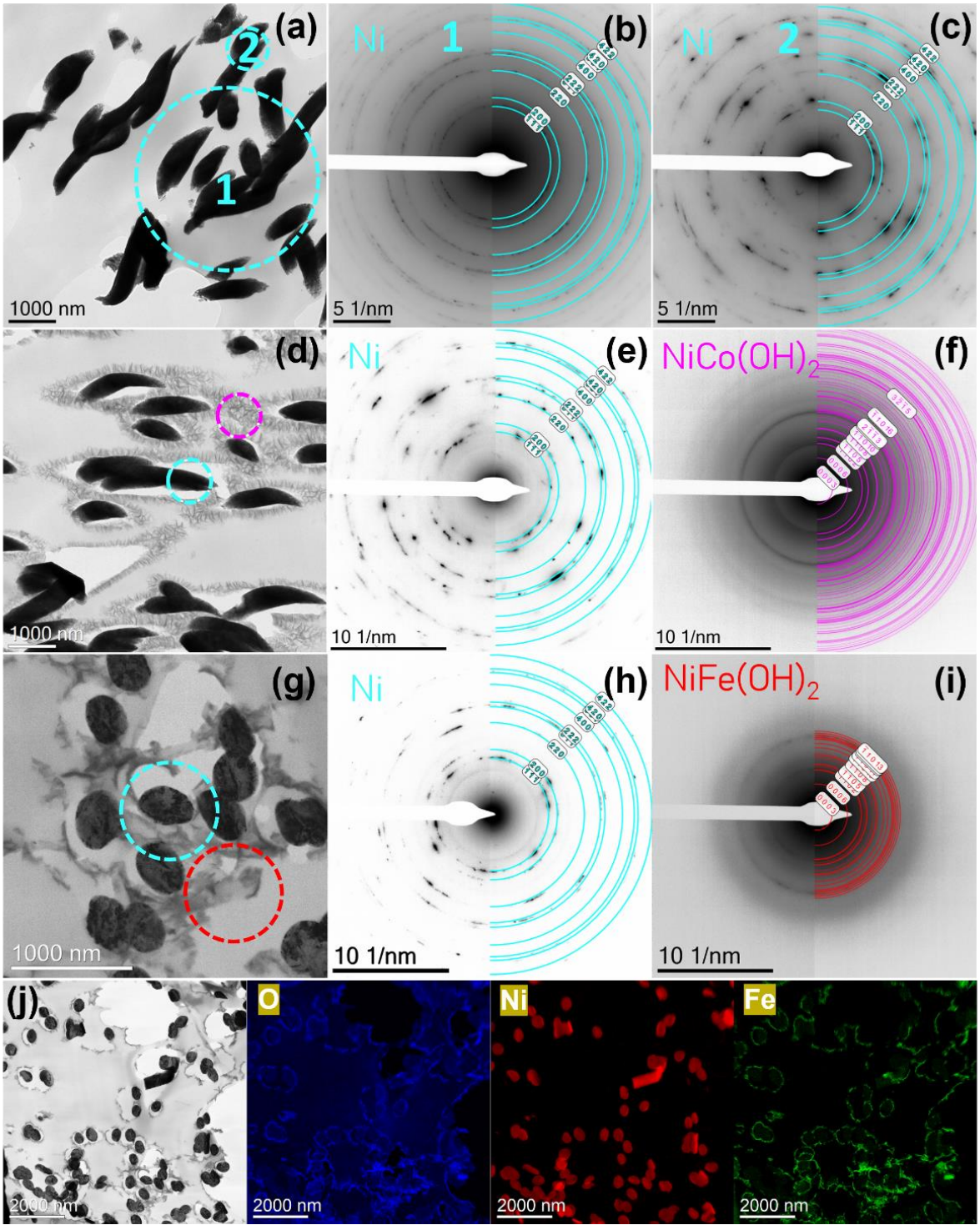

Figure 2.3. *TEM images of (a) Ni-NWN, (d) NiCo LDH/Ni-NWN, and (g) NiFe LDH/Ni-NWN. SAED of (b, c) Ni-NWN, (e, f) NiCo LDH/Ni-NWN, and (h, i) NiFe LDH/Ni-NWN conducted at different spots highlighted with circles in the TEM micrographs (a), (d), and (g), respectively. (j) EDX mapping images of the NiFe LDH/Ni-NWN catalyst.*

The chemical and structural compositions and elemental valence states of the prepared catalysts were further investigated using XPS. As shown in Figure 2.4b, the survey spectrum of NiCo LDH/Ni-NWN revealed the existence of Ni, Co, and O, and that of NiFe LDH/Ni-NWN confirmed the existence of Ni, Fe, and O, while no Co or Fe signals were present in the spectrum of Ni-NWN, which agree with the EDX results (Figures 2.3 j, S2.2, and S2.3). The Ni 2p spectra of NiCo LDH/Ni-NWN and NiFe LDH/Ni-NWN (Figure 2.4c) revealed two peaks around 855.6 eV (Ni $2p_{3/2}$) and 873.4 eV (Ni $2p_{1/2}$) along with two shakeup satellite peaks (861.6 and 879.7 eV) which are indicative of the $Ni(OH)_2$ phase as reported in the previous studies. [83,195] At the same time, Ni-NWN showed extra peaks at 851.8 and 869.1 eV, which are characteristic of Ni^0, emanating from the underlying nanowire network. These two peaks disappear upon the deposition of the surface LDH layer over the core metal, as observed in the case of NiCo LDH/Ni-NWN and NiFe LDH/Ni-NWN. Furthermore, in comparison to Ni-NWN, the Ni $2p_{3/2}$ and Ni $2p_{1/2}$ peaks in NiCo LDH/Ni-NWN and NiFe LDH/Ni-NWN are shifted to higher binding energy by approximately 0.4 eV. This shift is attributed to the electron transfer from the Ni d band to the Co d and Fe d bands, indicating a strong interaction between Co and Fe ions with Ni ions in NiCo LDH/Ni-NWN and NiFe LDH/Ni-NWN, respectively.[196] In the high-resolution Co 2p region, two binding peaks at approximately 781 and 796.4 eV, along with satellite peaks, as illustrated in Figure 2.4d, are indicative of the characteristic behavior of $Co(OH)_2$,[197] The Fe 2p spectrum, as shown in Figure 2.4e, exhibits two distinct peaks at approximately 711.4 and 725.1 eV, corresponding to Fe $2p_{3/2}$ and Fe $2p_{1/2}$, respectively. This suggests the presence of Fe species in a +3 oxidation state within NiFe-LDH/Ni-NWN.[83] The O 1s spectrum of the three composites (Figure 2.4f) reveals two main peaks assigned to M-O (Ni-O, Co-O, and Fe-O) species at 528.7-529.3 eV and M-OH species at 531.4 eV.[193] The findings from the XPS measurement confirm the existence of Ni, Co, and Fe in multiple oxidation states within the NiCo and NiFe LDH nanosheets. These solid-state redox couples including Ni^{2+}/Ni^{3+}, Fe^{2+}/Fe^{3+}, and Co^{2+}/Co^{3+}, are known to contribute significantly to electrochemical activity, particularly because Ni^{3+}, Fe^{3+}, and Co^{3+} represent catalytically active sites toward OER. Moreover, the Ni^0 peak disappeared in the case of NiCo LDH/Ni-NWN and NiFe LDH/Ni-NWN due to the coverage of the core Ni network.

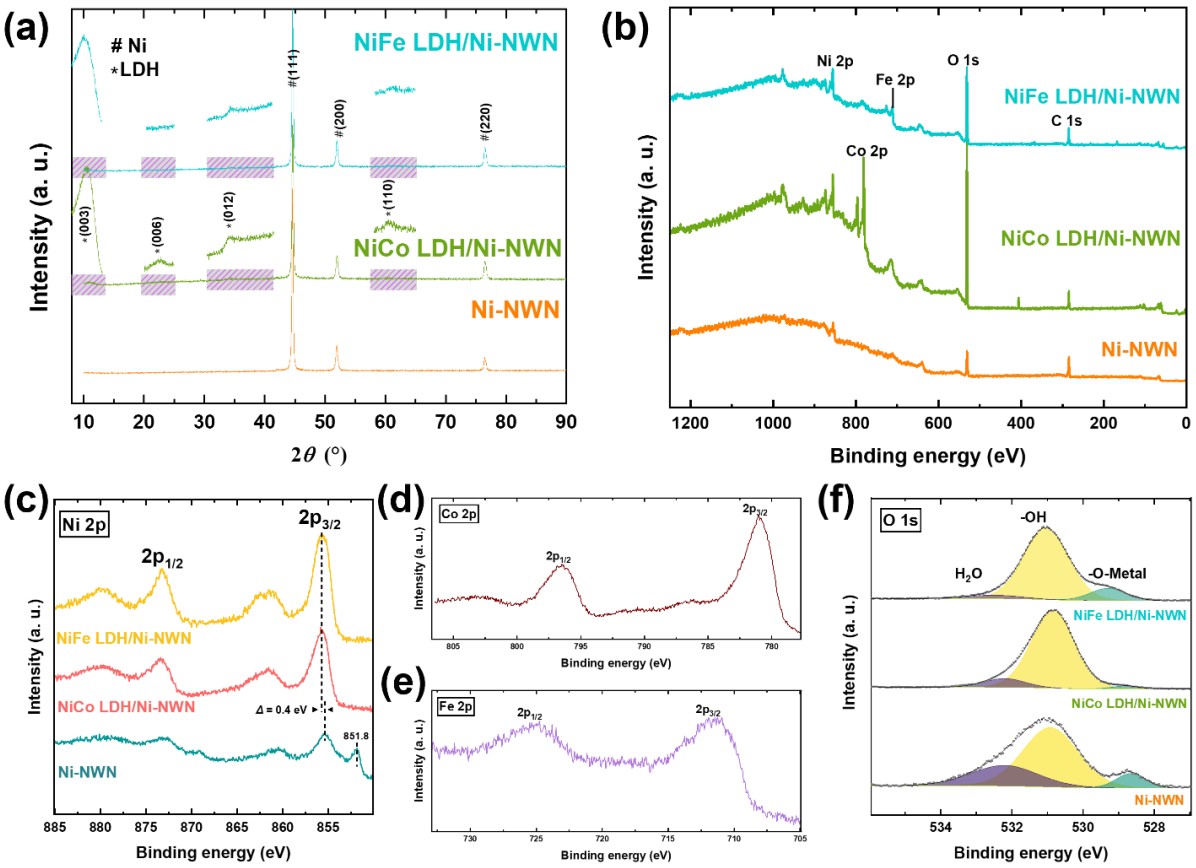

Figure 2.4. *(a) XRD patterns (highlighted insets show the characteristic peaks of LDH under slow scan rate), and (b) XPS survey scan of Ni-NWN, NiCo LDH/Ni-NWN, and NiFe LDH/Ni-NWN. High-resolution XPS spectra of (c) Ni 2p region of the three catalysts, (d) Co 2p region of NiCo LDH/Ni-NWN, and (e) Fe 2p region of NiFe LDH/Ni-NWN and (f) O 1s XPS spectra of the three electrodes.*

2.1.3.2. Oxygen Evolution Reaction Performance.

To assess the OER activity, the performance of hierarchical architectures was evaluated by using a typical three-electrode system in a 1 M KOH electrolyte. The performance of the architectures was evaluated based on three key parameters: (1) overpotential, (2) Tafel slope, and (3) long-term stability. Figure 2.5a depicts the polarization curves of the three catalysts at a scan rate of 1 mV s^{-1}. Upon analysis, it is evident that the peak potential for Ni^{2+} oxidation into Ni^{3+} shifts from 1.33 V *vs.* RHE for Ni-NWN to 1.22 V *vs.* RHE for NiCo LDH/Ni-NWN. This shift indicates that the presence of Co facilitates the $Ni^{2+/3+}$ transition at lower potentials. This phenomenon can be attributed to a charge transfer process from Co to the neighboring Ni atoms within the lattice. The charge transfer is influenced by Ni's higher electronegativity, leading to a greater charge density in Ni compared to Co.[198] Additionally, another peak, corresponding to the oxidation of Co^{3+} ions into Co^{4+} ions, is observed at 1.34 V *vs.* RHE.

Conversely, this potential increases in the case of NiFe LDH/Ni-NWN and the transition occurs at 1.38 V *vs.* RHE, which nearly overlaps with the onset of the OER, indicating that the presence of Fe stabilizes the Ni^{2+} oxidation state. The inclusion of Fe contributes to the creation of more disorders within the local structure, a characteristic associated with α-$Ni(OH)_2$.[199,200] These observations match with the previous literature, which confirms that the introduction of Fe into Ni films leads to a reduction in the average oxidation state of Ni, as opposed to pure Ni oxides. This corroborates that the presence of Fe induces an anodic shift in the $Ni^{2+/3+}$ redox pair.[201] This shift can be attributed to the relatively greater ionic character of Fe–O bonds in comparison to Ni–O. As Fe ions become incorporated into their lattice, Ni–O acquires increased covalent character. This augmented covalent nature in Ni–O demands additional potential for their electrochemical oxidation.[202] The LSV showed a lower onset potential of 1.41 V *vs.* RHE for NiFe LDH/Ni-NWN, which is far below 1.49 V *vs.* RHE of NiCo LDH@ Ni-NWN, and 1.58 V *vs.* RHE of Ni-NWN. The negative shift of the onset potential for the LDH-decorated networks reflects faster OER kinetics. The remarkable catalytic activity of the NiFe LDH/Ni-NWN electrocatalyst is evident from the significantly lower overpotential required to achieve a current density of 10 mA cm^{-2} (η_{10}), as marked by the dotted horizontal line in Figure 2.5a. The NiFe LDH/Ni-NWN exhibits an η_{10} of only 222 mV, surpassing the performance of both NiCo LDH/Ni-NWN (316 mV) and Ni-NWN (424 mV). Moreover, even at a higher current density of 100 mA cm^{-2}, the NiFe LDH/Ni-NWN retained low η_{100} of only 487 mV, which is approximately two-thirds that of the NiCo LDH/Ni-NWN (601 mV) as demonstrated in Figure S2.4. In the quest for the OER kinetics, Tafel plots were constructed based on the polarization curves of the three electrocatalysts as represented in Figure 2.5b. The NiFe LDH/Ni-NWN exhibited a notably smaller Tafel slope of 42 mV dec^{-1} compared to 92 mV dec^{-1} for NiCo LDH/Ni-NWN, and 140 mV dec^{-1} for Ni-NWN. These results solidify that the NiFe LDH/Ni-NWN not only offers the lowest overpotential required to initiate the OER but also provides the most favorable OER kinetics among the three electrocatalysts (Figure 2.5c). Furthermore, to evaluate the electrochemically active surface area (ESCA) of the electrocatalysts, we calculated the double-layer capacitance (C_{dl}) based on the cyclic voltammetry curves obtained in the non-Faradaic region (Figure S2.5). Figure S2.6 shows a linearity between the capacitive current and the scan rate. Ni-NWN revealed a higher C_{dl} value (3.37 mF cm^{-2}). Interestingly, despite the highest OER activity observed for NiFe LDH/Ni-NWN, it displayed a lower ECSA compared to that of bare Ni-NWN, ruling out that ECSA is not the main parameter that drives the activity. However, determining ECSA for LDH based on C_{dl} is challenging due to the potential-dependent conductivity of LDHs, which requires good electronic conductivity to obtain reliable

C_{dl} data.[203] In addition, the possible pseudocapacitive nature of the NiFe materials could lead to misleading results when using the C_{dl} method to estimate the real active surface area. Moreover, using a standard value of specific capacitance for different electrocatalysts can introduce significant errors when estimating ECSA.[204] Hence, the superior catalytic activity of NiFe LDH/Ni-NWN is not solely attributed to a higher number of active sites, as both NiCo- and NiFe-LDH nanosheets have a comparable surface area, but rather to the presence of more potent intrinsic catalytic centers with higher reaction efficiency.

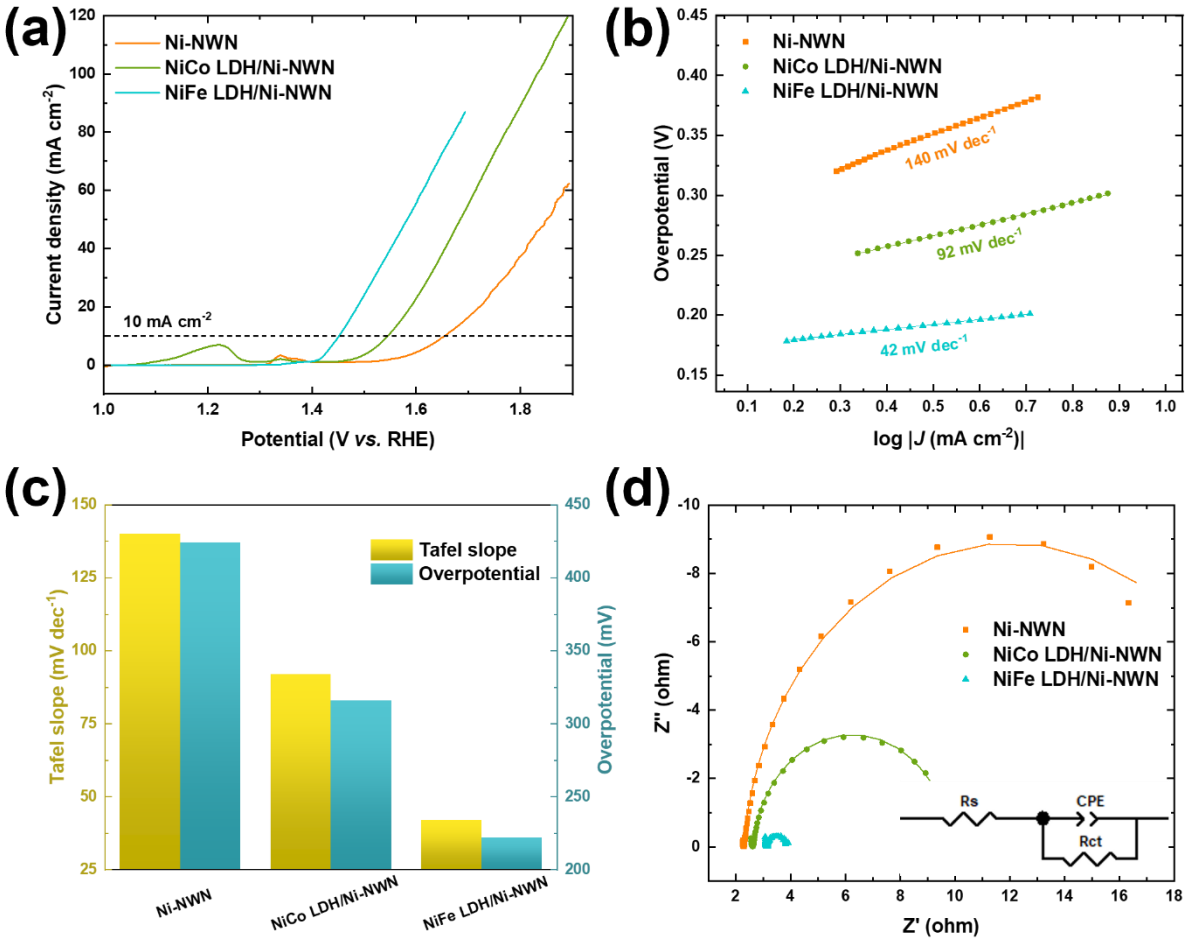

Figure 2.5. *(a) Polarization curves of Ni-NWN, NiCo LDH/Ni-NWN, and NiFe LDH/Ni-NWN at a scan rate of 1 mV s^{-1} in 1 M KOH. (b) The corresponding Tafel plots. (c) Performance comparison of Tafel slope and overpotential at 10 mA cm^{-2} for different electrocatalysts. (d) Nyquist plots of the electrodes at a potential of 1.5 V vs. RHE; inset: the corresponding equivalent circuit.*

The purposeful multilevel design of the 3D architectures offers several notable advantages. When compared to larger-scale sponge-type catalyst electrodes, our fine structuring demonstrates an excellent degree of miniaturization achieved with our fine structuring,

requiring only a comparably thin layer of decorated nanonetwork to achieve outstanding catalytic activity. NWNs, owing to their porous and interconnected structure, provide continuous and effective routes for both mass and charge transfer, thereby enhancing the electrode performance by facilitating reaction kinetics.[184] The integrated Ni-NWN functions as a metallic 1D current collector, establishing efficient electric conduction pathways from the rear electrode surface to the hierarchically branched catalyst-solution interface. As the NWN framework simultaneously serves as the working electrode and active material, the reinforcement of the underlying Ni surface area becomes pivotal. Notably, the structural elements of classical Ni foams, such as the diameter of Ni struts, typically fall within the range of a few hundred micrometers. In contrast, our system exhibits features that are approximately 2 orders of magnitude smaller. This outstanding catalytic activity of NiFe LDH@Ni-NWN could be attributed to the presence of more potent catalytic sites with higher reaction efficiency, and the lower Tafel slope also implies that the rapid OER kinetics originate from the inclusion of Fe with its high intrinsic catalytic potency.[205,206] In detail, the significantly enhanced activity introduced upon the inclusion of Fe in the NiFe LDH/Ni-NWN electrocatalyst could be attributed to the following reasons: (i) The inclusion of Fe enhances the electrical conductivity of the Ni matrix. However, this outstanding OER performance can not only be assigned to this effect which highlights the previous findings that Fe represents the active site in the structure.[199] (ii) Although FeOOH alone does not possess enough conductivity to act as a catalyst at low overpotentials, the inclusion of Fe sites in the conductive Ni matrix demonstrates perfect energy of binding with -OH and -OOH intermediates.[207] Hence, the additional improvement in OER activity in the NiFe LDH/Ni-NWN electrocatalyst could be attributed to the activation of Ni^{3+} in the NiOOH phase at lower overpotentials due to the charge transfer from Fe. This phase is more conductive compared with the nonconductive $Ni(OH)_2$ phase. (iii) The presence of Fe^{3+} ions facilitates the diffusion of hydroxyl ions into the network.[208] The incorporation of Fe ions plays a pivotal role in expediting the O-O coupling process on the surface of Ni, which subsequently enhances the multielectron transfer mechanism of Ni. This transformation process is intricately linked to the presence of Fe on the material's surface. The reduction in overpotential can be attributed to a sequence of oxidation steps and successive deprotonation of H_2O molecules bound to Fe^{4+} ions within the NiFe oxyhydroxide. Intriguingly, when only Fe ions are present, a notably subdued OER activity is observed, primarily due to the insulating nature of FeOOH.[209] These findings agree with the density functional theory (DFT) data that were used to determine the structural motif and identify the active metal sites for each reaction step through the calculation of the Gibbs free energy (ΔG). For instance, *Guo*

et. al. reported ΔG values of the metal sites in NiFe-LDH, which revealed that Fe has a lower ΔG value, confirming its role as the active site.[210] The results further confirmed that the inclusion of Fe into the NiOOH lattice not only affects the electronic structure but also substantially alters the chemical bonding of the metal ions and intermediates involved in the OER.

To gain deeper insights into the remarkable OER performance of NiFe LDH/Ni-NWN, EIS measurements of the three electrodes were conducted at 1.5 V *vs.* RHE. The Nyquist plots of the comparative samples were then fitted using the corresponding equivalent circuit, as illustrated in the inset of Figure 2.5d. R_s, R_{ct}, and *CPE* refer to the solution resistance, charge transfer resistance, and capacitance, respectively; the fitting values of the components are reported in Table S2.1. It can be clearly observed that the semicircle of the Nyquist plot, which represents the R_{ct} is much smaller in the case of NiFe LDH/Ni-NWN. The calculated R_{ct} of NiFe LDH/Ni-NWN (0.8 Ω) is smaller than that of NiCo LDH/Ni-NWN (7.2 Ω) and Ni-NWN (19.4 Ω) as reported in Table S2.1. The small R_{ct} confirms the fastest charge transfer at the interface and the easiest catalytic kinetics of NiFe LDH/Ni-NWN toward the OER among the other samples.[211–213] EIS measurements were conducted for the three electrocatalysts at different potentials of 1.5, 1.51, and 1.52 V *vs.* RHE (Figures S2.7-9), and the corresponding fitting parameters of the equivalent circuits are summarized in Table S2.2. As shown in Figure S2.9, the R_{ct} of the NiFe LDH/Ni-NWN decreases as the potential increases, indicating faster kinetics at higher potentials. Similar observations were acquired for Ni-NWN and NiCo LDH/Ni-NWN (Figures S2.7 and S2.8, respectively).

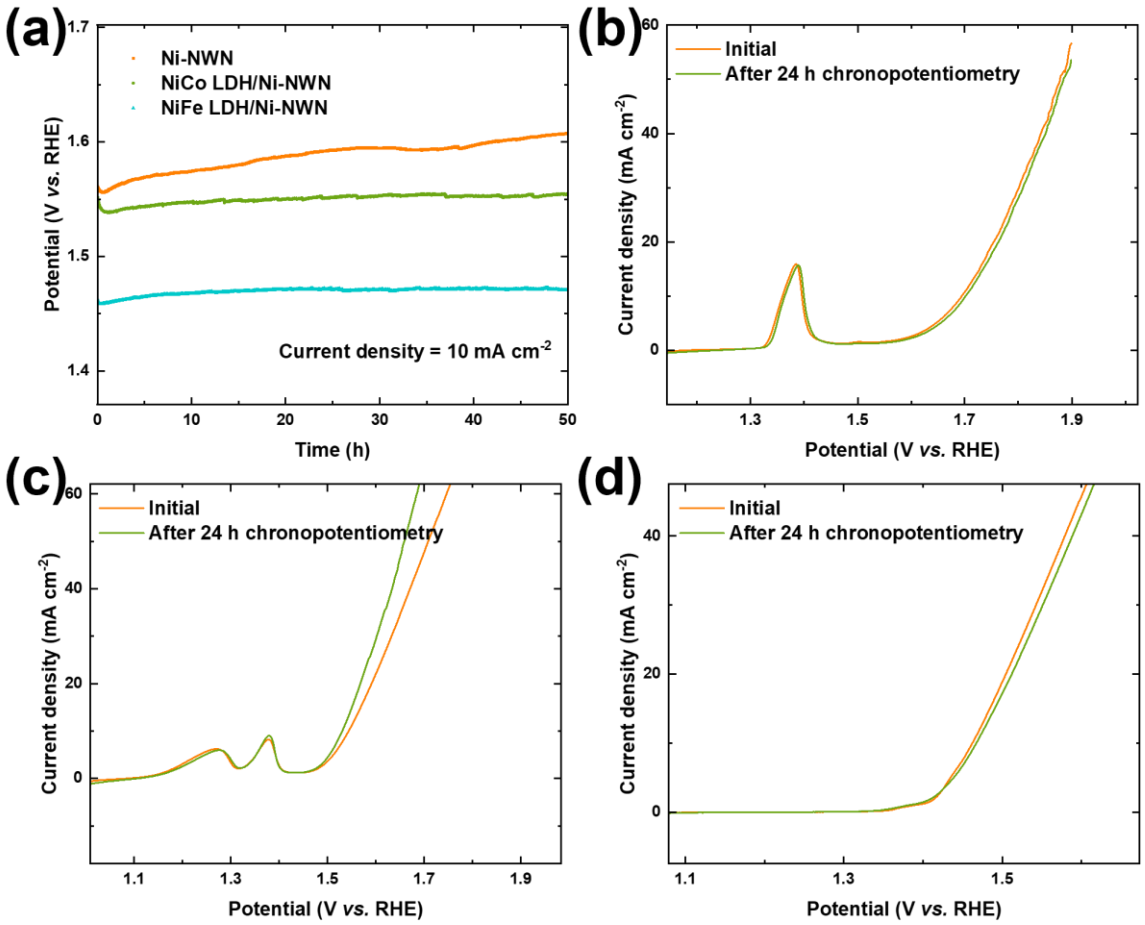

Figure 2.6. *(a) Chronopotentiometry of Ni-NWN, NiCo LDH/Ni-NWN, and NiFe LDH/Ni-NWN at a current density of 10 mA cm^{-2} for 50 h in 1 M KOH. LSV of (b) Ni-NWN, (c) NiCo LDH/Ni-NWN, and (d) NiFe LDH/Ni-NWN before and after the experiments.*

Long-term stability is another critical aspect of the evaluation of electrocatalysts. The robustness of the hierarchical architectures is further proven through long-term chronopotentiometry measurement at 10 mA cm^{-2} for a period of 50 h. Additionally, the LSV curves of three catalysts were compared before and after the experiments. Remarkably, both NiFe LDH/Ni-NWN and NiCo LDH/Ni-NWN showed outstanding stability of potential over 50 h during the potentiometry while Ni-NWN revealed slight fluctuations over time, as shown in Figure 2.6a. The NiFe LDH/Ni-NWN achieved a potential of 1.45 V *vs.* RHE while delivering a current density of 10 mA cm^{-2}, retaining stability for 50 h. The LSV of the three electrocatalysts exhibited consistent behavior before and after the experiments, with a slight current attenuation observed at high potential (Figure 2.6b-d). Lastly, SEM and EDX measurements were conducted to investigate the morphological and structural changes of the Ni-NWN, NiCo LDH/Ni-NWN, and NiFe LDH/Ni-NWN elctrocatalysts after conducting the OER. As depicted in Figure S2.10, Ni-NWN retained the 3D wirelike network structure with

some roughness on the surface of the wires. The accompanying EDX measurement (Figure S2.10c) confirmed the existence of only Ni in the sample. SEM images of NiCo LDH/Ni-NWN (Figure S2.11) and NiFe LDH/Ni-NWN (Figure S2.12) show no noticeable differences compared to the as-prepared architectures prior to the OER performance tests. This indicates that the Ni backbone and the LDH layer maintain their integrity, while the porous structure is retained even after rigorous testing, thus confirming the mechanical stability of the catalysts. The improved mechanical strength of the electrocatalysts can be attributed to their purposeful design, which incorporates a supporting layer that provides structural support to the entire network, along with sufficient interconnections between the nanowires, preventing network collapse. The EDX spectra of NiCo LDH/Ni-NWN and NiFe LDH/Ni-NWN (Figures S2.11c and S2.12c, respectively) indicate no changes in the initial composition of the electrocatalysts, which further proves the high catalytic durability toward the OER. Furthermore, after the long-term chronopotentiometry and LSV testing, XRD patterns revealed that the three electrocatalysts retained their crystal structures with no obvious new phases, as shown in Figure S2.13.

Generally, the OER mechanism involves three main steps: (i) water adsorption onto the surface of the electrocatalysts, (ii) water splitting into molecular oxygen, and (iii) oxygen evolution. The remarkable catalytic performance of the LDH-decorated NWN could be illustrated in light of the previously discussed results and observations. First, the NiCo and NiFe LDH nanosheets, with their distinguished layered structure, offer large intersheet spaces, which in turn facilitate the diffusion of water molecules and hydroxide ions between the layers, ensuring ultimate contact between the electroactive species involved in the OER and the active sites of the electrocatalyst. Consequently, the electrocatalysis process has larger accessible spaces not limited to the active electrode surface, which is crucial for the third step in the OER mechanism as it promotes the O_2 evolution from the electrocatalyst.[214] Figure S2.14 shows the O_2 evolution from the working electrode at the bottom of the cell upon increasing the potential. Second, the distinctive porous architecture of the Ni-NWN with its tortuous structure and interconnected nanoskeleton plays a critical role in increasing active surface area. Additionally, each nanowire acts as a nanocurrent collector which has direct contact with the coating LDH sheets, forming an open 3D efficiently conductive network. Such a well-designed architecture can not only preserve the catalyst's mechanical and structural stability and prevent the nanowires' collapse but also promote the charge transfer efficiency through the enhanced electrical conductivity of the metallic Ni backbone.[182,184] Noteworthy, our hierarchical paradigm of the electrocatalyst represents an efficient alternative for the commonly used

assisting electrodes such as nickel foam and carbon felt without any need for conductive additives or polymer binders to mount active material on the electrode, which in turn reduces the dead volume of the electrode.[184] Third, the high valence states of Ni, Co, and Fe are the most critical to facilitate the OER, which agrees with the predictions from the Pourbaix diagram of these elements.[215–217] In alkaline media, the metal hydroxides undergo oxidation, transforming into a catalytically active oxyhydroxide form. In the case of Co and Fe, this further evolves into the oxide form, which represents the favorable metal species for electrocatalytic OER.[218,219] The transformation of the $Ni(OH)_2$/NiOOH redox couple could be approved through the visible color changes. Correspondingly, the green NiCo LDH/Ni-NWN turned into a darker color upon oxidation during the OER process (Figure S2.15), agreeing with the observation in previous studies.[220] A plausible mechanism, as proposed by *Friebel et al*., sheds light on the improved OER activity associated with the incorporation of Fe, even though Fe is known to be an insulator in FeOOH.[221] According to this mechanism, the presence of Fe ions within the lattices leads to a significantly contracted Fe–O bond length. As a result, conductivity is imparted to Fe^{3+} sites within the NiOOH lattice not by direct inclusion but by leveraging the existing conductivity of the NiOOH lattice. This suggests that the modification in effective conductivity (which varies with potential) due to Fe incorporation could contribute to the enhancement of the OER activities in Ni-based electrocatalysts, although it is not the sole contributing factor. These outstanding characteristics of the LDH-based architectures play a crucial role in enhancing the OER. Moreover, water oxidation in an alkaline medium includes a proton-coupled electron transfer. Besides the rapid diffusion of the interlayer ions in the NiCo and NiFe LDH, the redox activity of Ni, Co, and Fe enables more charges to mediate the H^+ transfer in coordination with the electron transfer reactions.[214] The previously discussed advantages of the free-standing hierarchical design of the electrocatalysts highlight their outstanding catalytic activity toward OER.

The enhanced activity of NiFe LDH/Ni-NWN toward OER in terms of overpotential and Tafel slope allowed it to perform outstandingly compared with the recently reported non-noble metal-based counterparts such as NiFe-LDH/300MoCN (323 mV, 132.9 mV dec^{-1}),[222] NiFe-LDH (195 mV, 95 mV dec^{-1}),[223] Co-Fe LDH (1:0.35) (350 mV, 49 mV dec^{-1}),[224] NiFe/NF (191 mV, 44.1 mV dec^{-1}),[225] $NiFe_{0.5}$ nanospheres (287 mV, 52.9 mV dec^{-1}),[226] and others as presented in Figure 2.7 and reported in detail in Table S2.3. As such, besides its enhanced OER activity and outstanding mechanical and electrochemical stability, NiFe LDH/Ni-NWN was synthesized *via* a facile and scalable approach, which is the primary prerequisite for

industrialization.

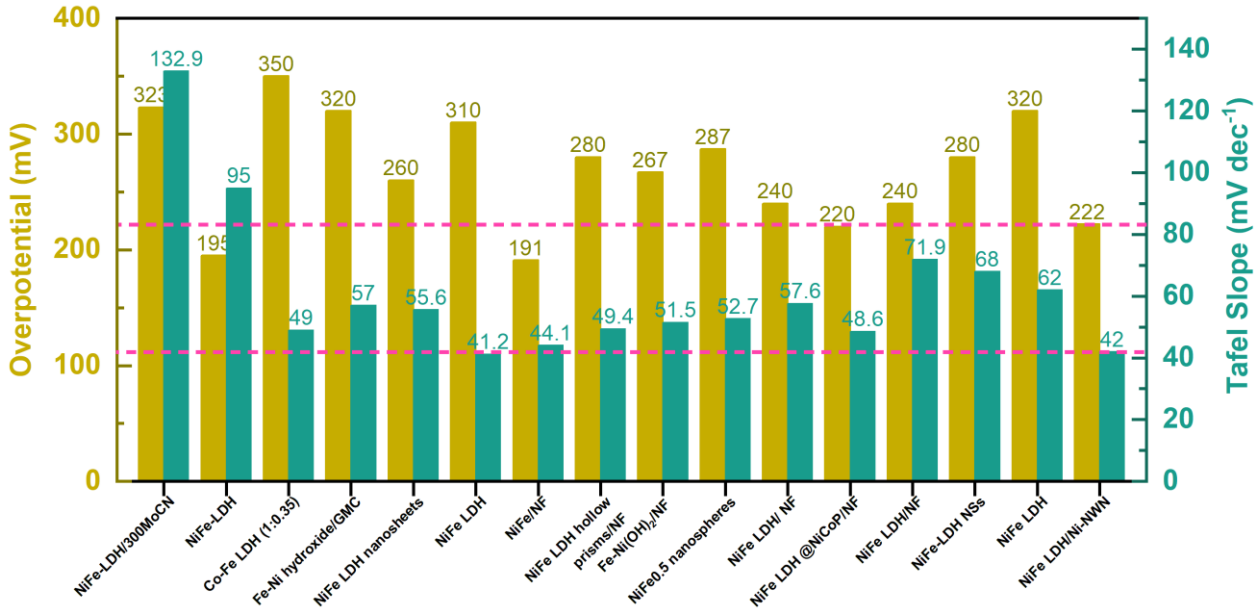

Figure 2.7. *Comparison of the OER performance in terms of Tafel slopes and overpotentials@10 mA cm^{-2} of NiFe LDH/Ni-NWN and the recently reported non-noble metal-based electrocatalysts (refs* [79,83,230–233,222–229]*).*

Conclusions

In summary, a novel hierarchical core-shell architecture, NiFe LDH/Ni-NWN, has been developed for the OER in alkaline media. This electrocatalyst exhibited outstanding electrocatalytic activity and long-term durability toward the OER. The remarkable performance of the electrode primarily originates from the prolific engineering of the catalyst and the solid synergistic effect between the NiFe LDH sheets and the 3D interconnected Ni-NWN core. Specifically, the NiFe LDH/Ni-NWN structure facilitates not only a fast charge transfer through the metallic Ni nanowires but also a high mass transportation rate through the 3D porous network, characterized by tortuous pathways, which enhance the accessibility to the active sites. An overpotential of 222 mV was required to force a current density of 10 mA cm^{-2} for the OER using the NiFe LDH/Ni-NWN electrode. The NiFe LDH/Ni-NWN exhibited a small Tafel slope of 42 mV dec^{-1} compared to 92 and 140 mV dec^{-1} for NiCo LDH/Ni-NWN and Ni-NWN, respectively, surpassing many recently reported metal-based electrocatalysts for the OER. Furthermore, the assembled electrocatalyst proved outstanding long-term durability over 50 h, ensuring its applicability on an industrial scale. Given its simple and feasible synthetic strategy using naturally abundant and low-cost materials, coupled with the high electrocatalytic activity and long-term stability, the as-prepared NiFe LDH/Ni-NWN electrocatalyst holds tremendous promise and grand feasibility for practical OER in various industrial applications.

Supporting Information

SEM images, EDX spectra and mappings, CV plots at different scan rates, Polarization curves and EIS plots of the relevant samples, Optical images of the electrodes, Photographs showing the cell and the oxygen evolution, Fitting parameters of EIS data (Table S2.1 and S2.2), comparison of OER performance with reported literature (Table S2.3) (PDF).

Acknowledgments

The authors would like to acknowledge Christopher Gort from the Surface Science Group at TU Darmstadt for Conducting XPS measurements. The authors also thank Jean-Christophe Jaud (Strukturforschung Group, TU Darmstadt) for conducting the XRD measurements and Ulrike Kunz (Physical Metallurgy Group, TU Darmstadt) for providing assistance with the TEM measurements. Khaled M. Amin gratefully acknowledges the financial support provided by the Ministry of Higher Education & Scientific Research (Egypt) and DAAD (Germany) for his Ph.D. scholarship under the GERLS program (Grant No. 57403037).

2.1.4. Supporting Information

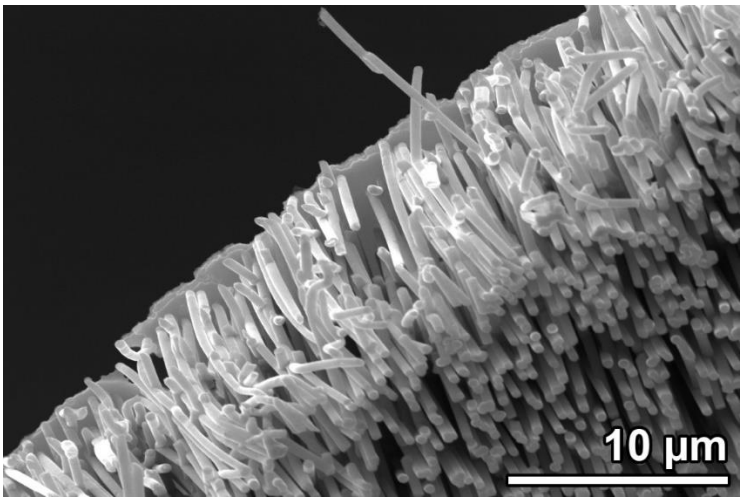

Figure S2.1. *Lateral view SEM of the free-standing Ni-NTNW with the sputtered Ni reinforcing back layer.*

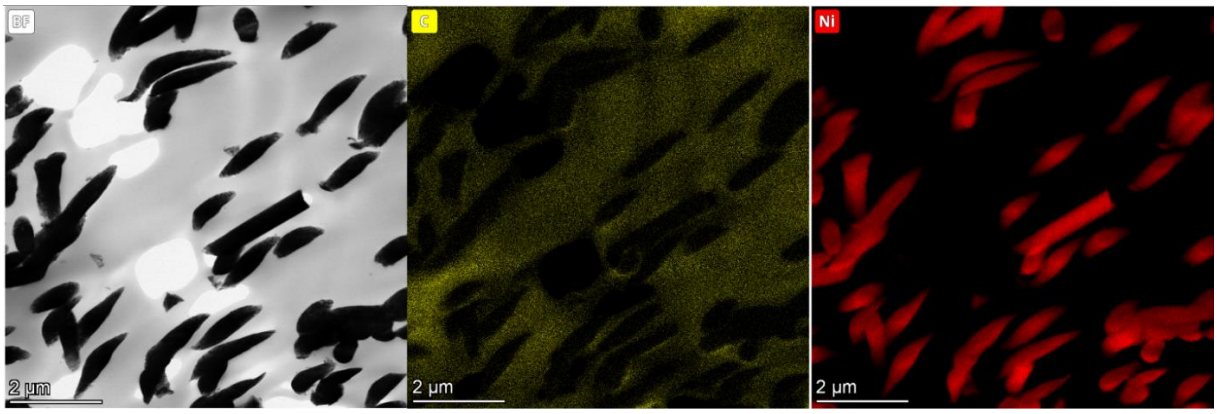

Figure S2.2. *EDX mapping images of Ni-NWN catalyst.*

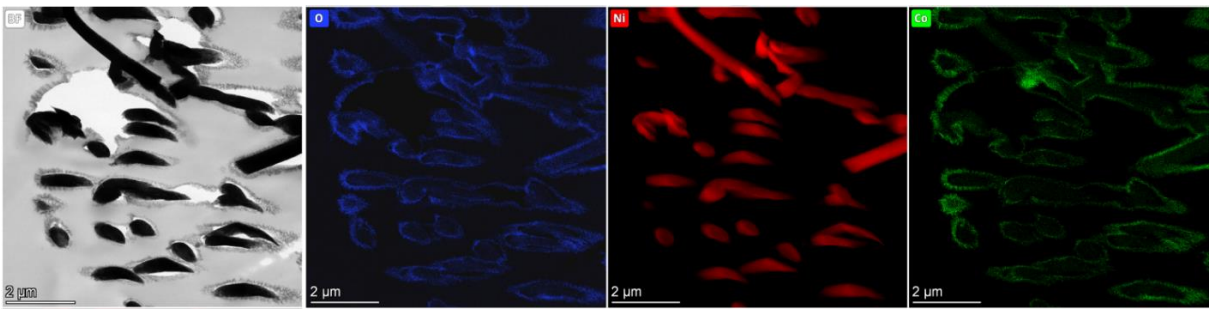

Figure S2.3. *EDX mapping images of NiCo LDH/Ni-NWN catalyst.*

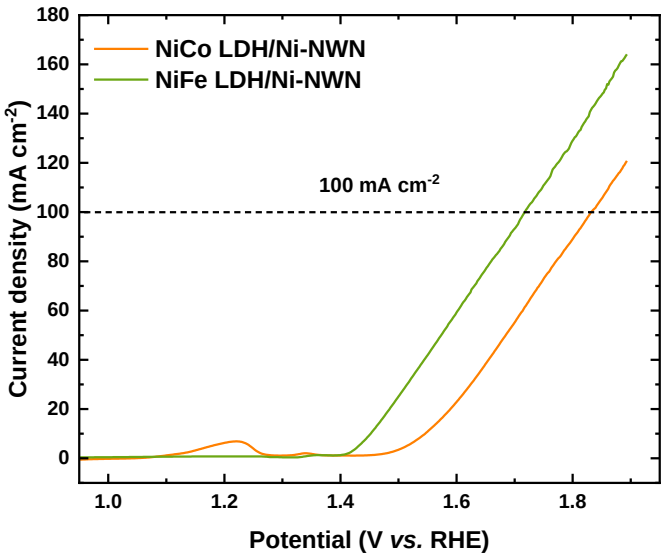

Figure S2.4. *Polarization curves of NiCo LDH/Ni-NWN, and NiFe LDH/Ni-NWN at a scan rate of 1 mV* s^{-1} *in 1 M KOH (dotted line represents* η_{100}*).*

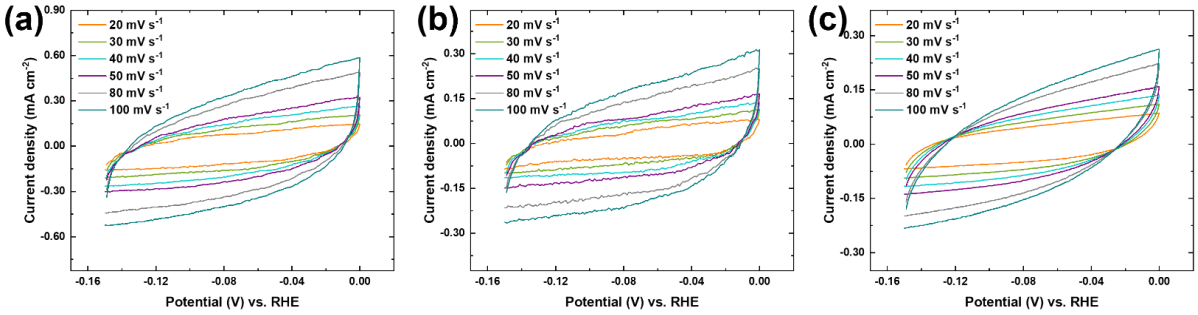

Figure S2.5. *CV curves of (a) Ni-NWN, (b) NiCo LDH/Ni-NWN, and (c) NiFe LDH/Ni-NWN at different scan rates between 20-100 mV* s^{-1}*.*

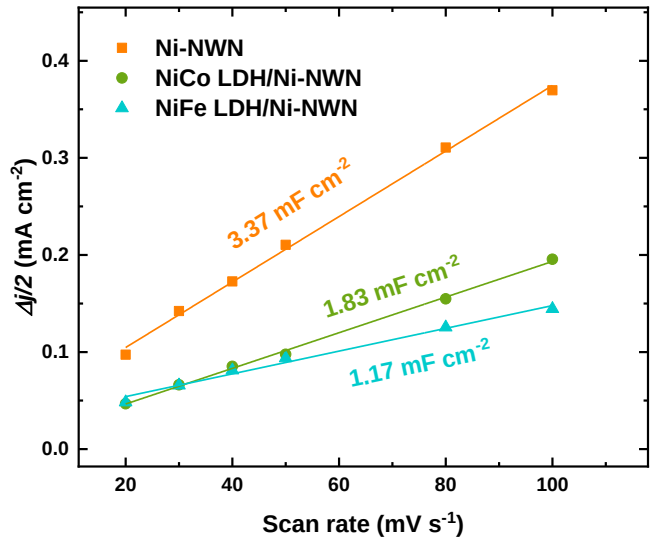

Figure S2.6. *Capacitive current (ΔJ/2 = (Ja – Jc)/2) vs scan rate of the three electrocatalysts and the corresponding linear slopes.*

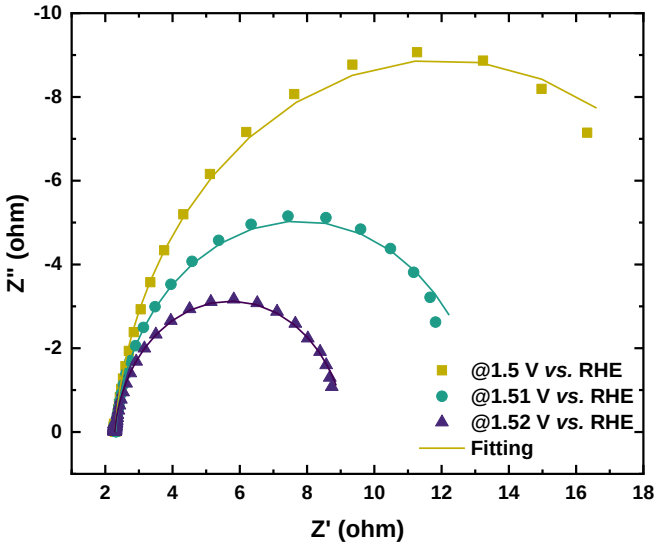

Figure S2.7. *Nyquist plots of the Ni-NWN measured at different potentials in 1 M KOH.*

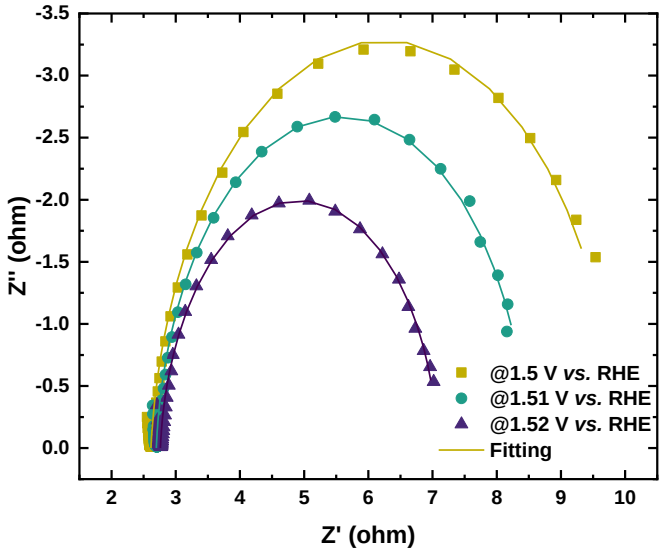

Figure S2.8. *Nyquist plots of the NiCo LDH/Ni-NWN measured at different potentials in 1 M KOH.*

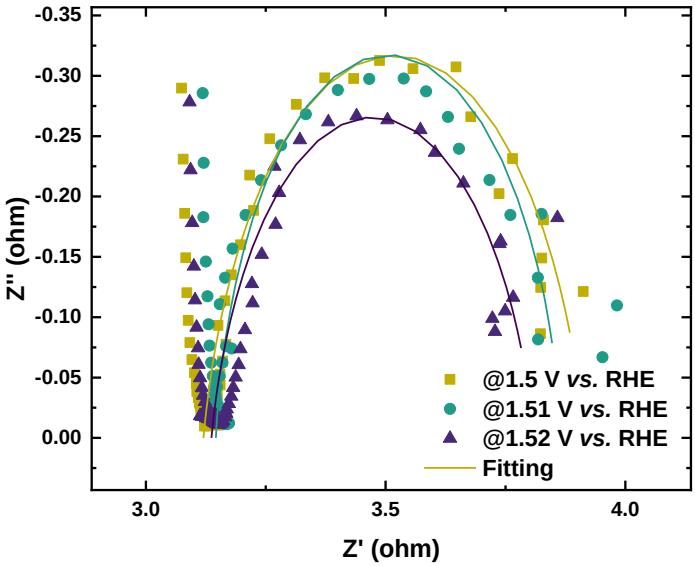

Figure S2.9. *Nyquist plots of the NiFe LDH/Ni-NWN measured at different potentials in 1 M KOH.*

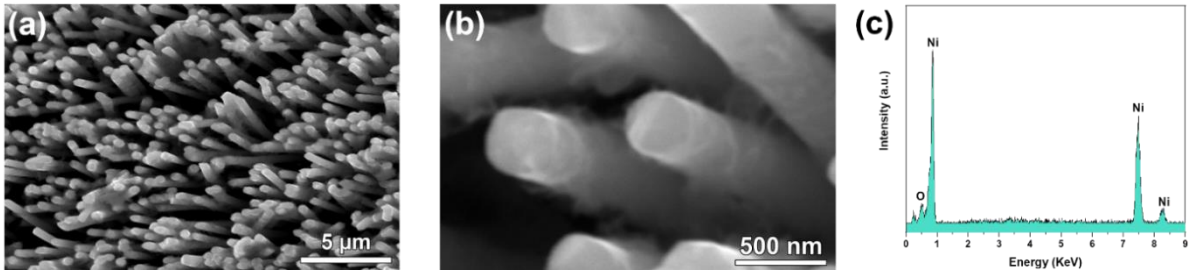

Figure S2.10. *SEM and EDX of Ni-NWN after conducting the OER tests.*

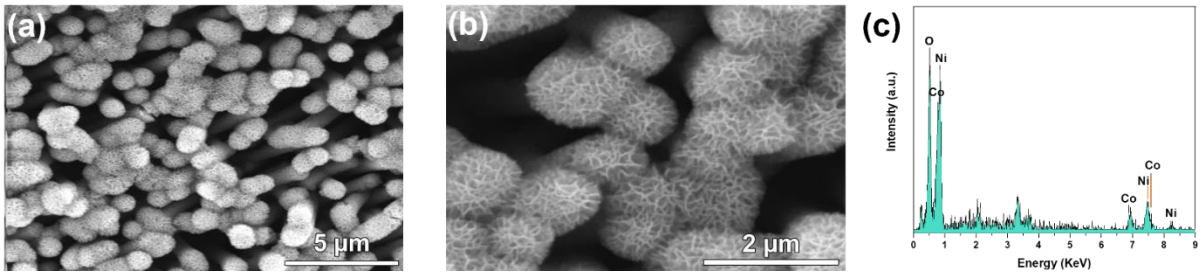

Figure S2.11. *SEM and EDX of NiCo LDH/Ni-NWN after conducting the OER tests.*

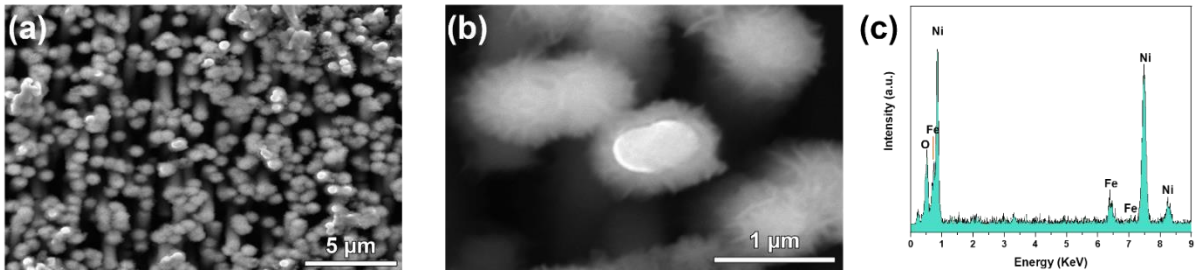

Figure S2.12. *SEM and EDX of NiFe LDH/Ni-NWN after conducting the OER tests.*

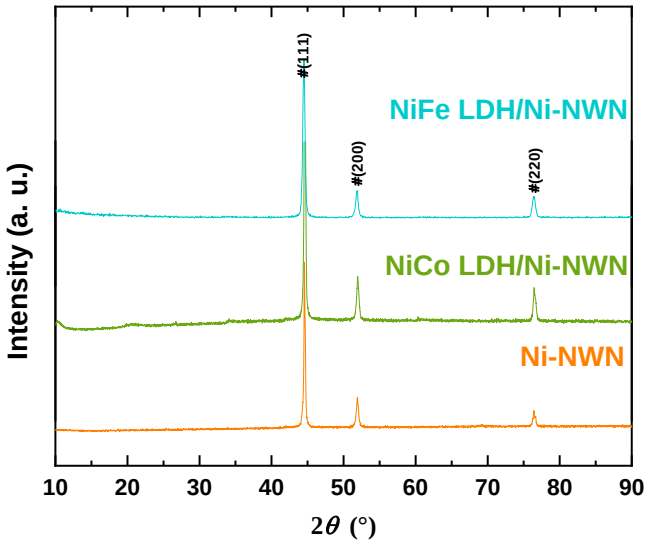

Figure S2.13. *XRD patterns of the three electrocatalysts after conducting the OER tests.*

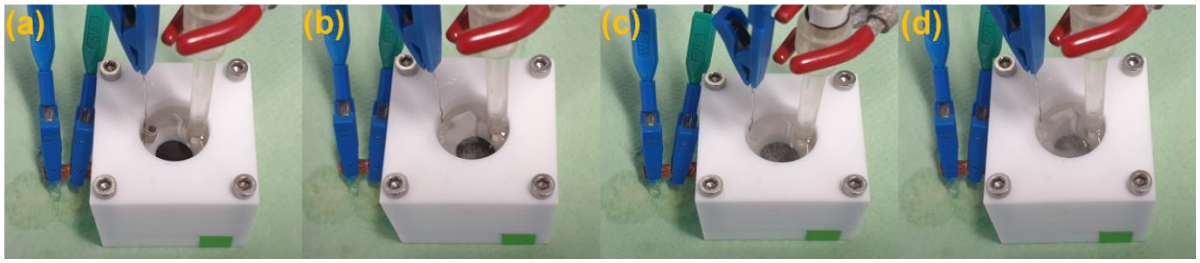

Figure S2.14. *Photographs of NiFe LDH/Ni-NWN electrode during OER measurement; the bubbles confirm the O_2 evolution from the working electrode at the bottom of the cell upon increasing the potential from (a) to (d).*

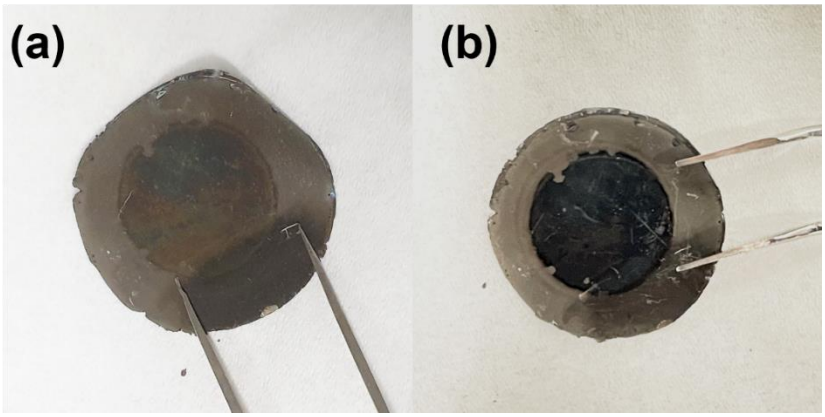

Figure S2.15. *Optical images of NiCo LDH/Ni-NWN electrode, illustrating the electrochromism of the material at different redox states. (a) The electrode before running LSV; the light green color corresponds to* $Ni(OH)_2$*. (b) The electrode after running LSV; the dark color corresponds to NiOOH.*

Table S2.1. *Fitting parameters of the equivalent circuits of the three catalysts at a potential of 1.5 V vs. RHE in 1 M KOH.*

Catalyst	R_s (Ω)	R_{ct} (Ω)	*CPE* (Ω^{-1} s^n)	*n*
Ni-NWN	2.291	19.44	0.39876	0.94309
NiCo LDH/Ni-NWN	2.613	7.268	0.45178	0.93536
NiFe LDH/Ni-NWN	3.12	0.795	0.49509	0.85693

Table S2.2. *Fitting parameters of the equivalent circuits of the three catalysts at different potentials in 1 M KOH.*

Potential (V *vs.* RHE)	R_s	R_{ct}	*CPE*	*n*
Ni-NWN				
1.5	2.291	19.44	0.39876	0.94309
1.51	2.307	10.96	0.36173	0.94606
1.52	2.285	6.876	0.33691	0.93959
NiCo LDH/Ni-NWN				
1.5	2.613	7.268	0.45178	0.93536
1.51	2.698	5.786	0.43528	0.94907
1.52	2.761	4.329	0.41777	0.94805
NiFe LDH/Ni-NWN				
1.5	3.12	0.795	0.49509	0.85693
1.51	3.146	0.7205	0.45946	0.91942
1.52	3.137	0.67289	0.48332	0.85104

Table S2.3. *Comparison of the OER performance of NiFe LDH/Ni-NWN and the recently reported non-noble metal-based electrocatalysts.*

Catalyst	Electrolyte	η at 10 mA cm^{-2} (mV)	Tafel slope (mV dec-1)	Ref.
NiFe-LDH/Ni-NWN	1 M KOH	221	42	This work
NiFe-LDH/300MoCN	1 M KOH + 0.5 M NaCl	323	132.9	[222]
NiFe-LDH	1 M KOH	195*	95	[223]
Co-Fe LDH (1:0.35)	1 M KOH	350	49	[224]
Fe-Ni hydroxide//GMC	1 M KOH	320	57	[231]
NiFe LDH nanosheets	1 M KOH	260	55.6	[232]
NiFe LDH	1 M KOH	310	41.2	[233]
NiFe/NF	1 M KOH	191	44.1	[225]
Ni-Fe LDH hollow Nanoprisms/NF	1 M KOH	280	49.4	[227]
Fe-Ni(OH)$_2$/NF	1 M KOH	267	51.5	[228]
NiFe$_{0.5}$ nanospheres	1 M KOH	287	52.7	[226]
NiFe LDH/ NF	1 M KOH	240	57.6	[230]
NiFe LDH @NiCoP/NF **NiFe LDH/NF**	1 M KOH	220 240	48.6 71.9	[79]
NiFe-LDH NSs	1 M KOH	280	68	[83]
NiFe LDH	1 M KOH	320	62	[229]

MoCN: Mo-doped graphitic carbon nitride

GMC: graphitic mesoporous carbon

***** Estimated from Figure 7

CHAPTER III

3. Nanotube networks-based electrodes

This chapter presents the main findings related to the design and synthesis of self-supported nanotube network electrode architectures for nonenzymatic glucose sensing and supercapacitor applications. The chapter delves into the detailed synthesis strategy, methodologies, surface and structural characterization techniques, and electrochemical performance evaluation of these integrated electrode architectures, providing valuable insights for researchers in the field of electrochemical science and engineering.

This chapter includes the results reported in the following two peer reviewed publications:

[1] **K.M. Amin**, F. Muench, U. Kunz, W. Ensinger, 3D NiCo-Layered double Hydroxide@Ni nanotube networks as integrated free-standing electrodes for nonenzymatic glucose sensing, *J. Colloid Interface Sci.* 591 (2021) 384–395.

[2] **K.M. Amin,** K. Krois, F. Muench, B.J.M. Etzold, W. Ensinger, Hierarchical pipe cactus-like Ni/NiCo-LDH core-shell nanotube networks as a self-supported battery-type electrode for supercapacitors with high volumetric energy density, *J. Mater. Chem. A.* 10 (2022) 12473–12488.

The objective of this work was two-fold. Firstly, it aimed to demonstrate the potential of integrated self-supported electrode architectures based on nanotube networks for enhancing the electrochemical performance of the electrode architectures. Specifically, the focus was on their applicability as substrates for carrying various LDH nanosheets. Secondly, it aimed to evaluate their performance in different electrochemical applications that require distinct characteristics, namely nonenzymatic glucose sensing and supercapacitors. By combining hierarchical nanostructures with high-performance electroactive materials, significant improvements were achieved in in terms of improved sensitivity, selectivity, and stability as glucose sensors and high volumetric energy density as electrodes for supercapacitors. These findings contribute to the advancement of electrode design paradigms and pave the way for the development of highly efficient and miniaturized electrochemical devices.

3.1. 3D NiCo-Layered Double Hydroxide@Ni Nanotube Networks as Integrated Free-standing Electrodes for Nonenzymatic Glucose Sensing

Khaled M. Amin[a, b, *], Falk Muench[a], Ulrike Kunz[a], and Wolfgang Ensinger[a]

[a] Department of Materials Science, Technische Universität Darmstadt, Darmstadt 64287, Germany

[b] Department of Polymer Chemistry, Atomic Energy Authority, Cairo 11787, Egypt

* Corresponding author, Email: amin@ma.tu-darmstadt.de

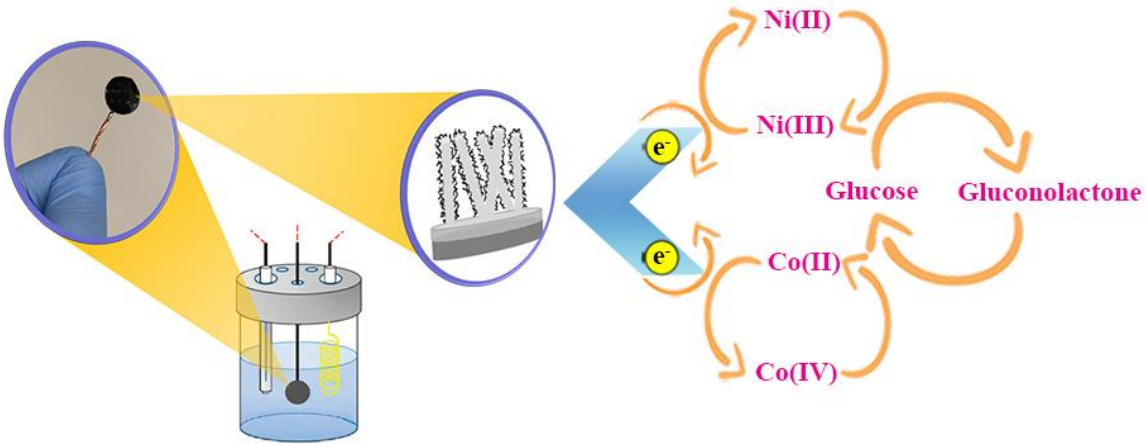

J. Colloid Interface Sci., 2021, *591*, 384-395, **DOI:** 10.1016/j.jcis.2021.02.023

Abstract

Nickel cobalt layered double hydroxide (NiCo-LDH)-based materials have recently emerged as catalysts for important electrochemical applications. However, they frequently suffer from low electrical conductivity and agglomeration, which in turn impairs their performance. Herein, we present a catalyst design based on integrated, self-supported nickel nanotube networks (Ni-NTNWs) loaded with NiCo-LDH nanosheets, which represents a binder-free, hierarchically nanostructured electrode architecture combining continuous conduction paths and openly accessible macropores of low tortuosity with an ultrahigh density of active sites. Similar to macroscale metallic foams, the NTNWs serve as three-dimensionally interconnected, robust frameworks for the deposition of active material, but are structured in the submicron range. Our synthesis is solely based on scalable approaches, namely templating with commercial track-etched membranes, electroless plating, and electrodeposition. Morphological and compositional characterization proved the successful decoration of the inner and outer nanotube surfaces with a conformal NiCo-LDH layer. Ni-NTNW electrodes and hydroxide-decorated variants showed excellent performance in glucose sensing. The highest activity was achieved for the catalyst augmented with NiCo-LDH nanosheets, which surpassed the modification with pure $Ni(OH)_2$. Despite its low thickness of 20 µm, the optimized catalyst layer provided an outstanding sensitivity of 4.6 mA mM^{-1} cm^{-2}, a low detection limit of 0.2 µM, a fast response time of 5.3 s, high selectivity and stability, and two linear ranges covering four orders of magnitude, up to 2.5 mM analyte. As such, derivatized interconnected metal nano-networks represent a promising design paradigm for highly miniaturized yet effective catalyst electrodes and electrochemical sensors.

Keywords: *self-supported electrodes, electroless plating, electrodeposition, Ni nanotubes, layered double hydroxides, glucose sensors*

3.1.1. Introduction

The performance of catalyst electrodes strongly depends on the electrode architecture, which determines vital parameters such as the surface area, porosity, density of active sites, electron conduction paths, mass transfer, and mechanical robustness. Foams, felts, meshes and 3D-printed substrates are frequently utilized as efficient macroscale electrode frameworks [234,235]. Similar architectures combining advantages such as stability, high porosity and the presence of a fully interconnected network for 3D charge transport are available at the micro- and nanoscale levels [235–237]. While electrodes such as nano-networks [30,46,238–240] somewhat resemble the open-porous, free-standing spatial arrangement of their macroscale counterparts, they are much more finely structured, allowing for the realization of higher specific surface areas, which represents a pivotal property in electrochemical applications [235]. Further optimization can be achieved by simultaneously tailoring the architecture on multiple length scales [235,241], for instance by decorating the support backbone with nanostructured active materials for catalysis, energy storage or photochemistry [36,242,243]. Hierarchical structuring can be very impactful at the macro-nano as well as within the submicron range, since different aspects of the functionality can be addressed, such as diffusion proceeding at much larger scale compared to chemical conversions in carefully constructed, local nanoreactor environments [190,242,244].

The need for efficient glucose sensing, which is important in fields such as clinical diagnosis [245], biotechnology industries [246], and food processing [247], sparked efforts in the development of a new generation of sensors that combine high performance, ease of synthesis, and low cost. Since glucose molecules are redox-active, their selective conversion by electrocatalysts can be used to detect them [243,248]. Glucose sensors are mainly classified into enzymatic and nonenzymatic [249]. Enzymatic glucose sensors have different drawbacks which limit its application on large scale such as the high cost of enzyme manufacturing, and the poor long-term stability. In addition, the difficulty of enzyme immobilization limits its reproducibility. On the other hand, nonenzymatic glucose sensors serve as excellent alternatives due to their superior performance in terms of high sensitivity, fast response and ecofriendly nature [249,250]. Last years witnessed a surge in applying nanomaterials for developing glucose sensing platforms. Using of such materials offer an effective approach for manufacturing enhanced glucose sensing as it enables exploitation of large surface area, high electrocatalytic activity, and effective electron transfer. Different nanomaterials based on metals and metal oxides, chalcogenides and carbides have been employed in diverse morphologies as active materials for designing efficient electrochemical glucose sensors [243,248,251–253]. Among them, transition-metal-based nanostructures are considered as one of the most promising alternatives for

nonenzymatic glucose sensing applications due to their abundance, high electroactivity, ease of synthesis and cost efficiency [254–257]. As such, glucose oxidation represents a well-established model reaction for nanostructured, nickel-based electrocatalysts, allowing us to investigate structure / composition-property relationships and to demonstrate the favourable characteristics of our electrode design.

Layered double hydroxides (LDHs) are a class of two-dimensional (2D) redox-active structures with a high electrocatalytic activity which allows them to be candidate catalysts for nonenzymatic glucose sensing [250,258]. In addition, LDHs comprise the advantages of environmental friendliness and low cost [258]. Among LDHs, NiCo-LDH attracts great attention. It has an inverse spinel crystal structure, where Ni^{2+} is distributed at the octahedral sites and Co^{3+} on both tetrahedral and octahedral sites [259]. This composition offers higher conductivity than that of Ni-and Co-LDH, which in turn enhances the electron transfer and improves glucose detection. Moreover, incorporation of Co in LDHs sheets provides more active sites and further enhances ion transport [258]. However, NiCo-LDHs suffer from fast agglomeration besides a still quite limited conductivity which disturbs the electrochemical stability of the electrode and makes them still inappropriate for the detection of glucose traces [82].

In order to overcome the limitations of NiCo-LDHs, different solutions have been investigated, including delamination, the formation of composites, and morphology optimization [260,261]. Among these techniques, the inclusion of conducting material as a support layer and forming a composite electrode is considered as an effective method to enhance the conductivity and improve the electrochemical activity of NiCo-LDHs toward glucose sensing. Self-supported networks composed of interconnected, one-dimensional (1D) nickel nanotubes (Ni-NTNWs) can offer a suitable conductive supporting layer for NiCo-LDHs to fabricate efficient sensors due to their initial electrochemical activity in an alkaline medium. In addition, Ni is one of the most naturally abundant elements and has low cost [262]. Being highly porous and efficiently percolated, metal NTNWs offer continuous and efficient pathways for both electron and mass transport, which in turn can improve the electrode performance by facilitating the kinetics of the redox reaction [30]. Furthermore, properly structured NTNWs possess a robust, interconnected architecture and thus can act as self-supported electrocatalyst layers, without the need for additives such as binders or conductive fillers [46].

In the present study, we present a new generation of stand-alone electrodes based on Ni-NTNWs, whose activity and selectivity are investigated in the nonenzymatic electrochemical detection of glucose. Electroless plating (EP) has been used as a facile route for synthesizing Ni-NTNWs, onto which nanostructured $Ni(OH)_2$ and NiCo-LDH coatings were

electrodeposited as redox mediators to further enhance their glucose sensing performance. Due to its scalability and low cost, EP represents a convenient and effective method for producing nanotube- or nanowire-based electrocatalysts [46,263]. Aside hierarchical functionalization, additional improvements over our previous metal NTNW-based sensors [32,46] include integration into a stand-alone electrode and enhanced network accessibility, demonstrating the considerable performance potential of catalyst and sensor electrodes with rationally designed multilevel architecture and composition.

3.1.2. Experimental section

3.1.2.1. Chemicals

borane dimethylamine complex (DMAB) (Sigma-Aldrich, 97%), dichloromethane (Sigma-Aldrich, puriss. p.a.), fructose (Merck, puriss.), D-(+)-glucose (Sigma- Aldrich, ACS reagent), KCl (Sigma, ≥99.0 %), NaOH solution 32% (Sigma-Aldrich, purum), $NiSO_4 \cdot 7H_2O$ (Sigma-Aldrich, purum p.a. cryst.), boric acid (Sigma), $Ni(NO_3)_2 \cdot 6H_2O$ (Merck), $Co(NO_3)_2 \cdot 6H_2O$ (Acros Organics), $PdCl_2$ (Alfa Aesar, 99.9% metal basis), Trifluoroacetic acid (Carl Roth, ≥99.9 %), methanol (AppliChem Panreac, 99.5 %), trisodium citrate dihydrate (Sigma-Aldrich, puriss. p.a.), ascorbic acid (Merck, 99.7%) L-glutamine (Sigma, 99.5%), NaCl (Merck, suprapur) and uric acid (Sigma, 99%). All the previous chemicals were used directly as received without further purification. Deionized water (Milli Q, > 18 MΩ cm) was used in all procedures.

3.1.2.2. Synthesis of Ni–NTNW

Ni-NTNWs were prepared via template seeding followed by EP of Ni over ion track-etched polycarbonate membranes (Whatman, nominal thickness 20 μm) with a pore density of 1.5×10^8 cm^{-2} and a nominal pore size of 200 nm according to a previously reported procedure [46]. Briefly, the as-obtained templates were sensitized and activated by coating with Pd nanoparticle seeds. Firstly, the membranes were immersed in a solution of the Sn^{+2} sensitization path which consists of 42 mM $SnCl_2$ and 71.4 mM Trifluoroacetic acid in ethanol for 30 min, washed, and transferred to the activation solution containing the Pd nanoparticles (1 mM $PdCl_2$ and 33 mm KCl) for 4 min. The templates were washed with ethanol. This process was repeated three times to increase the seeding nanoparticle density. The final template was turned into a brown color resulting from Pd NPs covering the template's surface and the pores. EP of Ni was performed by immersing the activated templates in the EP bath for around 40 min. EP path consists of two components mixed together in 1:1 volume ratio: (1) the oxidation component containing 100 mM $NiSO_4.7H_2O$ (metal source) and 100 mM trisodium citrate dihydrate (ligand), (2) the reduction component containing 100 mM DMAB (reducing agent). Nickel-boron plating was

chosen since it yields smooth, coherent and strong deposits, which facilitates the realization of free-standing, robust nano-network architectures [264]. With ongoing plating and growing of Ni film, a shiny film will appear on the surface of the template. After the end of plating, the templates were thoroughly washed with water.

3.1.2.3. Electrodeposition of the nickel supporting layer and exposure of the NTNWs

One side of the Ni-NTNW was contacted by pressing the metallized membrane onto a Cu ring, immersed in Ni electrolyte (0.5 M $NiSO_4.7H_2O$ and 0.5 M H_3BO_3 in water), and a constant potential of -1 V was applied, resulting in the reinforcement of the electrolessly plated Ni surface layer on top of the opposing template side. The amount of charge consumed during electrodeposition was fixed to 100 C to keep the thickness of the supporting layer constant in all samples. To obtain the final stand-alone electrodes for the electrochemical experiments, Cu wires were soldered to the Ni supporting layer, and the back side and the edge of the electrode were coated with insulating lacquer to prevent areas other than the NTNW to contribute to the electrochemical response. Afterwards, the non-reinforced, very thin Ni surface layer on the other side stemming from EP was removed via careful chemical polishing with nitric acid (65% diluted with water in a 1:2 ratio). Finally, the polymer matrix was removed by thorough washing the sample, with dichloromethane, resulting in full exposure of the NTNW.

3.1.2.4. NTNW derivatization and integration

Hierarchical electrodes were fabricated by electrodepositing $Ni(OH)_2$ and NiCo-LDH nanosheet coatings onto the Ni-NTNW parent structure, using aqueous electrolytes containing an overall metal ion concentration of 0.05 M (pure $Ni(NO_3)_2{\cdot}6H_2O$ for the $Ni(OH)_2$@Ni-NTNW, and a 1:1 molar mixture of $Ni(NO_3)_2{\cdot}6H_2O$ and $Co(NO_3)_2{\cdot}6H_2O$ for the NiCo-LDH@Ni-NTNW). Electrodeposition was performed under pulsed conditions (-1 V vs. Ag|AgCl separated by repeated pulses of +1 V vs. Ag|AgCl for 0.5 s every 3 s), and the extent of deposition was controlled by changing the deposition time. After the hydroxide deposition, the samples were thoroughly washed with water and dried in air.

3.1.2.5. Physical characterization

X-ray diffraction (XRD) measurements were performed using Seifert PTS 3003 (Germany) diffractometer using a Cu anode. on the primary side, an X-ray mirror installed, and a long Soller-slit and graphite monochromator built-in on the secondary side to separate the Cu Kα-line (40 kV/40 mA). The crystallite size, *D*, was estimated using the Scherrer equation for Ni-NTNW crystals [265]:

$$D = (\mathrm{K} \times \lambda)/(\mathrm{FWHM} \times \cos\theta) \qquad \text{(Eq. 3.1)}$$

where D is the crystallite size, K is the shape factor, λ is the X-ray wavelength, FWHM is the full width at the half maximum of the peak, and θ is the Bragg angle. Scanning electron microscopy (SEM) was conducted using a Philips XL30 FEG (Netherlands) with acceleration voltages of 10–30 kV. Transmission electron microscopy (TEM) experiments were performed with a FEI CM20 (Netherlands) (200 kV acceleration voltage, LaB_6 cathode) accompanied with energy dispersive X-ray analysis (EDX) unit.

3.1.2.6. Electrochemistry

The electrodeposition experiments were performed in a three-electrode setup (counter electrode: Pt spiral; reference electrode: Ag|AgCl; working electrode: circular, electrolessly nickelated membrane pieces of 12 mm diameter) using a Keithley 2602 System SourceMeter unit (USA). The electrochemical characterization and the glucose sensing were performed in a three-electrode setup (counter electrode: Pt spiral; reference electrode: Hg|HgO filled with 1 M NaOH, resulting in a potential of 140 mV versus the standard hydrogen electrode; working electrode: circular self-supported NTNW electrodes (11 mm diameter after insulation) connected to Cu wire) using a Gamry Reference 600 potentiostat. In all experiments, the temperature was adjusted to 25 °C with a thermostat. Before the electrochemical measurements, the as-prepared NTNW electrodes were cycled between -200 mV and 800 mV using a scan rate of 50 mV s^{-1} until a stable response was obtained (50 cycles). Amperometric glucose sensing was conducted at a potential of 0.6 V, which was maintained before the experiment until a steady-state current was achieved, starting with 50 mL of stirred 0.1 M NaOH as base electrolyte. To this base electrolyte, 50 µL aliquots of glucose stock solutions of four different concentrations (3, 10, 100, and 500 mM glucose, dissolved in 0.1 M NaOH) were successively injected resulting in the change of concentration for glucose by ~3, 10, 100, and 500 µM, respectively. For the selectivity measurements, 50 µL glucose aliquots were alternated with 50 µL aliquots of interference solutions. All injections were pointed away from the working electrode in order to avoid concentration surges and corresponding current spikes.

3.1.3. Results and Discussion

3.1.3.1. Fabrication of the stand-alone NTNW electrodes

The formation of robust nano-networks through the replication of ion track-etched polycarbonate templates requires a sufficient density of pore intersections, which can be achieved via the overlapping of inclined pores and increases with increased pore density and size, and with widened pore orientation distribution [63].

In order to initiate EP on substrates that do not have an intrinsic catalytic activity such as the polycarbonate templates used in our case, metal seeds are required. Our seeding process involves the successive immersion of the template membranes in Sn^{+2} and Pd^{+2} salt solutions, resulting in the formation of a conformal Pd nanoparticle coating according to Eq. 3.2 and 3.3 [64,65,68]:

$$Sn^{+2}_{aq} \rightarrow Sn^{+2}_{ads} \qquad \text{(Eq. 3.2)}$$

$$Sn^{+2}_{ads} + Pd^{+2}_{aq} \rightarrow Sn^{+4}_{ads} + Pd_{ads} \qquad \text{(Eq. 3.3)}$$

The second reaction is derived by the difference in the electrochemical reduction potentials between the two elements. According to previous studies, Sn residues remain on the substrate surface after activation, and the surface density of seeds can be optimized by varying the number of seeding cycles [66]. The Pd nanoparticle seeds act as catalysts, oxidizing the chemical reducing agent DMAB in the electroless plating bath, and in turn providing electrons for reducing the Ni^{2+} citrate complex present in the same solution. This process includes different side reactions such as hydrolysis of DMAB and hydrogen evolution in parallel with nickel reduction resulting in the formation of different DMAB derivatives depending on the degree of oxidation. The overall reduction of Ni^{2+} using DMAB can be represented by Eq. 3.4 [266]:

$$3Ni^{2+} + (CH_3)_2NHBH_3 + 3H_2O \rightarrow 3Ni + (CH_3)_2H_2N^+ + H_3BO_3 + 5H^+ \qquad \text{(Eq. 3.4)}$$

The resulting Ni deposit is active in this reaction as well and thus continues to grow autocatalytically [67], initially forming island-like nanoparticle coatings [66,68], which later merge to create continuous Ni nanotube walls in the interior and Ni surface films on the top and bottom of the exterior surfaces of the template membrane (Figure 3.1, step 1). The Pd seeds typically are small (< 5 nm diameter) and only cover a small fraction of the initial substrate surface [64,65,68]; moreover, they get embedded in the Ni and hydroxide deposits, cannot be detected by XRD, as shown below. As such, they do not significantly contribute to the catalytic activity of our NTNWs.

Previously, we fabricated working electrodes for electrochemical sensors by simply attaching free-standing NTNW films to glassy carbon electrodes with carbon paste [32,46]. Disadvantages of this approach include the limited robustness and conductivity of the catalyst-electrode connection, wicking up of mineral oil from the carbon paste into the porous NTNW, and the partial blocking of the underlying NTNW by the metal surface layer.

To overcome these problems, we directly integrated the Ni-NTNW into the electrode by first reinforcing one of the Ni surface layers by Ni electrodeposition (Figure 3.1, step 2), followed by soldering the Ni support layer to a Cu wire, resulting in a stable stand-alone electrode which greatly facilitates handling. Afterwards, the metal surface layer was removed by chemical

etching with nitric acid from the other side of the template (Figure 3.1, step 3), and the polymer matrix was dissolved with dichloromethane, resulting in the full exposure of the Ni-NTNW (Figure 3.1, step 4). Etching off the Ni surface layer improves the diffusion of reagents into the catalyst network and is vital for achieving homogeneous coverage of the Ni nanotubes through the consecutive hydroxide nanosheet decoration, which is accomplished by pulsed electrodeposition (Figure 3.1, step 5). Two different electrolyte compositions were employed, resulting in the formation of either $Ni(OH)_2$ or NiCo-LDH. During the growth of the hydroxide layer via ED, NO^{3-} ions are reduced and generation of OH^- ions occurs; subsequently, these hydroxide ions react with Ni^{2+} or Co^{2+} present in the electrolyte, forming hydroxide layers by precipitation [99]. Trials with different electrodeposition times were employed to control the extent of deposition and to determine the optimum conditions for preparation, as discussed below.

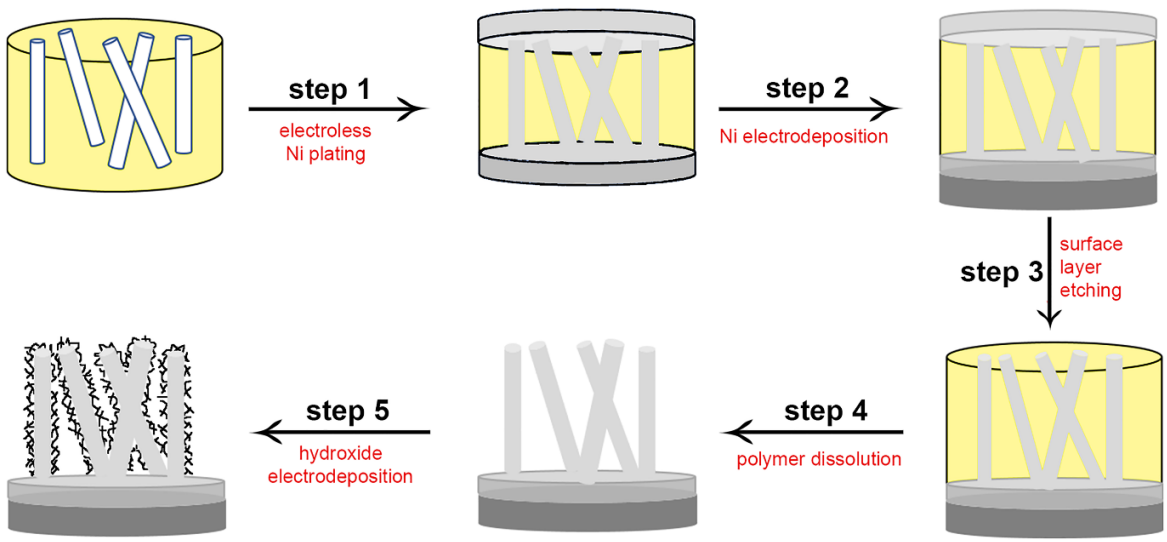

Figure 3.1. *Schematic representation of the NTNW electrode fabrication.*

3.1.3.2. Structural characterization

The electrolessly plated NTNW formed free-standing films, whose robustness was further increased by the reinforcement of the Ni back layer, as was confirmed by SEM analysis, proving the Ni deposit to be dense, homogeneous and ~ 10 μm thick (Figure 3.2a). As seen, the NTNW is sandwiched between the electrodeposited back layer and the electrolessly-formed surface layer on the top side. Top view images revealed the closure of the NTNW by the electroless Ni layer, despite the nanotube openings and their interior surfaces still being accessible from the outside (Figure 3.2b). After etching off the electrolessly plated Ni surface layer and dissolving

the polymer, the NTNW is completely exposed and appears free of polymer residues, but still remains free-standing due to the anchoring to the Ni back layer and the nanotube interconnection (Figure 3.2c). At this stage, the NTNW is suitable for electrochemical derivatization.

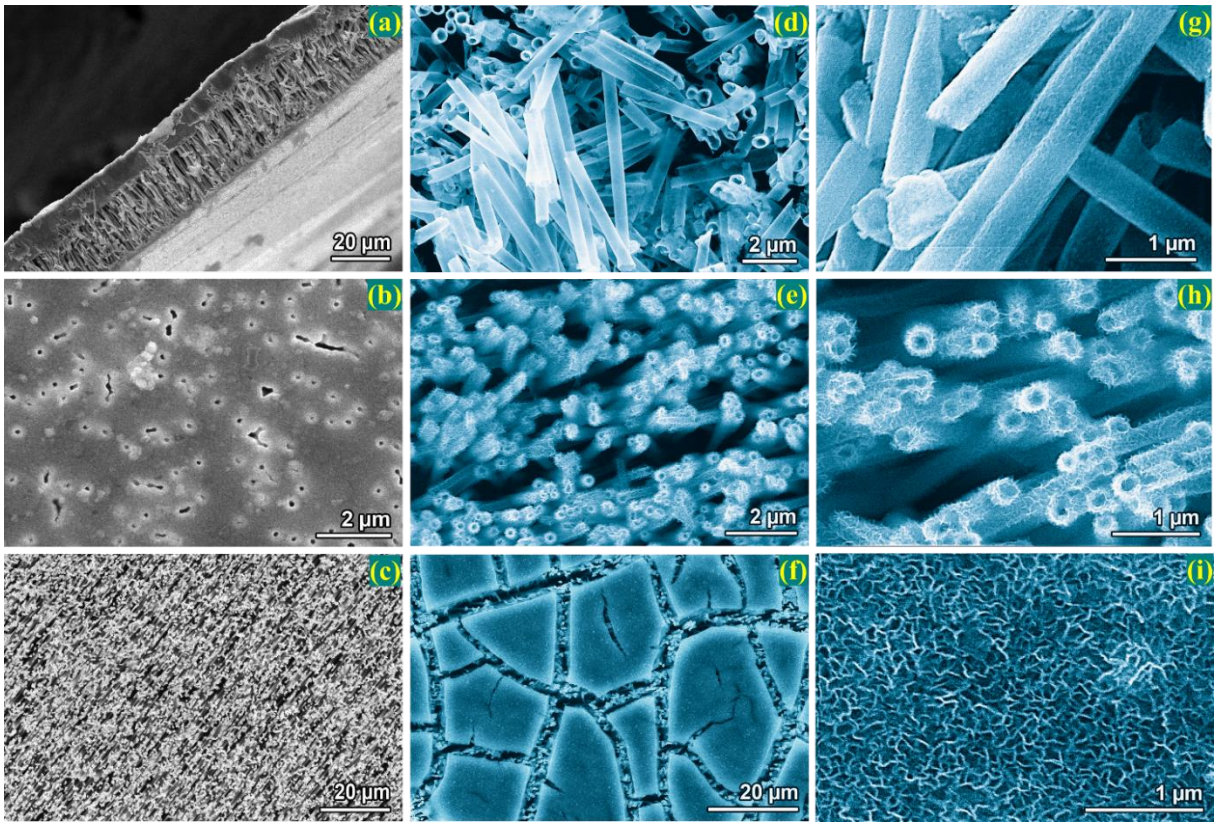

Figure 3.2. *SEM images illustrating different steps of the integrated electrode fabrication, and the dependence of the LDH deposit thickness on the electrodeposition time. a) Side view of the Ni-NTNW with the electrochemically reinforced Ni back layer b) Top view of the NTNW before surface etching. c) Top view of the NTNW after removal of the surface layer by etching. SEM top view images of NiCo-LDH@Ni-NTNWs after (d, g) 60 s, (e, h) 120 s and (f, i) 300 s of hydroxide electrodeposition.*

Direct current electrodeposition was firstly applied to deposit the decorating hydroxide layer, but it did not yield satisfying deposits as shown in the SEM micrographs (Figure S3.1), which may be attributed to the formation of gas bubbles that hinder the easy access of ions to the inner parts of the network, and reagent depletion within the deeper catalyst layers. By using a discontinuous deposition, these issues could be resolved. Figure 3.2d-i depicts the morphologies of NiCo-LDH-decorated Ni-NTNWs created using different electrodeposition times. After 60 s (Figure 3.2d, g), the micrographs show an ultrathin layer of NiCo-LDH nanosheets grown over the 3D Ni-NTNWs that is clearly recognizable at higher magnification

(Figure 3.2g), indicating a very low hydroxide loading on the smooth Ni nanotube surface. By increasing the deposition time to 120 s, a thicker LDH nanosheet layer is formed, which appears homogenous and covers the tubes from top to bottom (Figure 3.2e, h). While the LDH deposit somewhat obscures the outer surface of the Ni nanotubes, the interconnected macropore network between the crossing nanotubes still is intact. Further increasing the deposition time to 300 s results in the formation of a thick, cracking deposit layer which covers the majority of the outer Ni-NTNW surface (Figure 3.2f). The corresponding high magnification SEM top view micrograph of the cracked hydroxide layer (Figure 3.2i) shows that the wrinkly, ultrathin nanosheet structure still resembles morphology of the deposit on the Ni nanotubes (Figure 3.2h). This bulk layer considerably reduces the accessibility of the inner network surface area to the electrolyte, which in turn is detrimental to the catalytic activity of the electrode. Consequently, the deposition time was fixed to 120 s as an optimum condition for the synthesis of the hydroxide-derivatized NTNW electrodes, which represents a good compromise between depositing sufficient amounts of active material while simultaneously avoiding clogging of the porous catalyst layer.

The phase composition of the Ni-NTNW and the corresponding $Ni(OH)_2$@Ni-NTNW and NiCo-LDH@Ni-NTNW electrodes were investigated with XRD (Figure 3.3). The XRD pattern of the Ni-NTNW reveals sharp reflexes located at 44.4˚, 51.8˚ and 76.3˚ which correspond to the (111), (200) and (220) crystalline planes of face-centered cubic Ni (JCPDS No. 04-0850) [267]. Their strong intensity reveals that the Ni-NTNWs have a crystalline nature [267]. The average crystallite size, D, of Ni has been calculated using the Scherrer equation (Eq. 3.1) considering a shape factor of K = 0.94, amounts to 19±3 nm. The original Pd seeds cannot be detected here because of their small amount compared to the amount of material in the nanotube walls. Beside the three characteristic Ni reflexes, the XRD pattern of the $Ni(OH)_2$@Ni-NTNW shows three broad reflexes of low intensity at 10.7˚, 21˚ and 33.9˚, which are attributed to α-$Ni(OH)_2$ [268], while the NiCo-LDH@Ni-NTNW shows reflexes at 11.3˚, 19.3˚, 33.3˚ and 38.1˚, which are assigned to the α-phase of Ni-Co hydroxides [269,270]. The weak intensity of the hydrotalcite-like $Ni(OH)_2$ and NiCo-LDH characteristic peaks likely results from the ultrathin thickness and poor crystallinity of the nanosheets, which is in consistence with the literature [271,272]. The absence of the thermodynamically preferred β-phase as well as the disturbed crystallinity of the deposits renders the added active material promising for the oxidation of small organic molecules, which scales with the ease of Ni(II) oxidation as the underlying mechanistic foundation for creating active sites [273,274].

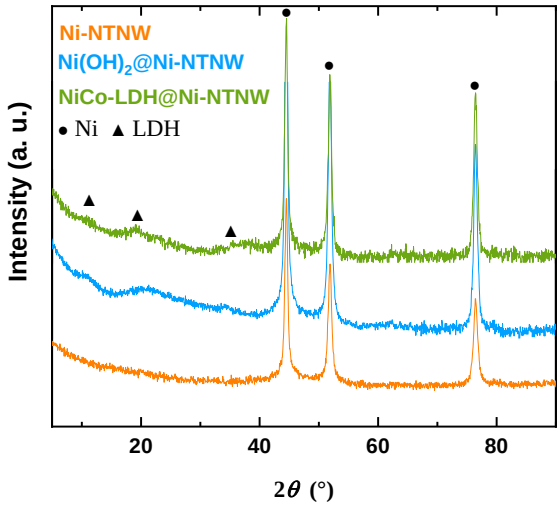

Figure 3.3. *XRD patterns of the three NTNW catalysts investigated in this study.*

Before the electrochemical experiments, the Ni-NTNW, $Ni(OH)_2$@Ni-NTNW, and NiCo-LDH@Ni-NTNW catalysts were characterized with SEM (Figure 3.4). Due to the exceptional conformality of the EP reaction, Ni was deposited within the whole template, forming homogenous, smooth and intact tubes of ~20 μm length and of ~ 200 nm diameter, which corresponds to the thickness and the pore diameter of the parent template, respectively (Figure 3.4a-c). The higher magnification SEM (Figure S3.2) shows that the deposited particles merged into a dense, nanocrystalline film. The electrodeposited $Ni(OH)_2$ coating (Figure 3.4d-f) very much resembles the NiCo-LDH nanosheets both in morphology (small, wrinkled flakes forming a 3D, porous coating) and amount of material (Figure 3.4g-i), confirming the ability of the electrodeposition protocol to produce catalysts of close to identical structure, but differing composition. Close views of the nanotube openings show that hydroxide nanosheets are deposited both on the outer and the inner surfaces of the Ni nanotubes (Figure 3.4e, h) and thus fully utilize their surface area, which is increased over nanowires of the same diameter due to their hollow structure.

Figure 3.4j-l shows photographs of the final stand-alone catalyst electrodes after soldering Cu wire to the reinforced Ni supporting layer, which can be directly immersed in the electrolyte and connected to the potentiostat without using any kind of assisting electrodes (*e.g.*, glassy carbon), which are commonly employed for carrying the active materials. The interconnection between the Ni nanotubes prevents bundling and detachment from the back electrode, which is commonly observed for parallel arrays of 1D nanostructures, and results in a loss of active surface [275]. These self-supported electrodes are binder-free, and the active material is directly grown on the Ni nanotubes, facilitating electrical contact and the mechanical connection. While the nanosheets offer large surface area, consequently, facilitate the contact between the

electrolyte and electrode and allow for a fast ion transfer, the embedded Ni nanotubes act as metallic, one-dimensional current collectors which ensure short and efficient electronic conduction paths from the back electrode to the hierarchically branched catalyst-solution interface. Similar effects have been observed in NiO@Ni nanowire networks, where the presence of metallic cores in the crossing 1D building blocks improved reversibility, charge collection and ion diffusion [50].

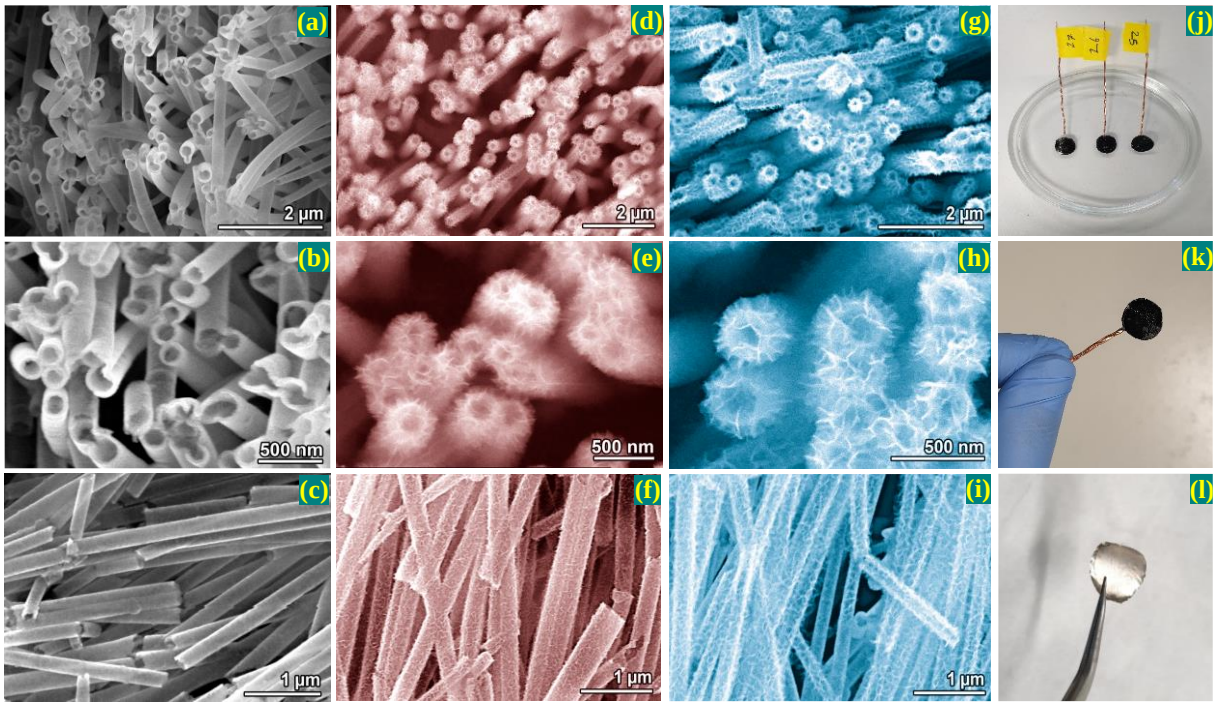

Figure 3.4. *SEM images of (a-c) Ni-NTNW, (d-f) $Ni(OH)_2$@Ni-NTNW, and (g-i) NiCo-LDH@Ni-NTNW electrodes, accompanied by photographs of the three as-prepared stand-alone electrodes (j), higher magnification of a single NiCo-LDH@Ni-NTNW electrode (k), and Ni back supporting layer before soldering (l).*

The hierarchical structure of the NiCo-LDH@Ni-NTNW was further investigated with TEM, accompanied by EDX. Figure 3.5 shows the bright-field TEM image of a single nanotube opening, in which the nanotube support can be easily recognized by its dark contrast, which is more pronounced at the nanotube edges where the tube walls are oriented roughly parallel to the beam. The grainy texture of the nanotube, which is caused by its formation from merging nanoparticle deposits, is evident as well as the flaky deposit on its surface. As anticipated from the hierarchical architecture (a pure Ni nanotube core overgrown by a mixed NiCo-LDH shell), EDX spectra recorded at the nanotube center, which cover the Ni walls, show a much higher Ni-to-Co ratio as compared to the nanotube vicinity, which is dominated by the nanosheets.

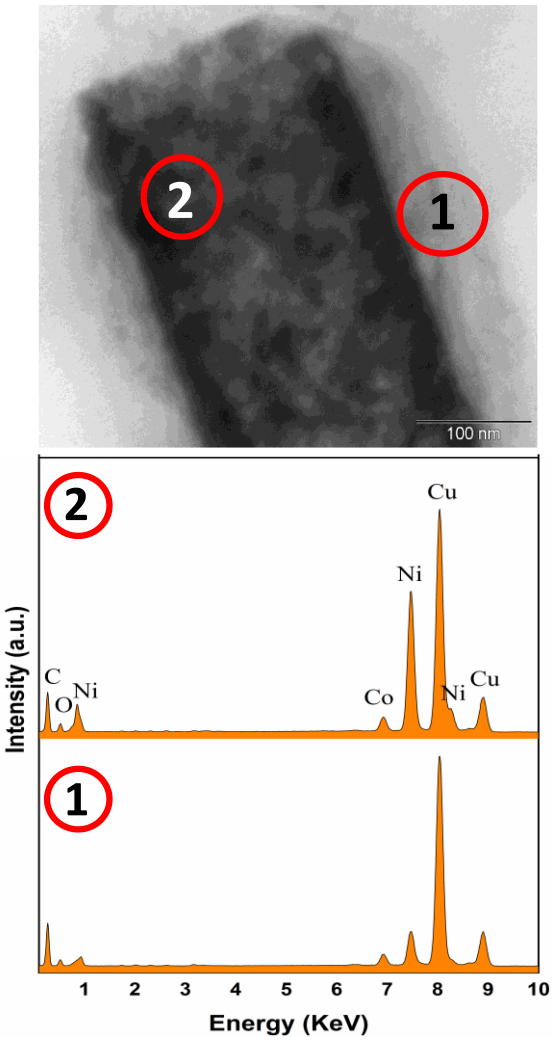

Figure 3.5. *TEM analysis of the NiCo-LDH@Ni-NTNW catalyst, including EDX spectra obtained for the highlighted shell (1) and core (2) regions of the hierarchical nanotube. The Cu signal stems from the TEM holder.*

3.1.3.3. Amperometric nonenzymatic glucose sensing

First, the general electrochemical behaviour of the three catalyst electrodes was investigated by recording cyclic voltammograms (CVs) in the alkaline, glucose-free base electrolyte. As shown in Figure 3.6a, the CV curves of Ni-NTNW and the $Ni(OH)_2$@Ni-NTNW reveal a couple of redox waves centered around the potential of ~480 mV, which can be attributed to the redox conversions between $Ni(OH)_2$ and NiOOH (Eq.3.5) [276]. The higher current response found for the $Ni(OH)_2$@Ni-NTNW electrode can be attributed to the higher surface area offered by the deposited hydroxide nanosheets [258]. On the other hand, NiCo-LDH@Ni-NTNW shows a pair of anodic peaks which start at more negative potential compared to that of Ni-NTNW and appear at about 540 and 690 mV, corresponding to the irreversible redox processes of Co^{2+}/Co^{3+} and Co^{3+}/Co^{4+} couples in the alkaline medium, respectively (Eq.3.6 and 3.7) [276–278]. In detail,

the Co^{2+} ions are firstly transformed into Co^{3+} ions, then the Co^{3+} ions are further oxidized into Co^{4+} ions at a higher potential. During the reverse scan, a broad cathodic peak is observed around 200 mV which represents the reduction of Co^{4+}/Co^{3+} and Co^{3+}/Co^{2+}, respectively. Importantly, the NiCo-LDH modified electrode exhibits both a larger currents throughout the complete potential range and a distinctly negative-shifted onset of the metal hydroxide oxidation, indicating both a higher density of active sites (electrochemically produced high valence metal centers) and a reduced oxidation potential as compared to the pristine and $Ni(OH)_2$-derivatized Ni-NTNW electrodes [274].

$$Ni(OH)_2 + OH^- \rightarrow NiO(OH) + H_2O + e^- \quad \text{(Eq. 3.5)}$$

$$Co(OH)_2 + OH^- \rightarrow CoO(OH) + H_2O + e^- \quad \text{(Eq. 3.6)}$$

$$CoO(OH) + OH^- \rightarrow CoO_2 + H_2O + e^- \quad \text{(Eq. 3.7)}$$

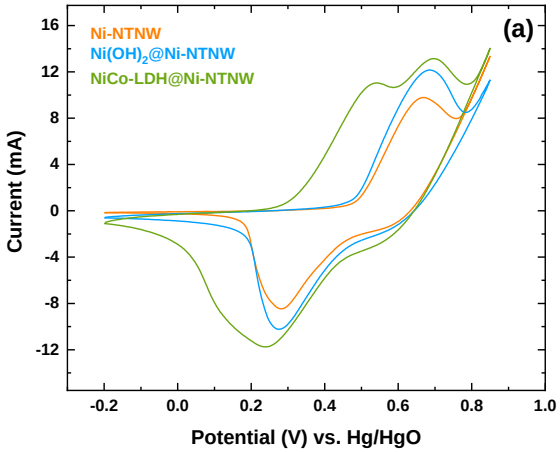

Figure 3.6. *(a) CV curves of the pristine Ni-NTNW and its $Ni(OH)_2$ and NiCo-LDH derivatives (electrolyte: 0.1 M NaOH; scan rate: 10 mV s^{-1}).*

Gradually increasing the scan rate from 10 mV s^{-1} to 80 mV s^{-1} resulted in an increase of the anodic (I_{pa}) and cathodic peak currents (I_{pc}), whereas the anodic (E_{pa}) and cathodic peak potentials (E_{pc}) were shifted to more positive and negative values, respectively (Figure 3.7a-c). This behavior can be attributed to the internal resistance of the electrodes [279]. In order to evaluate the electrochemical mechanism of the redox reactions, I_{pa} and I_{pc} were plotted against the square root of scan rate for the three electrodes (Figure 3.7d-f). As can be seen, both the anodic and cathodic peak current is proportional to the square root of scan rate for the three electrodes at scan rates ranging from 10-50 mV s^{-1}. At higher scan rates, it becomes difficult to distinguish the anodic peak current from other interfering reactions like oxygen evolution. Such a linear relation implies a typical diffusion-controlled electrochemical process [258,280].

When adding glucose to the electrolyte, the current of the reduction wave is reduced, whereas the oxidation wave is boosted, and the peak potentials are shifted to slightly more positive values (Figure S3.3). This behavior is usually explained by the "Incipient Hydrous Oxide Adatom Mediator" model [281], where either the metal M or the hydroxide $M(OH)_2$ is oxidized in an alkaline medium into $M^{3+}OOH$ or $M^{4+}O_2$. After the glucose addition, the high valent metal ions are oxidizing the glucose, forming gluconolactone and restoring the initial metal oxidation states (Eq. 3.8, 3.9) [276], sacrificing these Ni^{3+} and Co^{4+} species and simultaneously producing $Ni(OH)_2$ and CoO(OH), respectively. However, the general correlation of the catalytic activity of Ni-based catalysts in oxidizing small organic molecules with the Ni(II)-Ni(III) redox potential, as well as the similar Tafel slopes of Ni and Ni-Co (which are smaller than the slope of pure Co), indicate that high oxidation state Ni represent the active sites in this system [274].

$$\text{Glucose} + \text{NiO(OH)} \rightarrow \text{gluconolactone} + \text{Ni(OH)}_2 \qquad \text{(Eq. 3.8)}$$

$$\text{Glucose} + 2\text{CoO}_2 \rightarrow \text{gluconolactone} + 2\text{CoOOH} \qquad \text{(Eq. 3.9)}$$

As such, the decrease of the reduction peak current with increasing glucose concentration as visible in Figure S3.3 can be explained by the metal ions being chemically reduced by glucose, instead of being electrochemically converted. Conversely, the oxidation peak current is increased because the formed high valence metal oxides get consumed by reaction with glucose at a potential at which they can reform electrochemically, which produces additional anodic charge. For further insight into the reaction kinetics, Tafel plots were constructed for the three electrodes at 10 mV s^{-1} in 0.1 M NaOH solution containing 4 mM glucose (Figure S3.4). The slope of the three electrodes varies from 106 to 163 mV dec^{-1}. It is clear that NiCo-LDH@Ni-NTNW shows the highest kinetic current, confirming its superior activity. Tafel slope of that electrode (123 mV dec^{-1}) is close to the theoretical value of 120 mV dec^{-1} suggesting that the rate-determining step during glucose oxidation is the first one-electron transfer step.

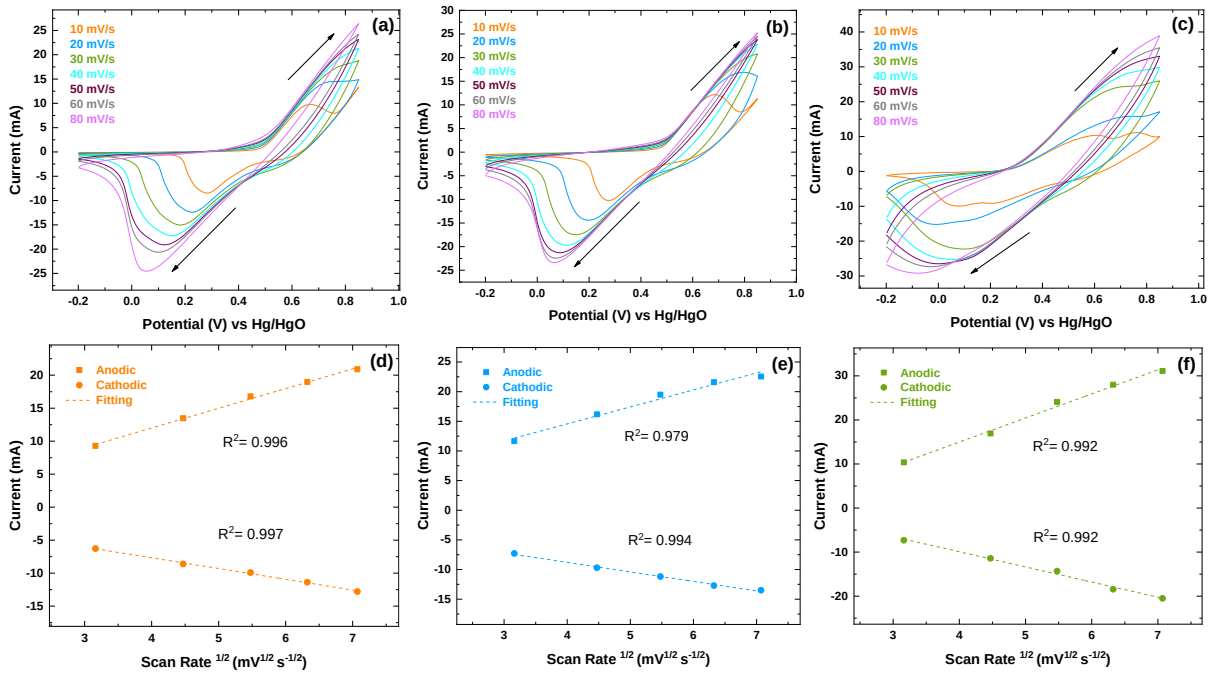

Figure 3.7. *CV curves of (a) Ni-NTNW, (b) $Ni(OH)_2$@Ni-NTNW, and (c) NiCo-LDH@Ni-NTNW at various scan rates in 0.1 M NaOH. (d-f) the corresponding peak currents as function of the square root of scan rate.*

The glucose sensing performance of the Ni-NTNW-based catalyst electrodes was determined by amperometry, following the increase in current during the addition of defined amounts of glucose to the stirred base electrolyte (Figure 3.8). For the measurement, a potential of 0.6 V was chosen, since at this value, all samples showed pronounced metal hydroxide oxidation (Figure 3.6), which is the prerequisite for the mediated oxidation of glucose (Eq. 3.5-9). All electrodes clearly resolved even the smallest glucose concentration increment of 3 µM (inset of Figure 3.8a). Also, upon glucose injection, the steady state current of the increased analyte level was quickly reached, with typical response times ranging from ~5-9 s (Figure S3.5). Amongst the three catalysts, the NiCo-LDH@Ni-NTNW showed the quickest response (5.3 s, averaged over 3 additions, see Figure S3.5), followed by the pristine Ni-NTNW (6.4 s) and the $Ni(OH)_2$-decorated variant (8.4 s). The value of the NiCo-LDH@Ni-NTNW can be considered very fast, surpassing pure NiCo-LDH, which displayed a response time of ~10 s [258], and is comparable to the best values obtained for similar open-porous catalyst architectures based on Ni-Co active materials, such as NiCo-LDH-coated carbon cloth and NiCo oxyhydroxide covered 3D Ni foam, both of which display response times of ~5 s [258,282]. Since the architecture of all electrodes is closely related and ensures efficient diffusion through the open, low tortuosity macropores of the catalyst layer, which at most might be slightly affected by the presence of nanosheet deposits, the short response time of our LDH catalyst cannot be explained by

improved analyte diffusion into the network and to the active sites, but instead indicates a particularly efficient turnover in the Ni-Co system. The delayed response of the $Ni(OH)_2$-decorated catalyst compared to the LDH variant (which are both covered by similarly sized nanosheets) likewise hints at compositional synergy and accelerated electrochemical regeneration of active sites rather than a structural effect.

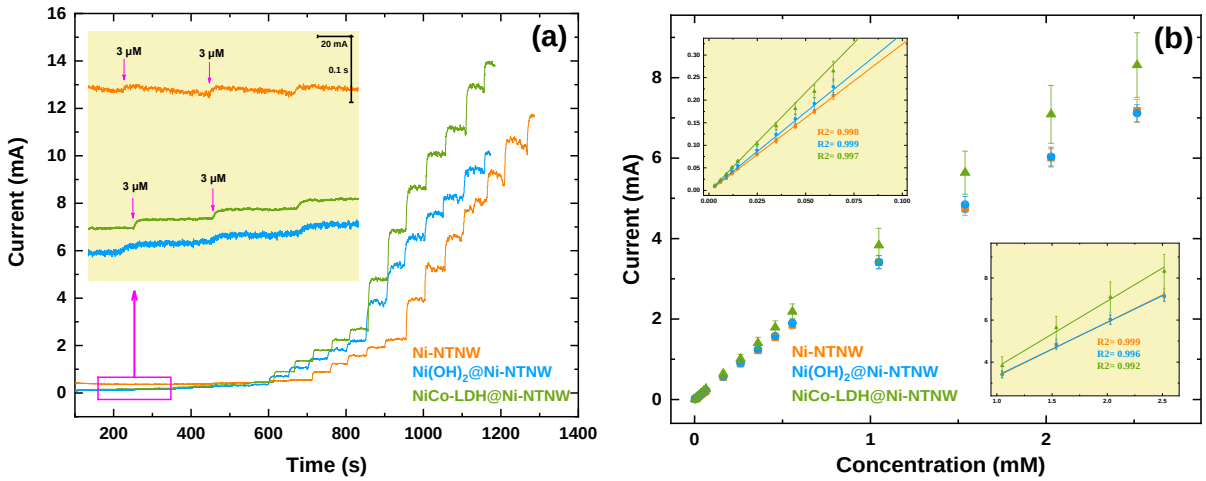

Figure 3.8. *(a) Amperometric glucose sensing curves of the three catalyst electrodes (0.6 V, 0.1 M NaOH, stepwise addition of 3 µM, 10 µm, 100, and 500 µM glucose, respectively). Inset: I−t curves at the lowest glucose concentration change. (b) Calibration curves derived from the sensing measurements (The error bars represent the standard error of triplicate determinations for each concentration). Inset: Linear fits of the two linear concentration regimes used to extract the sensitivity of the electrodes.*

The efficient analyte conversion at the NiCo-LDH@NI-NTNW catalyst is further corroborated by the observation that aside the shortest response time, the LDH-decorated NTNW also features the highest sensitivity (Figure 3.8b). Plotting the current response of the three electrodes reveals an almost linear increase up to a concentration of ~2.5 mM. By linear regression of the current response, the electrode sensitivities were obtained as the slope of the lines of best fit (inset of Figure 3.8b). To ensure very high coefficients of determination, we divided the concentration range into two linear regimes (up to 1.05 mM, and from 1.05 mM to 2.52 mM glucose). In the first range, the pristine Ni-NTNW electrode exhibits a sensitivity of 3.4 mA mM^{-1} cm^{-2}, which is only slightly increased by $Ni(OH)_2$ modification (3.7 mA mM^{-1} cm^{-2}), but considerably in the case of the LDH catalyst (4.6 mA mM^{-1} cm^{-2}). In the second range, the electrode sensitivities are reduced by ~25%.

The glucose concentration representing the limit of detection (LOD) can be calculated using the following equation [279]:

$$LOD = 3\sigma/S \qquad \text{(Eq. 3.10)}$$

where σ represents the noise of the measurement (in our case, the standard deviation of the current baseline before the glucose addition), and S the sensitivity. Using the data from our catalyst electrodes, the LOD values roughly scale with the respective sensitivities, with the lowest LOD value found for the NiCo-LDH@Ni-NTNW with a value of 0.2 µM. As such, the LDH-based catalyst covers a dynamic range of roughly four orders of magnitude, from the LOD value of 0.2 µM to the upper limit of the linear range at 2.52 mM. In summary, the NiCo-LDH@Ni-NTNW electrode yields the best analytical performance in terms of sensitivity, response time, and detection limit (Table 3.1). It worth mention that all the three electrodes yield high performance compared to the existing glucose sensors as will be indicated later.

Table 3.1. *Comparison of glucose sensing performance of the nano-network electrodes*

Electrode	Linear range (*mM*)	Sensitivity (*mA mM^{-1}cm^{-2}*)	Regression quality (R^2)	LOD (*µM*)	Response time (*s*)
Ni-NTNW	0.03 - 1.05 1.05 - 2.52	3.4 2.7	0.998 0.999	0.69	6.4
$Ni(OH)_2$@Ni-NTNW	0.03 - 1.05 1.05 - 2.52	3.7 2.7	0.999 0.996	0.36	8.4
NiCo-LDH@Ni-NTNW	0.03 - 1.05 1.05 - 2.52	4.6 3.3	0.997 0.992	0.20	5.3

Since both the Ni-NTNW electrode and the $Ni(OH)_2$-coated variant are based on Ni(III) active sites formed *in situ* by anodization, the distinct surface area increase from the nanosheet decoration (compare Figure 3.4a-c with d-f) apparently is not fully translated into sensitivity, either due to a reduced intrinsic activity of the $Ni(OH)_2$ deposit, or a poor conductivity of the $Ni(OH)_2$ nanosheets (and thus their incomplete electrical accessibility). The ability of 3D porous Ni architectures such as our Ni-NTNW or macroscale Ni foam [283] to efficiently oxidize glucose without further modification can serve as a rationale for designing improved Ni-based catalysts for the electrooxidation of small (organic) molecules [284,285]: Since the Ni framework simultaneously acts as working electrode and electrocatalyst, it is of primary importance to increase the baseline Ni surface area. The efficacy of this guiding principle is evidenced by the superior geometrical-surface-normalized sensitivity of our Ni-NTNW, which adopts the 7-fold value of macroscale Ni foam (~0.5 mA mM^{-1} cm^{-2}, estimated from the linear fit in Figure 2 of the reference) [283], despite its low thickness of only ~20 µm. While our network architecture

shares general features with conventional Ni foams (both constitute 3D interconnected, highly porous frameworks composed of pure metal), structural differences include the hollow nature of our nanotubes, and their straight orientation. The most striking difference, though, is their scale: Whereas the size of structural elements of typical Ni foams (diameter of the Ni struts or the pores) are in the range of few 100 µm, these features are about two orders of magnitude smaller in our system. To increase the performance of 3D porous Ni catalysts by derivatization, it is mandatory to cover the already quite active Ni surface with an enhancing material, such as our LDH nanosheet layer with its Ni-Co synergy.

To ensure good accessibility of the active sites embedded within the networked catalyst layer, we removed the Ni surface film (Figure 3.1, step 3). The associated performance gain can be assessed by comparing our open Ni-NTNW catalyst with our previous, still surface-blocked Ni@Cu-NTNW catalyst design [46]. In this case, a sensitivity of 2.83 mA mM^{-1} cm^{-2} was obtained, which is ~20% lower than the corresponding value of the present Ni-NTNW, despite the larger thickness (~25 µm) and pore diameter (~770 nm) of the former catalyst, which leads to a larger overall metal surface, given the nominally identical pore density.

Glucose sensors are usually operated in complex environments containing multiple electroactive species. Thus, one of the most important parameters to be considered for an amperometric sensor is its ability to differentiate the analyte from interfering species. Due to the general character of the redox-mediated mechanism, Ni-based electrodes can oxidize several types of organic molecules, so it is difficult to completely avoid interferential response [285]. Considering the determination of glucose levels in blood serum, frequently probed interferents include uric acid (UA), ascorbic acid (AA), or free amino acids such as glutamine (Glu) [46,249]. Even if not redox-active under the present conditions, ionic species could also affect electrocatalysis, which we investigated by including NaCl to our list of interferents. Normally, the physiological level of glucose is around 3-8 mM, which is much higher than that of the other interfering species (*e.g.*, AA and UA are around 0.1 mM) [286]. Regardless, to allow for a direct comparison of the relative current responses in our selectivity experiments, we added the analyte glucose as well as our interferents UA, AA, Glu and NaCl at the same concentration increment of 50 µM (Figure 3.9a). Compared to the interferents, glucose causes the most pronounced response, with AA only showing ~35 % of the oxidation current, while UA and Glu only contribute to a very minor degree (~6 % of the glucose current), and NaCl being negligible. The height of the glucose oxidation step is maintained in the second and third addition series, proving that the presence of the interferents does not alter the analyte recognition (Figure 3.9a). The strong response of the NTNW catalysts towards glucose,

compounded by the considerably reduced analyte-interferent ratio in real-life samples, illustrates the good selectivity of our catalyst in the target application. To investigate the sensor stability, we performed an extended amperometric experiment (Figure 3.9b). All catalyst electrodes showed a stable response up to 3000 s, which confirms the good stability of the electrode structures in the alkaline electrolyte. Post analysis of the three electrodes was conducted to approve their stability. Surface morphology and electrochemical behaviour of the three electrodes were investigated after performing the whole experiments set. Cyclic voltammograms (Figure S3.6) of the three electrodes retained the same redox behaviour with a slight shift in peak positions compared to those performed before running the experiments set. SEM verified that both the NTNW backbone and the decorating hydroxide layer remain intact after running the complete sensing experiments (Figure S3.7). These findings confirm the stability of the prepared electrode materials.

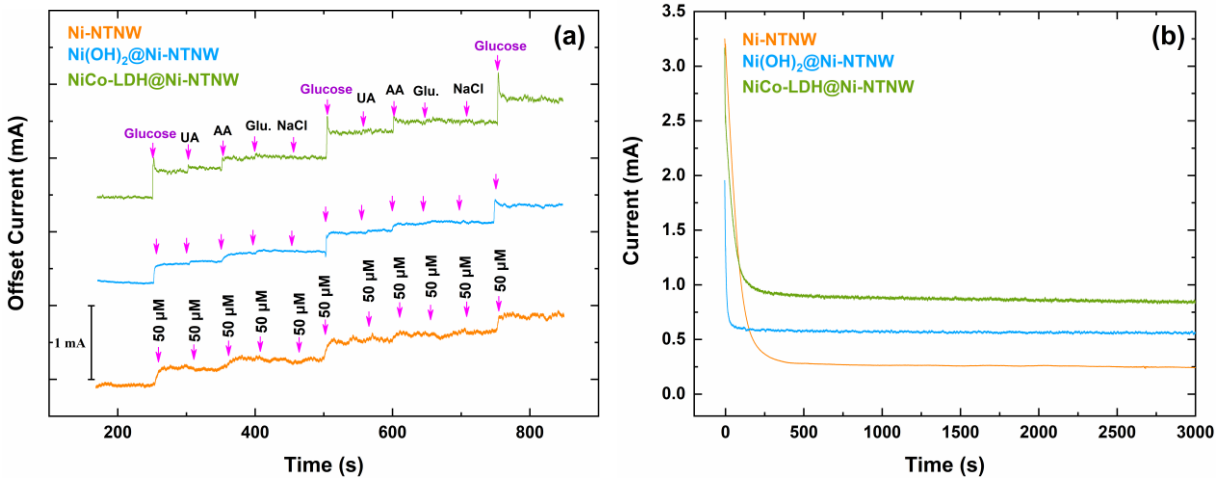

Figure 3.9. *(a) Interference study, comparing the current response of the different electrodes towards the analyte glucose oxidation in 0.1 M NaOH with the successive step addition of 50 µM of glucose and other interferents. (b) Amperometric investigation of the catalyst stability at 0.6 V (100 mM glucose in stirred 0.1 M NaOH).*

Our integrated catalyst electrodes compare favorably with other nanostructured, nonenzymatic, Ni- and Co-based glucose sensors. Table 3.2 contrasts key performance parameters of our NiCo-LDH@Ni-NTNW with recently reported catalysts, highlighting its excellent overall performance, particularly in terms of sensitivity and detection limit. While the first entry (macroscale Ni foam supported Ni-Co-oxyhydroxide) surpasses the sensitivity of our LDH electrode, it is likely that its thickness greatly exceeds the 20 µm of our NTNW film, although no concrete value is stated in the literature [282]. As such, besides its intense response, good selectivity and linear range, our LDH catalyst electrode quickly adapts to changed analyte

concentrations and exhibits an outstanding volumetric density of active sites. Both of the latter qualities can be linked to its carefully designed, binder-free architecture, comprising an openly accessible, highly porous, fully interconnected network of high aspect ratio Ni nanotubes, which are evenly overgrown but not occluded by synergetic Ni-Co-LDH nanosheets, and fully integrated into a stand-alone Ni back electrode. The flexibility of the proposed approach can be used to identify efficient electrocatalyst designs, which then can be mimicked with more simple synthetic procedures (such as moving away from templating, using aggregating nanowire colloids to create similar electrode frameworks [287]).

Table 3.2. *Comparison of the glucose sensing performance of the NiCo-LDH@Ni-NTNW with other nanostructured Ni- / Co-based glucose sensors*

Electrode	Sensitivity ($mA\ mM^{-1}cm^{-2}$)	Electrolyte	Maximum of linear range (mM)	LOD (μM)	Ref.
NiCo Oxyhydroxide/Ni foam	6.6	0.1 M KOH	1.02	-	[282]
NiO-buckypaper	2.7	0.4 M NaOH	9	14	[288]
Ni@Cu NTNW	2.8	0.1 M NaOH	1.9	1.2	[46]
$NiCo_2O_4$/ stainless steel	1.7	0.1 M NaOH	1	0.16	[259]
Ni LDH/ carbon cloth	1.3	0.1 M KOH	0.6	1	[258]
Co_3O_4 nanosheets-$Ni(OH)_2$/GCE	1.1	0.1 M NaOH	0.04	1.08	[289]
$NiCo_2O_4$/GCE	1.9	0.1 M NaOH	0.3	0.6	[290]
$Ni(OH)_2$ flakes/Ni foam	2.6	0.1 M NaOH	1.05	2.5	[291]
Au@NiCo LDH	0.865	1.0 M NaOH	12	0.03	[292]
Ti_3C_2/NiCo-LDH/GCE	0.064	0.1 M KOH	4.096	0.53	[293]
Amorphous CoNi hydroxide	1.9	0.5 M NaOH	5	0.12	[279]
NiCo-LDH@Ni-NTNW	4.6	0.1 M NaOH	2.52	0.20	This work

Conclusion

We designed a stand-alone electrode based on thin NiCo-LDH nanosheets electrodeposited onto a framework composed of interconnected Ni nanotubes, which were prepared using the facile and scalable method of electroless plating. A thick layer of Ni was electrodeposited to anchor the Ni nanotubes and allow for their straightforward device integration. Such a combination of LDHs and Ni-NTNWs takes advantage of the electrocatalytic properties of the active material, the high conductivity of the 3D current collector onto which is its grown, and the efficient diffusion through the fully bicontinuous, distinctly porous catalyst layer. Owing to their microscale network architecture, such catalyst electrodes exhibit an ultrahigh density of easily accessible active sites, which is reflected in the superior sensitivity and quick response demonstrated in the electrochemical, nonenzymatic detection of glucose. Due to the pronounced flexibility of the utilized deposition reactions with respect to the metal type of the nanotube support and the active material, our electrode platform can be easily adapted to match the compositional requirements of other electrochemical applications and showcases the advantages of binder-free 3D nano-network catalysts designed and optimized on multiple length scales.

Acknowledgement

Khaled M. Amin gratefully acknowledge the financial support provided by MHESR (Egypt) and DAAD (Germany) for his PhD scholarship under GERLS program. The Authors would like to thank Martin C. Scheuerlein and Tim Boettcher for help with the XRD measurements.

3.1.4. Supplementary Materials

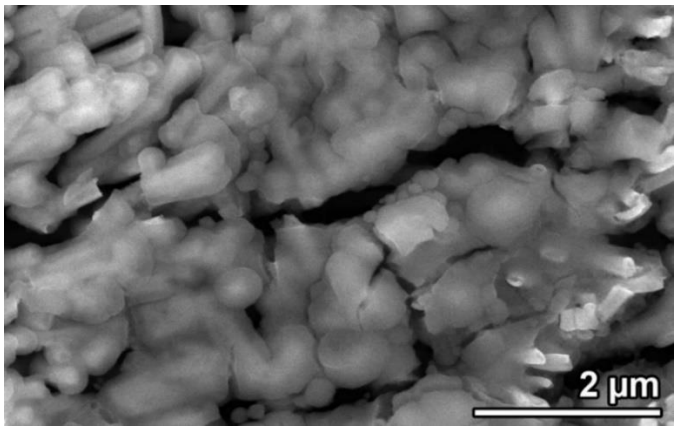

Figure S3.1. *SEM of NiCo-LDH@Ni-NTNW formed by the direct electrodeposition technique.*

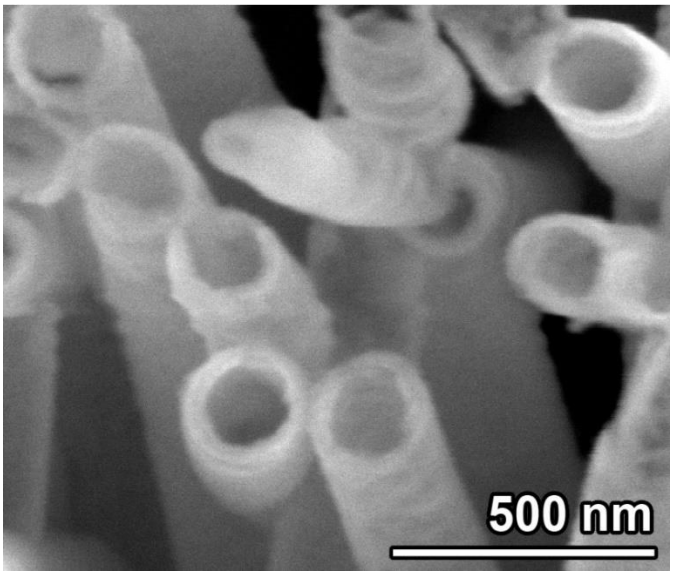

Figure S3.2. *High magnification SEM of Ni-NTNW shows the merging of the deposited Ni particles into dense nanocrystalline tubes.*

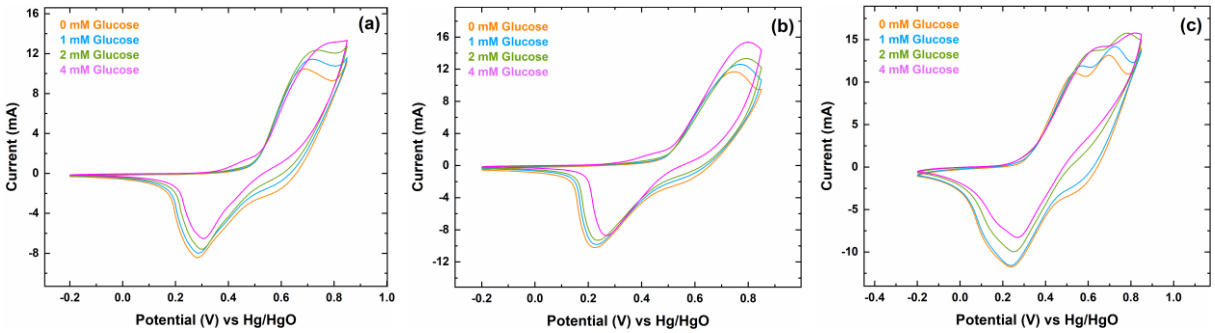

Figure S3.3. *CV curves of (a) Ni-NTNW, (b) $Ni(OH)_2$@Ni-NTNW, and (c) NiCo-LDH@Ni-NTNW in 0.1 M NaOH containing different concentrations of glucose at 10 mV s^{-1}.*

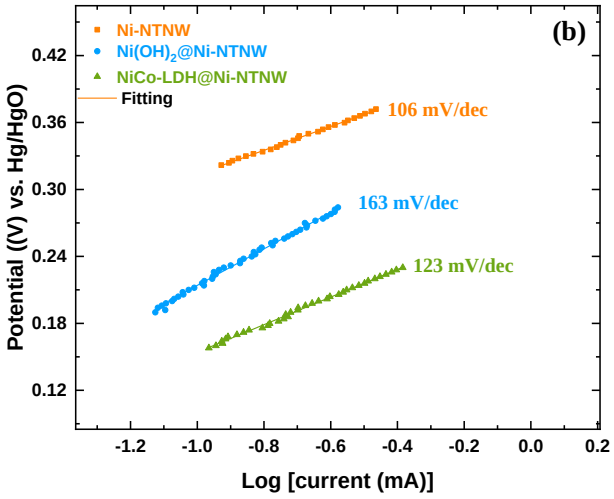

Figure S3.4. *Tafel plots of the three electrodes (electrolyte: 0.1 M NaOH containing 4 mM glucose; scan rate: 10 mV s^{-1}).*

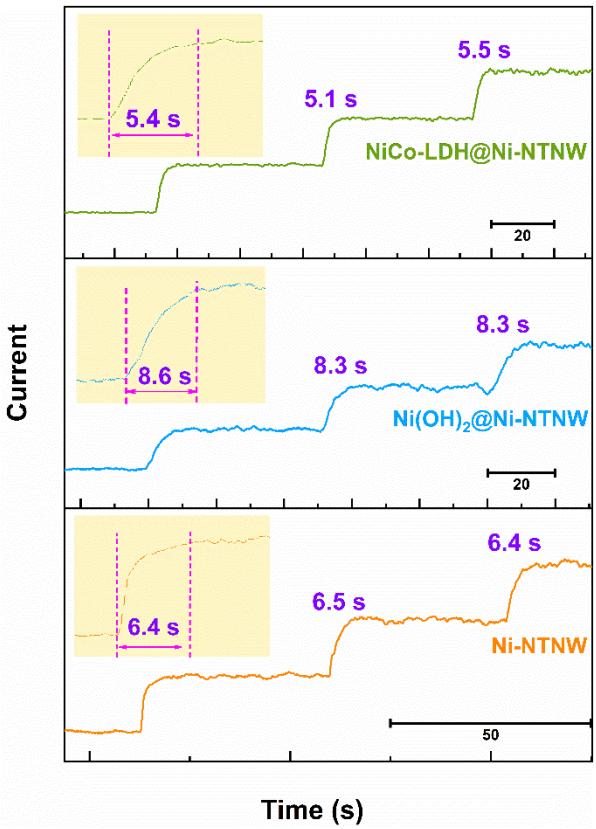

Figure S3.5. *Response time study of the different electrodes after successive step addition of 50 μM of glucose in 0.1 M of NaOH.*

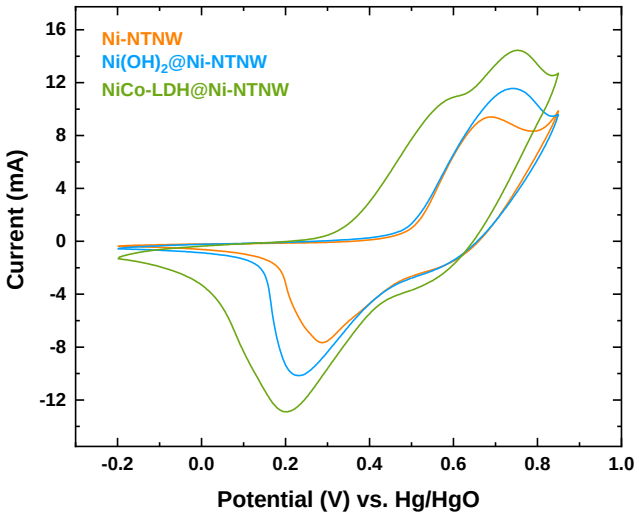

Figure S3.6. *CV curves of (a) Ni-NTNW, (b) $Ni(OH)_2$@Ni-NTNW, and (c) NiCo-LDH@Ni-NTNW in 0.1 M NaOH at 10 mV s^{-1} after performing the sensing set of measurements including different sensing cycles.*

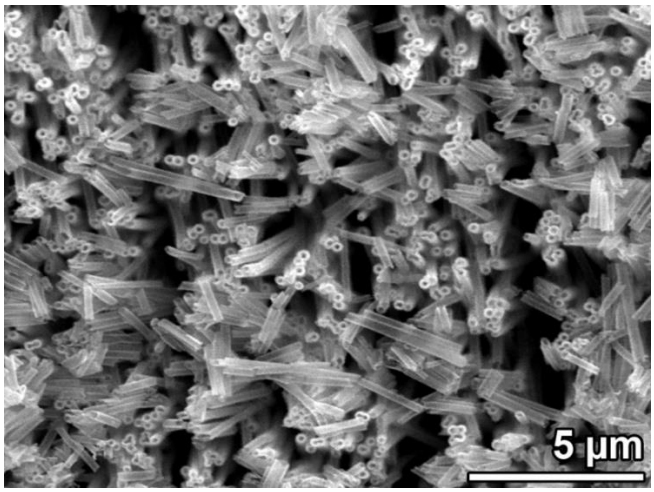

Figure S3.7. *SEM analysis of NiCo-LDH@Ni-NTNW after performing the sensing set of measurements including different sensing cycles.*

3.2. Hierarchical pipe cactus-like Ni/NiCo-LDH core-shell nanotube networks as self-supported battery-type electrode for supercapacitors with high volumetric energy density

Khaled M. Amin,* [a, b] Konrad Krois,[c] Falk Muench,[d] Bastian J. M. Etzold,[c] Wolfgang Ensinger [a]

[a] Department of Materials Science, Technical University of Darmstadt, Darmstadt 64287, Germany
[b] Department of Polymer Chemistry, Atomic Energy Authority, Cairo 11787, Egypt
[c] Ernst-Berl-Institut für Technische und Makromolekulare Chemie, Department of Chemistry, Technical University of Darmstadt, Darmstadt 64287, Germany
[d] MagnoTherm Solutions GmbH, Pfungstädter Straße 102, Darmstadt-Eberstadt 64297, Germany
* Email: amin@ma.tu-darmstadt.de

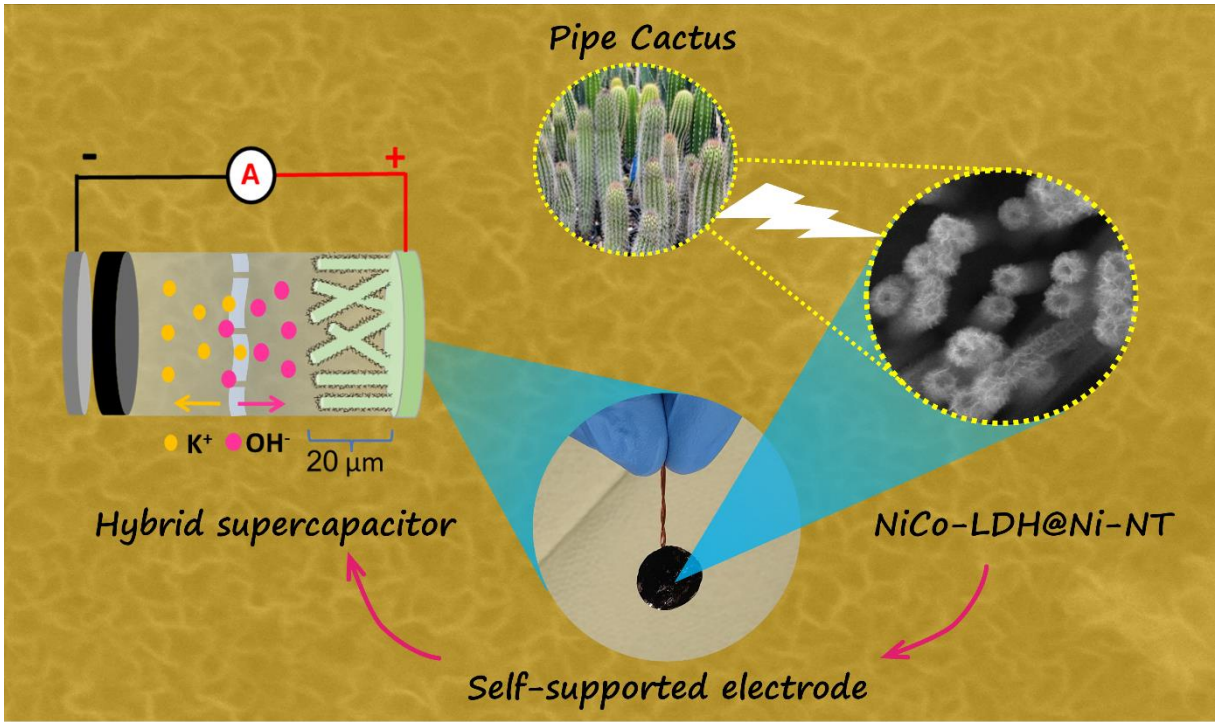

This article is reprinted from the Royal Society of Chemistry, ***Copyright (2022).***
J. Mater. Chem. A, 2022, 10, 12473-12488, **DOI:** 10.1039/D2TA00235C

Abstract:

High-performancing yet thin hybrid supercapacitors (HSC) are urgently needed to meet the increasing demands of wearable and portable electronic devices. Nevertheless, most of the current electrode designs employed to enhance the electrode capacity and conductivity provide limited volumetric capacity because they commonly rely on macroscopic, heavy support materials such as nickel foam or carbon cloth. Hence, micro- and nanostructuring strategies towards tailored electrode architectures will be vital for their utilization in practical applications. Herein, a three-dimensional (3D) self-supported hierarchical electrode was obtained by directly growing NiCo layered double hydroxide (NiCo-LDH) nanosheets on Ni nanotube network (Ni-NTNW) *via* electrodeposition. The resulting electrode takes advantages of the large interface and the high redox activity of the two-dimensional (2D) coating nanosheets, whose properties are augmented by the highly porous network architecture of the one-dimensional (1D) Ni-NTNW support, which enables fast mass transfer and acts as "highway" for fast electron transfer. The fabricated NiCo-LDH@Ni-NTNW architecture replicates the thickness of the parent template (20 μm) employed for the electroless plating of the Ni-NTNW, resulting in an ultrathin battery-type electrode with a superb volumetric capacity of 126.4 C/cm^3, remarkable rate capability, and outstanding cycling stability. Additionally, the assembled NiCo-LDH@Ni-NTNW//activated carbon (AC) HSC can deliver a high volumetric capacitance of 76.7 F/cm^3 at a current density of 1 mA/cm^2. Meanwhile, it exhibits a high energy density of 14.7 mWh/cm^3 with a maximum power density of 4769 mW/cm^3, surpassing most state-of-the-art supercapacitors that deliver high volumetric energy density. As such, hybrid core-shell nanotube networks represent an up-and-coming design paradigm for high-performance supercapacitor devices in portable devices.

Keywords:

Layered double hydroxides; nanostructured electrodes; electroless plating; electrodeposition; nanotube arrays; hybrid supercapacitor.

3.2.1. Introduction

The increasing growth in energy consumption during the last decades raised the demand for clean and renewable energy sources which in turn has excited more efforts in developing high-performance energy storage devices, particularly supercapacitors [294–296]. Supercapacitors represent one of the most promising candidates for power devices due to their outstanding power density, superior cycling stability, and fast charge-discharge rates [297,298]. However, the use of supercapacitors in practical applications is still hindered compared to lithium-ion batteries due to their low energy density [299–302]. The overall performance of a supercapacitor mainly stems from the electrode architecture and composition. Hence, ongoing efforts are focused on realizing efficient electrode materials and designs that combine outstanding power density and long lifetime with high energy density within a controlled small size [303–308]. Recent research has reported devices with high specific capacitances, but still, the challenge is to achieve high volumetric capacitance which is a pivotal parameter, especially for the application in wearable devices and smart electronics with limited space allocated for the energy source [309–312]. The traditional way to enhance the volumetric capacitance is to increase the mass loading of active material per cubic centimeter, which however comes at the cost of an increased dead mass of the electrode, because of missing electrical contact, or deterioration of contact during operation due to morphological changes or stresses breaking off parts of the material and collapse of the three-dimensional (3D) architecture, or less porous electrode layer due to more filling [309,313]. Hence, optimization of the electrode architecture is very important to maximize the performance in terms of volumetric capacitance and energy density within the same electrode geometry and without increasing the mass loading.

Supercapacitors are classified based on the energy storage mechanism of the electrode material into three classes: double-layer capacitors, pseudocapacitors, and battery-type capacitors. Among them, the battery-type capacitors have recently induced expanded attention because of their high capacities and short ion-diffusion paths [314]. Battery-type electrode materials include transition metal hydroxides, sulfides, phosphides, selenides, and oxides which have been extensively investigated as electrode materials for hybrid supercapacitors (HSC), delivering higher energy density than double-layer capacitors [315–323]. The last years witnessed a surge in employing metal layered double hydroxides (LDH), particularly NiCo-LDH as a battery-type electrode material with its layered structure, high redox activity, and outstanding anion exchange which enhance the charge storage [324,325]. Moreover, the synergy between $Ni(OH)_2$

with its high theoretical specific capacity and $Co(OH)_2$ with its good electrical conductivity plays an important role in enhancing the energy storage performance [325,326].

However, LDHs still struggle to realize their theoretical capacity due to agglomeration issues [155,184]. To overcome this weakness, the construction of a rational architecture of the electrode material is one of the most effective strategies. Developing a 3D hierarchical structure in a core-shell form can provide not only a great number of redox-active sites through the enlarged surface area, but also ensure efficient transport pathways for the electrolyte to enhance the ion transport rate. Generally, one-dimensional (1D) core structures such as nanotubes, nanowires, and nanorods offer continuous and undisturbed conduction paths and represent efficient platforms for electron transfer. In the form of interconnected 3D networks, 1D nanostructures offer increased robustness as a support layer [275], combining high electrical conductivity and enhanced mechanical robustness with an open-porous platform offering efficient paths for both mass and charge transfer, enhancing the kinetics of the redox reactions occurring on the NiCo-LDH surface [30,184]. Meanwhile, the two-dimensional (2D) nanosheets are employed as a shell with a large surface area. Such a combination of different dimensionalities brings a supportive effect of the two components, which in turn is reflected in the enhanced energy storage. Moreover, the direct growth of the active material (NiCo-LDH) over the interconnected Ni-network core can hasten the charge transfer rate because of the high conductivity of the Ni core and the strong connection between the active material and the substrate which acts as current collector without using any binders or conductive agents [184]. Compared to bulk materials, hierarchical nanostructures offer synergetic effects from individual counterparts at that multi-level architecture [327]. Several free-standing NiCo-LDH-based electrodes have been reported in different forms including nanowires, nanosheets, and microflowers, and demonstrated high electrochemical performance because of the direct contact with the current collector [155,328,329]. Nevertheless, the dimensions of the electrode are commonly defined by the dimensions of standard substrates including felts, foams, cloths, and 3D-printed materials, which have a large thickness. Consequently, most of these electrodes can achieve high gravimetric capacities but limited volumetric capacity and energy density which is crucial for portable and wearable devices. While nanotube network structures share general features with conventional conductive substrates (both constitute 3D highly porous interconnected frameworks composed of conductive materials), structural differences include the hollow nature of nanotubes and their straight orientation. The most striking difference, though, is their nanoscale. Accordingly, a suitable fabrication strategy is pivotal for realizing a device that fulfills these requirements in a cost-effective way. Tailoring a hierarchical structure at the nanoscale accompanied by

decoration with an electroactive material can address different functionality aspects including high diffusion rates through these nanoreactors [184,190,242].

Herein, inspired by the natural world, we demonstrate a new feasible strategy to fabricate a stand-alone hierarchical NiCo-LDH@Ni-NTNW heterostructure that imitates the structure of the pipe cactus plant as a new generation of ultrathin electrodes for HSC that resolves the above issues (Figure 3.10). Our approach employs facile and tunable methods for electrode fabrication, namely electroless plating for synthesizing the Ni-NTNW core, and electrodeposition for decorating the nanostructured electrode network with a shell of electroactive NiCo-LDH nanosheets. The proposed strategy is based on scalable and cost-effective techniques which can be adopted for developing different nanotube-based architectures. The as-prepared battery-type NiCo-LDH@Ni-NTNW electrode was encompassed with activated carbon (AC) in a HSC device with outstanding performance. In turn, the assembled device demonstrated high volumetric capacitance, high rate capability, and excellent cycling stability. More importantly, it delivers an ultrahigh volumetric energy density of 14.7 mWh/cm^3. The introduced fabrication approach holds important promise in realizing a new generation of ultrathin electrodes with high volumetric energy density for practical applications.

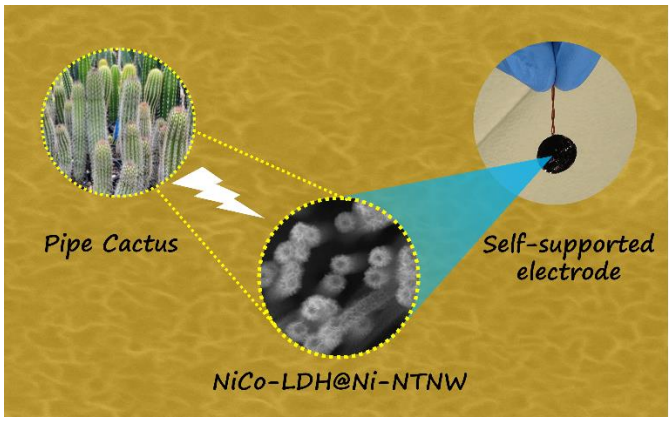

Figure 3.10. *Pipe cactus-inspired design philosophy of the NiCo-LDH@Ni-NTNW self-supported electrode.*

3.2.2. Experimental section

3.2.2.1. Materials

Polycarbonate membranes (Whatman, nominal thickness 20 μm) with a nominal pore diameter of 200 nm and a pore density of 5×10^8 cm^{-2}. Nickel sulfate heptahydrate ($NiSO_4 \cdot 7H_2O$, purum

p.a. cryst., Sigma- Aldrich), borane dimethylamine complex ($(CH_3)_2NH.BH_3$, 97%, Sigma-Aldrich), potassium chloride (KCl, ≥99.0%, Sigma,), dichloromethane (CH_2Cl_2, puriss. p.a., Sigma-Aldrich), potassium hydroxide (KOH, Sigma-Aldrich), boric acid (H_3BO_3, 99.5%, Sigma), nickel nitrate hexahydrate ($Ni(NO_3)_2 \cdot 6H_2O$, GR, Merck), cobalt nitrate hexahydrate ($Co(NO_3)_2 \cdot 6H_2O$, 99+%, Acros Organics), palladium chloride ($PdCl_2$, 99.9% metal basis, Alfa Aesar), trifluoroacetic acid (TFA) (CF_3COOH, ≥99.9%, Carl Roth), trisodium citrate dihydrate ($HOC(COONa)(CH_2COONa)_2.2H_2O$, puriss. p.a., Sigma-Aldrich), methanol (CH_3OH, 99.5%, AppliChem Panreac), activated carbon (AC) YP-80f (Kuraray Europe GmbH, Finland), Polytetrafluorethylen (PTFE, 60 wt% dispersion in H_2O, Sigma-Aldrich), and carbon black (CB) (Imerys, C-NERGY™ SUPER C65). All chemicals were used as received without any further purification. Deionized H_2O (Milli Q, >18 MΩ cm) was used in all processes.

3.2.2.2. Fabrication of self-supported Ni-NTNW electrode

Ni-NTNW self-supported electrode was prepared *via* template-assisted electroless plating (EP), followed by electrodeposition [184]. Briefly, ion track-etched polycarbonate membranes were exposed to three successive runs of sensitization and activation for 30 and 4 min, respectively. The templates were firstly soaked in the sensitization bath (42 mM $SnCl_2$ and 71.4 mM TFA in ethanol) then transferred to the activation bath (11.3 mM $PdCl_2$ and 33.9 mM KCl). In the Pd solution, the templates turn brown, indicating the deposition of Pd nanoparticles. After washing, the activated templates were immersed in the EP bath which contains 100 mM $NiSO_4.7H_2O$, 100 mM trisodium citrate dihydrate, and 100 mM borane dimethylamine for around 40 min until a shiny layer of Ni appeared on the outer surface of the template. After the electroless plating, the templates were thoroughly washed with water.

In order to reinforce one side of the template with a supporting layer of Ni, electrodeposition was employed using a Ni electrolyte containing 0.5 M $NiSO_4.7H_2O$ and 0.5 M H_3BO_3 and applying a constant potential of -1 V vs. Ag|AgCl. Afterwards, the thin Ni surface layer on the other side stemming from EP was removed *via* swapping with aqua regia. Finally, the polymer matrix was dissolved with dichloromethane to achieve full exposure of the NTNW and obtain a self-supported Ni-NTNW electrode.

3.2.2.3. Growth of NiCo-LDH nanosheets over Ni-NTNW electrodes

Hierarchical NiCo-LDH @Ni-NTNW electrode was prepared by further electrodeposition of NiCo-LDH nanosheets onto the Ni-NTNW parent electrode. Pulsed electrodeposition was employed using a 1:1 molar mixture containing 0.05 M $Co(NO_3)_2 \cdot 6H_2O$ and 0.05 M

$Ni(NO_3)_2 \cdot 6H_2O$ as electrolyte and applying -1 V vs. Ag|AgCl for 120 s separated by pulses of +1 V vs Ag|AgCl for 0.5 s every 3 s. Finally, the samples were thoroughly washed with water. The mass of Ni-NTNW and NiCo-LDH nanosheets was estimated by weighing the template after each step of the preparation procedure. The average mass loadings (estimated from different samples) of the Ni-NTNW and NiCo-LDH nanosheets were 1.87 and 0.42 mg/cm^2, respectively.

3.2.2.4. Fabrication of NiCo-LDH @Ni-NTNW//AC HSC

The HSC was assembled in a two-electrode Swagelok®- cell. The HSC was packed in a sealed assembly by face-to-face sandwiching the hierarchical NiCo-LDH@Ni-NTNW as a positive electrode and self-standing AC sheet (90 wt% AC, 5 wt% CB, 5 wt% PTFE) as a negative electrode, separated by a filter paper (EDLC 20-30 TC from SWM company) soaked in 1 M KOH. The mass of NiCo-LDH@Ni-NTNW (m^+) and AC (m^-) electrodes was balanced based on the charge balance according to the following equations [330]:

$$q^+ = q^- \qquad \text{(Eq. 3.11)}$$

$$C^+ m^+ \Delta V^+ = C^- m^- \Delta V^- \qquad \text{(Eq. 3.12)}$$

where C^+ and C^- represent the specific capacitance of NiCo-LDH@Ni-NTNW and the AC, respectively, and ΔV^+ and ΔV^- stand for the potential window of NiCo-LDH@Ni-NTNW and AC electrodes, respectively. The average total mass of the positive (NiCo-LDH layer) and negative (AC sheet) electrodes was calculated to be about 4.6 mg. The overall thickness of NiCo-LDH@Ni-NTNW//AC HSC including the two electrodes and the separator was calculated to be about 90 µm (20 µm NTNW + ~30 µm filter paper + ~40 µm AC).

3.2.2.5. Materials characterization

Scanning electron microscopy (SEM) was performed by using a Philips XL30 FEG with acceleration voltages of 10-30 kV. X-ray diffraction (XRD) measurements were conducted using a Seifert PTS 3003 diffractometer equipped with a Cu anode in Bragg-Brentano geometry, an X-ray mirror built-in on the primary side, and a long Soller-slit and graphite monochromator on the secondary side to separate the Cu Kα-line (40 kV/40 mA). Raman spectra were obtained by a Horiba LabRam HR 800 Raman spectrometer with an excitation light of ~ 514 nm. Transmission electron microscopy (TEM) micrographs were collected using a FEI CM20 (LaB_6 cathode, 200 kV acceleration voltage) accompanied with an energy dispersive X-ray analysis (EDX) unit.

3.2.2.6. Electrochemical experiments

The electrodeposition of Ni supporting layer was performed in a three-electrode setup containing a circular piece (12 mm diameter) of the electrolessly plated polymer membranes as the working electrode; Ag|AgCl as the reference electrode; and a Pt spiral wire as the counter electrode using a Keithley 2602 System SourceMeter unit. The electrodeposition of NiCo-LDH nanosheets was achieved using the previously prepared Ni-NTNW as working electrodes under the same conditions.

The electrochemical experiments were conducted using OctoStat5000 (Ivium Technologies) electrochemical workstation and Gamry Reference 600 potentiostat. For electrochemical characterization of Ni-NTNW and NiCo-LDH@Ni-NTNW electrodes including cyclic voltammetry (CV), galvanostatic charge-discharge (GCD), and electrochemical impedance spectroscopy (EIS) measurements, a typical three-electrode setup was employed using a Pt spiral as a counter electrode, Hg|HgO filled with 1 M KOH as a reference electrode (140 mV versus the standard hydrogen electrode), and a circular self-supported NTNW (11 mm diameter after insulating the backside), connected to a Cu wire, as a working electrode. 1 M KOH was used as an electrolyte throughout all measurements. CV was measured in a potential window between 0 and 0.6 V (vs. Hg|HgO), and GCD was performed between 0 and 0.5 V (vs. Hg|HgO). EIS was conducted with open circuit potential in the frequency range between 0.01 Hz and 100 kHz combined with a 10 mV disturbing signal.

The gravimetric, areal, and volumetric capacities of the electrodes in the three-electrode cell were estimated from the CV curves according to the following formulas [331]:

$$q_m = \frac{1}{2 \times \nu \times m} \int I \, dV \quad \text{or} \quad q_a = \frac{1}{2 \times \nu \times A} \int I \, dV \quad \text{or} \quad q_d = \frac{1}{2 \times \nu \times d} \int I \, dV \qquad \text{(Eq. 3.13)}$$

where q_m (C/g) is the gravimetric capacity, q_a (C/cm^2) is the areal capacity, q_d (C/cm^3) is the volumetric capacity, $\int I\,dV$ represents the integrated area of the entire CV curve, m (g), A (cm^2), and d (cm^3) are the mass, area, and volume of the active material, respectively, and ν (V/s) is the scan rate.

They were also calculated from GCV curves according to the following equation [332]:

$$q_m = \frac{I \times \Delta t}{m} \quad \text{or} \quad q_a = \frac{I \times \Delta t}{A} \quad \text{or} \quad q_d = \frac{I \times \Delta t}{d} \qquad \text{(Eq. 3.14)}$$

where I (A) represents the discharge current, Δt (s) is the discharge time.

The gravimetric, areal, and volumetric capacitances, energy density, and power density of the active materials in the two-electrode setup were calculated using the stepwise integration of the following equation [143,333]:

$$C_m = \frac{I}{m}\int \frac{1}{V}\, dt \quad \text{or} \quad C_a = \frac{I}{A}\int \frac{1}{V}\, dt \quad \text{or} \quad C_d = \frac{I}{d}\int \frac{1}{V}\, dt \qquad \text{(Eq. 3.15)}$$

$$E_m = \frac{I}{m \times 3.6}\int V\, dt \quad \text{or} \quad E_a = \frac{I}{A \times 3600}\int V\, dt \quad \text{or} \quad E_d = \frac{I}{d \times 3600}\int V\, dt \quad \text{(Eq. 3.16)}$$

$$P = \frac{E \times 3600}{\Delta t} \qquad \text{(Eq. 3.17)}$$

where C_m (F/g) is the gravimetric capacitance, C_a (F/cm^2) is the areal capacitance, C_d (F/cm^3) is the volumetric capacitance. C_d of the HSC device was estimated using the total thickness of the HCS including the AC and the separator, not only the thickness of the electrode. E_m (Wh/kg) is the gravimetric energy density, E_a (Wh/cm^2) is the areal energy density, E_d (Wh/cm^3) is the volumetric energy density, and P is the power density (i.e., gravimetric, areal, or volumetric power density).

3.2.3. Results and Discussion

Our 3D-NTNW is characterized by interconnected dense arrays of nanotubes replicating the initial density and intersections of the nanochannels in the used ion track-etched polycarbonate membranes. The process of Ni electroless plating demands a large enough areal density of metal seeds uniformly distributed over the inner surface of the template pores to initiate the autocatalytic Ni-plating process and obtain continuous and homogenous deposition on the inner template surfaces. The seeding process includes sensitization and activation of the templates, where Sn^{2+} ions are electrostatically attached to the polymer template surface from the sensitization bath and employed to reduce the Pd^{2+} ions from the activation bath forming metallic Pd nanoparticles which are adsorbed on the template surface and act as seeds for the later plating process [57]. Electroless plating was employed as a simple technique to grow a uniform layer of Ni nanoparticles inside the seeded pores and over the outer surface. The plating process is accompanied by hydrogen evolution which decreases gradually with the decrease of deposition rate until a shiny film of Ni completely covers the template and blocks access to the inner surface of the pores as indicated in the first step in Figure 3.11.

A new approach has been developed *via* hierarchical functionalization to achieve a flexible paradigm of free-standing electrodes that can be adopted to decorate the NTNW with different active materials for different applications. In order to fabricate such a free-standing nanostructured electrode, the Ni-NTNW was reinforced with a back layer of Ni to work as a mechanically robust layer that carries the Ni-NTNW and can be easily connected to the potentiostat using a copper wire. Electrodeposition was employed to form a uniform layer of Ni over one side of the electrolessly-plated membrane forming a silver shiny layer of Ni supporting layer (step 2 in Figure 3.11). Such an approach offers a robust integrated design of

the electrode that enhances the conductivity and can be easily handled without damage. Afterwards, the thin surface layer plated on the other side during the electroless plating step was chemically etched (step 3 in Figure 3.11) to fully expose the Ni-NTNW and facilitate the dissolution of the polymer matrix using dichloromethane, which in turn enhances the accessibility of electrolyte to the active sites of the Ni-NTNW. As a result, only the central supported area remained intact while the surrounding area of NTNW was separated (step 4 in Figure 3.11).

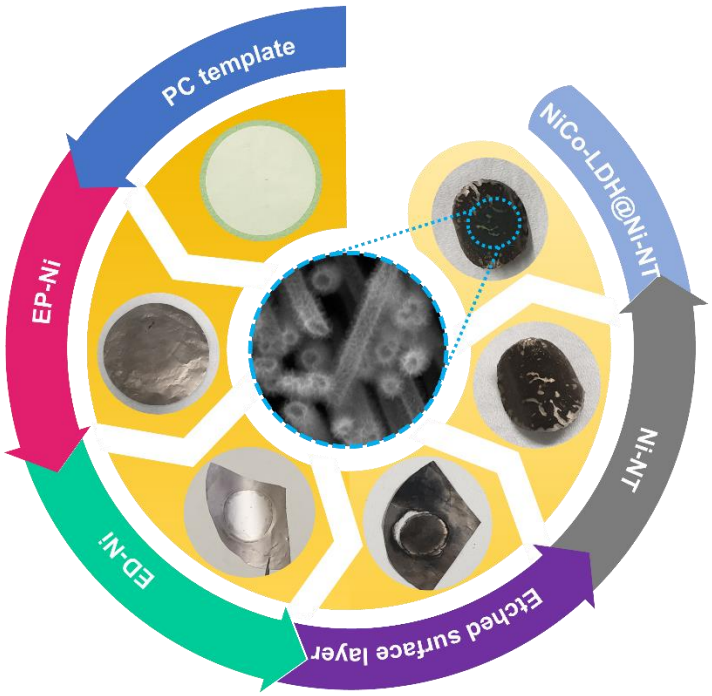

Figure 3.11. *Schematic illustration presenting photographs of the self-supported NiCo-LDH@Ni-NTNW electrode through the fabrication process. After electroless plating of Ni (step1), electrodeposition is conducted (step 2) to get a thicker supporting layer of Ni on one side of the template (the bright round area in the sample center). In step 3, the other side of the sample is chemically etched to eliminate the electrolesssly deposited surface layer, followed by dissolution of the polymer matrix to isolate the Ni-NTNW (step 4). The final NiCo-LDH@Ni-NTNW electrode is obtained by electrodeposition of LDH (step 5).*

The Ni-NTNW was further decorated with NiCo-LDH nanosheets *via* pulsed electrodeposition to obtain a modified NiCo-LDH@Ni-NTNW core-shell nanostructure (step 5 in Figure 3.11). The single-step electrodeposition of NiCo-LDH includes the electrochemical reduction of nitrate ions and the consequent production of hydroxyl ions which afterward react with the existing Ni^{2+} and Co^{2+} ions in the electrolyte forming NiCo-LDH nanoflakes over Ni-NTNW [334]. The as-prepared NiCo-LDH@Ni-NTNW acts as a self-supported electrode where NiCo-

LDH nanosheets are grown over the interconnected Ni nanotube array which keeps the whole structure attached to the back supporting layer. Such a well-designed electrode architecture comprises a 3D interconnected porous network that enables high accessibility of the electrolyte and a highly conductive metal core that accelerates the electron transfer acting as a binder-free current collector. Meanwhile, the NiCo-LDH nanosheets offer numerous numbers of electroactive sites.

The morphology of the nanostructured integrated electrode was explored using SEM (Figure 3.12). The top view of the pristine Ni-NTNW (Figure 3.12a, b) shows uniform nanotubes with a diameter of around 200 nm reflecting the original diameter of the nanopores in the used polycarbonate templates. The lateral view of Ni-NTNW (Figure 3.12c) confirms the conformal deposition during the electroless Ni plating, resulting in intact and homogenous Ni nanotubes replicating the whole pores of the parent templates. This nanotube array has a free-standing interconnected structure (Figure 3.12c) due to the frequent intersections between the tubes, forming a highly conductive 3D metallic core which in turn acts as an efficient current collector.

As for the NiCo-LDH@Ni-NTNW electrode displayed in Figure 3.12d and e, the NiCo-LDH nanosheets covering the Ni-NTNW skeleton can be easily distinguished due to their wrinkled structure. As result, a core-shell architecture is obtained in which the NiCo-LDH nanosheets evenly cover the nanotube support while still maintaining the features of the Ni-NTNW backbone. This structural motif is characterized by a firm connection of the nanosheets to the metal core and the homogenous covering across the whole surface of the Ni-NTNW, providing good mechanical and electrical contact (Figure 3.12f). The employed deposition time represents a compromise between a high amount of NiCo-LDH as redox-active material to boost the energy density while keeping the porous structure of the catalyst with its torturous pathways free from clogging [184], which facilitates the accessibility of the electrolyte to the active sites on the tubes, resulting in a great contribution to the reversible and fast Faradaic reactions and an enhanced capacity of the electrode [335,336]. The successful incorporation of NiCo-LDH was further confirmed by EDX measurements performed on the large area lateral view of the as-prepared Ni-NTNW and NiCo-LDH@Ni-NTNW as shown in Figure 3.12 c and f, respectively. The EDX spectrum of Ni-NTNW shows only the peaks of Ni which are assigned to Ni-Kα, and Ni-Kβ at ~7.4 and 8.2 KeV, respectively [337], while that of NiCo-LDH@Ni-NTNW shows an additional characteristic peak for Co which is assigned to Co-Kα at ~6.9 KeV besides the Ni peaks, confirming the presence of Ni as well as Co content. These findings are consistent with SEM observations and further confirm the successful deposition of NiCo-LDH nanosheets on

the Ni-NTNW core structure. From the EDX spectrum of the NiCo-LDH@Ni-NTNW, the atomic ratio of Ni:Co is 41:12 and the mass ratio is 59:17. The atomic ratio of Ni is higher than that of Co due to the great contribution of the Ni-NTNW as the percentage of the NiCo-LDH represent around 18% of the NiCo LDH@Ni-NTNW total mass.

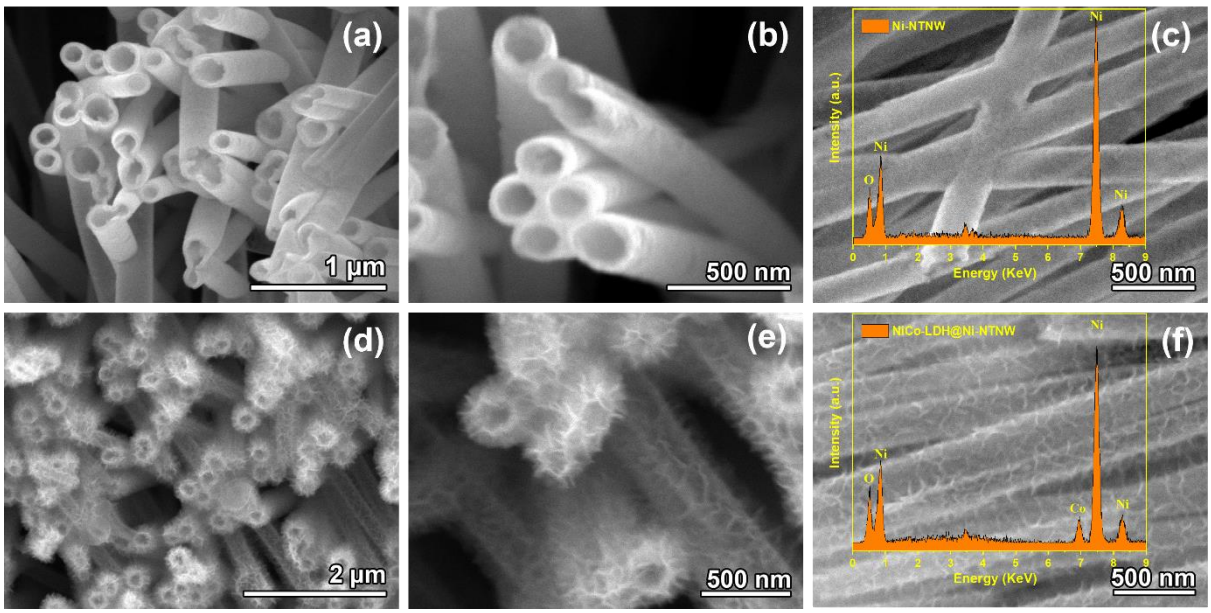

Figure 3.12. *SEM top view of Ni-NTNW (a, b) and NiCo-LDH@Ni-NTNW (d, e). SEM lateral view with EDX spectra of Ni-NTNW (c) and NiCo-LDH@Ni-NTNW (f).*

The crystalline structure of Ni-NTNW and NiCo-LDH@Ni-NTNW was investigated using XRD. As represented in Figure 3.13a, both electrode materials display intense and sharp diffraction peaks at 44.4°, 51.9°, and 76.3° which well correspond to the (111), (200), and (220) crystalline planes of face-centered cubic Ni, respectively [184]. These peaks can be assigned to the metallic Ni-NTNW core. The broad diffraction peak in between 15-35° can be assigned to the used glass [338]. As we can see in the XRD pattern of NiCo-LDH@Ni-NTNW, some new wide characteristic peaks appear (distinguished with black label) which match well with the hydrotalcite-like NiCo-LDH phase (JCPDS 40-0216), confirming that NiCo-LDH has been successfully grown over the nanotube network [271,339]. The reflexes of this hydrotalcite-like structure have weak intensities (compared to those of metallic Ni core) due to the weak crystallinity and ultrathin structure of the NiCo-LDH nanosheets [184]. Raman spectroscopy was employed to assure the loading of NiCo-LDH and investigate the chemical structure of NiCo-LDH@Ni-NTNW (Figure 3.13b). The spectrum shows two characteristic peaks at 461 and 527 cm^{-1}, which can be assigned to the vibrational modes of Ni-O and Co-O confirming the findings from the XRD measurement [340,341].

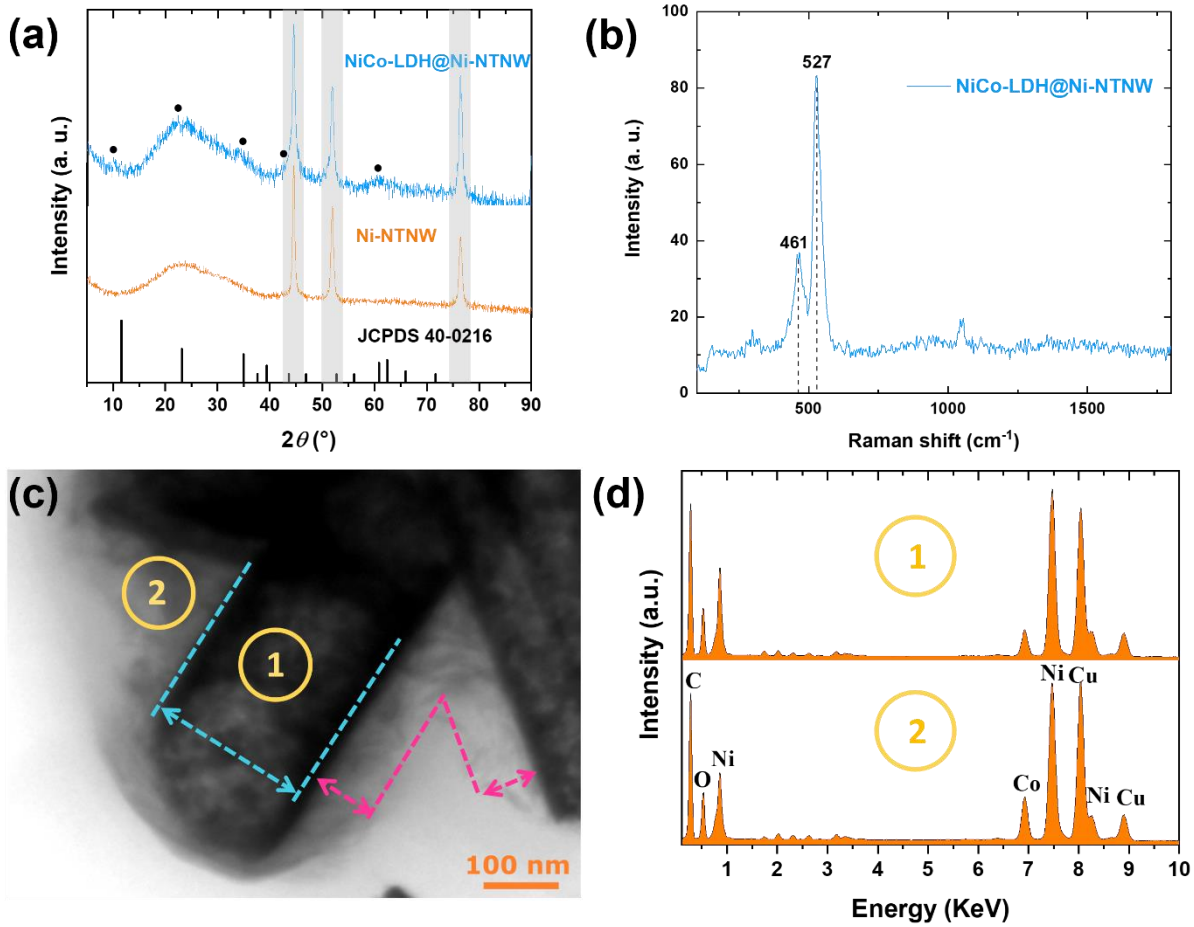

Figure 3.13. *(a) XRD patterns of Ni-NTNW, NiCo-LDH@Ni-NTNW, and the reference peaks of the JCPDS file No. 40-0216. (b) Raman spectrum of NiCo-LDH@Ni-NTNW, (c)TEM lateral view of NiCo-LDH@Ni-NTNW with a dashed turquoise line representing the borders of the core Ni-NTNW and dashed rose color representing the surrounding NiCo-LDH shell, and (d) EDX spectra at two different spots in the TEM micrograph representing the center of the tube (position 1) and the center of NiCo-LDH coating nanosheets (position 2).*

The hierarchical structure of the as-prepared electrode has been explored with TEM accompanied with EDX. Figure 3.13c shows the TEM micrograph of NiCo-LDH@Ni-NTNW, in which the core Ni network appears darker than the surrounding NiCo-LDH shell. The Ni-NTNW is composed of fine nanoparticles which are reflected in the homogenous and uniform structure of the tubes without any gaps. The deposition of the NiCo-LDH nanosheets with their flaky morphology can be observed covering the Ni-NTNW from all sides. Elemental analysis was conducted for the core and shell of the NiCo-LDH@Ni-NTNW composite (distinguished by positions 1 and 2, in Figure 3.13c, respectively) and the corresponding spot EDX spectra are represented in Figure 3.13d. As it can be seen, the spectrum collected at the surrounding shell at position 2, which contains the NiCo-LDH nanosheets, reveals a higher Co-to-Ni ratio compared to the center of the Ni-NTNW (position 1), which is attributed to the contribution of

the additional Ni content from the walls of the core nanotubes under the covering NiCo-LDH sheets. The EDX spectra confirm the well-defined hierarchical structure of the NiCo-LDH@Ni-NTNW electrode with homogenous distribution of the LDH on the core Ni tubes which is consistent with the findings from the SEM, XRD, and Raman measurements.

To evaluate the electrochemical performance of the as-prepared Ni-NTNW and NiCo-LDH@Ni-NTNW composites as efficient positive electrodes for HSC, different electrochemical techniques including CV, GCD, and EIS have been employed as represented in Figure 3.14. A three-electrode cell was used to monitor the behavior of the self-supported electrodes. As shown in Figure 3.14a, the prepared electrodes which are soldered to a Cu wire are directly soaked in the electrolyte solution and can be easily connected to the potentiostat without any need for binders or supporting electrodes, which are commonly used to carry the active material. CV curves of the Ni-NTNW and NiCo-LDH@Ni-NTNW electrodes were recorded in the potential window between 0 and 0.6 V (vs. Hg/HgO) at a scan rate of 10 mV/s, indicating a typical battery-like behavior with pairs of distinct redox peaks that originate from the Faradaic reactions of OH^- ions with $Ni(OH)_2$ in case of Ni-NTNW electrode, and with $Ni(OH)_2$ and $Co(OH)_2$ in case of NiCo-LDH@Ni-NTNW electrode (Figure 3.14b). The displayed peak pair of Ni-NTNW can be corresponded to the Ni^{2+}/Ni^{3+} conversion, while NiCo-LDH@Ni-NTNW exhibits two oxidation peaks corresponding to Co^{2+}/Co^{3+} and Co^{3+}/Co^{+4} conversions according to the following equations [184,298]:

$$Ni(OH)_2 + OH^- \rightarrow NiO(OH) + H_2O + e^- \qquad (Eq.\ 3.18)$$

$$Co(OH)_2 + OH^- \rightarrow CoO(OH) + H_2O + e^- \qquad (Eq.\ 3.19)$$

$$CoO(OH) + OH^- \rightarrow CoO_2 + H_2O + e^- \qquad (Eq.\ 3.20)$$

It is apparent in Figure 3.14b that NiCo-LDH@Ni-NTNW electrode demonstrates much larger peak current densities and greater integrated area under the CV curves compared to the Ni-NTNW electrode, indicating enhanced electrochemical activity and higher storage capacity, albeit the surface of the Ni backbone itself also contributes to the redox activity to a minor extent. Comparing the CV curves of both electrodes at different scan rates, namely 20 and 50 mV/s, demonstrated the same behavior as shown in Figure S3.8, confirming the enhanced capacity offered by the NiCo-LDH@Ni-NTNW electrode. This can be attributed to the larger surface area introduced upon decorating the core Ni nanotubes with the NiCo hydroxide layer which in turn is reflected in the number of the available active sites on the surface and the better exposure to the electrolyte. Moreover, the reversibility of NiCo-LDH@Ni-NTNW electrode was enhanced due to the Co doping, which is vital for improving the Coulumbic efficiency and

utilization of the electrode. CV curves of the NiCo-LDH@Ni-NTNW electrode were recorded within the potential window of 0-0.6 V (vs. Hg/HgO) at different scan rates between 2 and 100 mV/s (Figure 3.14c) and the redox peaks at different scan rates confirmed the same battery-like behavior of the electrode with a clear increase in the peak current and a shift in the positive and negative directions for the anodic and cathodic peaks, respectively, upon increasing the scan rate due to the internal resistance of the electrode or polarization [342]. As it can be seen in Figure 3.14c, the NiCo-LDH@Ni-NTNW electrode shows clear redox peaks at different scan rates because of the rapid electron transfer through the hierarchical structure which is confirmed by the linear fitting of the peak current vs. the square root of the scan rate (Figure 3.14d). For comparison, the cyclic voltammograms were recorded for the Ni-NTNW electrode at the same scan rates (Figure S3.9) and revealed the same battery-like behavior at all scan rates with good electrochemical reversibility which is further evidenced by the direct proportion between the peak currents and the square root of the scan rate (Figure S3.10). The volumetric and gravimetric capacities of both electrodes (Figure 3.14e) have been estimated from the corresponding CV curves at different scan rates. There is a slight change between the capacities estimated from CV curves and those calculated from GCD measurements because the accumulated area under CV curves includes a small contribution from oxygen evolution reaction which results in higher capacities. The NiCo-LDH@Ni-NTNW electrode showed much higher volumetric and gravimetric capacities compared to the Ni-NTNW electrode at all scan rates as seen in Figure 3.14e. It is worth mentioning that the main advantage of our electrode design is its ultrathin thickness (20 μm) imitating the thickness of the parent template as shown in the cross-sectional micrograph of the electrode (Figure S3.11), which is clearly reflected in its exceptional volumetric capacity. At 2 mV/s, the NiCo-LDH@Ni-NTNW electrode revealed a capacity of 171 C/cm^3 which is about 7 times as much as the corresponding value of Ni-NTNW (23.7 C/ cm^3). Moreover, at a high scan rate of 50 mV/s, the NiCo-LDH@Ni-NTNW electrode still retains a high capacity of 97.4 C/cm^3 which represents around 56 % of that at 2 mV/s for the same electrode. The demonstrated huge volumetric capacity opens the door for this ultrathin hierarchical design to be used in different applications which have dimensional limitations such as portable electronics and wearable devices. Moreover, the thickness of the NTNW could be controlled to boost the capacity. Larger thicknesses up to about 60 μm can be realized with ion track etching or through the preparation of bulky nanowire aerogels [343,344]. NiCo-LDH@Ni-NTNW electrode exhibited much higher gravimetric capacity (Figure 3.14e) and areal capacity (Figure S3.12) in comparison with the Ni-NTNW electrode

at all scan rates. These findings prove that the capacitive properties are significantly improved *via* the synergistic effect of the decoration with NiCo-LDH nanosheets.

GCD measurements for Ni-NTNW and NiCo-LDH@Ni-NTNW electrodes were conducted between 0-0.5 V (vs. Hg/HgO) at different current densities ranging from 0.2 to 50 mA/cm^2 (Figure S3.13 and S3.14, respectively). The GCD curves of both electrodes reveal nonlinear charge and discharge behaviors at all current densities implying that the dominant capacitive behavior is of battery type which is consistent with the results from CV measurements and the literature-known properties of redox-active Ni LDHs [155,328]. It is also clear in the GCD curves of both electrodes that they have approximately similar charge and discharge times which in turn indicates high Coulombic efficiency and thus that the charge-discharge process is reversible [328]. GCD processes of Ni-NTNW and NiCo-LDH@Ni-NTNW electrodes at a current density of 0.2 mA/cm^2 are represented in Figure 3.14f, and as shown the NiCo-LDH@Ni-NTNW electrode demonstrates a much longer discharge time (1116 s) compared to the Ni-NTNW (147 s) which reflects the higher capacity offered by this improved electrode design. The same discharge behavior was observed at a current density of 0.5 mA/cm^2 (Figure S3.15). The areal and gravimetric specific capacities (Figure 3.14g) were obtained from the discharge part of GCD curves of Ni-NTNW (Figure S3.13) and NiCo-LDH@Ni-NTNW (Figure S3.14) electrodes at different current densities. The gravimetric and areal capacities of NiCo-LDH@Ni-NTNW at a current density of 0.2 mA/cm^2 reached 601.1 C/g (=1202.2 F/g) and 0.25 C/cm^2, respectively, compared to 17.3 C/g and 0.032 C/cm^2 for Ni-NTNW at the same current density. The calculated gravimetric and areal capacities of Ni-NTNW are much lower and incomparable to those of NiCo-LDH@Ni-NTNW at all current densities. More importantly, the NiCo-LDH@Ni-NTNW electrode was able to offer a superior volumetric capacity which can be attributed to the thin-layered hierarchical structure (20 μm) enriched with active sites and the enhanced charge transfer due to the improved electrical conductivity arising from valence interchange or charge hopping between the Ni and Co cations [345]. As displayed in Figure 3.14h, the NiCo-LDH@Ni-NTNW electrode achieved a high capacity of 66 C/cm^3 (=132 F/cm^3) at a high current density of 20 mA/cm^2, retaining 53% of the initial capacity at 0.2 mA/cm^2 (126.4 C/cm^3, corresponding to 252.8 F/cm^3) which implies high rate capability. It is important to highlight that the main advantage of our 3D porous architecture is that it offers a much higher interior surface area compared to other substrates like Ni foams or fibers. This principle is evidenced by the values of volumetric capacity of our NiCo-LDH@Ni-NTNW electrode which was 2.5-fold that of NiCo LDH/3D-Ni electrode (13.56 mAh/cm^3) at 0.5 mA, which is based on thick Ni wires as a substrate, as recently reported in ref [346]. The outstanding

volumetric capacities of our NiCo-LDH@Ni-NTNW electrode are markedly superior and surpass most of the recently reported NiCo-based battery-type electrodes, moreover, it delivers higher/comparable gravimetric and areal capacities as presented in Table S3.1.

Consequently, it is concluded that these remarkable capacitive properties of the NiCo-LDH@Ni-NTNW electrode are linked to the unique hierarchical design of the electrode with its 3D nanostructured core-shell architecture. The electrode kinetics was investigated by EIS measurements for both electrodes. As represented in the inset of Figure 3.14i, the Nyquist plot of NiCo-LDH@Ni-NTNW electrode reveals a semicircle with a smaller diameter compared to Ni-NTNW in the high-frequency region, suggesting a lower charge transfer resistance during the electrochemical reaction due to the inclusion of Co into the NiCo-LDH which leads to the formation of that conductive CoOOH during the discharging process, resulting in the increase of electrode conductivity [347]. Moreover, it shows a slightly steeper line compared to Ni-NTNW in the low-frequency region, indicating a fast ion diffusion process that enhances the capacitive behavior of the electrode [300,348]. The cyclic stability is one of the most important factors for evaluating the overall performance of the electrode in the different applications. The as-prepared NiCo-LDH@Ni-NTNW electrode exhibited outstanding cyclic stability. Over the course of 4000 cycles at a current density of 20 mA/cm^2, the capacity not only did not decline but even slightly increased to 106%, while the Coulombic efficiency fluctuated around 98% (Figure 3.14i). This indicates that a small amount of active sites in the 3D porous hierarchical structure are gained after starting the operation of the device, which could be attributed to an electrochemical restructuring of the LDH layer, or superficial oxidation of the Ni nanotubes. This introduced interconnected porous structure can effectively compensate for the volume expansion of electrode materials [349]. Cycling of Ni-NTNW electrode showed a sudden increase during the first cycles then gradually decreased (Figure S3.16) which may be attributed to the self-activation of the electrode material that grants increased diffusion of the electrolyte into the interior spaces of the Ni network which in turn activates the pseudo-capacitive process [349,350]. Post-analysis of the electrode surfaces confirmed the stability of the electrodes after cycling as demonstrated in the SEM micrographs (Figure S3.17). SEM showed that both the Ni-NTNW and the decorating hydroxide layer remain intact after running the cycling test and the accompanied EDX spectra confirmed the elemental composition of the electrodes (Figure S3.17). Based on the previously mentioned characteristics and the enhanced performance of the NiCo-LDH@Ni-NTNW electrode, namely high capacity, elevated redox activity, and enhanced cyclic stability, the self-supported hierarchical structure is assumed to offer different merits during the electrochemical process including (i) novel highly-porous interconnected structure

with high ion diffusion rate, (ii) efficient metallic pathways through the Ni core that offer high conductivity and fast charge transfer, (iii) synergy established upon insertion of the LDH shell, enriched with redox-active sites, moreover the combination between Ni and Co can increase the OH^- adsorption energy [350]. These distinguishing characteristics of the NiCo-LDH@Ni-NTNW electrode enable it to serve as an efficient candidate electrode in the HSC.

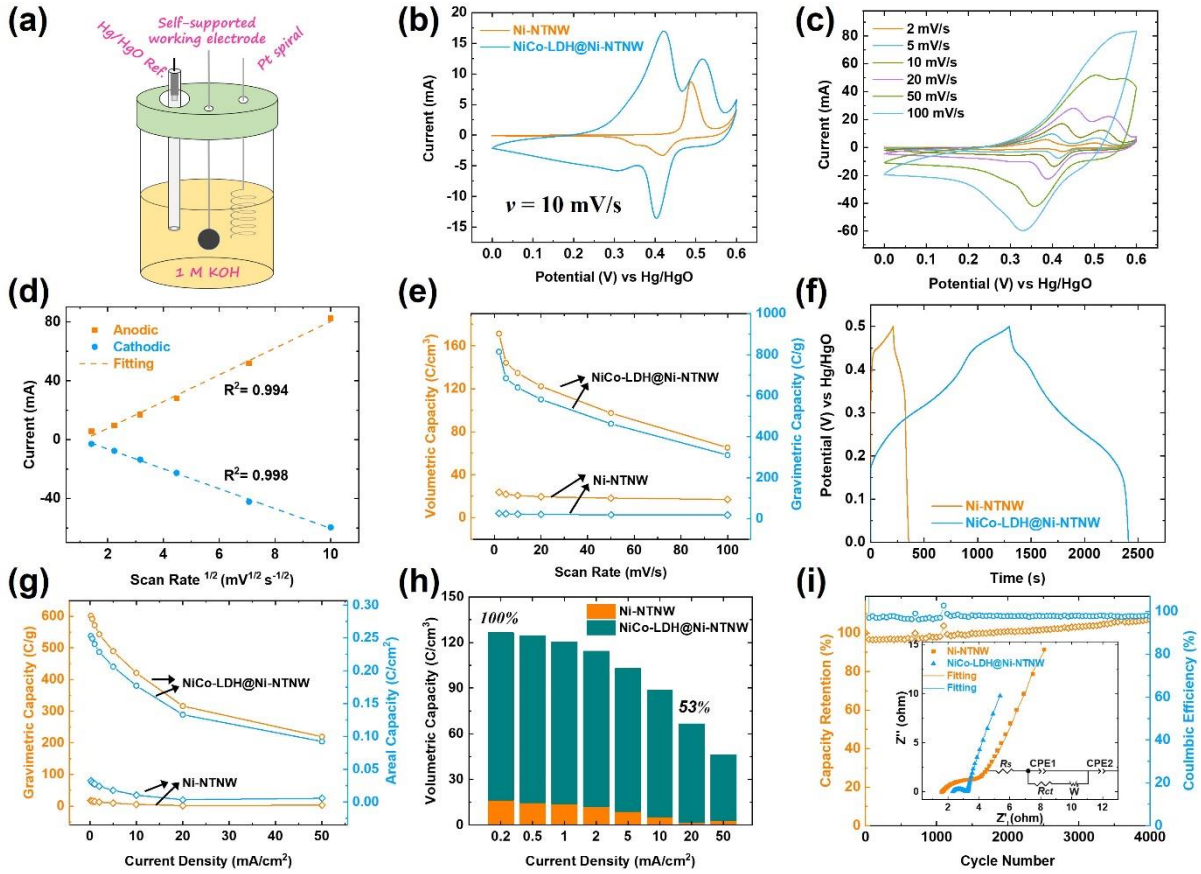

Figure 3.14. *(a) Schematic illustration of the three-electrode cell employed for electrochemical evaluation. (b) CV of Ni-NTNW and NiCo-LDH@Ni-NTNW electrodes at 10 mV/s. (c) CV curves conducted at different scan rates between 2-100 mV/s and (d) the corresponding oxidation and reduction peak currents as a function of $v^{1/2}$ of NiCo-LDH@Ni-NTNW electrode. (e) Volumetric and gravimetric capacities of Ni-NTNW and NiCo-LDH@Ni-NTNW electrodes estimated from CV curves at different scan rates. (f) GCD curves of Ni-NTNW and NiCo-LDH@Ni-NTNW electrodes at 0.2 mA/cm^2. (g) Gravimetric and areal capacities (h) volumetric capacities of Ni-NTNW and NiCo-LDH@Ni-NTNW electrodes estimated from GCD curves at different current densities. (i) Cycling stability of the NiCo-LDH@Ni-NTNW electrode at a current density of 20 mA/cm^2 (Inset: EIS plots of both electrodes and the corresponding equivalent circuit).*

In order to ensure high-energy storage of the as-prepared NiCo-LDH@Ni-NTNW electrodes in practical applications, HSC of NiCo-LDH@Ni-NTNW//AC was assembled in a two-electrode system as sketched in Figure 3.15a, in which NiCo-LDH@Ni-NTNW electrode is employed as the positive electrode (battery-type electrode) and AC as the negative electrode (capacitive electrode). Employing the conventional carbonaceous materials with their high surface area in HSCs helps in maintaining satisfactory power density [143,351]. The mass loadings of the two electrodes were adjusted based on the charge balance according to equation (2) to boost the energy density of the device [352]. The CV curves of the AC electrode were obtained at different scan rates between 2-100 mV/s (Figure S3.18) and revealed the typical rectangular shape of the capacitive electrodes. CV curves of NiCo-LDH@Ni-NTNW and AC electrodes were conducted at a scan rate of 10 mV/s to determine the optimum operating voltage window of the HSC. As represented in Figure 3.15b, the AC electrode demonstrated typical performance of double-layer materials in the potential window between -1 and 0 V (vs. Hg/HgO), while NiCo-LDH@Ni-NTNW electrode showed typical capacitance of the battery-like materials with redox activity in the potential window between 0 and 0.6 V (vs. Hg/HgO), delivering a theoretical working voltage around 1.6 V. Figure 3.15c demonstrates the CV curves of the hybrid NiCo-LDH@Ni-NTNW//AC device at a scan rate of 10 mV/s within different voltage windows ranging between 1.2 and 1.8 V. the assembled supercapacitor maintained the same behavior in the CV curves, as the voltage window increased from 1.2 to 1.6 V, without any evidence of oxygen evolution. Further increasing the maximum voltage limit to 1.8 V resulted in oxygen evolution accompanied by a sharp increase in the current density, confirming that the most suitable voltage window for sustained operation of the device without any fluctuations is 0-1.6 V. It can be seen that the areas under the CV curves increase as the voltage window increases indicating higher capacities.

As shown in Figure 3.15d, a mixed behavior of pseudocapacitance and electrical double-layer capacitance is observed in the CV curves of the assembled HSC in the voltage window of 0-1.6 V at different scan rates from 5 to 100 mV/s, compared to the typical battery-type behavior demonstrated by CV curves of the NiCo-LDH@Ni-NTNW electrode in the three-electrode system (Figure 3.14c), confirming the association of two charge storage mechanisms. The CV curves retained similar shapes with increased redox peak current and area upon increasing the scan rate, demonstrating fast electron transport and good reversibility [294]. The kinetics of the NiCo-LDH@Ni-NTNW//AC hybrid device was evaluated by analyzing the CV curves at different scan rates. The total measured current (i) can be derivatized using the power law into two components: (1) the current resulting from the diffusion-controlled battery-type process

(i_{diff}) and (2) the current resulting from the surface capacitance-dominated process (i_{cap}), according to the following equations [300]:

$$i = av^b \qquad \text{(Eq. 3.21)}$$

$$i = \log a + b \log v \qquad \text{(Eq. 3.22)}$$

where a and b are empirical constants. The ideal behavior either of a diffusion-controlled process or a capacitive-controlled process results in a b value of 0.5 and 1.0, respectively [300,353]. The inset of Figure S3.19 displays the plots of log I vs. log v of the anodic peaks of CV curves in Figure 3.15d at different voltages covering the whole CV curve. The calculated b values varied between 0.7 and 1.0 at all voltages ranging from 0.2 to 1.6 V (except at voltage of 0.8 V) as shown in Figure S3.19, confirming combined pseudocapacitive diffusion-controlled and double-layer capacitive processes. These mixed charge storage mechanisms play an important role in establishing a device with high capacity, in which the battery-type material offers multiple electrons through the redox reactions, while the double-layer capacitive material assures fast charging through the ionic adsorption [354].

To investigate the capacitance and evaluate the rate capability of the assembled HSC device, GCD measurements were accomplished at different current densities between 1 and 50 mA/cm^2 (Figure 3.15e). GCD curves in the voltage window of 0-1.6 V revealed symmetric charge and discharge behavior with nearly the same times indicating high Coulombic efficiency and reversibility. It is also noticed that the curves followed a non-linear charging and discharging pattern confirming the combined energy storage mechanisms (pseudocapacitive and double-layer capacitive) of both NiCo-LDH@Ni-NTNW and AC electrodes which is usually demonstrated by the hybrid devices and in good consistency with the findings from CV analyses.

Based on the GCD tests, the volumetric, gravimetric, and areal capacitances of the as-assembled HSC were calculated, ranging from 34.9-76.7 F/cm^3 (volumetric) upon increasing the current density from 1 to 50 mA/cm^2, which correspond to gravimetric capacitances (calculated based on the total mass of the two electrodes) of 64.9-142.6 F/g as represented in Figure 3.15f. It has to be pointed out that the volumetric capacitance was calculated based on the total volume of the HSC including the two electrodes and the separator. Such high volumetric capacitance (76.7 F/cm^3 at 1 mA/cm^2) significantly surpasses those offered by most of the asymmetric and hybrid devices with high volumetric capacitances including $Co(OH)_2$@CW//CW [355], Co_9S_8// Co_3O_4@RuO_2 [356], NiCoP/Ti_3C_2 MXene//AC [357], MnO_2/TCC//TCC [358] and others as reported in table S3.2. Moreover, the device was able to retain high capacitances of 70% and 45.5% even

at higher current densities of 20 and 50 mA/cm^2, respectively, confirming the excellent rate capability of the HSC device. The areal capacitance of the device was also reported in Figure S3.20 and showed the same behavior with 0.7 F/cm^2 at 1 mA/cm^2 which dropped to 0.48 F/cm^2 at 20 mA/cm^2. The excellent performance of the NiCo-LDH@Ni-NTNW//AC HSC can be evidenced by the EIS measurement as represented by the Nyquist plot and the corresponding equivalent circuit in Figure 3.15g. The device demonstrated low series resistance (R_s) and charge transfer resistance (R_{ct}) of 1.8 and 6.8 Ω, respectively, indicating good charge transfer kinetics of the assembled device [212,213]. The long-term Coulombic efficiency and cycling stability are other vital parameters, which determine the suitability of the device for use in practical applications. Hence, the assembled HSC was cycled up to 20000 cycles at a current density of 20 mA/cm^2 (Figure 3.16h). The device retained around 120% of the initial capacitance. As shown in Figure 3.15h, at the beginning of the process, the capacitance increases by around 20% of the initial capacitance then it stabilizes during the last 5000 cycles, which may be attributed to the activation of the NiCo-LDH@Ni-NTNW and AC electrodes and the wettability of the interior active sites of NiCo-LDH@Ni-NTNW in the alkaline aqueous media, which in turn get involved in the charging and discharging processes as reported in the previous studies confirming the superb cycling stability [359,360]. Previous studies showed the same trend of increased capacitance upon cycling. For example, NiCo-LDH/Graphene/Ni foam revealed 116% retention after 5000 cycles in a three-electrode setup [340], NiCo-LDH//graphene revealed 110% retention [361], and NiCo-LDH//CNT retained 104% of the initial capacitance [360]. However, better stability may be accomplished by prior activation of the device until it reaches a steady state as the capacity increase is mainly focused at the beginning of cycling. Table S3.3 summarizes the recently reported advanced asymmetric and hybrid supercapacitors with excellent cycling stability. In addition, the Coulombic efficiency maintained a high value of around 98% throughout the cycling process, demonstrating the good reversibility of the device. The long-term cycling stability of the HSC device profits from the huge surface area and hierarchical structure of the electrode, which in turn facilitates the diffusion of OH^- ions and provides enough space for buffering the expansions during the charge and discharge processes [359].

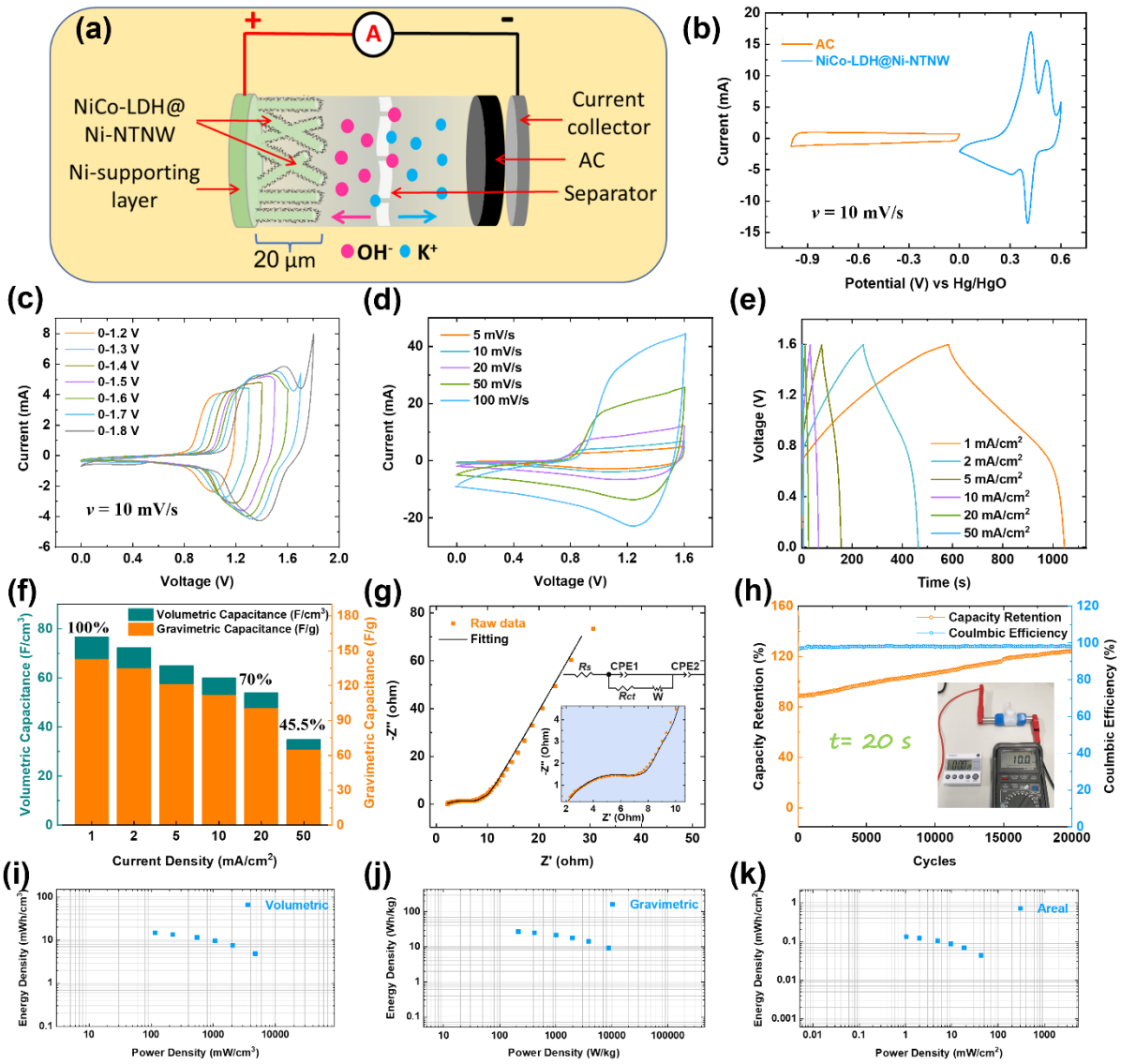

Figure 3.15. *(a) Schematic illustration of the assembled NiCo-LDH@Ni-NTNW//AC HSC. (b) CV curves of the AC and NiCo-LDH@Ni-NTNW electrodes at 10 mV/s. (c) and (d) CV curves of the HSC at different voltage ranges and different scan rates, respectively. (e) GCD curves of the HSC at different current densities. (f) Calculated volumetric and gravimetric capacitances of the HSC at different current densities. (g) EIS plot and the corresponding equivalent circuit of the device. (h) Cycling stability of the HSC (inset; image of the assembled device after 20 s of discharging). Ragone plots of (i) volumetric, (j) gravimetric, and (k) areal energy and power densities of the assembled HSC device.*

The energy and power densities of the NiCo-LDH@Ni-NTNW//AC HSC were calculated from the measured values of capacitances according to equations 6 and 7, respectively. Ragone plots of the device (Figure 3.15i-k) present the volumetric, gravimetric, and areal energy densities as a function of the volumetric, gravimetric, and areal power densities, respectively. With a current density of 1 mA/cm^2, the HSC delivers a high energy density of 27.5 Wh/kg (0.13 mWh/cm^2)

at power density of 214.7 W/kg (1.03 mW/cm^2). Upon increasing the power density to 8867.5 W/kg (42.9 mW/cm^2), the energy density dropped to 9.1 Wh/kg (0.04 mWh/cm^2) at a higher current density of 50 mA/cm^2, indicating the good overall properties of the device. More significantly, our device with its ultrathin structure was able to achieve a remarkable volumetric energy density. It exhibits a volumetric energy density of 14.7 mWh/cm^3 at a power density of 115.4 mW/cm^3 with a current density of 1 mA/cm^2. Furthermore, with a higher current density of 50 mA/cm^2, it retains an energy density of 4.9 mWh/cm^3 at a higher power density of 4769.3 mW/cm^3. The accomplished superior volumetric energy density (14.7 mWh/cm^3) outperforms the emerging symmetric, asymmetric, and hybrid devices, with outstanding volumetric energy density, encompassing GF/$NiCo_2S_4$//CF (12.3 mWh/cm^3) [312], MnO_2/TCC//TCC (9.4 mWh/cm^3) [358], WC@Ag@$NiCo_2S_4$//WC@Ag (3.93 mWh/cm^3) [362], Co_9S_8//Co_3O_4@RuO_2 (1.44 mWh/cm^3) [356], symmetric NiCo-LDH@Ni-coated textile (1.25 mWh/cm^3) [363], NiCoP/Ti_3C_2 MXene//AC (2.2 mWh/cm^3) [357], $Co(OH)_2$@CW//CW (14.1 mWh/cm^3) [355], $CuCo_2O_4$//AC (0.81 mWh/cm^3) [364], symmetric mesoporous network-like $NiCo_2O_4$ (0.69 mWh/cm^3) [365], and $Ni(OH)_2$//Mn_3O_4 (0.35 mWh/cm^3) [366], as represented in Table S2 and Figure 3.16a.

A comprehensive comparison of the overall performance of our outstanding NiCo-LDH@Ni-NTNW//AC device with the recently reported state-of-the-art symmetric, asymmetric, and hybrid supercapacitors (mentioned above) in terms of volumetric, areal, and gravimetric capacitances, energy density, and capacitance retention is presented in the radar plots in Figure 3.16b and Table S3.2. It is obvious that the overall performance of the demonstrated HSC is superior in comparison with the other devices. Such remarkable performance is ascribed not only to the unique Ni network-based hierarchical structure which boosts the rapid electron transport at high current density through the highly conductive metallic core, but also the NiCo-LDH nanosheets decorating the core Ni network with its longitudinal pathways that accelerate the ion diffusion and enhance the accessibility of the electrolyte into the interior parts of the electrode and offer a larger number of active sites through its massive surface area.

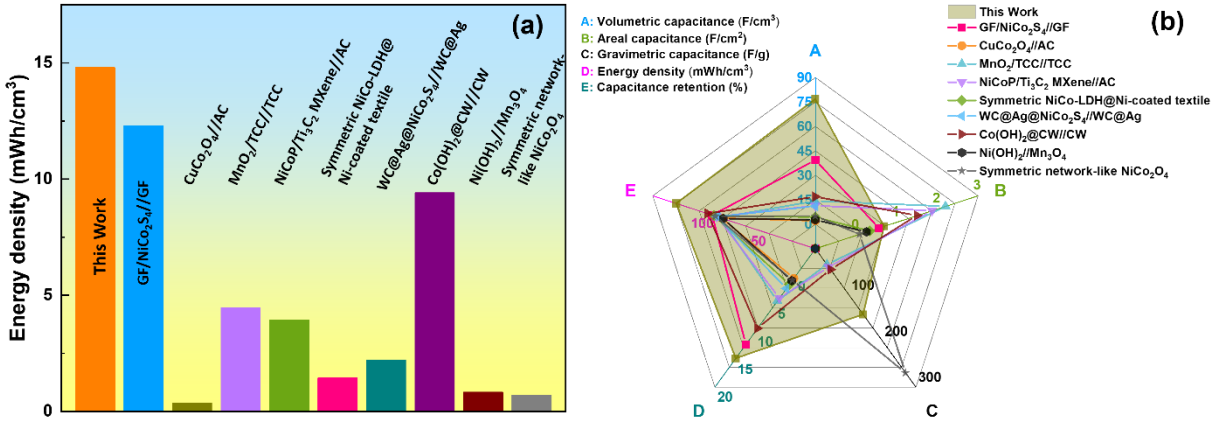

Figure 3.16. *(a) Comparison of the energy storage performance between our NiCo-LDH@Ni-NTNW//AC HSC and other previously reported supercapacitors. (b) Radar plots of the overall device performance with recently reported symmetric, asymmetric, and hybrid supercapacitors.*

Conclusions

In summary, a prolific approach has been developed to design a self-supported hierarchical structure as an electrode with superior volumetric energy storage capacity. Inspired by the pipe cactus shape, a free-standing NiCo-LDH@Ni-NTNW electrode has been fabricated using facile and cost-effective techniques, namely electroless plating and electrodeposition. The prepared 3D core-shell structure combines the advantages of the Ni network core such as high conductivity and fast electron transfer rate with the synergy offered by the NiCo-LDH nanosheets in terms of increased redox-active sites and active surface area. Moreover, the distinguished design of such a hierarchical paradigm provides a highly-porous interconnected structure that accelerates the ion diffusion rate. Meanwhile, our NiCo-LDH@Ni-NTNW electrode delivers a superior volumetric capacity of 126.4 C/cm^3 maintaining a good rate capability of 53% at high current of 20 mA/cm^2 and 106% capacity retention after 4000 cycles. More importantly, the ultrathin design of the electrode enabled the assembling of a promising HSC device (NiCo-LDH@Ni-NTNW//AC) for practical applications with outstanding performance in terms of volumetric capacitance, energy density, and capacitance retention. The device demonstrated a volumetric capacitance of 76.7 F/cm^3 and a volumetric energy density of 14.7 mWh/cm^3 putting itself as a remarkable device among the best symmetric, asymmetric, and hybrid supercapacitors that demonstrate high volumetric energy density. Such superb and well-designed electrode corroborates the advantages of the 3D hierarchical structure and offers a tunable route for the development of versatile electrode architectures through integrating different active materials, targeting high energy storage.

Author contributions

Khaled M. Amin: Conceptualization, Investigation, Methodology, Visualization, Writing - original draft. **Konrad Krois:** Investigation, Writing - review & editing. **Falk Muench**: Writing - review & editing. **Bastian J. M. Etzold:** Supervision, Writing - review & editing. **Wolfgang Ensinger:** Supervision, Writing - review & editing.

Conflicts of interest

There are no conflicts to declare.

Acknowledgments

The authors would like to thank Ulrike Kunz (Physical Metallurgy Group, TU Darmstadt) for conducting TEM measurements. The authors also acknowledge the Structural Research Group at TU Darmstadt for providing access to their XRD instrument and the Dispersive Solids Group at TU Darmstadt for access to their Raman Spectroscope. Khaled M. Amin gratefully acknowledges the financial support provided by the Ministry of Higher Education & Scientific Research (Egypt) and DAAD (Germany) for his PhD scholarship under GERLS program (Grant No. 57403037). Konrad Krois and Bastian J. M. Etzold acknowledge the financial support by the Federal Ministry of Education and Research of Germany within the project 03ZZ0346A.

3.2.4. Supplementary information

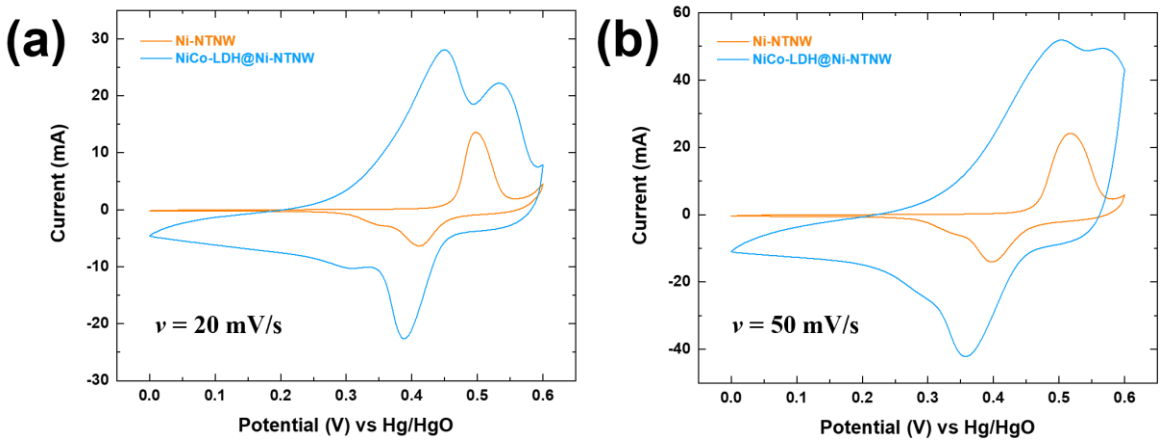

Figure S3.8. *CV of Ni-NTNW and NiCo-LDH@Ni-NTNW electrodes at scan rates of (a) 20 mV/s and (b) 50 mV/s.*

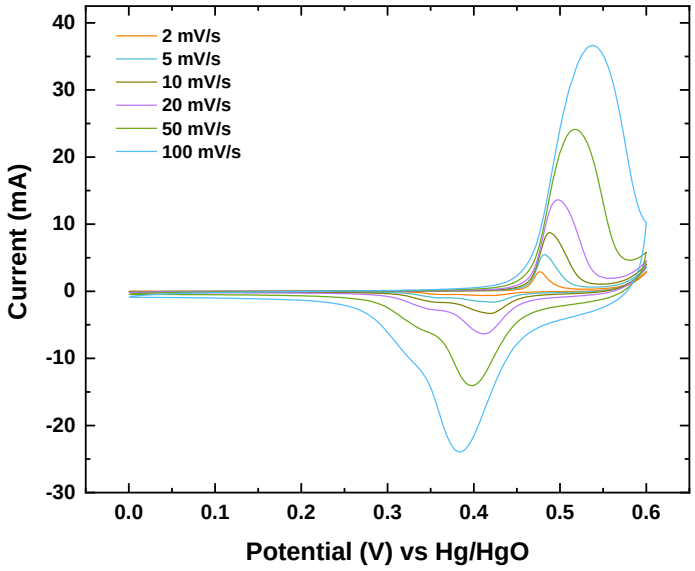

Figure S3.9. *CV curves of Ni-NTNW at different scan rates between 2-100 mV/s.*

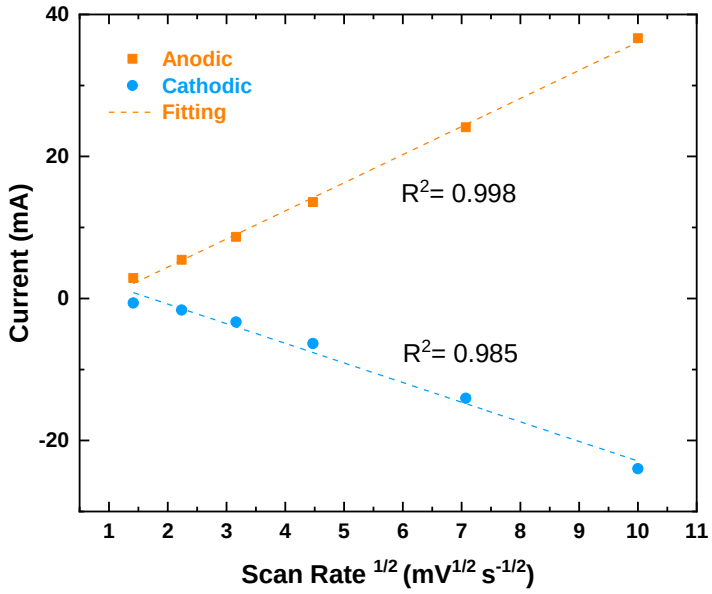

Figure S3.10. *The oxidation and reduction peak currents as a function of $v^{1/2}$ of Ni-NTNW electrode.*

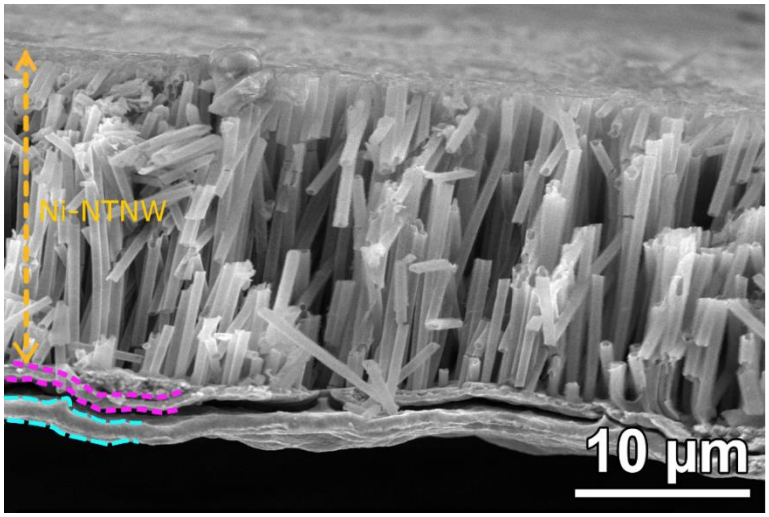

Figure S3.11. *SEM cross-sectional micrograph of the Ni-NTNW based electrode (with 400 nm nanotubes).*

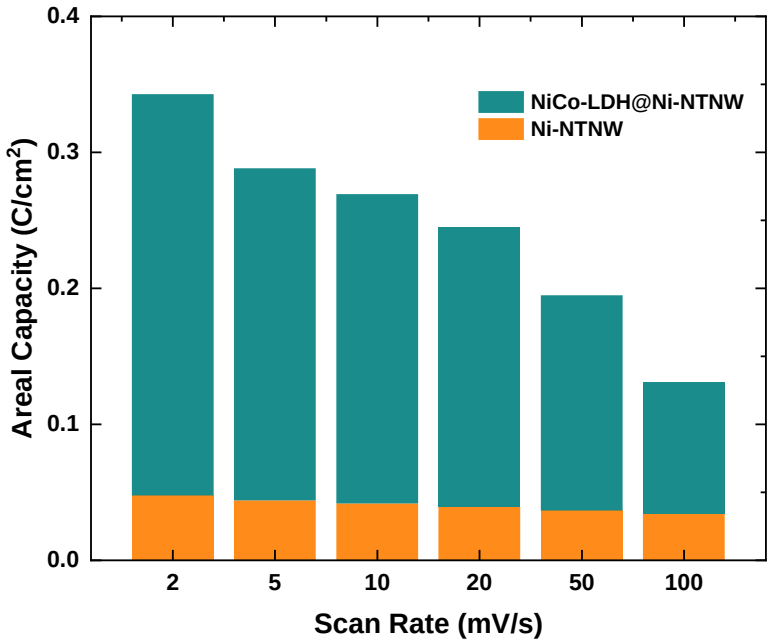

Figure S3.12. *Areal capacities of Ni-NTNW and NiCo-LDH@Ni-NTNW electrodes estimated from CV curves at different scan rates.*

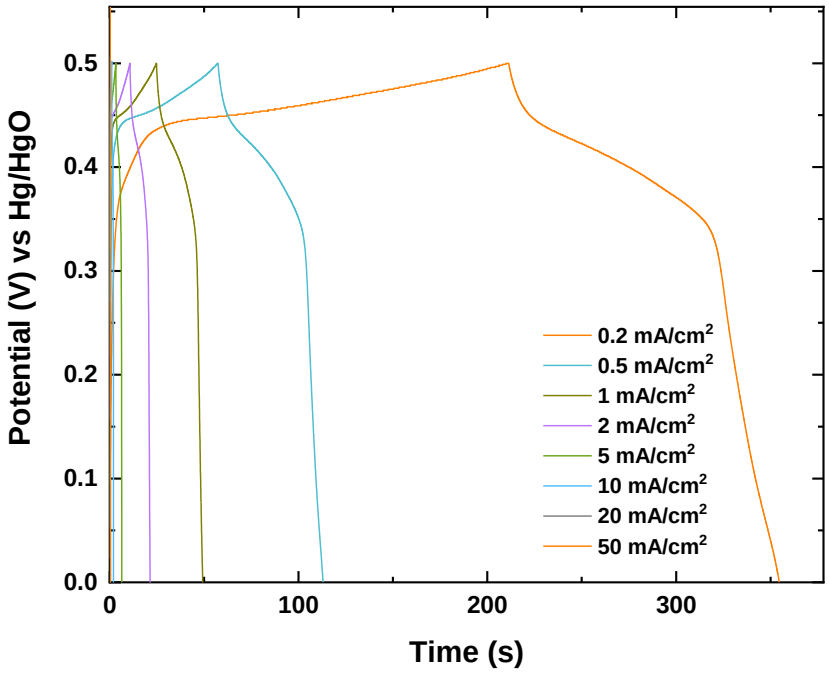

Figure S3.13. *GCD curves for Ni-NTNW electrode at different current densities between 0.2 and 50 mA/cm^2.*

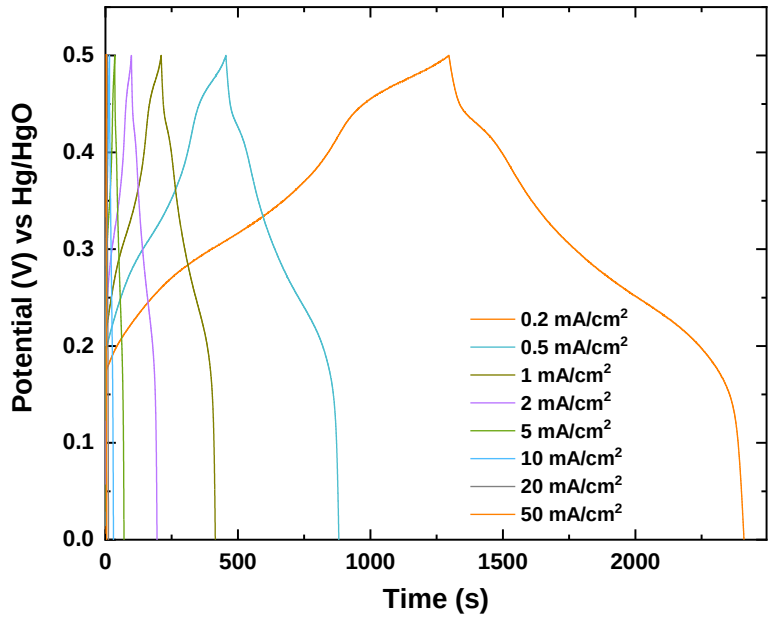

Figure S3.14. *GCD curves for NiCo-LDH@Ni-NTNW electrode at different current densities between 0.2 and 50 mA/cm^2.*

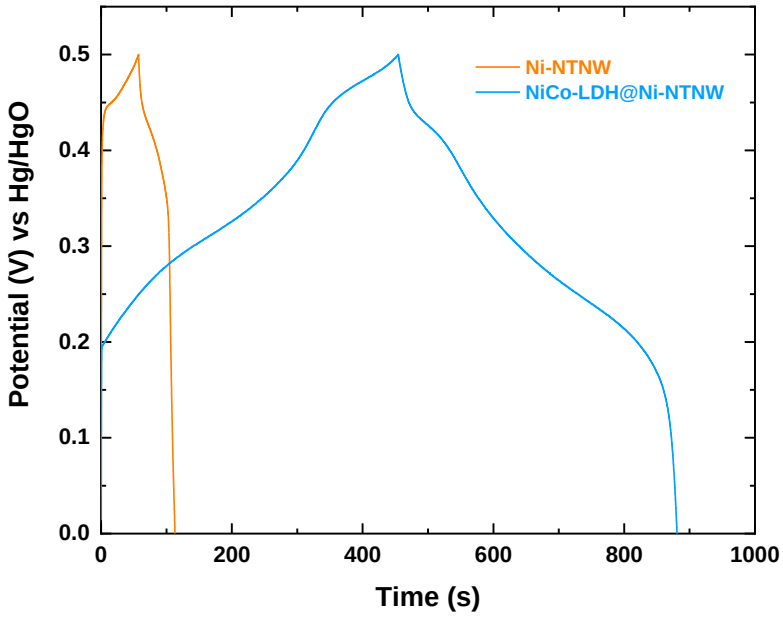

Figure S3.15. *GCD curves of Ni-NTNW and NiCo-LDH@Ni-NTNW electrodes at 0.5 mA/cm^2.*

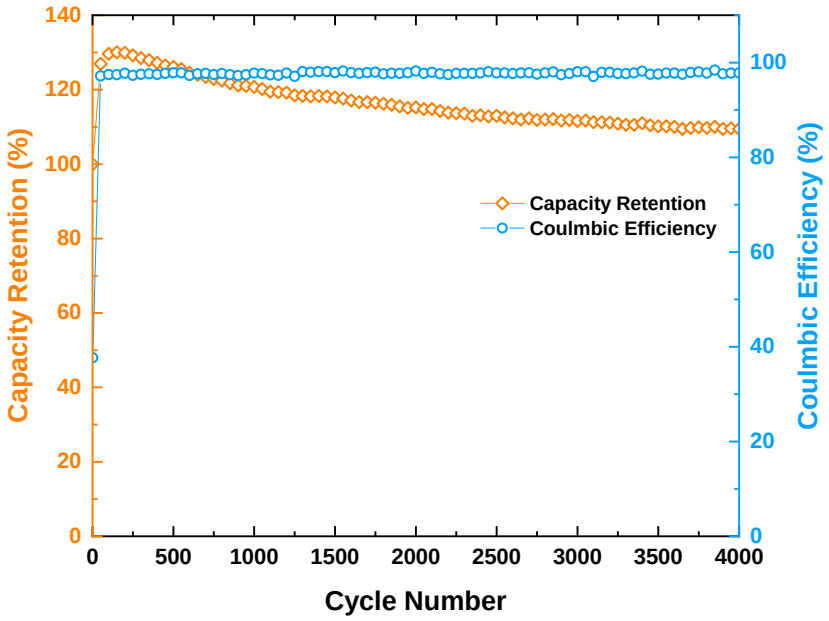

Figure S3.16. *Cycling stability of the Ni-NTNW electrode at current density of 10 mA/cm^2.*

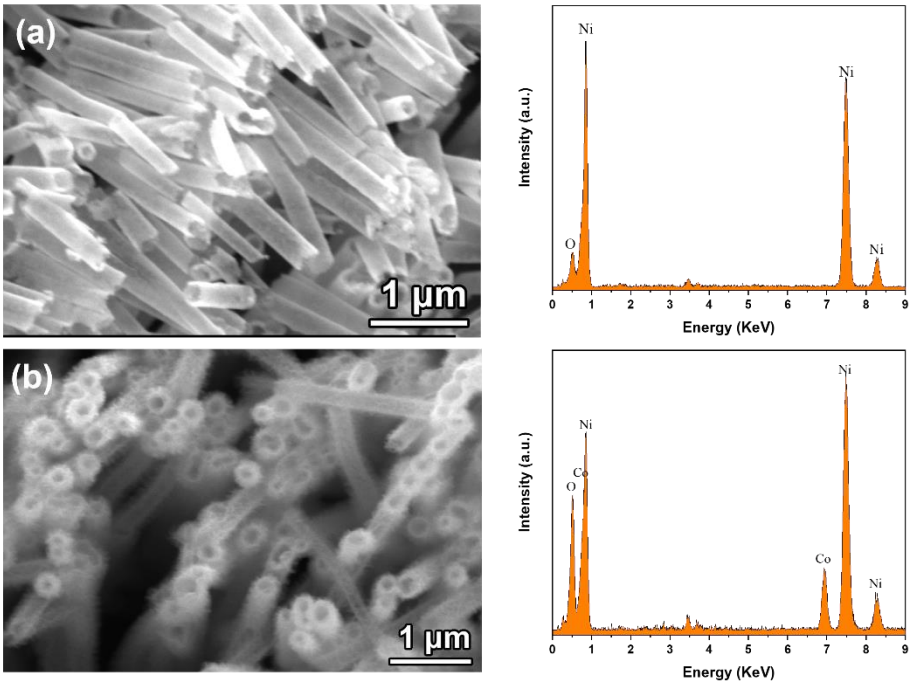

Figure S3.17. *SEM and EDX of (a) Ni-NTNW and (b) NiCo-LDH@Ni-NTNW electrodes after cycling test.*

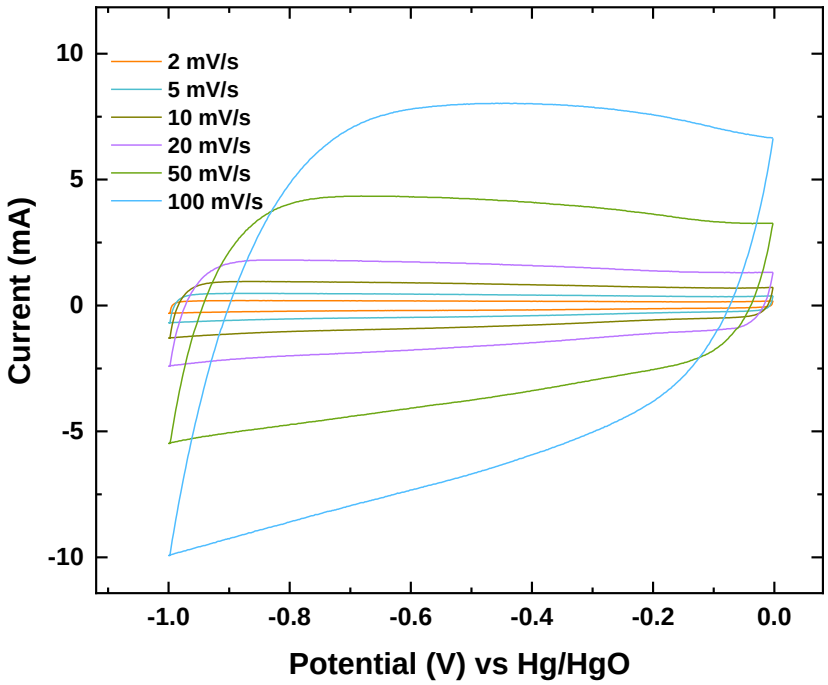

Figure S3.18. *CV curves of AC electrode at different scan rates between 2-100 mV/s.*

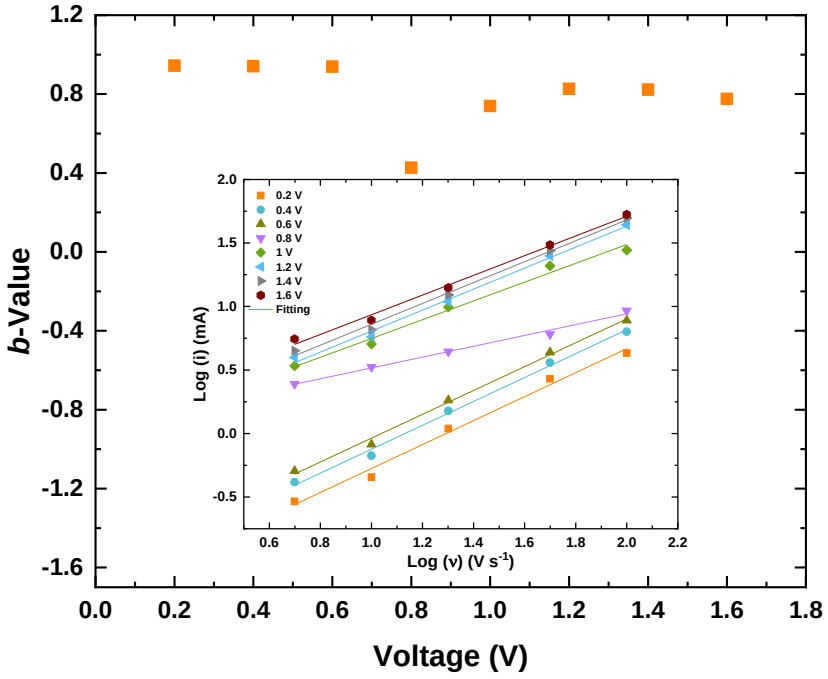

Figure S3.19. *b-Values for the assembled HSC at different voltages (Inset: the plots of log I as a function of log v at different stages of the CV potential window).*

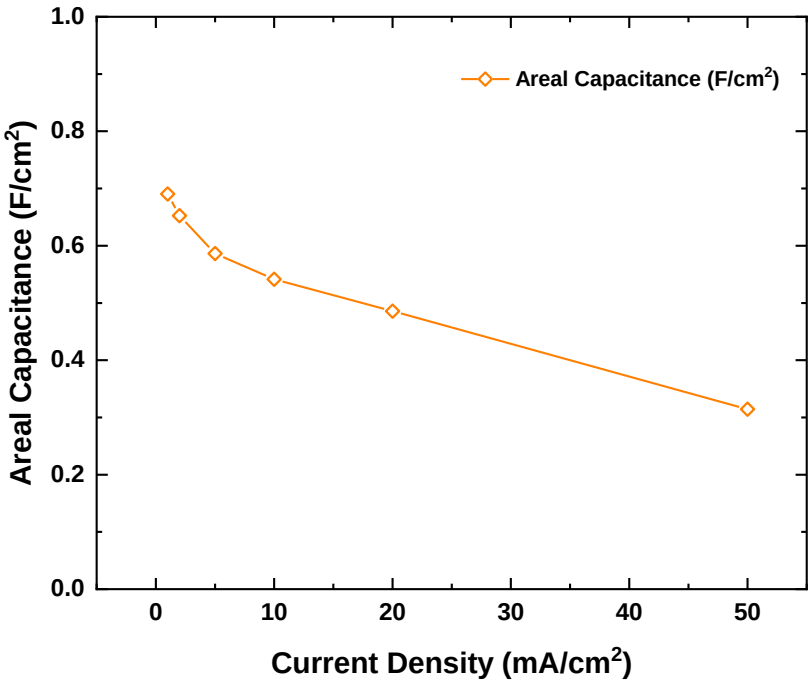

Figure S3.20. *Areal capacitance of the HSC device at different current densities.*

Table S3.1. *Performance comparison of NiCo-LDH@Ni-NTNW electrode with recently reported NiCo-based battery-type electrodes in three-electrode setup.*

Electroactive material	Current collector	Current density	Electrolyte	Capacity	Ref.
$NiCoP/Ti_3C_2$ MXene	3D printed CNT based ink	-	2 M KOH	68.5 C/cm^3 10 C/cm^2	[357]
NiCo–LDH	Ni–coated textile	1 A/g	1 M KOH	420 C/g	[363]
$Ag@NiCo_2S_4$	WC	1 mA/cm^2	6 M KOH	341 C/g 3.04 C/cm^2	[362]
$Co(OH)_2$	CW	1 mA/cm^2	2 M KOH	261 C/g 1.48 C/cm^2	[355]
NiO/ZnO	Ni foam	1.3 A/g	3 M KOH	248.5 C/g	[367]
NiCo-LDH/Co_9S_8	Ni foam	4 A/g	1 M KOH	~742 C/g *	[368]
Co-doped $Ni_{11}(HPO_3)_8(OH)_6$	Ni foam	0.5 A/g	3 M KOH	300.6 C/g	[369]
$NiCo_2S_4$	Ni foam	2 A/g	6 M KOH	508 C/g	[370]
2D/2D NiCo-MOF@GO	-	0.5 A/g	2 M KOH	413.6 C/g	[371]
Honeycomb Co@$Co(OH)_2$ sheets	Cellulose paper	2 mA/cm^2	6 M KOH	479 C/g 0.321 C/cm^2	[372]
Ni-Co LDH nanorods	Carbon nanofiber	0.02 mA/cm^2	1 M NaOH	551.2 C/g 0.011 C/cm^2	[373]
mesoporous network-like $NiCo_2O_4$	Carbon cloth	0.33 mA/cm^2	3 M KOH	16.2 C/cm^3 0.29 C/cm^2	[365]
NiCo-LDH@Ni-NTNW electrode	Integrated Ni supporting layer	0.2 mA/cm^2	1 M KOH	126.4 C/cm^3 601.0 C/g 0.252 C/cm^2	This work

* Estimated from specific capacitance figure

WC: wood-derived carbon

CW: carbonized wood

NGP: Ni/graphite/paper

Table S3.2. *Comparison of electrochemical performance of our NiCo-LDH@Ni-NTNW//AC hybrid supercapacitor with state-of-the-art symmetric/asymmetric and hybrid supercapacitors with high volumetric capacitance and energy density.*

Positive electrode	Negative electrode	j (mA/cm^2)	C_m (F/g)	C_a (F/cm^2)	C_d (F/cm^3)	Retention / Cycles	Voltage (V)	E_d (mWh/cm^3)	Ref.
Mesoporous network-like $NiCo_2O_4$	Mesoporous network-like $NiCo_2O_4$	0.33	269	0.09	5	89% 4000	1	0.69 *	[365]
$CuCo_2O_4$	AC	1	-	0.262 **	2.62 **	82% 3000	1.5	0.81	[364]
MnO_2/TCC	TCC	2	45.3	1.5	16.8	96% 20000	2	9.4	[358]
NiCoP/Ti_3C_2 MXene	AC	2	-	3.29	10.97	87.5% 5000	1.4	2.2	[357]
NiCo-LDH@Ni-coated textile	NiCo-LDH@Ni-coated textile	-	-	-	-	-	0.65	1.25	[363]
Co_9S_8	Co_3O_4@RuO_2	2.5	-	0.34	4.28	90.2% 2000	1.6	1.44	[356]
WC@Ag@$NiCo_2S_4$	WC@Ag	1	40.2	1.87	11.3	87.7% 10000	1.5	3.93	[362]
$Co(OH)_2$@CW	CW	1	34.8	2.2	14.19	85% 10000	1.5	4.45	[355]
$Ni(OH)_2$	Mn_3O_4	1	-	-	2.07	83.3% 12000	1.3	0.35	[366]
GF/$NiCo_2S_4$	GF	0.5	-	0.568	39.4	92% 2000	1.5	12.3	[312]
NiCo-LDH@Ni-NTNW	AC	1	142.6	0.69	76.7	124% 20000	1.6	14.8	This work

C_m : Gravimetric capacitance C_a : Areal capacitance

C_d : Volumetric capacitance E_d : Volumetric capacitance

* calculated based on the mass loading ** estimated from specific capacitance figure

TCC: porous carbon cloth GF: graphene fiber

Table S3.3. *Cyclic stability comparison of our NiCo-LDH@Ni-NTNW//AC hybrid supercapacitor with recently reported asymmetric and hybrid supercapacitors with high-capacitance retention.*

Device composition	Current density	Cycles	Retention	Ref.
CNTs/NiCo LDH //AC	5 A/g	10000	99.4 %	[374]
PPNF@Co−Ni MOF//CNF-G	10 A/g	10000	100 %	[359]
Layered CuCo hydroxide//ACC	8.33 mA/cm^2	3500	96.55%	[309]
NiCoP/Ti_3C_2 MXene//AC	12 mA/cm^2	5000	87.5%	[357]
WC@Ag@$NiCo_2S_4$// WC@Ag	50 mA/cm^2	10000	87.7%	[362]
$Co(OH)_2$@CW//CW	50 mA/cm^2	10000	85%	[355]
$Ni(OH)_2$//Mn_3O_4	-	12000	83.3%	[366]
NiCo-LDH//CNT	4 A/g	5000	103.9 %	[360]
NiCo-LDH//graphene	-	700	110 %	[361]
NiCo-LDH@Ni-NTNW//AC	20 mA/cm^2	20000	124 %	This work

AC: activated carbon

ACC: activated carbon cloth

CHAPTER IV

4. Conclusions and Future Perspectives

4.1. Summary

This PhD thesis was devoted to developing a flexible strategy for designing a 3D self-supported electrode paradigm for various electrochemical applications, including water splitting, sensing, and energy storage. The fabricated electrode models are based on hierarchical architectures of free-standing nanowire and nanotube networks decorated with different LDH materials. This synthetic approach utilizes template-assisted synthesis, electroless plating, and electrodeposition as feasible and scalable synthetic approaches. In this context, novel electrode systems were developed:

(i) A Ni nanotube-based system that includes $Ni(OH)_2$@Ni-NTNW and NiCo-LDH@Ni-NTNWs that was applied as non-enzymatic glucose sensor and battery-type electrode for supercapacitors.

(ii) A Ni nanowire-based system that comprises NiCo LDH/Ni-NWN and NiFe LDH/Ni-NWN as active electrocatalysts for the OER.

This thesis includes three peer-reviewed publications that delve into the design, synthesis, and characterization of the above-mentioned advanced electrode materials for various electrochemical applications. The primary objective of the study is to overcome the current limitations associated with conventional electrode designs, such as low conductivity, agglomeration of active material, and constrained volumetric capacity, particularly in the case of supercapacitors. The study thus explores rational design strategies to enhance electrode performance through the efficient integration of nanostructured architectures and active materials. The following are the main conclusions from each section of the study.

- ✓ LDH-decorated nanowires for OER

This approach was focused on the engineering of active sites enriched with NiCo LDH and NiFe LDH on a free-standing 1D Ni-NWN for the OER. We developed a facile strategy to fabricate a highly efficient free-standing nanowire network instead of the nanotube network. TEM revealed a unique 2D-on-1D structure with intact wires, and spot EDX analysis confirmed the existence of only Ni in the core tubes, while the shell layer contained Ni and Co in the case of NiCo LDH and Ni and Fe in the case of NiFe LDH. HRTEM and SAED measurements

revealed the characteristic crystal planes of NiCo and NiFe hydroxides, consistent with the data obtained from XRD and XPS. The resulting NiFe LDH/Ni-NWN electrocatalyst demonstrated excellent OER performance, characterized by a low overpotential of 222 mV to achieve a current density of 10 mA cm-2. NiFe LDH/Ni-NWN electrode revealed a lower Tafel slope of 42 mV dec-1 compared to NiCo LDH/Ni-NWN (92 mV dec-1) and Ni-NWN (140 mV dec-1). EIS measurements were conducted for the three electrodes at different potentials to investigate the charge transfer resistance. NiFe LDH/Ni-NWN showed much lower charge transfer resistance (0.8 Ω) than NiCo LDH/Ni-NWN (7.2 Ω) and Ni-NWN (19.4 Ω). The 3D architecture of the electrocatalysts, featuring a "nanosheet on nanowire" structure, enhanced the mechanical stability, efficient electron transport, and high ionic diffusion rates, facilitating the generation of active phases during OER. Moreover, these electrocatalysts exhibited exceptional durability over an extended period of time (50 hours). The offered OER performance surpasses many LDH-based electrocatalysts. The proposed strategy and flexible engineering approaches hold promise for developing electrocatalysts for diverse applications.

- ✓ LDH-decorated nanotubes for glucose sensing

A novel catalyst design based on Ni-NTNWs was developed for nonenzymatic glucose sensing. This scalable synthesis involves templating with commercial track-etched membranes, electroless plating, and electrodeposition steps. By filling the nanopores of an ion track-etched polycarbonate membrane with metallic nickel through electroless plating, a free-standing network of nickel nanotubes was achieved. These interconnected nanotubes with diameters resembling the parent nanopores were anchored to a nickel layer, creating a Ni-NTNW platform that is further decorated with $Ni(OH)_2$ or NiCo-LDH nanosheets using electrodeposition. Different synthesis parameters, including metal concentration, applied potential, and deposition time, were optimized to achieve a uniform distribution over the entire tubes. SEM and TEM micrographs confirmed the uniform deposition of $Ni(OH)_2$ and NiCo-LDH nanosheets over the inner and outer surfaces of the Ni-NTNW. Through the combination of openly accessible macropores, continuous conduction paths, and an ultra-high density of active sites, the hierarchical nanostructured electrode architecture exhibited improved performance toward glucose sensing. The resulting electrode demonstrated remarkable glucose sensing capabilities, outperforming modifications with pure $Ni(OH)_2$. The NiCo-LDH@Ni-NTNW electrocatalyst layer demonstrated a lower detection limit of 0.2 µM compared to 0.36 µM for $Ni(OH)_2$@Ni-NTNW and 0.7 µM for Ni-NTNW alone. It also exhibited outstanding sensitivity (4.6 mA mM^{-1} cm^{-2}) and fast response time (5.3 s). The catalyst revealed high selectivity towards glucose

oxidation in the presence of other interferents such as fructose, ascorbic acid, uric acid, and glutamine. These findings thus render this electrode material a highly promising candidate for nonenzymatic glucose sensing applications.

- ✓ LDH-decorated nanotubes for supercapacitor application

Traditional electrode designs that offer high volumetric energy density rely on increasing the loading of active material per cubic centimeter. To address this limitation, we employed a micro- and nanostructuring strategy to create an electrode architecture with high volumetric energy density. This approach compromises efficient contact and mechanical strength. This part of the study focused on the utilization of the 3D self-supported hierarchical architectures as battery-type electrodes for supercapacitors with excellent volumetric energy density. This unique architecture combines the large interface and high redox activity of the 2D LDH coating nanosheets with the highly porous network structure of the 1D Ni-NTNW support, facilitating ion diffusion. Ni-NTNW demonstrated much lower capacities than NiCo-LDH@Ni-NTNW at all current densities. The NiCo-LDH@Ni-NTNW electrode delivered a remarkable volumetric capacity of 126.4 C cm^{-3} while maintaining a high-rate capability of 53% at a current density of 20 mA cm^{-2}. EIS measurements showed faster charge transfer for NiCo-LDH@Ni-NTNW. Additionally, the electrode exhibited high-capacity retention over 4000 cycles. When NiCo-LDH@Ni-NTNW was integrated with activated carbon (AC), the hybrid supercapacitor demonstrated higher volumetric capacitance (76.7 F cm^{-3}) and energy density (14.7 mWh cm^{-3}), benefiting from its distinguished thin structure (20 µm). The assembled HSC maintained high cycling stability over 20,000 cycles. Its exceptional performance sets it apart from other symmetric, asymmetric, and hybrid supercapacitors known for achieving high volumetric energy density. This research emphasizes the significance of tailored electrode architectures in enhancing the overall performance of supercapacitors, particularly in the context of portable electronic devices.

In conclusion, this PhD thesis demonstrated the significance of tailored electrode architectures and nano-structuring in enhancing the performance of electrochemical devices. Hence, the research outcomes contribute to the advancement of glucose sensors, supercapacitors, and electrocatalytic water splitting.

4.2. Future Research Perspectives

Although self-supported architectures decorated with LDH have gained significant attention due to their distinct merits, rational design, and enhanced activity, there is still room for

performance improvement. To boost the practical application of LDH-based nanostructured electrocatalysts, further research efforts should be devoted to the following research points:

1. Exploring new methods to improve substrate compatibility with different active materials: Nano and micro substrates offer advantages over traditional metal foam and foil current collectors. Hence, investigating the compatibility of metal substrates with different classes of active materials is crucial. Special pre-treatment methods may be required to ensure successful growth of specific materials and avoid compatibility issues. Finding new ways to improve substrate compatibility will be instrumental in advancing the field.

2. Developing materials with high mechanical strength under bending or stretching conditions: With the rapid development of wearable electronics, there is a growing need for flexible nanonetworks with high energy and power densities for flexible energy storage. These devices experience constant stretching and bending, making it essential for the active materials to maintain functionality and deliver satisfactory output under such conditions. Therefore, the development of free-standing electrodes with high mechanical strength is highly desirable to ensure the durability and performance of flexible energy storage systems.

3. Better understanding of OER mechanism and catalyst transformations: The limited understanding of oxygen intermediates and real active species hampers the design of effective self-supported LDH catalysts. Obtaining atomic-level insights into the catalytic mechanisms of self-supported LDHs can be achieved through a combination of theoretical analysis and practical investigations. Density functional theory (DFT) analysis can provide fundamental insights into catalytic activity and aid in predicting potential electrocatalysts. In situ techniques such as Raman and XAS spectroscopies can offer valuable information on catalyst transformations under OER operation, further enhancing our understanding of the catalytic processes.

4. Addressing low active-mass loading per unit area in nanostructured electrodes: The low active-mass loading per unit electrode area presents a challenge for both supercapacitors and battery applications. Although nanostructured electrodes are suitable for micro-power sources in low-power microsystems, increasing their energy density and expanding their applications require developing approaches to significantly increase the mass loading of the active material. By enhancing the mass loading, the overall capacity of nanoelectrodes can be improved, enabling their utilization in a broader range of applications with higher energy storage capabilities.

5. Exploring heteroatom doping as a method to enhance catalytic performance: Heteroatom doping has the potential to modify the morphology, electronic structure, conductivity, and reaction kinetics of LDH-based electrocatalysts. Introducing heteroatoms into NiCo and NiFe LDH-based electrocatalysts can further enhance their catalytic activity for water splitting, making them more efficient and effective in electrochemical processes. Research efforts should focus on providing procedures for the precise design of efficient electrodes by understanding the synergistic effects between different metals in LDHs.

6. Overcoming challenges for industrial applications: While the OER performance of LDH self-supported electrocatalysts has been significantly enhanced on the lab-scale, their catalytic activity under industrially relevant conditions such as large current densities (1 A cm^{-2}) still fall short. Long-term water splitting can lead to catalyst deactivation and thus hinders its durability in practical applications. Therefore, it is crucial to address these challenges and improve the durability and stability of LDH-based electrocatalysts for long-term industrial applications. Economic considerations should also be taken into account to ensure the cost-effectiveness of self-supported LDHs in large-scale applications. Moreover, the use of earth-abundant elements in catalysts is essential to ensure sustainability and reduce dependency on scarce resources.

By addressing these research prospects, I believe there would be a promising future for the field of self-supported LDH-based electrocatalysts and this would pave the way for their large-scale applications in a wide range of electrochemical and energy-related technologies.

References

[1] A. D. Ambaye, K. K. Kefeni, S. B. Mishra, E. N. Nxumalo, B. Ntsendwana, *Talanta* **2021**, *225*, 121951.

[2] W. Xu, X. Zhao, F. Zhan, Q. He, H. Wang, J. Chen, H. Wang, X. Ren, L. Chen, *Energy Storage Mater.* **2022**, *53*, 79.

[3] P. A. Shinde, A. M. Patil, S. Lee, E. Jung, S. Chan Jun, *J. Mater. Chem. A* **2022**, *10*, 1105.

[4] J. I. Orege, O. Oderinde, G. A. Kifle, A. A. Ibikunle, S. A. Raheem, O. Ejeromedoghene, E. S. Okeke, O. M. Olukowi, O. B. Orege, E. O. Fagbohun, T. O. Ogundipe, E. P. Avor, O. O. Ajayi, M. O. Daramola, *Energy Convers. Manag.* **2022**, *258*, 115406.

[5] H. Karimi-Maleh, F. Karimi, M. Alizadeh, A. L. Sanati, *Chem. Rec.* **2020**, *20*, 682.

[6] H. Teymourian, M. Parrilla, J. R. Sempionatto, N. F. Montiel, A. Barfidokht, R. Van Echelpoel, K. De Wael, J. Wang, *ACS Sensors* **2020**, *5*, 2679.

[7] S. Tajik, H. Beitollahi, F. Garkani Nejad, I. Sheikhshoaie, A. S. Nugraha, H. W. Jang, Y. Yamauchi, M. Shokouhimehr, *J. Mater. Chem. A* **2021**, *9*, 8195.

[8] F. Y. AlJaberi, S. A. Ahmed, H. F. Makki, A. S. Naje, H. M. Zwain, A. D. Salman, T. Juzsakova, S. Viktor, B. Van, P. C. Le, D. D. La, S. W. Chang, M. J. Um, H. H. Ngo, D. D. Nguyen, *Sci. Total Environ.* **2023**, *867*.

[9] S. Zahmatkesh, M. Hajiaghaei-Keshteli, A. Bokhari, S. Sundaramurthy, B. Panneerselvam, Y. Rezakhani, *Environ. Res.* **2023**, *216*.

[10] X. Y. Yu, Z. G. Liu, X. J. Huang, *Trends Environ. Anal. Chem.* **2014**, *3*, 28.

[11] C. Jia, P. Yan, P. Liu, Z. Li, *Renew. Sustain. Energy Rev.* **2021**, *135*, 110224.

[12] S. Carvajal, S. N. Fera, A. L. Jones, T. A. Baldo, I. M. Mosa, J. F. Rusling, C. E. Krause, *Biosens. Bioelectron.* **2018**, *104*, 158.

[13] Y. Li, J. Qu, F. Li, Z. Qu, H. Tang, L. Liu, M. Zhu, O. G. Schmidt, *Nano Mater. Sci.* **2021**, *3*, 140.

[14] D. Zhang, H. Zhao, F. Liang, W. Ma, Y. Lei, *J. Power Sources* **2021**, *493*.

[15] Y. Xu, M. Zhou, Y. Lei, Y. Xu, M. Zhou, Y. Lei, *Adv. Energy Mater.* **2016**, *6*, 1502514.

[16] C. Cao, D. D. Ma, Q. Xu, X. T. Wu, Q. L. Zhu, *Adv. Funct. Mater.* **2019**, *29*, 1807418.

[17] C. Liang, P. Zou, A. Nairan, Y. Zhang, J. Liu, K. Liu, S. Hu, F. Kang, H. J. Fan, C. Yang, *Energy Environ. Sci.* **2020**, *13*, 86.

[18] F. Zhang, L. Qi, F. Zhang, L. Qi, *Adv. Sci.* **2016**, *3*, 1.

[19] Q. Xiang, J. Wang, Q. Miao, P. Tao, C. Song, W. Shang, T. Deng, Z. Yin, J. Wu, *Mater. Today Nano* **2021**, *15*.

[20] G. Zhao, K. Rui, S. X. Dou, W. Sun, *Adv. Funct. Mater.* **2018**, *28*, 1803291.

[21] B. Hui, K. Zhang, Y. Xia, C. Zhou, *Electrochim. Acta* **2020**, *330*, 135274.

[22] X. X. Liu, C. Chen, Q. He, Q. Kong, D. J. Blackwood, N. W. Li, L. Yu, J. S. Chen, *Chem. Rec.* **2022**, *22*.

[23] V. B. Mbayachi, E. Ndayiragije, T. Sammani, S. Taj, E. R. Mbuta, A. ullah khan, *Results Chem.* **2021**, *3*, 100163.

[24] O. Okhay, A. Tkach, M. J. H. Gallo, G. Otero-Irurueta, S. Mikhalev, P. Staiti, F. Lufrano, *J. Energy Storage* **2020**, *32*, 101839.

[25] Y. Wu, F. Li, W. Chen, Q. Xiang, Y. Ma, H. Zhu, P. Tao, C. Song, W. Shang, T. Deng, J. Wu, Y. Wu, F. Li, W. Chen, Q. Xiang, Y. Ma, H. Zhu, P. Tao, C. Song, W. Shang, T. Deng, J. Wu, *Adv. Mater.* **2018**, *30*, 1803151.

[26] B. Cai, S. Henning, J. Herranz, T. J. Schmidt, A. Eychmüller, *Adv. Energy Mater.* **2017**, *7*, 1700548.

[27] H. Yang, M. Driess, P. W. Menezes, H. Yang, M. Driess, P. W. Menezes, *Adv. Energy Mater.* **2021**, *11*, 2102074.

[28] X. L. Tian, Y. Y. Xu, W. Zhang, T. Wu, B. Y. Xia, X. Wang, *ACS energy Lett.* **2017**, *2*, 2035.

[29] B. P. Setzler, Z. Zhuang, J. A. Wittkopf, Y. Yan, *Nat. Nanotechnol. 2016 1112* **2016**, *11*, 1020.

[30] F. Muench, *Catalysts* **2018**, *8*, 597.

[31] C. J. Ni, F. Chau-Nan Hong, *RSC Adv.* **2014**, *4*, 40330.

[32] F. Muench, D. M. De Carolis, E. M. Felix, J. Brötz, U. Kunz, H. J. Kleebe, S. Ayata, C. Trautmann, W. Ensinger, *Chempluschem* **2015**, *80*, 1448.

[33] J. Liu, D. Jia, J. M. Gardner, E. M. J. Johansson, X. Zhang, *Mater. Today Energy* **2019**, *13*, 152.

[34] H. Zheng, X. Chen, Y. Yang, L. Li, C. Q. Feng, S. Q. Wang, *Rare Met.* **2021**, *40*, 3485.

[35] Z. Liang, C. Qu, W. Zhou, R. Zhao, H. Zhang, B. Zhu, W. Guo, W. Meng, Y. Wu, W. Aftab, Q. Wang, R. Zou, *Adv. Sci.* **2019**, *6*.

[36] H. Zhao, L. Liu, R. Vellacheri, Y. Lei, *Adv. Sci.* **2017**, *4*, 1700188.

[37] J. Qi, Y. Yan, Y. Cai, J. Cao, J. Feng, J. Qi, Y. Yan, Y. Cai, J. Cao, J. Feng, *Wiley Online Libr.* **2020**, *31*.

[38] J. Liu, D. Zhu, Y. Zheng, A. Vasileff, S. Z. Qiao, *ACS Catal.* **2018**, *8*, 6707.

[39] A. Kaur, B. Bajaj, A. Kaushik, A. Saini, D. Sud, *Mater. Sci. Eng. B* **2022**, *286*, 116005.

[40] N. Swain, B. Saravanakumar, M. Kundu, L. Schmidt-Mende, A. Ramadoss, **2021**.

[41] A. M. Md Jani, D. Losic, N. H. Voelcker, *Prog. Mater. Sci.* **2013**, *58*, 636.

[42] C. R. Martin, *Science (80-.).* **1994**, *266*, 1961.

[43] K. Froehlich, M. C. Scheuerlein, M. Ali, S. Nasir, W. Ensinger, *Nanotechnology* **2021**, *33*, 045301.

[44] F. Muench, M. Oezaslan, M. Rauber, S. Kaserer, A. Fuchs, E. Mankel, J. Brötz, P. Strasser, C. Roth, W. Ensinger, *J. Power Sources* **2013**, *222*, 243.

[45] P. Apel, *Radiat. Meas.* **2001**, *34*, 559.

[46] F. Muench, L. Sun, T. Kottakkat, M. Antoni, S. Schaefer, U. Kunz, L. Molina-Luna, M. Duerrschnabel, H. J. Kleebe, S. Ayata, C. Roth, W. Ensinger, *ACS Appl. Mater. Interfaces* **2017**, *9*, 771.

[47] C. McKeown, F. M. F. Rhen, *J. Appl. Electrochem.* **2018**, *48*, 165.

[48] F. Muench, E. M. Felix, M. Rauber, S. Schaefer, M. Antoni, U. Kunz, H. J. Kleebe, C. Trautmann, W. Ensinger, *Electrochim. Acta* **2016**, *202*, 47.

[49] T. Boettcher, S. Stojkovikj, P. Khadke, U. Kunz, M. T. Mayer, C. Roth, W. Ensinger, F. Muench, *J. Mater. Sci.* **2021**, *56*, 12620.

[50] A. Vlad, V. A. Antohe, J. M. Martinez-Huerta, E. Ferain, J. F. Gohy, L. Piraux, *J. Mater. Chem. A* **2016**, *4*, 1603.

[51] T. da Câmara Santa Clara Gomes, J. De La Torre Medina, M. Lemaitre, L. Piraux, *Nanoscale Res. Lett.* **2016**, *11*, 1.

[52] M. Rauber, I. Alber, S. Muöller, R. Neumann, O. Picht, C. Roth, A. Schoökel, M. E. Toimil-Molares, W. Ensinger, *Nano Lett.* **2011**, *11*, 2304.

[53] M. Boehme, W. Ensinger, *Adv. Eng. Mater.* **2011**, *13*, 373.

[54] E. Matei, M. Enculescu, N. Preda, C. Florica, A. Costas, C. Busuioc, M. E. T. Toimil Molares, V. Kuncser, I. Enculescu, *Springer Ser. Mater. Sci.* **2014**, *205*, 137.

[55] X. Wei, D. K. Roper, *J. Electrochem. Soc.* **2014**, *161*, D235.

[56] I. V Korolkov, D. B. Borgekov, A. A. Mashentseva, O. Gü Ven, • Ayse, B. Atıcı, • Artem, L. Kozlovskiy, M. V Zdorovets, *Chem. Pap. 71*.

[57] T. Stohr, A. Fischer, F. Muench, M. Antoni, S. Wollstadt, C. Lohaus, U. Kunz, O. Clemens, A. Klein, W. Ensinger, *ChemElectroChem* **2020**, *7*, 855.

[58] M. C. Scheuerlein, F. Muench, U. Kunz, T. Hellmann, J. P. Hofmann, W. Ensinger, *ChemElectroChem* **2020**, *7*, 3496.

[59] T. Walbert, M. Antoni, F. Muench, T. Späth, W. Ensinger, *ChemElectroChem* **2018**, *5*,

1087.
[60] F. Guo, Y. Li, B. Fan, Y. Liu, L. Lu, Y. Lei, *ACS Appl. Mater. Interfaces* **2018**, *10*, 4705.
[61] Y. Wu, X. Sun, Y. Yang, J. Li, Y. Zhang, D. Qin, *Acc. Chem. Res.* **2017**, *50*, 1774.
[62] Y. Yoon, A. Shoji Hall, Y. Surendranath, Y. Yoon, A. S. Hall, Y. Surendranath, *Angew. Chemie Int. Ed.* **2016**, *55*, 15282.
[63] A. Y. Didyk, S. N. Dmitriev, W. Vutsadakis, *High Energy Chem.* **2003**, *37*, 89.
[64] R. Sard, *J. Electrochem. Soc.* **1970**, *117*, 864.
[65] J. P. Marton, M. Schlesinger, *J. Electrochem. Soc.* **1968**, *115*, 16.
[66] F. Muench, U. Kunz, H. F. Wardenga, H. J. Kleebe, W. Ensinger, *Langmuir* **2014**, *30*, 10878.
[67] J. Sudagar, J. Lian, W. Sha, *J. Alloys Compd.* **2013**, *571*, 183.
[68] F. Muench, G. A. El-Nagar, T. Tichter, A. Zintler, U. Kunz, L. Molina-Luna, V. Sikolenko, C. Pasquini, I. Lauermann, C. Roth, *ACS Appl. Mater. Interfaces* **2019**, *11*, 43081.
[69] Y. Zhang, H. Xu, S. Lu, *RSC Adv.* **2021**, *11*, 24254.
[70] M. Zhao, Q. Zhao, B. Li, H. Xue, H. Pang, C. Chen, *Nanoscale* **2017**, *9*, 15206.
[71] J. Zhang, C. Si, T. Kou, J. Wang, Z. Zhang, *Sustain. Energy Fuels* **2020**, *4*, 2625.
[72] L. Wan, P. Wang, *Int. J. Hydrogen Energy* **2021**, *46*, 8356.
[73] J. Mittal, *J. Environ. Manage.* **2021**, *295*, 113017.
[74] Z. Cao, B. Li, L. Sun, L. Li, Z. Ping Xu, Z. Gu, Z. Cao, Z. Gu, B. Li, L. Sun, L. Li, Z. P. Xu, *Small Methods* **2020**, *4*, 1900343.
[75] H. Sohrabi, E. Dezhakam, A. Khataee, E. Nozohouri, M. R. Majidi, N. Mohseni, E. Trofimov, Y. Yoon, *Environ. Res.* **2022**, *211*, 113068.
[76] Xue Li, Jianning Ren, Deepak Sridhar, B. Bin Xu, Hassan Algadi, Z. M. El-Bahy, Yong Ma, Tingxi Li, Zhanhu Guo, *Mater. Chem. Front.* **2023**.
[77] L. Lv, Z. Yang, K. Chen, C. Wang, Y. Xiong, L. Lv, Z. Yang, C. Wang, K. Chen, Y. Xiong, *Adv. Energy Mater.* **2019**, *9*, 1803358.
[78] R. Yang, Y. Zhou, Y. Xing, D. Li, D. Jiang, M. Chen, W. Shi, S. Yuan, *Appl. Catal. B Environ.* **2019**, *253*, 131.
[79] H. Zhang, X. Li, A. Hähnel, V. Naumann, C. Lin, S. Azimi, S. L. Schweizer, A. W. Maijenburg, R. B. Wehrspohn, *Adv. Funct. Mater.* **2018**, *28*, 1706847.
[80] J. Hu, C. Zhang, L. Jiang, H. Lin, Y. An, D. Zhou, M. K. H. Leung, S. Yang, *Joule* **2017**, *1*, 383.
[81] M. Duan, M. Qiu, S. Sun, X. Guo, Y. Liu, X. Zheng, F. Cao, Q. Kong, J. Zhang, *Appl. Clay Sci.* **2022**, *216*, 106360.
[82] T. Guan, L. Fang, L. Liu, F. Wu, Y. Lu, H. J. Luo, J. Hu, B. S. Hu, M. Zhou, *J. Alloys Compd.* **2019**, *799*, 521.
[83] X. Teng, L. Guo, L. Ji, J. Wang, Y. Niu, Z. Hu, Z. Chen, *ACS Appl. Energy Mater.* **2019**, *2*, 5465.
[84] R. Liu, J. Duay, S. B. Lee, *Chem. Commun.* **2011**, *47*, 1384.
[85] B. Cao, Y. Cheng, M. Hu, P. Jing, Z. Ma, B. Liu, R. Gao, J. Zhang, *Adv. Funct. Mater.* **2019**, *29*, 1906316.
[86] H. Sun, Z. Yan, F. Liu, W. Xu, F. Cheng, J. Chen, *Adv. Mater.* **2020**, *32*, 1806326.
[87] Y. Wang, J. Ju, S. Dong, Y. Yan, F. Jiang, L. Cui, Q. Wang, X. Han, G. Cui, *Adv. Funct. Mater.* **2021**, *31*, 2101523.
[88] Y. Cong, S. Huang, Y. Mei, T. T. Li, *Chem. – A Eur. J.* **2021**, *27*, 15866.
[89] X. L. Teng, X. T. Sun, L. Guan, H. Hu, M. B. Wu, *Tungsten 2020 24* **2020**, *2*, 337.
[90] L. Wu, L. Yu, X. Xiao, F. Zhang, S. Song, S. Chen, Z. Ren, *Research* **2020**, *2020*.
[91] J. Maier, *Nat. Mater.* **2005**, *4*, 805.
[92] B. L. Ellis, P. Knauth, T. Djenizian, *Adv. Mater.* **2014**, *26*, 3368.

[93] F. Vacandio, M. Eyraud, P. Knauth, T. Djenizian, *Electrochem. commun.* **2011**, *13*, 1060.
[94] M. Heim, S. Reculusa, S. Ravaine, A. Kuhn, *Adv. Funct. Mater.* **2012**, *22*, 538.
[95] D. Santiago, G. G. Rodríguez-Calero, A. Palkar, D. Barraza-Jimenez, D. H. Galvan, G. Casillas, A. Mayoral, M. Jose-Yacamán, L. Echegoyen, C. R. Cabrera, *Langmuir* **2012**, *28*, 17202.
[96] H. Zhang, X. Yu, P. V. Braun, *Nat. Nanotechnol.* **2011**, *6*, 277.
[97] R. C. Rohit, A. D. Jagadale, S. K. Shinde, D. Y. Kim, *Mater. Today Commun.* **2021**, *27*, 102275.
[98] N. Zhao, Y. Feng, H. Zhao, H. Fan, S. Tian, B. Hu, *J. Alloys Compd.* **2022**, *901*, 163566.
[99] T. Nguyen, M. Boudard, M. J. Carmezim, M. F. Montemor, *Sci. Rep.* **2017**, *7*, 1.
[100] J. D. Holladay, J. Hu, D. L. King, Y. Wang, *Catal. Today* **2009**, *139*, 244.
[101] A. G. Stern, *Int. J. Hydrogen Energy* **2018**, *43*, 4244.
[102] B. You, Y. Sun, *Acc. Chem. Res.* **2018**, *51*, 1571.
[103] J. Song, C. Wei, Z. F. Huang, C. Liu, L. Zeng, X. Wang, Z. J. Xu, *Chem. Soc. Rev.* **2020**, *49*, 2196.
[104] Z. Cai, X. Bu, P. Wang, J. C. Ho, J. Yang, X. Wang, *J. Mater. Chem. A* **2019**, *7*, 5069.
[105] Y. Cheng, S. P. Jiang, *Prog. Nat. Sci. Mater. Int.* **2015**, *25*, 545.
[106] N. T. Suen, S. F. Hung, Q. Quan, N. Zhang, Y. J. Xu, H. M. Chen, *Chem. Soc. Rev.* **2017**, *46*, 337.
[107] H. Kim, T. Y. Yoo, M. S. Bootharaju, J. H. Kim, D. Y. Chung, T. Hyeon, *Adv. Sci.* **2022**, *9*, 2104054.
[108] Q. Shi, C. Zhu, D. Du, Y. Lin, *Chem. Soc. Rev.* **2019**, *48*, 3181.
[109] Z. Qin, W. Liu, W. Que, J. Feng, W. Shi, F. Wu, X. Cao, *ChemPhysMater* **2022**.
[110] Z.-P. Wu, F. Lu, S.-Q. Zang, X. Wen, D. Lou, Z.-P. Wu, X. F. Lu, X. W. Lou, S.-Q. Zang, *Adv. Funct. Mater.* **2020**, *30*, 1910274.
[111] P. Babar, A. Lokhande, H. Ho Shin, B. Pawar, M. Gil Gang, S. Pawar, J. Hyeok Kim, P. Babar, A. Lokhande, H. H. Shin, M. G. Gang, J. H. Kim, B. Pawar, S. Pawar, *Small* **2018**, *14*, 1702568.
[112] J. Wang, W. Cui, Q. Liu, Z. Xing, A. M. Asiri, X. Sun, J. Wang, W. Cui, Q. Liu, Z. Xing, X. Sun, A. M. Asiri, *Adv. Mater.* **2016**, *28*, 215.
[113] C. C. L. McCrory, S. Jung, J. C. Peters, T. F. Jaramillo, *J. Am. Chem. Soc.* **2013**, *135*, 16977.
[114] S. Kim, C. Ahn, Y. Cho, G. Hyun, S. Jeon, J. H. Park, *Nano Energy* **2018**, *54*, 184.
[115] Y. Fu, Q. An, R. Ni, Y. Zhang, Y. Li, H. Ke, *Colloids Surfaces A Physicochem. Eng. Asp.* **2018**, *559*, 289.
[116] M. Mohammadniaei, J. Yoon, T. Lee, B. G. Bharate, J. Jo, D. Lee, J.-W. Choi, M. Mohammadniaei, J. Yoon, B. G. Bharate, J. Jo, J.-W. Choi, T. Lee, D. Lee, *Small* **2018**, *14*, 1703970.
[117] K. Li, W. Liu, Y. Ni, D. Li, D. Lin, Z. Su, G. Wei, *J. Mater. Chem. B* **2017**, *5*, 4811.
[118] M. Wei, Y. Qiao, H. Zhao, J. Liang, T. Li, Y. Luo, S. Lu, X. Shi, W. Lu, X. Sun, *Chem. Commun.* **2020**, *56*, 14553.
[119] B. W. Bode, T. Battelino, *Int. J. Clin. Pract.* **2010**, *64*, 11.
[120] A. Manikandan, V. Veeramani, S. M. Chen, R. Madhu, L. Lee, H. Medina, C. W. Chen, W. H. Hung, Z. M. Wang, G. Shen, Y. L. Chueh, *J. Phys. Chem. C* **2016**, *120*, 25752.
[121] D. L. Williams, A. R. Doig, A. Korosi, *Anal. Chem.* **1970**, *42*, 118.
[122] T. Hu, Z. Gu, G. R. Williams, M. Strimaite, J. Zha, Z. Zhou, X. Zhang, C. Tan, R. Liang, *Chem. Soc. Rev.* **2022**, *51*, 6126.
[123] Q. Xue, Z. Li, Q. Wang, W. Pan, Y. Chang, X. Duan, *Nanoscale Horizons* **2020**, *5*, 934.
[124] J. Okuda-Shimazaki, H. Yoshida, K. Sode, *Bioelectrochemistry* **2020**, *132*, 107414.
[125] L. C. Clark, C. Lyons, *Ann. N. Y. Acad. Sci.* **1962**, *102*, 29.

[126] L. Lin, J. Yan, J. Li, *Anal. Chem.* **2014**, *86*, 10546.
[127] Z. Wen, S. Ci, J. Li, *J. Phys. Chem. C* **2009**, *113*, 13482.
[128] K. Tian, M. Prestgard, A. Tiwari, *Mater. Sci. Eng. C. Mater. Biol. Appl.* **2014**, *41*, 100.
[129] D. W. Hwang, S. Lee, M. Seo, T. D. Chung, *Anal. Chim. Acta* **2018**, *1033*, 1.
[130] H. Teymourian, A. Barfidokht, J. Wang, *Chem. Soc. Rev.* **2020**, *49*, 7671.
[131] D. Luo, L. Wu, J. Zhi, *ACS Nano* **2009**, *3*, 2121.
[132] Z. Shami, S. M. Amininasab, P. Shakeri, *ACS Appl. Mater. Interfaces* **2016**, *8*, 28964.
[133] Y. Lu, B. Jiang, L. Fang, S. Fan, F. Wu, B. Hu, F. M. Meng, *Electroanalysis* **2017**, *29*, 1755.
[134] J. Cui, Z. Li, K. Liu, J. Li, M. Shao, *Nanoscale Adv.* **2019**, *1*, 948.
[135] M. Shen, W. Li, L. Chen, Y. Chen, S. Ren, D. Han, *Anal. Chim. Acta* **2021**, *1177*, 338787.
[136] A. Gani, *J. Clean. Prod.* **2021**, *297*, 126526.
[137] H. Chen, T. N. Cong, W. Yang, C. Tan, Y. Li, Y. Ding, *Prog. Nat. Sci.* **2009**, *19*, 291.
[138] W. Bai, H. Tong, Z. Gao, S. Yue, S. Xing, S. Dong, L. Shen, J. He, X. Zhang, Y. Liang, *J. Mater. Chem. A* **2015**, *3*, 21891.
[139] Y. Wang, Y. Song, Y. Xia, *Chem. Soc. Rev.* **2016**, *45*, 5925.
[140] N. Choudhary, C. Li, J. Moore, N. Nagaiah, L. Zhai, Y. Jung, J. Thomas, *Adv. Mater.* **2017**, *29*, 1605336.
[141] G. Z. Chen, **2016**, *62*, 173.
[142] L. Guan, L. Yu, G. Z. Chen, *Electrochim. Acta* **2016**, *206*, 464.
[143] A. Noori, M. F. El-Kady, M. S. Rahmanifar, R. B. Kaner, M. F. Mousavi, *Chem. Soc. Rev.* **2019**, *48*, 1272.
[144] M. Zhou, Y. Xu, Y. Lei, *Nano Today* **2018**, *20*, 33.
[145] R. Xu, L. Du, D. Adekoya, G. Zhang, S. Zhang, S. Sun, Y. Lei, R. Xu, Y. Lei, L. Du, G. Zhang, S. Sun, D. Adekoya, S. Zhang, *Adv. Energy Mater.* **2021**, *11*, 2001537.
[146] M. Yang, C. H. Zhang, N. W. Li, D. Luan, L. Yu, X. W. Lou, *Adv. Sci.* **2022**, *9*, 2105135.
[147] W. Zhou, X. Cao, Z. Zeng, W. Shi, Y. Zhu, Q. Yan, H. Liu, J. Wang, H. Zhang, *Energy Environ. Sci.* **2013**, *6*, 2216.
[148] S. Min, C. Zhao, Z. Zhang, G. Chen, X. Qian, Z. Guo, *J. Mater. Chem. A* **2015**, *3*, 3641.
[149] S. Kulandaivalu, N. H. N. Azman, Y. Sulaiman, *Front. Mater.* **2020**, *7*, 521536.
[150] H. Lv, H. Rao, Z. Liu, Z. Zhou, Y. Zhao, H. Wei, Z. Chen, *J. Energy Storage* **2022**, *52*, 104940.
[151] Y. Tang, W. Guo, R. Zou, *Coord. Chem. Rev.* **2022**, *451*, 214242.
[152] G. Nagaraju, S. Chandra Sekhar, L. Krishna Bharat, J. S. Yu, *ACS Nano* **2017**, *11*, 10860.
[153] B. R. Wiston, P. Prabhakaran, M. Ashok, *J. Energy Storage* **2022**, *50*, 104226.
[154] H. Chen, L. Hu, M. Chen, Y. Yan, L. Wu, H. Chen, L. F. Hu, M. Chen, Y. Yan, L. M. Wu, *Adv. Funct. Mater.* **2014**, *24*, 934.
[155] H. Liang, J. Lin, H. Jia, S. Chen, J. Qi, J. Cao, T. Lin, W. Fei, J. Feng, *J. Power Sources* **2018**, *378*, 248.
[156] S. Krevor, H. de Coninck, S. E. Gasda, N. S. Ghaleigh, V. de Gooyert, H. Hajibeygi, R. Juanes, J. Neufeld, J. J. Roberts, F. Swennenhuis, *Nat. Rev. Earth Environ.* **2023**, *4*, 102.
[157] K. Du, L. Zhang, J. Shan, J. Guo, J. Mao, C.-C. Yang, C.-H. Wang, Z. Hu, T. Ling, *Nat. Commun.* **2022**, *13*, 5448.
[158] H. Liu, Y. Zhu, J. Ma, Z. Zhang, W. Hu, *Adv. Funct. Mater.* **2020**, *30*, 1910534.
[159] X. Li, L. Liu, X. Ren, J. Gao, Y. Huang, B. Liu, *Sci. Adv.* **2020**, *6*, 6833.
[160] Z. H. Dong, Z. Jiang, T. Tang, Z. C. Yao, D. Xue, S. Niu, J. Zhang, J. S. Hu, *J. Mater. Chem. A* **2022**, *10*, 12764.
[161] Q. Lu, X. Zou, Y. Bu, Z. Shao, *Energy Storage Mater.* **2023**, *55*, 166.

[162] A. Ndubuisi, S. Abouali, K. Singh, V. Thangadurai, *J. Mater. Chem. A* **2022**, *10*, 2196.
[163] X. Feng, Q. Jiao, W. Chen, Y. Dang, Z. Dai, S. L. Suib, J. Zhang, Y. Zhao, H. Li, C. Feng, *Appl. Catal. B Environ.* **2021**, *286*, 119869.
[164] W. Li, H. Tian, L. Ma, Y. Wang, X. Liu, X. Gao, *Mater. Adv.* **2022**, *3*, 5598.
[165] A. A. Kashale, C. H. Yi, K. Y. Cheng, J. S. Guo, Y. H. Pan, I. W. P. Chen, *ACS Appl. Energy Mater.* **2020**, *3*, 10831.
[166] D. Escalera-López, K. D. Jensen, N. V. Rees, M. Escudero-Escribano, *Adv. Sustain. Syst.* **2021**, *5*, 2000284.
[167] K. W. Park, A. M. Kolpak, *J. Mater. Chem. A* **2019**, *7*, 6708.
[168] K. Zhang, R. Zou, *Small* **2021**, *17*, 2100129.
[169] Z. Y. Wu, F. Y. Chen, B. Li, S. W. Yu, Y. Z. Finfrock, D. M. Meira, Q. Q. Yan, P. Zhu, M. X. Chen, T. W. Song, Z. Yin, H. W. Liang, S. Zhang, G. Wang, H. Wang, *Nat. Mater.* **2023**, *22*, 100.
[170] F. Wang, K. Zhang, S. Li, Q. Zha, Y. Ni, *ACS Sustain. Chem. Eng.* **2022**, *10*, 10383.
[171] J. Jiang, X. L. Zhou, H. G. Lv, H. Q. Yu, Y. Yu, *Adv. Funct. Mater.* **2022**, 2212160.
[172] X. Guo, M. Duan, J. Zhang, B. Xi, M. Li, R. Yin, X. Zheng, Y. Liu, F. Cao, X. An, S. Xiong, *Adv. Funct. Mater.* **2022**, *32*, 2209397.
[173] P. Prabhu, J. M. Lee, *Chem. Soc. Rev.* **2021**, *50*, 6700.
[174] X. Guo, S. Liu, X. Wan, J. Zhang, Y. Liu, X. Zheng, Q. Kong, Z. Jin, *Nano Lett.* **2022**, *22*, 4879.
[175] Q. Kong, H. Zhu, S. Huang, T. Wu, F. Zhu, Y. Zhang, Y. Wang, J. Zhang, *Thermochim. Acta* **2022**, *707*, 179112.
[176] Z. Wang, W. Liu, Y. Hu, M. Guan, L. Xu, H. Li, J. Bao, H. Li, *Appl. Catal. B Environ.* **2020**, *272*, 118959.
[177] G. Mu, G. Wang, Q. Huang, Y. Miao, D. Wen, D. Lin, C. Xu, Y. Wan, F. Xie, W. Guo, R. Zou, *Adv. Funct. Mater.* **2023**, 2211260.
[178] S. Zhu, J. Wang, H. Li, J. Cai, Y. Li, J. Hu, Y. He, Y. Zhou, *ACS Appl. Nano Mater.* **2022**, *2022*, 13047.
[179] L. Gong, H. Yang, A. I. Douka, Y. Yan, B. Y. Xia, *Adv. Sustain. Syst.* **2021**, *5*, 2000136.
[180] X. Li, Y. Liu, Q. Sun, Z. Huangfu, W. H. Huang, Z. Wang, C. C. Chueh, C. L. Chen, Z. Zhu, *ACS Sustain. Chem. Eng.* **2022**, *10*, 14474.
[181] Y. Zhou, X. Sun, K. Zhong, D. G. Evans, Y. Lin, X. Duan, *Ind. Eng. Chem. Res.* **2012**, *51*, 4215.
[182] K. M. Amin, K. Krois, F. Muench, B. J. M. Etzold, W. Ensinger, *J. Mater. Chem. A* **2022**, *10*, 12473.
[183] K. M. Amin, T. Boettcher, M. C. Scheuerlein, W. Ensinger, In *World Congress on Recent Advances in Nanotechnology*, **2022**.
[184] K. M. Amin, F. Muench, U. Kunz, W. Ensinger, *J. Colloid Interface Sci.* **2021**, *591*, 384.
[185] P. M. Bodhankar, P. B. Sarawade, G. Singh, A. Vinu, D. S. Dhawale, *J. Mater. Chem. A* **2021**, *9*, 3180.
[186] G. A. Gebreslase, M. V. Martínez-Huerta, M. J. Lázaro, *J. Energy Chem.* **2022**, *67*, 101.
[187] J. Li, L. Wang, H. He, Y. Chen, Z. Gao, N. Ma, B. Wang, L. Zheng, R. Li, Y. Wei, J. Xu, Y. Xu, B. Cheng, Z. Yin, D. Ma, *Nano Res.* **2022**, *15*, 4986.
[188] F. Dionigi, J. Zhu, Z. Zeng, T. Merzdorf, H. Sarodnik, M. Gliech, L. Pan, W. X. Li, J. Greeley, P. Strasser, *Angew. Chemie - Int. Ed.* **2021**, *60*, 14446.
[189] E. Jiang, C. Guo, P. Huo, Y. Yan, P. Zhou, Y. Yan, *ACS Sustain. Chem. Eng.* **2022**, *10*, 16335.
[190] Z. Qi, J. Weissmüller, *ACS Nano* **2013**, *7*, 5948.
[191] D. C. Palmer, S. E. Palmer, *SingleCrystalTM: a single-crystal diffraction program for Mac and Windows*.
[192] N. Fairley, V. Fernandez, M. Richard-Plouet, C. Guillot-Deudon, J. Walton, E. Smith,

D. Flahaut, M. Greiner, M. Biesinger, S. Tougaard, D. Morgan, J. Baltrusaitis, *Appl. Surf. Sci. Adv.* **2021**, *5*.

[193] Q. Xiang, Y. Xu, R. Chen, C. Yang, X. Li, G. Li, D. Wu, X. Xie, W. Zhu, L. Wang, *ChemNanoMat* **2021**, *7*, 314.

[194] Y. Gao, Z. Zhao, H. Jia, X. Yang, X. Lei, X. Kong, F. Zhang, *J. Mater. Sci.* **2019**, *54*, 14515.

[195] M. C. Biesinger, L. W. M. Lau, A. R. Gerson, R. S. C. Smart, *Phys. Chem. Chem. Phys.* **2012**, *14*, 2434.

[196] H. Yang, C. Wang, Y. Zhang, Q. Wang, *Sci. China Mater.* **2019**, *62*, 681.

[197] P. Yin, G. Wu, X. Wang, S. Liu, F. Zhou, L. Dai, X. Wang, B. Yang, Z. Q. Yu, *Nano Res.* **2021**, *14*, 4783.

[198] F. Wu, Y. Wang, S. Fei, G. Zhu, *Nanomaterials* **2023**, *13*, 1939.

[199] M. K. Bates, Q. Jia, H. Doan, W. Liang, S. Mukerjee, *ACS Catal.* **2016**, *6*, 155.

[200] F. Dionigi, Z. Zeng, I. Sinev, T. Merzdorf, S. Deshpande, M. B. Lopez, S. Kunze, I. Zegkinoglou, H. Sarodnik, D. Fan, A. Bergmann, J. Drnec, J. F. de Araujo, M. Gliech, D. Teschner, J. Zhu, W. X. Li, J. Greeley, B. Roldan Cuenya,, P. Strasser, *Nat. Commun.* **2020**, *11*, 1.

[201] M. W. Louie, A. T. Bell, *J. Am. Chem. Soc.* **2013**, *135*, 12329.

[202] S. Anantharaj, S. Kundu, S. Noda, *Nano Energy* **2021**, *80*, 105514.

[203] A. S. Batchellor, S. W. Boettcher, *ACS Catal.* **2015**, *5*, 6680.

[204] R. Boggio, A. Carugati, S. Trasatti, *J. Appl. Electrochem.* **1987**, *17*, 828.

[205] A. E. Praveen, S. Ganguli, V. Mahalingam, *Nanoscale Adv.* **2020**, *2*, 1927.

[206] S. Yin, W. Tu, Y. Sheng, Y. Du, M. Kraft, A. Borgna, R. Xu, *Adv. Mater.* **2018**, *30*, 1705106.

[207] D. Friebel, M. W. Louie, M. Bajdich, K. E. Sanwald, Y. Cai, A. M. Wise, M. J. Cheng, D. Sokaras, T. C. Weng, R. Alonso-Mori, R. C. Davis, J. R. Bargar, J. K. Nørskov, A. Nilsson, A. T. Bell, *J. Am. Chem. Soc.* **2015**, *137*, 1305.

[208] H. Pourfarzad, M. Shabani-Nooshabadi, M. R. Ganjali, H. Kashani, *Electrochim. Acta* **2019**, *317*, 83.

[209] C. Qiao, Z. Usman, T. Cao, S. Rafai, Z. Wang, Y. Zhu, C. Cao, J. Zhang, *Chem. Eng. J.* **2021**, *426*, 130873.

[210] P. F. Guo, Y. Yang, W. J. Wang, B. Zhu, W. T. Wang, Z. Y. Wang, J. L. Wang, K. Wang, Z. H. He, Z. T. Liu, *Chem. Eng. J.* **2021**, *426*, 130768.

[211] J. Nie, M. Hong, X. Zhang, J. Huang, Q. Meng, C. Du, J. Chen, *Dalt. Trans.* **2020**, *49*, 4896.

[212] A. Galal, K. M. Amin, N. F. Atta, H. A. Abd El-Rehim, *J. Alloys Compd.* **2017**, *695*, 638.

[213] N. F. Atta, K. M. Amin, H. A. Abd El-Rehim, A. Galal, *RSC Adv.* **2015**, *5*, 71627.

[214] J. Jiang, A. Zhang, L. Li, L. Ai, *J. Power Sources* **2015**, *278*, 445.

[215] B. Beverskog, I. Puigdomenech, *Corros. Sci.* **1997**, *39*, 969.

[216] L. G. Bloor, P. I. Molina, M. D. Symes, L. Cronin, *J. Am. Chem. Soc.* **2014**, *136*, 3304.

[217] S. C. Perry, S. M. Gateman, L. I. Stephens, R. Lacasse, R. Schulz, J. Mauzeroll, *J. Electrochem. Soc.* **2019**, *166*, C3186.

[218] L. Trotochaud, S. L. Young, J. K. Ranney, S. W. Boettcher, *J. Am. Chem. Soc.* **2014**, *136*, 6744.

[219] A. Moysiadou, S. Lee, C. S. Hsu, H. M. Chen, X. Hu, *J. Am. Chem. Soc.* **2020**, *142*, 11901.

[220] L. A. Stern, X. Hu, *Faraday Discuss.* **2014**, *176*, 363.

[221] D. Friebel, M. W. Louie, M. Bajdich, K. E. Sanwald, Y. Cai, A. M. Wise, M. J. Cheng, D. Sokaras, T. C. Weng, R. Alonso-Mori, R. C. Davis, J. R. Bargar, J. K. Nørskov, A. Nilsson, A. T. Bell, *J. Am. Chem. Soc.* **2015**, *137*, 1305.

[222] Y. Du, Y. Zhang, X. Pu, X. Fu, X. Li, L. Bai, Y. Chen, J. Qian, *Chemosphere* **2023**, *312*, 137203.
[223] M. Praveen Kumar, M. Sasikumar, A. Arulraj, V. Rajasudha, G. Murugadoss, M. R. Kumar, S. Gouse Peera, R. V. Mangalaraja, *Catalysts* **2022**, *12*, 1470.
[224] Y. Hu, W. Liu, K. Jiang, L. Xu, M. Guan, J. Bao, H. Ji, H. Li, *Inorg. Chem. Front.* **2020**, *7*, 4461.
[225] J. Jin, J. Xia, X. Qian, T. Wu, H. Ling, A. Hu, M. Li, T. Hang, *Electrochim. Acta* **2019**, *299*, 567.
[226] M. Chen, S. Lu, X. Z. Fu, J. L. Luo, *Adv. Sci.* **2020**, *7*, 1903777.
[227] L. Yu, J. F. Yang, B. Y. Guan, Y. Lu, X. W. D. Lou, *Angew. Chemie - Int. Ed.* **2018**, *57*, 172.
[228] J. Liu, Y. Zheng, Z. Wang, Z. Lu, A. Vasileff, S. Z. Qiao, *Chem. Commun.* **2018**, *54*, 463.
[229] Y. Bi, Z. Cai, D. Zhou, Y. Tian, Q. Zhang(m), Q. Zhang(f), Y. Kuang, Y. Li, X. Sun, X. Duan, *J. Catal.* **2018**, *358*, 100.
[230] P. Babar, A. Lokhande, V. Karade, B. Pawar, M. G. Gang, S. Pawar, J. H. Kim, *ACS Sustain. Chem. Eng.* **2019**, *7*, 10035.
[231] L. Wang, X. Huang, J. Xue, *ChemSusChem* **2016**, *9*, 1835.
[232] H. Yang, S. Luo, Y. Bao, Y. Luo, J. Jin, J. Ma, *Inorg. Chem. Front.* **2017**, *4*, 1173.
[233] J. Zhou, L. Yu, Q. Zhu, C. Huang, Y. Yu, *J. Mater. Chem. A* **2019**, *7*, 18118.
[234] X. Su, X. Li, C. Y. A. Ong, T. S. Herng, Y. Wang, E. Peng, J. Ding, *Adv. Sci.* **2019**, *6*, 1801670.
[235] F. C. Walsh, L. F. Arenas, C. Ponce de León, *J. Chem. Technol. Biotechnol.* **2018**, *93*, 3073.
[236] H. Sun, J. Zhu, D. Baumann, L. Peng, Y. Xu, I. Shakir, Y. Huang, X. Duan, *Nat. Rev. Mater.* **2019**, *4*, 45.
[237] Q. Xu, Y. Lv, C. Dong, T. S. Sreeprased, A. Tian, H. Zhang, Y. Tang, Z. Yu, N. Li, *Nanoscale* **2015**, *7*, 10883.
[238] J. Kim, D. Ouyang, H. Lu, F. Ye, Y. Guo, N. Zhao, W. C. H. Choy, *Adv. Energy Mater.* **2020**, *10*, 1903919.
[239] R. Ahmad, N. Tripathy, M. S. Ahn, J. Y. Yoo, Y. B. Hahn, *ACS Sensors* **2018**, *3*, 772.
[240] R. Ahmad, S. M. Majhi, X. Zhang, T. M. Swager, K. N. Salama, *Recent progress and perspectives of gas sensors based on vertically oriented ZnO nanomaterials*, Vol. 270, Elsevier B.V., **2019**, pp. 1–27.
[241] J. Weng, X. Lu, P. X. Gao, *Catalysts* **2017**, *7*, 253.
[242] H. Chen, S. Yang, *Nanoscale Horizons* **2016**, *1*, 96.
[243] H. Zhu, L. Li, W. Zhou, Z. Shao, X. Chen, *J. Mater. Chem. B* **2016**, *4*, 7333.
[244] X. Ke, Z. Li, L. Gan, J. Zhao, G. Cui, W. Kellogg, D. Matera, D. Higgins, G. Wu, *Electrochim. Acta* **2015**, *170*, 337.
[245] Y. Chen, S. Lu, S. Zhang, Y. Li, Z. Qu, Y. Chen, B. Lu, X. Wang, X. Feng, *Sci. Adv.* **2017**, *3*, e1701629.
[246] Y. Wang, Z. Li, J. Wang, J. Li, Y. Lin, *Trends Biotechnol.* **2011**, *29*, 205.
[247] G. Jayanthi Kalaivani, S. K. Suja, *Food Chem.* **2019**, *298*, 124981.
[248] S. Bag, A. Baksi, S. H. Nandam, D. Wang, X. Ye, J. Ghosh, T. Pradeep, H. Hahn, *ACS Nano* **2020**, *14*, 5543.
[249] N. I. Chandrasekaran, M. Manickam, *Sensors Actuators, B Chem.* **2019**, *288*, 188.
[250] S. Moolayadukkam, S. Thomas, R. C. Sahoo, C. H. Lee, S. U. Lee, H. S. S. R. Matte, *ACS Appl. Mater. Interfaces* **2020**, *12*, 6193.
[251] S. Wu, H. Huang, X. Feng, C. Du, W. Song, *Talanta* **2017**, *167*, 385.
[252] S. Mani, S. Ramaraj, S. M. Chen, B. Dinesh, T. W. Chen, *J. Colloid Interface Sci.* **2017**, *507*, 378.

[253] A. T. E. Vilian, B. Dinesh, M. Rethinasabapathy, S. K. Hwang, C. S. Jin, Y. S. Huh, Y. K. Han, *J. Mater. Chem. A* **2018**, *6*, 14367.
[254] M. Ko, L. Mendecki, A. M. Eagleton, C. G. Durbin, R. M. Stolz, Z. Meng, K. A. Mirica, *J. Am. Chem. Soc.* **2020**, jacs. 9b13402.
[255] A. Esmaeeli, A. Ghaffarinejad, A. Zahedi, O. Vahidi, *Sensors Actuators, B Chem.* **2018**, *266*, 294.
[256] C. Wei, X. Zou, Q. Liu, S. Li, C. Kang, W. Xiang, *Electrochim. Acta* **2020**, *334*, 135630.
[257] D. Chu, F. Li, X. Song, H. Ma, L. Tan, H. Pang, X. Wang, D. Guo, B. Xiao, *J. Colloid Interface Sci.* **2020**, *568*, 130.
[258] X. Wang, Y. Zheng, J. Yuan, J. Shen, J. Hu, A. J. Wang, L. Wu, L. Niu, *Electrochim. Acta* **2017**, *224*, 628.
[259] J. Yang, M. Cho, Y. Lee, *Biosens. Bioelectron.* **2016**, *75*, 15.
[260] J. Zhao, J. Chen, S. Xu, M. Shao, Q. Zhang, F. Wei, J. Ma, M. Wei, D. G. Evans, X. Duan, *Adv. Funct. Mater.* **2014**, *24*, 2938.
[261] M. Shao, F. Ning, Y. Zhao, J. Zhao, M. Wei, D. G. Evans, X. Duan, *Chem. Mater.* **2012**, *24*, 1192.
[262] N. Pal, S. Banerjee, A. Bhaumik, *J. Colloid Interface Sci.* **2018**, *516*, 121.
[263] F. Muench, S. Schaefer, L. Hagelüken, L. Molina-Luna, M. Duerrschnabel, H. J. Kleebe, J. Brötz, A. Vaskevich, I. Rubinstein, W. Ensinger, *ACS Appl. Mater. Interfaces* **2017**, *9*, 31142.
[264] M. Lelental, *J. Electrochem. Soc.* **1973**, *120*, 1650.
[265] J. I. Langford, A. J. C. Wilson, *J. Appl. Crystallogr.* **1978**, *11*, 102.
[266] Y. Yamauchi, T. Itagaki, T. Yokoshima, K. Kuroda, *Dalt. Trans.* **2012**, *41*, 1210.
[267] Z. Xia, W. Wen, *Nanomaterials* **2016**, *6*, 19.
[268] X. Tian, C. Cheng, L. Qian, B. Zheng, H. Yuan, S. Xie, D. Xiao, M. M. F. Choi, *J. Mater. Chem.* **2012**, *22*, 8029.
[269] M. Li, K. Y. Ma, J. P. Cheng, D. Lv, X. B. Zhang, *J. Power Sources* **2015**, *286*, 438.
[270] B. Xiao, W. Zhu, Z. Li, J. Zhu, X. Zhu, G. Pezzotti, *R. Soc. Open Sci.* **2018**, *5*.
[271] Y. Zhao, G. Fan, L. Yang, Y. Lin, F. Li, *Nanoscale* **2018**, *10*, 13555.
[272] Z. Zeng, P. Sun, J. Zhu, X. Zhu, *RSC Adv.* **2015**, *5*, 17550.
[273] P. E. Sharel, D. Liu, R. A. Lazenby, J. Sloan, M. Vidotti, P. R. Unwin, J. V. Macpherson, *J. Phys. Chem. C* **2016**, *120*, 16059.
[274] D. Martín-Yerga, G. Henriksson, A. Cornell, *Electrocatalysis* **2019**, *10*, 489.
[275] M. Tian, W. Wang, Y. Wei, R. Yang, *J. Power Sources* **2012**, *211*, 46.
[276] X. Gong, Y. Gu, F. Zhang, Z. Liu, Y. Li, G. Chen, B. Wang, *Front. Mater.* **2019**, *6*, 1.
[277] M. Yang, H. Cheng, Y. Gu, Z. Sun, J. Hu, L. Cao, F. Lv, M. Li, W. Wang, Z. Wang, S. Wu, H. Liu, Z. Lu, *Nano Res.* **2015**, *8*, 2744.
[278] S. Wu, H. Guo, K. S. Hui, K. N. Hui, *Electrochim. Acta* **2019**, *295*, 759.
[279] H. Li, L. Zhang, Y. Mao, C. Wen, P. Zhao, *Nanoscale Res. Lett.* **2019**, *14*, 135.
[280] J. Li, J. Li, Z. Ding, X. Zhang, Y. Li, T. Lu, Y. Yao, W. Mai, L. Pan, *Chem. Eng. J.* **2019**, *378*, 122108.
[281] L. D. Burke, *Electrochim. Acta* **1994**, *39*, 1841.
[282] P. Chaturvedi, S. Sarker, X. Chen, S. Das, H. Luo, S. N. Smirnov, *ACS Sustain. Chem. Eng.* **2019**, *7*, 11303.
[283] W. Lu, X. Qin, A. M. Asiri, A. O. Al-Youbi, X. Sun, *Analyst* **2013**, *138*, 417.
[284] M. Fleischmann, K. Korinek, D. Pletcher, *J. Electroanal. Chem.* **1972**, *34*, 499.
[285] M. Fleischmann, K. Korinek, D. Pletcher, *J. Electroanal. Chem.* **1971**, *31*, 39.
[286] L. M. Lu, L. Zhang, F. L. Qu, H. X. Lu, X. B. Zhang, Z. S. Wu, S. Y. Huan, Q. A. Wang, G. L. Shen, R. Q. Yu, *Biosens. Bioelectron.* **2009**, *25*, 218.
[287] S. M. Jung, H. Y. Jung, M. S. Dresselhaus, Y. J. Jung, J. Kong, *Sci. Rep.* **2012**, *2*, 1.

[288] T. Zhu, Y. Zhang, L. Luo, X. Zhao, *ACS Appl. Mater. Interfaces* **2019**, *11*, 10856.
[289] M. R. Mahmoudian, W. J. Basirun, P. M. Woi, M. Sookhakian, R. Yousefi, H. Ghadimi, Y. Alias, *Mater. Sci. Eng. C* **2016**, *59*, 500.
[290] W. Huang, Y. Cao, Y. Chen, J. Peng, X. Lai, J. Tu, *Appl. Surf. Sci.* **2017**, *396*, 804.
[291] K. Xia, C. Yang, Y. Chen, L. Tian, Y. Su, J. Wang, L. Li, *Sensors Actuators, B Chem.* **2017**, *240*, 979.
[292] L. Wang, X. Miao, Y. Qu, C. Duan, B. Wang, Q. Yu, J. Gao, D. Song, Y. Li, Z. Yin, *J. Electroanal. Chem.* **2020**, *858*, 113810.
[293] M. Li, L. Fang, H. Zhou, F. Wu, Y. Lu, H. Luo, Y. Zhang, B. Hu, *Appl. Surf. Sci.* **2019**, *495*, 143554.
[294] Z. Xu, C. Du, H. Yang, J. Huang, X. Zhang, J. Chen, *Chem. Eng. J.* **2021**, *421*, 127871.
[295] F. Liu, L. Zeng, Y. Chen, R. Zhang, R. Yang, J. Pang, L. Ding, H. Liu, W. Zhou, *Nano Energy* **2019**, *61*, 18.
[296] K. N. Dinh, Q. Liang, C. F. Du, J. Zhao, A. I. Y. Tok, H. Mao, Q. Yan, *Nano Today* **2019**, *25*, 99.
[297] C. Ye, Q. Qin, J. Liu, W. Mao, J. Yan, Y. Wang, J. Cui, Q. Zhang, L. Yang, Y. Wu, *J. Mater. Chem. A* **2019**, *7*, 4998.
[298] Y. Wang, Z. Yin, G. Yan, Z. Wang, X. Li, H. Guo, J. Wang, *Electrochim. Acta* **2020**, *336*, 135734.
[299] Y. Guo, X. Hong, Y. Wang, Q. Li, J. Meng, R. Dai, X. Liu, L. He, L. Mai, *Adv. Funct. Mater.* **2019**, *29*, 1809004.
[300] H. Liu, J. Zhu, Z. Li, Z. Shi, J. Zhu, H. Mei, *Chem. Eng. J.* **2021**, *403*, 126325.
[301] Y. Ouyang, X. Xia, H. Ye, L. Wang, X. Jiao, W. Lei, Q. Hao, *ACS Appl. Mater. Interfaces* **2018**, *10*, 3549.
[302] Y. Wu, C. Cao, *Sci. China Mater. 2018 6112* **2018**, *61*, 1517.
[303] X. He, R. Li, J. Liu, Q. Liu, R. R. chen, D. Song, J. Wang, *Chem. Eng. J.* **2018**, *334*, 1573.
[304] X. Wang, Y. Fang, B. Shi, F. Huang, F. Rong, R. Que, *Chem. Eng. J.* **2018**, *344*, 311.
[305] C. Li, J. Balamurugan, D. C. Nguyen, N. H. Kim, J. H. Lee, *ACS Appl. Mater. Interfaces* **2020**, *12*, 21505.
[306] P. Bandyopadhyay, G. Saeed, N. H. Kim, J. H. Lee, *Chem. Eng. J.* **2020**, *384*, 123357.
[307] J. Zhao, Z. Li, T. Shen, X. Yuan, G. Qiu, Q. Jiang, Y. Lin, G. Song, A. Meng, Q. Li, *J. Mater. Chem. A* **2019**, *7*, 7918.
[308] C. Chen, S. Wang, X. Luo, W. Gao, G. Huang, Y. Zeng, Z. Zhu, *J. Power Sources* **2019**, *409*, 112.
[309] A. D. Deshmukh, A. R. Urade, A. P. Nanwani, K. A. Deshmukh, D. R. Peshwe, P. Sivaraman, S. J. Dhoble, B. K. Gupta, *ACS Omega* **2018**, *3*, 7204.
[310] P. Sundriyal, S. Bhattacharya, *Sci. Reports 2020 101* **2020**, *10*, 1.
[311] W. Yuan, S. Zou, X. Liu, K. Liu, C. Lv, P. Xie, Y. Yin, Y. Li, Z. Wu, *ACS Sustain. Chem. Eng.* **2020**, *8*, 16869.
[312] W. Cai, T. Lai, J. Lai, H. Xie, L. Ouyang, J. Ye, C. Yu, *Sci. Reports 2016 61* **2016**, *6*, 1.
[313] K. Krois, L. Hüfner, J. Gläsel, B. J. M. Etzold, *Chemie Ing. Tech.* **2019**, *91*, 889.
[314] J. Zhu, L. Wei, Q. Liu, X. Kong, *Mater. Chem. Phys.* **2020**, *247*, 122786.
[315] M. Zhang, H. Fan, X. Ren, N. Zhao, H. Peng, C. Wang, X. Wu, G. Dong, C. Long, W. Wang, Y. Gao, L. Ma, P. Wu, H. Li, X. Jiang, *J. Power Sources* **2019**, *418*, 202.
[316] C. Su, S. Xu, L. Zhang, X. Chen, G. Guan, N. Hu, Y. Su, Z. Zhou, H. Wei, Z. Yang, Y. Qin, *Electrochim. Acta* **2019**, *305*, 81.
[317] L. Zhi, W. Zhang, L. Dang, J. Sun, F. Shi, H. Xu, Z. Liu, Z. Lei, *J. Power Sources* **2018**, *387*, 108.
[318] Y. Wang, Z. Yin, Z. Wang, X. Li, H. Guo, J. Wang, D. Zhang, *Electrochim. Acta* **2019**, *293*, 40.

[319] M. Zeiger, T. Ariyanto, B. Krüner, N. J. Peter, S. Fleischmann, B. J. M. Etzold, V. Presser, *J. Mater. Chem. A* **2016**, *4*, 18899.

[320] Ö. Budak, M. Geißler, D. Becker, A. Kruth, A. Quade, R. Haberkorn, G. Kickelbick, B. J. M. Etzold, V. Presser, *ACS Appl. Energy Mater.* **2020**, *3*, 4275.

[321] S. Rafai, C. Qiao, M. Naveed, Z. Wang, W. Younas, S. Khalid, C. Cao, *Chem. Eng. J.* **2019**, *362*, 576.

[322] W. Younas, M. Naveed, C. Cao, S. Khalid, S. Rafai, Z. Wang, Y. Wu, L. Yang, *Appl. Surf. Sci.* **2020**, *505*, 144618.

[323] Q. Zhu, D. Zhao, M. Cheng, J. Zhou, K. Asare Owusu, L. Mai, Y. Yu, Q. Zhu, D. Zhao, M. Cheng, J. Zhou, Y. Yu, K. A. Owusu, L. Mai, *Adv. Energy Mater.* **2019**, *9*, 1901081.

[324] S. C. Sekhar, G. Nagaraju, J. S. Yu, *Nano Energy* **2017**, *36*, 58.

[325] R. Patel, J. T. Park, M. Patel, J. K. Dash, E. B. Gowd, R. Karpoormath, A. Mishra, J. Kwak, J. H. Kim, *J. Mater. Chem. A* **2017**, *6*, 12.

[326] X. Li, D. Du, Y. Zhang, W. Xing, Q. Xue, Z. Yan, *J. Mater. Chem. A* **2017**, *5*, 15460.

[327] H. Guan, P. Cai, X. Zhang, Y. Zhang, G. Chen, C. Dong, *J. Mater. Chem. A* **2018**, *6*, 13668.

[328] T. Wang, S. Zhang, X. Yan, M. Lyu, L. Wang, J. Bell, H. Wang, *ACS Appl. Mater. Interfaces* **2017**, *9*, 15510.

[329] Y. Tao, L. Ruiyi, Z. Lin, M. Chenyang, L. Zaijun, *Electrochim. Acta* **2015**, *176*, 1153.

[330] S. M. Cha, G. Nagaraju, S. Chandra Sekhar, J. S. Yu, *J. Mater. Chem. A* **2017**, *5*, 2224.

[331] A. A. Ensafi, N. Ahmadi, B. Rezaei, *RSC Adv.* **2015**, *5*, 91448.

[332] N. Zhao, H. Fan, M. Zhang, C. Wang, X. Ren, H. Peng, H. Li, X. Jiang, X. Cao, *J. Alloys Compd.* **2019**, *796*, 111.

[333] L.-Q. Mai, A. Minhas-Khan, X. Tian, K. M. Hercule, Y.-L. Zhao, X. Lin, X. Xu, *Nat. Commun.* **2013**, *4*, 2923.

[334] H. S. Jadhav, A. C. Lim, A. Roy, J. G. Seo, *ChemistrySelect* **2019**, *4*, 2409.

[335] Q. Pan, F. Zheng, D. Deng, B. Chen, Y. Wang, *ACS Appl. Mater. Interfaces* **2021**, *13*, 56692.

[336] F. Wang, S. Sun, Y. Xu, T. Wang, R. Yu, H. Li, *Sci. Reports 2017 71* **2017**, *7*, 1.

[337] A. C. Gandhi, C. Y. Huang, C. C. Yang, T. S. Chan, C. L. Cheng, Y. R. Ma, S. Y. Wu, *Nanoscale Res. Lett.* **2011**, *6*, 1.

[338] J. Chen, L. Zeng, X. Chen, T. Liao, J. Zheng, *Bioact. Mater.* **2018**, *3*, 315.

[339] D. Zha, H. Sun, Y. Fu, X. Ouyang, X. Wang, *Electrochim. Acta* **2017**, *236*, 18.

[340] L. Liu, T. Guan, L. Fang, F. Wu, Y. Lu, H. Luo, X. Song, M. Zhou, B. Hu, D. Wei, H. Shi, *J. Alloys Compd.* **2018**, *763*, 926.

[341] X. Cai, X. Shen, L. Ma, Z. Ji, C. Xu, A. Yuan, *Chem. Eng. J.* **2015**, *268*, 251.

[342] T. -C. Liu, W. G. Pell, B. E. Conway, S. L. Roberson, *J. Electrochem. Soc.* **1998**, *145*, 1882.

[343] F. Qian, P. C. Lan, M. C. Freyman, W. Chen, T. Kou, T. Y. Olson, C. Zhu, M. A. Worsley, E. B. Duoss, C. M. Spadaccini, T. Baumann, T. Y. J. Han, *Nano Lett.* **2017**, *17*, 7171.

[344] O. Picht, S. Müller, I. Alber, M. Rauber, J. Lensch-Falk, D. L. Medlin, R. Neumann, M. E. Toimil-Molares, *J. Phys. Chem. C* **2012**, *116*, 5367.

[345] Y. Liu, N. Fu, G. Zhang, M. Xu, W. Lu, L. Zhou, H. Huang, *Adv. Funct. Mater.* **2017**, *27*, 1605307.

[346] K. N. Kang, A. Ramadoss, J. W. Min, J. C. Yoon, D. Lee, S. J. Kang, J. H. Jang, *Nano-Micro Lett.* **2020**, *12*, 1.

[347] R. Li, Z. Hu, X. Shao, P. Cheng, S. Li, W. Yu, W. Lin, D. Yuan, *Sci. Reports 2016 61* **2016**, *6*, 1.

[348] M. A. Abbasi, K. M. Amin, M. Ali, Z. Ali, M. Atif, W. Ensinger, W. Khalid, *J. Environ. Chem. Eng.* **2022**, *10*, 107078.

[349] X. Zhang, L. Zhang, G. Xu, A. Zhao, S. Zhang, T. Zhao, *J. Colloid Interface Sci.* **2020**, *561*, 23.
[350] X. Y. Yu, H. Bin Wu, L. Yu, F. X. Ma, X. W. Lou, *Angew. Chemie - Int. Ed.* **2015**, *54*, 4001.
[351] K. M. A. Amin, H. M. A. Amin, In *Corrosion Protection of Metals and Alloys Using Graphene and Biopolymer Based Nanocomposites* (Eds.: Amin, H. M. A.; Galal, A.), CRC Press, First. | Boca Raton : CRC Press is an imprint of Taylor &, **2021**, pp. 81–98.
[352] G. Nagaraju, S. C. Sekhar, B. Ramulu, J. S. Yu, *Small* **2019**, *15*.
[353] W. Xu, Z. Jiang, Q. Yang, W. Huo, M. S. Javed, Y. Li, L. Huang, X. Gu, C. Hu, *Nano Energy* **2018**, *43*, 168.
[354] S. Niu, Z. Wang, M. Yu, M. Yu, L. Xiu, S. Wang, X. Wu, J. Qiu, *ACS Nano* **2018**, *12*, 3928.
[355] Y. Wang, X. Lin, T. Liu, H. Chen, S. Chen, Z. Jiang, J. Liu, J. Huang, M. Liu, *Adv. Funct. Mater.* **2018**, *28*, 1806207.
[356] J. Xu, Q. Wang, X. Wang, Q. Xiang, B. Liang, D. Chen, G. Shen, *ACS Nano* **2013**, *7*, 5453.
[357] L. Yu, W. Li, C. Wei, Q. Yang, Y. Shao, J. Sun, *Nano-Micro Lett.* **2020**, *12*, 1.
[358] H. Wang, C. Xu, Y. Chen, Y. Wang, *Energy Storage Mater.* **2017**, *8*, 127.
[359] D. Tian, N. Song, M. Zhong, X. Lu, C. Wang, *ACS Appl. Mater. Interfaces* **2020**, *12*, 1280.
[360] R. Ramachandran, Y. Lan, Z. X. Xu, F. Wang, *ACS Appl. Energy Mater.* **2020**, *3*, 6633.
[361] X. Sun, G. Wang, H. Sun, F. Lu, M. Yu, J. Lian, *J. Power Sources* **2013**, *238*, 150.
[362] F. Wang, X. Liu, G. Duan, H. Yang, J. Y. Cheong, J. Lee, J. Ahn, Q. Zhang, S. He, J. Han, Y. Zhao, I. D. Kim, S. Jiang, *Small* **2021**, *17*, 1.
[363] Y. M. Jeong, I. Son, S. H. Baek, *Appl. Surf. Sci.* **2019**, *467–468*, 963.
[364] Q. Wang, D. Chen, D. Zhang, *RSC Adv.* **2015**, *5*, 96448.
[365] S. Gao, F. Liao, S. Ma, L. Zhu, M. Shao, *J. Mater. Chem. A* **2015**, *3*, 16520.
[366] J.-X. Feng, S.-H. Ye, X.-F. Lu, Y.-X. Tong, G.-R. Li, *ACS Appl. Mater. Interfaces* **2015**, *7*, 11444.
[367] G.-C. Li, P.-F. Liu, R. Liu, M. Liu, K. Tao, S.-R. Zhu, M.-K. Wu, F.-Y. Yi, L. Han, *Dalt. Trans.* **2016**, *45*, 13311.
[368] G. Yilmaz, K. M. Yam, C. Zhang, H. J. Fan, G. W. Ho, *Adv. Mater.* **2017**, *29*.
[369] B. Li, Y. Shi, K. Huang, M. Zhao, J. Qiu, H. Xue, H. Pang, *Small* **2018**, *14*.
[370] B. Y. Guan, L. Yu, X. Wang, S. Song, X. W. D. Lou, *Adv. Mater.* **2017**, *29*.
[371] S. Li, C. Shi, Y. Pan, Y. Wang, *Diam. Relat. Mater.* **2021**, *115*, 108358.
[372] C. Wan, Y. Jiao, D. Liang, Y. Wu, J. Li, *Adv. Energy Mater.* **2018**, *8*.
[373] F. Lai, Y. Huang, Y. E. Miao, T. Liu, *Electrochim. Acta* **2015**, *174*, 456.
[374] M. Huang, Y. Y. Wang, J. Chen, D. He, J. He, Y. Y. Wang, *Electrochim. Acta* **2021**, *381*, 138289.

List of Figures

electrochemically reinforced Ni back layer b) Top view of the NTNW before surface etching. c) Top view of the NTNW after removal of the surface layer by etching. SEM top view images of NiCo-LDH@Ni-NTNWs after (d, g) 60 s, (e, h) 120 s and (f, i) 300 s of hydroxide electrodeposition.

Figure 3.3. XRD patterns of the three NTNW catalysts investigated in this study.

Figure 3.4. SEM images of (a-c) Ni-NTNW, (d-f) $Ni(OH)_2$@Ni-NTNW, and (g-i) NiCo-LDH@Ni-NTNW electrodes, accompanied by photographs of the three as-prepared stand-alone electrodes (j), higher magnification of a single NiCo-LDH@Ni-NTNW electrode (k), and Ni back supporting layer before soldering (l).

Figure 3.5. TEM analysis of the NiCo-LDH@Ni-NTNW catalyst, including EDX spectra obtained for the highlighted shell (1) and core (2) regions of the hierarchical nanotube. The Cu signal stems from the TEM holder.

Figure 3.6. (a) CV curves of the pristine Ni-NTNW and its $Ni(OH)_2$ and NiCo-LDH derivatives (electrolyte: 0.1 M NaOH; scan rate: 10 mV s^{-1}).

Figure 3.7. CV curves of (a) Ni-NTNW, (b) $Ni(OH)_2$@Ni-NTNW, and (c) NiCo-LDH@Ni-NTNW at various scan rates in 0.1 M NaOH. (d-f) the corresponding peak currents as function of the square root of scan rate.

Figure 3.8. (a) Amperometric glucose sensing curves of the three catalyst electrodes (0.6 V, 0.1 M NaOH, stepwise addition of 3 µM, 10 µm, 100, and 500 µM glucose, respectively). Inset: $I-t$ curves at the lowest glucose concentration change. (b) Calibration curves derived from the sensing measurements (The error bars represent the standard error of triplicate determinations for each concentration). Inset: Linear fits of the two linear concentration regimes used to extract the sensitivity of the electrodes.

Figure 3.9. (a) Interference study, comparing the current response of the different electrodes towards the analyte glucose oxidation in 0.1 M NaOH with the successive step addition of 50 µM of glucose and other interferents. (b) Amperometric investigation of the catalyst stability at 0.6 V (100 mM glucose in stirred 0.1 M NaOH).

Figure 3.10. Pipe cactus-inspired design philosophy of the NiCo-LDH@Ni-NTNW self-supported electrode.

Figure 3.11. Schematic illustration presenting photographs of the self-supported NiCo-LDH@Ni-NTNW electrode through the fabrication process. After electroless plating of Ni (step1), electrodeposition is conducted (step 2) to get a thicker supporting layer of Ni on one side of the template (the bright round area in the sample center). In step 3, the other side of the sample is chemically etched to eliminate the electrolesssly deposited surface layer, followed by dissolution of the polymer matrix to isolate the Ni-NTNW (step 4). The final NiCo-LDH@Ni-NTNW electrode is obtained by electrodeposition of LDH (step 5).

Figure 3.12. SEM top view of Ni-NTNW (a, b) and NiCo-LDH@Ni-NTNW (d, e). SEM lateral view with EDX spectra of Ni-NTNW (c) and NiCo-LDH@Ni-NTNW (f).

Figure 3.13. (a) XRD patterns of Ni-NTNW, NiCo-LDH@Ni-NTNW, and the reference peaks of the JCPDS file No. 40-0216. (b) Raman spectrum of NiCo-LDH@Ni-NTNW, (c)TEM lateral view of NiCo-LDH@Ni-NTNW with a dashed turquoise line representing the borders of the core Ni-NTNW and dashed rose color representing the surrounding NiCo-LDH shell, and (d) EDX spectra at two different spots in the TEM micrograph representing the center of the tube (position 1) and the center of NiCo-LDH coating nanosheets (position 2).

Figure 3.14. (a) Schematic illustration of the three-electrode cell employed for electrochemical evaluation. (b) CV of Ni-NTNW and NiCo-LDH@Ni-NTNW electrodes at 10 mV/s. (c) CV curves conducted at different scan rates between 2-100 mV/s and (d) the corresponding oxidation and reduction peak currents as a function of $v^{1/2}$ of NiCo-LDH@Ni-NTNW electrode. (e) Volumetric and gravimetric capacities of Ni-NTNW and NiCo-LDH@Ni-NTNW electrodes estimated from CV curves at different scan rates. (f) GCD curves of Ni-NTNW and NiCo-LDH@Ni-NTNW electrodes at 0.2 mA/cm^2. (g) Gravimetric and areal capacities (h) volumetric capacities of Ni-NTNW and NiCo-LDH@Ni-NTNW electrodes estimated from GCD curves at

List of Tables